Semiconductors, Vol. 34, No. 6, 2000, pp. 615–617. Translated from Fizika i Tekhnika Poluprovodnikov, Vol. 34, No. 6, 2000, pp. 641–643.

ATOMIC STRUCTURE AND NONELECTRONIC PROPERTIES OF SEMICONDUCTORS

Investigation of the Influence of External Effects on the Behavior of Gold Impurity in Silicon

S. Z. Zaĭnabidinov, O. O. Mamatkarimov, I. G. Tursunov, and U. A. Tuĭchiev

Tashkent State University, Universitetskaya ul. 95, Vuzgorodok, Tashkent, 700095 Uzbekistan

Submitted May 2, 1999; accepted for publication November 29, 1999

Abstract—Properties of gold atoms in silicon and the change of their energy levels under uniform pressure are investigated. The investigations demonstrated that the band gap of silicon varies under the influence of pressure (P) and temperature (T) with a rate $\partial E/\partial P = -1.5 \times 10^{-11}$ eV/Pa and $\partial E/\partial T = -3.2 \times 10^{-6}$ eV/K. © *2000 MAIK "Nauka/Interperiodica".*

Deformation-induced variation of deep-level energies, which strongly affects the electrical properties of semiconductors and depends on the degree of distortion of internal bonds in the lattice, can provide important information about deep levels in semiconductor crystals.

The model of the deep center of Au in Si, in which the Au atom lattice site was related to a charge state of the center, was suggested in [1, 2]. A specific feature of this model is the possibility of varying the charge state of the center via the tunneling transition.

In this paper, the properties of the gold atom in silicon and the variation of its energy levels under hydrostatic pressure are considered.

The samples for investigations were $3 \times 3 \times 7$ mm^3 in size. Single crystals of Si were doped with gold from the diffusant layer, which was deposited on the surface of silicon in vacuum using a UVN-2M-2 installation. Diffusion was carried out in SOUL-4M furnaces in the temperature range of 950–1200°C. Subsequent to diffusion annealing, the samples were quenched in water; the cooling rate was $V = 200$ K/s.

In order to investigate the influence of defects induced by thermal treatment on the parameters of silicon, reference samples treated in similar conditions without doping were used in all of the experiments. Nonrectifying contacts were deposited on all of the samples according to [3], and their electrical conductivity was determined from the Hall measurements.

Electrophysical parameters (electron concentration N, mobility μ, and resistivity ρ) of the n-Si:Au samples investigated by us are listed in Table 1.

Properties of the n-Si:Au samples were studied using a setup for unifrom compression with a pneumatic amplifier [4] in the pressure range $P = (0–6) \times 10^8$ Pa at the temperature $T = 300$ K.

Time (t) dependences of the current relative variation I_P/I_0 in the n-Si:Au samples with different resistivity at various pressures are shown in Fig. 1. It can be seen from Fig. 1 that the current increases for all of the samples with an increase in pressure up to $P = (0–6) \times 10^8$ Pa. The current gradually decreased after exposure for 20 s (P = const). The peaks observed (maximum values of the current) depend on the degree of compensation of the sample; namely, the larger the resistivity, the higher the peak. It is our opinion that the gold atoms in the bulk of the Si:Au samples are temporary depleted; i.e., electrons are transferred to the conduction band and start contributing to the current under the influence of pressure. However, the duration of this process is no longer than 20 s. Then the electrons return

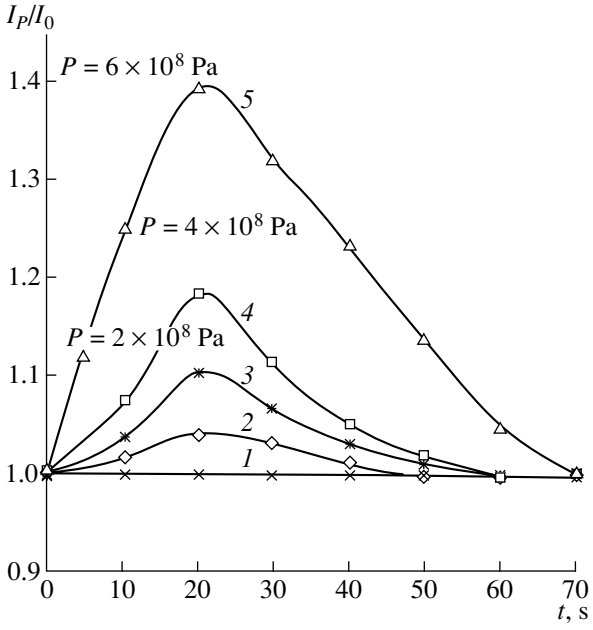

Fig. 1. Kinetic dependences of the current variation induced by pressure in the n-Si:Au samples. Samples: (*1*) Si:P, initial; (*2*) Si:P, reference; (*3*) Si:Au, $\rho \approx 10^2$ Ω cm; (*4*) Si:Au, $\rho \approx 10^3$ Ω cm; and (*5*) Si:Au, $\rho \approx 10^5$ Ω cm.

Table 1. Parameters of the samples

No.	Samples	Conduction type	Temperature of diffusion, °C	ρ, Ω cm	N, cm^{-3}	μ, cm^2/(V s)
1	Si:P	*n*	–	15	3.47×10^{14}	1200
2	Si:Au	*n*	920	1.3×10^2	3.94×10^{13}	1219
3	Si:Au	*p*	960	2×10^2	3.13×10^{14}	500
4	Si:Au	*n*	940	2.9×10^5	1.78×10^{10}	1214
5	Si:P	*n*	–	7	7.4×10^{14}	1200
6	Si:Au	*n*	1050	2.2×10^3	2.7×10^{12}	1073
7	Si:Au	*n*	1100	1.9×10^5	2.7×10^{10}	1220
8	Si:Au	*p*	1200	1.0×10^5	1.8×10^{11}	343
9	Si:Ni	*n*	1230	1.0×10^3	5.81×10^{11}	1080
		p	1250	3.6×10^4	4.67×10^{11}	249
10	Si:Gd	*n*	1260	20.4	2.12×10^{14}	1400

Table 2. Parameters of the levels

Samples	E_i, eV	ΔE_i, eV	α, 10^{-11} eV/Pa	P, 10^8 Pa	Source
Si:Au*	$E_c - 0.54$	0.53	1.81	6	–
Si:Au**	$E_v + 0.36$	0.34	1.97	6	–
Si:Ni	$E_c - 0.42$	0.41	1.12	6	[6]
Si:Ni	$E_v + 0.21$	0.20	1.33	6	–
Si:Gd	$E_v + 0.34$	0.33	0.8	6	[7]

Note: E_i are the energy levels, ΔE_i are the energy level variations under a pressure, * corresponds to sample 2 in Table 1, and ** corresponds to sample 8 in Table 1.

to the gold atoms, and the current begins to fall off to the initial value.

According to [1, 2], three various configuration curves correspond to three possible charge states of Au impurity; the minima of these curves do not coincide. It is important that the center $[V\mathrm{Au}_i]$, which comprises the complex formed by the Au atom displaced into the interstice and vacancy formed because of this displacement, corresponds to the curve with the lowest energy. The Au atom can be readily displaced from the interstice back to the lattice site as a result of compression, since this is precisely the configuration in the material compressed that corresponds to the energy minimum for a system as a whole. As this takes place, another electronic state corresponds to this configuration.

We note that each gold atom in this situation is displaced according to the quasi-chemical reaction

$$[V\mathrm{Au}_i] \xrightarrow{\text{compression}} \mathrm{Au}_s; \quad (1)$$

i.e., it moves from the interstice to the lattice site. Here, Au_s corresponds to the position of the gold atom at the lattice site. After the pressure relief, the system becomes metastable and the onset of spontaneous transition to the state $[V\mathrm{Au}_i]$ is observed:

$$\mathrm{Au}_s \xrightarrow{\text{pressure relief}} [V\mathrm{Au}_i]. \quad (2)$$

It is important that this transition occurs via tunneling according to [1].

The characteristic relaxation time can be calculated as

$$\tau_r = \tau_0 [F_{\mathrm{FC}}]^{-1}, \quad (3)$$

where τ_0 is a quantity with a dimension of time and involves the matrix element and F_{FC} is the Franck–Condon factor, which accounts for the overlapping of the wave functions for the gold atom in two states, namely, Au_s and Au_i.

According to experimental data, the pressure coefficient can be determined from the expression [5]

$$\alpha = (kT/\Delta P)\ln(N_P/N_0). \quad (4)$$

Processing of experimental data yielded the pressure coefficients for the samples containing gold and other impurities. These coefficients are listed in Table 2.

Using the data of Table 2, it is possible to construct an energy diagram for the Si:Au samples; this diagram is shown in Fig. 2.

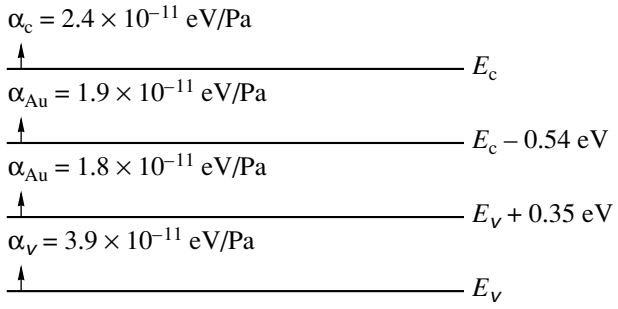

Fig. 2. Energy diagram of the Au levels in Si under pressure.

The bandgap of silicon varies under the influence of pressure and temperature with the rates $\partial E/\partial P = -1.5 \times 10^{-11}$ eV/Pa and $\partial E/\partial T = -3.2 \times 10^{-6}$ eV/K.

In conclusion, it is noteworthy that this effect can be apparently observed only in the case of relatively metastable impurity. From this point of view, it is clear why this effect is not observed in silicon doped with nickel and gadolinium [7]. However, a similar effect can be observed in Si:Mn, since, according to [8], manganese is a metastable impurity in silicon and can migrate, occupying alternatively interstices and lattice sites under the influence of external effects.

ACKNOWLEDGMENTS

We thank A.Yu. Leĭderman for his participation in discussion of the results and for his helpful comments.

REFERENCES

1. N. T. Bagraev and V. A. Mashkov, Pis'ma Zh. Éksp. Teor. Fiz. **39** (5), 211 (1984) [JETP Lett. **39**, 251 (1984)].
2. N. T. Bagraev and V. A. Mashkov, Solid State Commun. **51** (7), 515 (1984).
3. L. P. Pavlov, *Methods for Determination of Key Parameters of Semiconducting Materials* (Vysshaya Shkola, Moscow, 1975).
4. A. Abduraimov, S. Z. Zaĭnabidinov, O. O. Mamatkarimov, *et al.*, Prib. Tekh. Éksp., No. 5, 229 (1992).
5. A. L. Polyakova, *Deformation of Semiconductors and Semiconductor Devices* (Moscow, 1979).
6. A. Abduraimov, S. Z. Zaĭnabidinov, O. O. Mamatkarimov, *et al.*, Fiz. Tekh. Poluprovodn. (St. Petersburg) **27** (3), 516 (1993) [Semiconductors **27** (3), 290 (1993)].
7. O. O. Mamatkarimov, Candidate's Dissertation (Tashkent, 1993).
8. N. T. Bagraev, R. M. Marsaatov, I. S. Polovets, and A. Yusupov, Fiz. Tekh. Poluprovodn. (St. Petersburg) **26** (3), 870 (1992) [Sov. Phys. Semicond. **26** (3), 271 (1992)].

Translated by N. Korovin

Semiconductors, Vol. 34, No. 6, 2000, pp. 618–620. Translated from Fizika i Tekhnika Poluprovodnikov, Vol. 34, No. 6, 2000, pp. 644–646.

ATOMIC STRUCTURE AND NONELECTRONIC PROPERTIES OF SEMICONDUCTORS

Internal Friction Related to Changes in the Shape of Small Inclusions

Yu. N. Andreev*, B. M. Darinskiĭ*, V. A. Moshnikov, D. S. Saĭko***, and N. P. Yaroslavtsev***

** Voronezh State Technical University, Moskovskii pr. 14, Voronezh, 394026 Russia*

*** St. Petersburg State Electrotechnical University, St. Petersburg, 197376 Russia*

**** Voronezh State Technological Academy, pr. Revolyutsii 19, Voronezh, 394017 Russia*

e-mail: kalinin@nsl.vstu.ac.ru

Submitted December 9, 1999; accepted for publication December 21, 1999

Abstract—Sizes of the second-phase microinclusions typical of III–V, II–VI, and IV–VI semiconductor compounds and their derivatives were theoretically estimated. A formula relating the temperature shift of the internal-friction peak caused by the inclusion-shape changes under the effect of sign-alternating elastic stresses to linear inclusion dimensions was derived. The results were confirmed by data on the low-frequency internal friction in SnTe. © *2000 MAIK "Nauka/Interperiodica".*

Materials containing low-melting inclusions of another phase were shown in [1–3] to exhibit a specific internal-friction peak. Several atomic mechanisms that could be responsible for this peak have been proposed. A common feature of all mechanisms is the change in the cavity (inclusion) shape due to host elastic deformation. A subsequent irreversible change in the cavity or inclusion shape can proceed according to the following mechanisms: (i) bulk self-diffusion of host and inclusion materials, (ii) surface self-diffusion over the host–inclusion interface, (iii) viscous slip over the interface, and (iv) a change in the host and inclusion shapes due to plastic deformation.

All the above mechanisms were assessed for sufficiently large inclusions exceeding the unit cell size by several orders of magnitude. These mechanisms were shown to cause the internal-friction peak. The temperature dependence of internal friction, defining the relaxation peak shape, corresponds to the Debye peak if we assume that the most significant contribution is introduced by diffusive mechanisms. At the same time, the temperature dependence measured in [4] for a number of low-melting inclusions exhibited a pronounced asymmetry in the internal-friction peak observed at the inclusion melting point. This counts in favor of the assumption that mechanisms (iii) and (iv) are dominant. The peak height approximately corresponds to a relative volume fraction occupied by inclusions.

In many works, the temperature dependence of internal friction was used for the accurate determination of low-melting inclusion concentrations; this method is covered by an Inventor's Certificate [5].

An urgent problem concerns measuring the concentrations of relatively small inclusions with sizes amounting to 10^2–10^3 lattice constants. Experimental studies of the samples of IV–VI binary compounds showed that the internal-friction peak shifts to lower temperatures by $\Delta T \approx 10$°C and is wider for small inclusions as compared to large inclusions (see Fig. 1).

This work is aimed at explaining these laws inherent in materials with small inclusions.

We consider a medium consisting of a host and inclusions with a cubic lattice, for instance, GaAs–Ga. It is reasonable to believe that crystallographic axis directions coincide in the host and inclusion lattices in the thermodynamic equilibrium state reached during material productions, which allows the attainment of a minimum energy of the matrix–inclusion interface. Under such conditions, the cavity and inclusion should be shaped as regular polyhedrons with a face orientation controlled by the minimum surface energy of the interface.

For simplicity, we assume that the cavity is cubic. Let us designate the host and inclusion lattice constants as a and b, respectively. In general, these are incommensurable, that is, for any integers m and n, the value

$$\Delta = ma - nb \tag{1}$$

(where $nb = l$ is the inclusion edge length) cannot be equal to zero. Inclusion and host materials near the former are in the elastically stressed state. The value Δ and the elastic energy are minimized for the (m, n) spectrum defined by the incommensurability of parameters a and b. For this spectrum, the expression $\Delta(m, n) \le 0.5b$ is valid, where Δ can be positive and negative. In these cases, the inclusion has stretching and compressive strains, respectively. Due to the nonlinear dependence of energy on strain, the second case seems to be improbable; thus, a small number of inclusions is stretched. The inclusion volume increases on

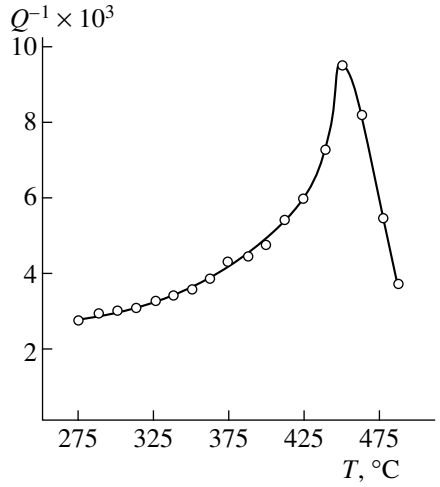

Fig. 1. Temperature dependence of internal friction.

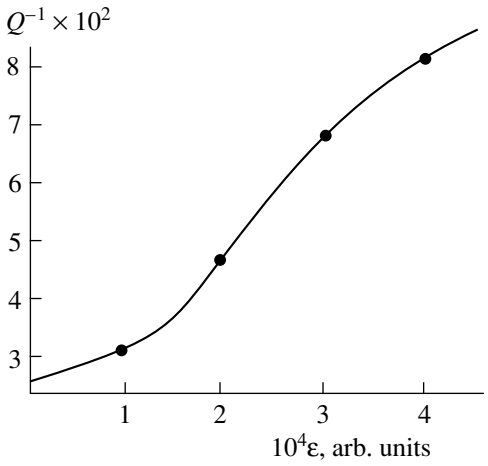

Fig. 2. Dependence of internal friction on strain.

melting, which is accompanied by a change in the elastic stresses. If a relative change in the molten material volume is $\Delta V/V = \gamma \sim 10^{-2}$, the greatest elastic energy decrease due to melting is inherent in inclusions with sizes defined by the condition $\gamma = \Delta/nb$. This yields the estimate $n = \Delta/\gamma b \sim 10^2$. Thus, an appreciable shift in the melting point is attained for relatively small inclusions with sizes not exceeding a few hundred lattice constants.

External stresses at the host–inclusion interface give rise to cleaving stresses τ_i given by

$$\tau_i = \sigma_{ij} n_j - \sigma_{lm} n_l n_m n_i, \quad (2)$$

where σ_{ij} is the stress tensor and n_i is the normal to the surface at a given point of the host–inclusion interface. This cleaving component decreases to zero due to slip at the interface. The slip time τ controls the frequency of the internal-friction peak related to this process and is defined by the effective viscosity coefficient η and the medium elastic modulus G as $\tau = \eta/G$.

The viscosity coefficient abruptly decreases as temperature grows in the vicinity of the inclusion melting point. Initially, the host–inclusion interface atomic structure is substantially rearranged, and then melting proceeds. This causes the internal-friction peak to be asymmetric in the temperature dependencies.

In this work, we pose the problem of the effect of low-melting inclusion sizes on the internal-friction peak temperature position.

The inclusion volume grows on melting, which is accompanied by stress relief. Therefore, a stressed inclusion is molten at a lower temperature. The melting temperature shift is found from the condition for the equality of chemical potentials of liquid (φ_1) and solid (φ_2) phases.

Assuming that the dependences of φ_1 and φ_2 on temperature T are linear in the vicinity of the phase-transition point, we have

$$\varphi_1 = \varphi_{10} - \alpha_1 kT, \quad \varphi_2 = \varphi_{20} - \alpha_2 kT. \quad (3)$$

Therefore, the phase-transition temperature is given by

$$(\varphi_{10} - \varphi_{20})/(\alpha_1 - \alpha_2) = kT. \quad (4)$$

If the inclusion material is stretched, we find the chemical potential additive

$$\varphi_2 \longrightarrow \varphi_{20} + a^3 \varepsilon^2 G/2. \quad (5)$$

Thus, the melting-point shift is given by

$$k\Delta T = Ga^3 \varepsilon^2/2(\alpha_1 - \alpha_2). \quad (6)$$

To estimate the strain ε, we should take into account the relationship between the host and inclusion unit cells. If the size $l \sim ma \sim nb$, the additional strain is $\varepsilon \sim a/l$.

Substituting this value into the formula for ΔT, we arrive at

$$\Delta T \sim (Ga^3/2k\Delta\alpha)(a/l)^2. \quad (7)$$

Assuming that $Ga^3 = 1$ eV, $a/l = 0.01$, and $\alpha_1 - \alpha_2 = 0.3$ in our estimates, which corresponds to tellurium parameters, we find $\Delta T \sim 2$°C. The experimentally observed peak shift (see Fig. 1) is about 10°C; thus, the internal-friction peak shift can be explained by inclusion stresses arising due to incommensurable host and inclusion lattice constants.

Formula (7) shows that the internal-friction peak shift to lower temperatures grows as the inclusion linear dimension decreases. If a sample contains a fairly large number of small inclusions, this effect is experimentally detected and can be a convenient method for estimating an average size of low-melting inclusions and their number in a sample.

In conclusion, we note that the considered pattern of stresses initiated by the three-dimensional incommensurability of host and inclusion lattice constants implies that the distribution over possible Δ is shifted to positive values. Hence, cleaving stresses can detach material from the host, which should be accompanied by an amplitude dependence of internal friction. This is what was observed in the experiment (see Fig. 2).

The considered data point to the efficiency of the internal-friction method as applied to determine specific parameters of a system composed of the host and an inclusion of another phase. Previously [1–3], it was established that the internal-friction peak height can be used to estimate the integral characteristic of the medium, that is, the volume concentration of the inclusion material. The above results show that the internal-friction data can also be used to estimate the average size of inclusions. It is virtually impossible to acquire such data by other techniques, such as X-ray microanalysis or electron microscopy.

REFERENCES

1. B. M. Darinskiĭ, Yu. I. Levin, V. S. Postnikov, and S. K. Turkov, Fiz. Khim. Obrab. Mater., No. 6, 46 (1967).
2. B. M. Darinskiĭ, Yu. I. Levin, and S. K. Turkov, Fiz. Khim. Obrab. Mater., No. 3, 51 (1968).
3. B. M. Darinskiĭ and N. P. Yaroslavtsev, Vysokochist. Veshchestva, No. 3, 80 (1990).
4. Yu. N. Andreev, M. V. Bestaev, D. Ts. Dimitrov, *et al.*, Fiz. Tekh. Poluprovodn. (St. Petersburg) **31** (7), 841 (1997) [Semiconductors **31** (7), 714 (1997)].
5. V. I. Mitrokhin, N. P. Yaroslavtsev, S. I. Rembeza, *et al.*, USSR Inventor's Certificate No. 105/42 SSSR G01N11/16 (1985).

Translated by A. Kazantsev

Semiconductors, Vol. 34, No. 6, 2000, pp. 621–625. Translated from Fizika i Tekhnika Poluprovodnikov, Vol. 34, No. 6, 2000, pp. 647–651.

ATOMIC STRUCTURE AND NONELECTRONIC PROPERTIES OF SEMICONDUCTORS

Specifics of MOCVD Formation of $In_xGa_{1-x}N$ Inclusions in a GaN Matrix

I. P. Soshnikov*, V. V. Lundin*, A. S. Usikov*, I. P. Kalmykova*, N. N. Ledentsov*, A. Rosenauer, B. Neubauer**, and D. Gerthsen****

** Ioffe Physicotechnical Institute, Russian Academy of Sciences, Politekhnicheskaya ul. 26, St. Petersburg, 194021 Russia*

*** Laboratorium für Electronenmikroskopie der Universität Karlsruhe, Postfach 6980, D-76128 Karlsruhe, Germany*

Submitted December 29, 1999; accepted for publication December 29, 1999

Abstract—MOCVD-grown heterostructures with one or several $In_xGa_{1-x}N$ layers in a GaN matrix have been studied by transmission electron microscopy. In heterostructures with thick InGaN layers, a noncoherent system of domains with lateral dimensions (~50 nm) on the order of the layer thickness (~40 nm) is formed. In the case of ultrathin InGaN inclusions, nanodomains coherent with the GaN matrix are formed. The content of indium in nanodomains, determined by the DALI method, is as high as $x \approx 0.6$ or more, substantially exceeding the average In concentration. The density of the nanodomains formed in the structures studied is $n \approx (2–5) \times 10^{11}$ cm^{-2}. In the structures with ultrathin InGaN inclusions, two characteristic nanodomain sizes are observed (3–6 and 8–15 nm). © *2000 MAIK "Nauka/Interperiodica".*

Studies of the growth and properties of InGaN-based heterostructures attract considerable interest for two reasons. One is the possible extension of the operation range of microelectronic and optoelectronic devices to green, blue, and near-UV spectral regions and the other is that self-organization effects can be observed in structures of this kind [1, 2].

The structural and optical properties of the III–V nitrides strongly depend on the growth conditions: substrate temperature, reactant flow rates, etc. It was shown in [3–5] that high-quality InGaN-based heterostructures with a high radiative recombination efficiency can be fabricated by MOCVD under special growth conditions. However, only a limited number of attempts have been made until recently to relate the optical properties to structural features: morphology, composition distribution, and the relationship of these with the configuration of the structures. This is explained by difficulties encountered in the structural analysis of the composition and morphology of nanometer-scale objects. In some cases, these problems can be resolved by determining the composition profile by the method of digital analysis of cross-sectional electron micrographs [6, 7] (the digital analysis of lattice images, a DALI software package). In this paper, we report the results of a comparative study of the formation and properties of InGaN inclusions in a GaN matrix in relation to the average thickness of the InGaN layer.

The samples were grown by MOCVD in a modified VP-50 RP (Epiquip) installation with a horizontal inductively heated reactor. A detailed description of the growth process can be found elsewhere [8, 9]. As substrates, we used ~400-μm-thick [0001] sapphire wafers. We note that quantum wells were formed by varying the substrate temperature from 730 to 850°C at constant flows of trimethylindium (TMI) and trimethylgallium (TMG). With this approach, no modulation of the TMI and TMG flow rates is necessary, because the incorporation of In in InGaN decreases strongly with increasing temperature. Figure 1 shows schematically the samples studied.

A Philips CM 200 FEG microscope was used for the transmission electron microscopy (TEM). The samples to be studied were prepared by the conventional method, using in the final stage etching with 4-keV

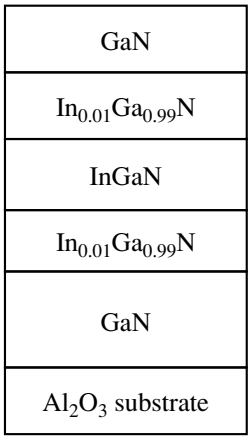

Fig. 1. Cross section of the samples. The InGaN-layer parameters are given in the table.

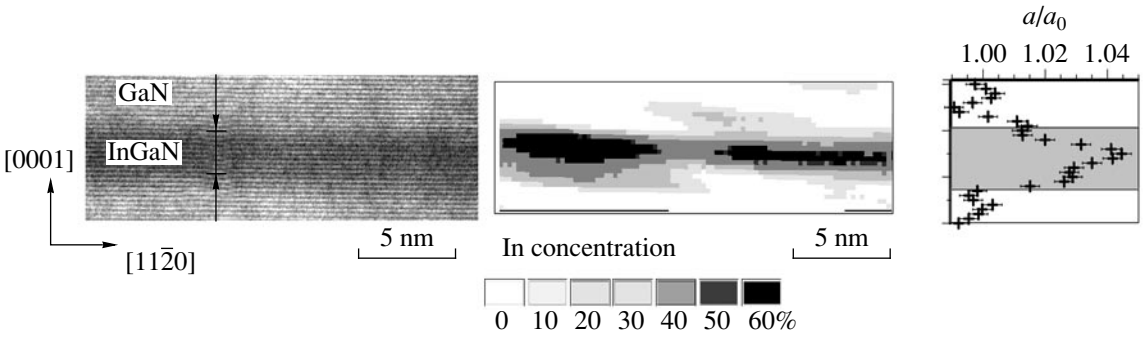

Fig. 2. Cross-sectional HRTEM image of coherent InGaN inclusions in a GaN matrix and the result of DALI processing. a/a_0 is the lattice mismatch.

Ar^+ ions. The composition was analyzed by the DALI method [6, 7] determining local values of the interplanar spacings in the *c*-axis direction. Figure 2 exemplifies the application of the DALI procedure for determining the composition distribution.

InGaN/GaN heterostructures of varied thickness and number of InGaN inclusions were fabricated for the study. The configuration of the heterostructures and the parameters revealed in structural studies are presented in the table.

Figure 3 shows a cross-sectional TEM image of a structure with a thick (~40 nm) InGaN layer. This layer has a domain structure that is noncoherent with the matrix lattice. Typical block dimensions in the lateral direction are between 50 and 150 nm. We note that in most cases the extension of dislocations in the growth direction is blocked by this layer. The observed type of structure (noncoherence, formation of blocks, large strain, and a large number of defects) is typical of spinodal decomposition during the growth of thick layers of materials with a pronounced lattice mismatch [1, 2].

Figure 4 presents cross-sectional and plan-view TEM images of a heterostructure with a single thin InGaN layer. In this case, the layer is coherent with the matrix lattice. The average thickness of the layer is about 4 nm. We note that in some cases the extension of dislocations growing from the buffer layer is terminated at the layer boundary. Figure 4a shows a plan-view image obtained in the (1000) reflection, demonstrating the structural perfection of the sample. Nanoregions with a dark contrast corresponding to a higher In content are observed. The nanodomains can be divided into two groups: single quantum dots (denoted SQD in Fig. 4a) and clusters of quantum dots (CQD). Typical dimensions of SQDs are in the range of 5–15 nm. It should be noted that it is difficult to reveal single domains less than 5 nm in size, which may lead to a certain underestimation of the nanodomain density. The nanodomains are nearly round or hexagonal in shape. The density of single nanoislands is $n \approx (3.5 \pm 1.0) \times 10^{11}$ cm^{-2}. In addition, clusters of islands are observed, with dimensions decreasing from the cluster center to its periphery. The cluster density is $n \approx 10^8$ cm^{-2}.

Structure of the samples and TEM data

Sample	Structure	Average composition and layer thickness	TEM data	Nanodomain density, cm^{-2}
A593	Single thick $In_xGa_{1-x}N$ layer	$x \approx 0.25$, 40 nm	$h = 40$ nm $d \approx 50$–100 nm	$n \approx 10^8$
A679	Single thin $In_xGa_{1-x}N$ layer	$x \approx 0.25$, 3 nm	$h = 3$ nm, $d_1 \approx 3$–15 nm $d_2 \approx 3$–30 nm $x \le 0.6$	$n_1 = 3.5 \times 10^{11}$ $n_2 = 3.5 \times 10^{10}$
A614	Superlattice $(In_xGa_{1-x}N/In_yGa_{1-y}N) \times 12$	$x \approx 0.25$, 3 nm; $y \approx 0.01$, 10 nm	$h = 3$ nm, $d_1 \approx 3$–7 nm $x_1 \approx 0.4$ $d_2 \approx 10$–15 nm $x_2 \approx 0.6$	

Note: Subscripts 1 and 2 refer to different types of domains. *h* is the InGaN layer thickness.

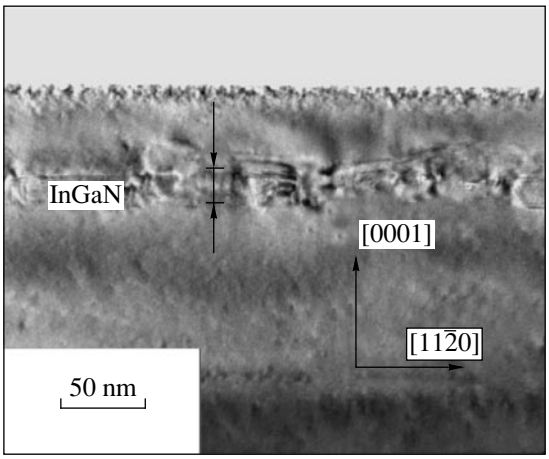

Fig. 3. Cross-sectional ($1\bar{1}00$) TEM image of a heterostructure with a thick InGaN layer in a GaN matrix.

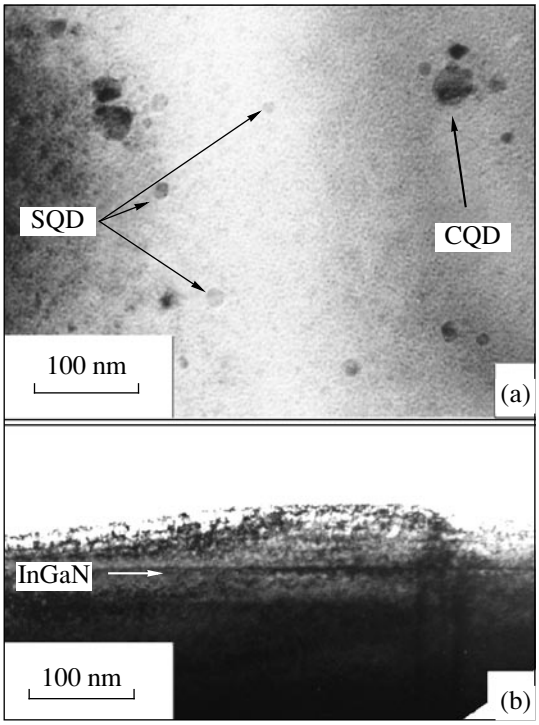

Fig. 4. Plan-view (a) and cross-sectional (b) TEM images of a heterostructure with a single ultrathin InGaN inclusion in the GaN matrix.

Figure 5 presents size (d) distributions of nanodomains. The nanodomain distribution in clusters is satisfactorily approximated by an exponential function

$$n \sim n_0 \exp(d/d_0),$$

where $n_0 \approx 10^9$ cm^{-2} is the zero-size approximation of nanodomain density in clusters; and d_0 is a characteristic size of nanodomains in clusters. At the same time,

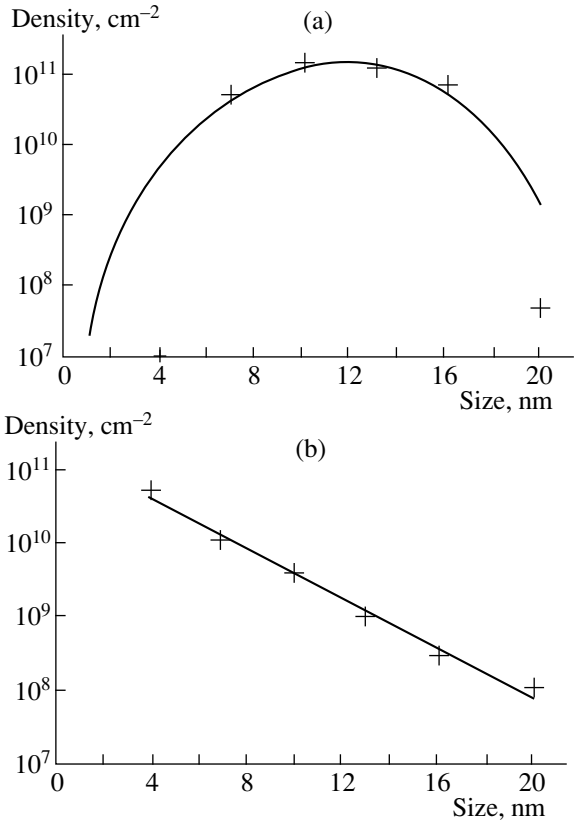

Fig. 5. Size distribution of (a) single nanodomains and (b) clusters of these in a heterostructure with a single ultrathin InGaN inclusion in a GaN matrix.

the distribution of single nanodomains can be approximated by

$$n \sim n_0 (d/d_0)^k \exp[-(d/d_0)^k],$$

where $n_0 = 1.5 \times 10^{11}$ cm^{-2} is the maximum nanodomain density, $d_0 \approx 12$ nm is an average nanocluster size, and $k = 6$ is a parameter. We note that the distribution for single domains can be distorted in the region of small sizes, in view of the problems associated with the detection of these clusters.

The existence of two nanodomain size distributions correlates with photoluminescence (PL) spectra [9] that demonstrate the presence of exciton localization centers with higher and lower binding energies.

Figure 6 shows a cross-sectional TEM image of an InGaN superlattice. Similarly to the case of a single thin layer, a satisfactory coherence is observed between the lattices of the matrix and layers with a high In content. The cross-sectional images were analyzed by the DALI method [6, 7]. Figure 7 presents the results of a DALI analysis demonstrating the modulation of layer composition in the lateral direction. The observed nanodomains can be classed into two main groups:

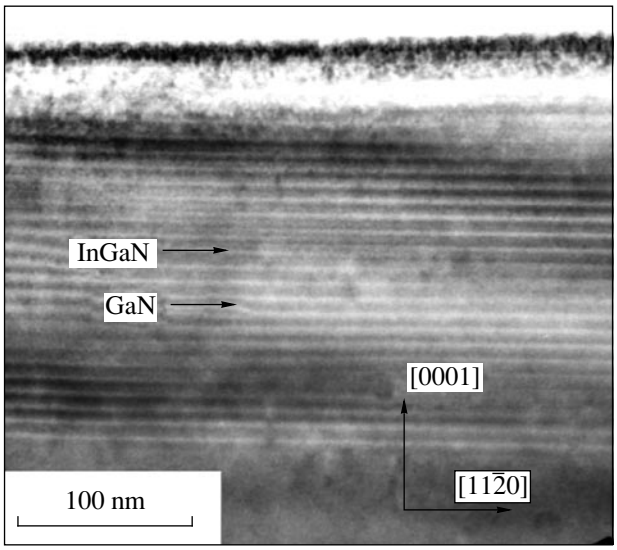

Fig. 6. Cross-sectional ($1\bar{1}00$) TEM image of a heterostructure with a multilayer system of ultrathin InGaN inclusions in the GaN matrix.

a) an indium content of up to $x \approx 0.4$, a domain size of 3–5 nm (Fig. 7a); uncorrelated positions of In-enriched regions;

b) an indium content of up to $x \approx 0.7$, a domain size of ~10 nm (Fig. 7b); in addition, the positions of larger nanodomains are apparently for the most part correlated in the vertical direction, in accordance with the correlated-growth theory [10]. The latter indicates that vertically correlated growth must be observed when the interlayer distance is smaller than the lateral nanodomain size or the superlattice period.

The period of the composition modulation is 15–25 nm for large nanodomains and 10–15 nm for small ones, corresponding to island densities in the layer, n, of $(3 \pm 2) \times 10^{11}$ cm^{-2} for large nanodomains and $(5 \pm 4) \times 10^{11}$ cm^{-2} for small ones for a sample thickness of 15–30 nm.

Similarly to the case of a single InGaN layer, in the case of a superlattice structure, the extension of dislocations growing from the buffer layer is partly terminated at the bottom heterointerface.

The fact that two groups of nanodomains with two characteristic sizes and compositions were observed in the structure correlates well with the results of the PL spectrum studies [11] where two types of centers were revealed.

A comparison of the results obtained for different samples shows that thin InGaN layers may self-organize into systems of nanoislands coherent with the matrix, with an In content of up to $x \approx 0.6$ or higher. Two systems of nanoislands are formed: single islands and clusters of these. The density of single nanoislands is 3.5×10^{11} cm^{-2}, with their sizes being in the range of 3–15 nm. An increase in the InGaN layer thickness

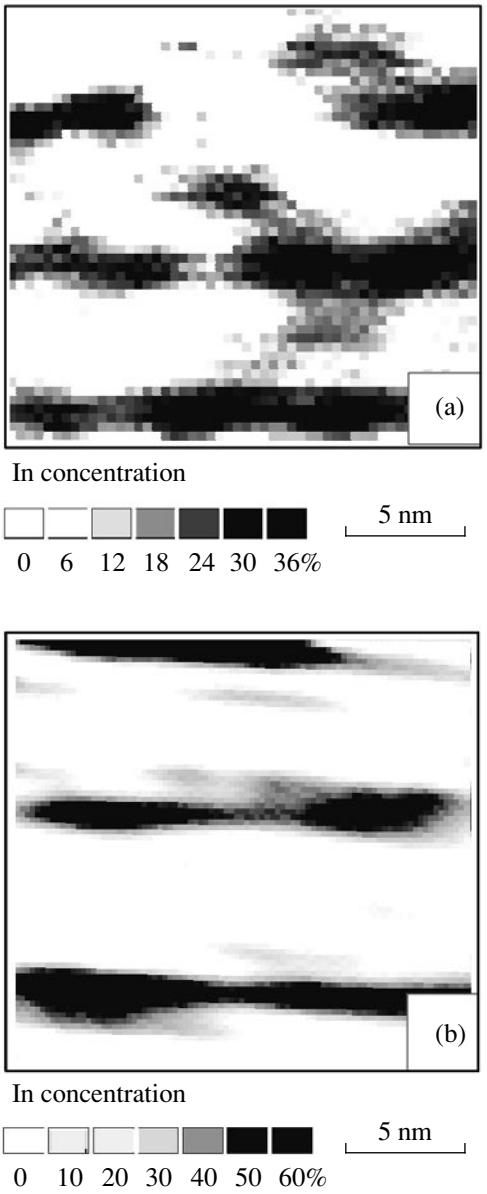

Fig. 7. Composition distribution maps for a heterostructure with a multilayer system of ultrathin InGaN inclusions in the GaN matrix, obtained by DALI processing of cross-sectional ($1\bar{1}00$) HRTEM images.

gives rise to a block-imperfect structure, allowing for a relaxation of the strain. At the same time, the multilayer InGaN/GaN system (superlattice) is formed similarly to single-inclusion structures: islands with a coherent atomic lattice and a high In content ($x \approx 0.6$ and higher) are formed in the layers. The density and size of the nanoislands in the coherent structures are determined by growth conditions (primarily, by temperature); they are ~10^{11} cm^{-2} and 3–15 nm, respectively.

In many cases, the extension of dislocations was terminated at the bottom heterointerface of the InGaN layer in the growth of InGaN/GaN heterostructures.

ACKNOWLEDGMENTS

We are grateful to A. Tsatsul'nikov, A. Sakharov, and I. Krestnikov for their helpful participation in discussions.

This work was supported by the Programs "Collective Phenomena in Solid-State Physics" and "NanoOp."

REFERENCES

1. D. Bimberg, M. Grundmann, and N. N. Ledentsov, *Quantum Dot Heterostructures* (Wiley, New York, 1999).
2. N. N. Ledentsov, Springer Tracts Mod. Phys. **156**, 82 (1999).
3. S. Nakamura and T. Mukai, Jpn. J. Appl. Phys. **31**, L1457 (1992).
4. S. Nakamura, T. Mukai, and M. Senoh, Appl. Phys. Lett. **64**, 1687 (1994).
5. H. Sato, T. Sugahara, Y. Naoi, and S. Sakai, Jpn. J. Appl. Phys. **37**, 2013 (1998).
6. B. Neubauer, A. Rosenauer, D. Gerthsen, *et al.*, Appl. Phys. Lett. **73**, 930 (1998).
7. B. Neubauer, A. Rosenauer, D. Gerthsen, *et al.*, Mater. Sci. Eng. B (2000) (in press).
8. A. V. Sakharov, W. V. Lundin, I. L. Krestnikov, *et al.*, Appl. Phys. Lett. **74**, 3921 (1999).
9. W. V. Lundin, A. V. Sakharov, V. A. Semenov, *et al.*, in *Proceedings of the 7th International Symposium "Nanostructures: Physics and Technology," St. Petersburg, 1999*, p. 485.
10. V. Shchukin and D. Bimberg, Rev. Mod. Phys. **71**, 1125 (1999).
11. A. V. Sakharov, V. V. Lundin, V. A. Semenov, *et al.*, Pis'ma Zh. Tekh. Fiz. **25** (12), 1 (1999) [Tech. Phys. Lett. **25** (12), 462 (1999)].

Translated by D. Mashovets

Semiconductors, Vol. 34, No. 6, 2000, pp. 626–628. Translated from Fizika i Tekhnika Poluprovodnikov, Vol. 34, No. 6, 2000, pp. 652–654.

ELECTRONIC AND OPTICAL PROPERTIES OF SEMICONDUCTORS

Interband Emission of Cadmium Thiogallate

A. I. Machuga*, V. F. Zhitar', and E. D. Arama****

** Technical University of Moldova, Chisinau, MD2012 Moldova*

*** Institute of Applied Physics, Academy of Sciences of Moldova, Chisinau, MD2028 Moldova*

Submitted November 12, 1999; accepted for publication November 16, 1999

Abstract—The edge cathodoluminescence of $CdGa_2S_4$ single crystals was studied at a temperature of 80 K. The true emission spectrum was obtained with allowance made for self-absorption. New intense lines related to band-to-band transitions and recombination via a deep acceptor level were observed. The results obtained are interpreted using the data on photoconductivity and fundamental absorption of this compound. © *2000 MAIK "Nauka/Interperiodica".*

1. INTRODUCTION

The $CdGa_2S_4$ compound is a wide-gap semiconductor (E_g^{opt} = 3.77 eV at T = 10 K) exhibiting the allowed direct optical transitions, high photosensitivity, and intense cathodoluminescence and photoluminescence [1–4]; consequently, this compound is a promising material for nonlinear optics and optoelectronics [5]. The single crystals of this compound exhibit especially intense cathodoluminescence bands in the blue and red regions of the visible spectrum and stimulated emission peaked at 2.1 eV (T = 80 K) [2, 6]. However, emission properties of this compound have been scarcely studied in the region of fundamental absorption. In connection with this, in this paper, we report the results of studying the emission properties of cadmium thiogallate in the energy range of 3.0–4.0 eV under the excitation with an electron beam.

The system for studying cathodoluminescence was equipped with an MZD-2 diffraction monochromator that ensured a resolution of ±0.02 eV in the spectral range of measurements. The electron-beam parameters (such as the energy, current density, and the pulse duration) were controlled within a wide range, which made it possible to choose optimal conditions that ensured the highest yield of emission in the spectral region of interest. We used samples grown by the method of chemical transport reactions, from a solution in the melt, and by the Bridgman–Stockbarger method. The wafers were cut from the single crystals grown by the Bridgman–Stockbarger method; these wafers were then reduced to ~0.3 mm in thickness by mechanical grinding and polished.

2. EXPERIMENTAL RESULTS

The figure shows the experimentally observed short-wavelength emission band (curve *1*) for cadmium thiogallate single crystals that were grown from a solution in the melt and were stoichiometric in composition. Cathodoluminescence was observed with the emission coming from the $[1\bar{1}2]$ face. The emission spectrum is shown for the energy range of 3.1–4.0 eV. The region of lower energies was studied in detail in [2, 4]. The energy position of the peak of the band under consideration (3.70 eV) makes it possible to assume that a severe distortion of the emission spectrum occurs in the range under consideration owing to self-absorption in the sample.

Indeed, it follows from the energy dependence of the penetration depth of electrons [4] that the beam of electrons with an energy of 50 keV penetrates into the cadmium thiogallate to a depth of about 5 μm; therefore, the absorption of radiation in a layer of such a thickness should be taken into account for a value of the absorption coefficient equal to $\alpha \sim 10^4$ cm^{-1}. The experimental plot of $\alpha \sim f(h\nu)$ is shown in the figure (curve *2*) according to the data reported in [7]. The true emission spectrum in the range of 3.1–4.0 eV was calculated (as in [8]) with the formula

$$I(\lambda) = (1 - R)I_0(\lambda)(1 - e^{-\alpha x})/\alpha x. \quad (1)$$

Here, $I(\lambda)$ is the experimental spectrum of cathodoluminescence emitted at a depth equal to the range of primary electrons with a given energy; R is the reflection coefficient of the crystal, with R being small (~10%) and constant in the range under consideration; and x is the penetration depth for electrons with a given energy.

Curve *3* in the figure represents the true cathodoluminescence spectrum of cadmium thiogallate in the region of fundamental absorption; this spectrum is a superposition of emission from various layers in the depth range of 0–5 μm. The emission spectrum in the range under consideration involves bands peaked at 3.80 and 3.19 eV. The approximated half-width of the former band is $\Delta h\nu$ = 0.45 eV. The lower energy emission is much less intense in comparison. In the experimental spectrum (curve *1*), the band peaked at 3.19 eV

is absent, although, in this range, the intensity of the blue-emission wing is comparable to the intensity of the emission band at shorter wavelengths.

The accuracy of determining the energy positions of the above peaks was assessed on the basis of expression (1). Analysis of this expression shows that an additional contribution to the errors may come from inaccuracy in determining the thickness of the emission layer. In order to evaluate the role of the thickness, we performed calculations according to several approaches. In each of them, different, although close in value, thicknesses were chosen. It was found that, in all cases, two peaks were clearly pronounced, with their energy positions varying within ±0.02 eV. It was this value that was taken as the measure of accuracy of determining the energy positions of the peaks of the bands.

3. DISCUSSION OF RESULTS

In order to interpret the $CdGa_2S_4$ cathodoluminescence in the fundamental-absorption edge region under investigation, we should rely on data obtained by other methods, such as measurements of photoconductivity and extrinsic electroabsorption [3]. It is reasonable to relate the highest energy peak of cathodoluminescence at 3.80 eV to radiative transitions of free electrons. In this case, the value of E_g = 3.80 eV corresponds to the $CdGa_2S_4$ bandgap at 80 K. The structure of the Brillouin zone was previously determined for $K = 0$ [9]. In [1], the energy of splitting the valence band Δ = 0.012 eV by an anisotropic crystal field at 4.2 K was determined. Taking into account the specific band structure of $CdGa_2S_4$ as related to radiative recombination [10], we may conclude that the transition $\Gamma_2 + \Gamma_4 \longrightarrow \Gamma_1$ (with $\perp$ polarization) is most likely involved. The energy positions of the reflection and cathodoluminescence peaks are close to each other. The direct-transition excitons in the compound under consideration are revealed from the reflection spectra [1] and indicate that the value of E_g is correct. The large half-width of the short-wavelength band peaked at 3.80 eV may indicate that this band is not elementary; this large half-width can be also caused by special features of $II–III_2–VI_4$ semiconductors (by the absorption-edge spreading owing to the exciton–phonon interaction [7] and by the presence of more than 10^{21} cm^{-3} vacant cation sites in the structure). It is this specificity of the $CdGa_2S_4$ compound that makes the detection and investigation of the edge luminescence difficult.

The band peaked at 3.19 eV can be related to recombination via a deep impurity level. This suggestion is supported by the previously revealed impurity-related peak in photoconductivity at T = 300 K; this peak was located at ~3.0 eV, and its magnitude decreased drastically if an electric field was applied to the sample [3]. Previously [6–8, 11], the analysis of the results of studying the luminescence, impurity-related electroabsorption, and thermally stimulated conduction made it possible to suggest the energy diagram of recombination phenomena in $CdGa_2S_4$, including also the origin of the levels. According to this diagram, the band peaked at 3.19 eV may correspond (with a high degree of certainty) to an optical transition of electrons from the conduction band to an acceptor level located near the valence band, i.e., $E_c \longrightarrow E_v$ + 0.6 eV at 300 K; this acceptor level can be assigned to cadmium atoms residing at the gallium sites [8]. In a similar $ZnIn_2S_4$ compound, cathodoluminescence bands peaked at 2.98 and 2.65 eV were observed at T = 10 K and were related to the $\Gamma_{3v} \longrightarrow \Gamma_{1c}$ and $E_c \longrightarrow E_v$ + 0.4 eV transitions, respectively [8]. Recently, two cathodoluminescence bands were also observed in the near-edge spectral region of ZnSe crystals at 293 K: a broad edge-related band peaked at 2.65 eV and a low-intensity band peaked at 2.58 eV [12].

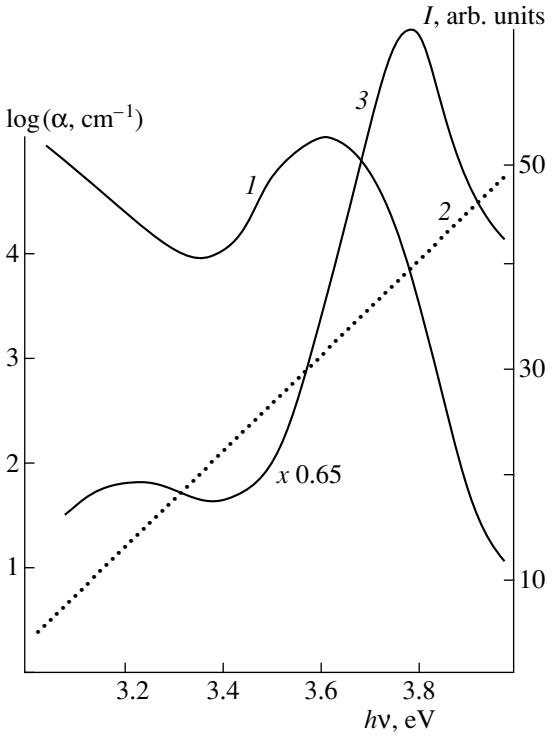

The spectra of edge cathodoluminescence of $CdGa_2S_4$ single crystals at T = 80 K: (*1*) experiment, (*2*) spectral dependence of absorption coefficient, and (*3*) the calculated emission with allowance made for self-absorption in the samples (electron energy was 40 keV and the beam current density was 10^{-5} A/cm^2).

Thus, taking into account the self-absorption in cadmium thiogallate, we revealed for the first time an intense emission caused by band-to-band optical transitions and a low-energy band related to recombination via a deep acceptor level.

REFERENCES

1. A. G. Areshkin, V. F. Zhitar', S. I. Radautsan, *et al.*, Fiz. Tekh. Poluprovodn. (Leningrad) **13**, 337 (1979) [Sov. Phys. Semicond. **13**, 194 (1979)].
2. V. F. Zhitar', A. I. Machuga, and S. I. Radautsan, Opt. Spektrosk. **51**, 948 (1981) [Opt. Spectrosc. **51**, 526 (1981)].
3. S. I. Radautsan, V. S. Donu, V. F. Zhitar', *et al.*, Phys. Status Solidi A **57**, 79 (1980).
4. V. F. Zhitar', A. I. Machuga, and V. S. Donu, Izv. Akad. Nauk Mold. SSR, Ser. Fiz.-Tekh. Mat. Nauk, No. 1, 57 (1982).
5. B. F. Levine, C. G. Betha, and H. M. Kasper, IEEE J. Quantum Electron. **QE-10** (12), 904 (1974).
6. V. F. Zhitar', A. I. Machuga, S. I. Radautsan, *et al.*, Izv. Akad. Nauk SSSR, Neorg. Mater. **22**, 1737 (1986).
7. D. V. Gitsu, V. F. Zhitar', V. Ya. Raĭlyan, *et al.*, in *Proceedings of the 6th International Conference on Amorphons and Liquid Semiconductors, 1976* (Nauka, Leningrad, 1976).
8. E. D. Arama, V. F. Zhitar', A. I. Machuga, *et al.*, Zh. Prikl. Spektrosk. **50** (3), 503 (1989).
9. A. Shileĭka, *Optical Studies of the Band Structure of II–III–VI Compounds* (MOKSLAS, Vilnius, 1978).
10. V. Ya. Raĭlyan and V. F. Zhitar', Izv. Akad. Nauk. Mold. SSR, Ser. Fiz.-Tekh. Mat. Nauk, No. 1, 57 (1984).
11. A. N. Georgobiani, S. I. Radautsan, and I. M. Tiginyanu, Fiz. Tekh. Poluprovodn. (Leningrad) **19** (2), 193 (1985) [Sov. Phys. Semicond. **19** (2), 121 (1985)].
12. A. I. Lipchak, V. I. Solomonov, I. V. Kisilev, *et al.*, Opt. Spektrosk. **83**, 927 (1997) [Opt. Spectrosc. **83**, 854 (1997)].

Translated by A. Spitsyn

Semiconductors, Vol. 34, No. 6, 2000, pp. 629–633. Translated from Fizika i Tekhnika Poluprovodnikov, Vol. 34, No. 6, 2000, pp. 655–659.

ELECTRONIC AND OPTICAL PROPERTIES OF SEMICONDUCTORS

Redistribution of Phosphorus Implanted into Silicon Doped Heavily with Boron

E. G. Tishkovskiĭ*, V. I. Obodnikov, A. A. Taskin, K. V. Feklistov, and V. G. Seryapin

Institute of Semiconductor Physics, Siberian Division, Russian Academy of Sciences, pr. Akademika Lavrent'eva 13, Novosibirsk, 630090 Russia

**e-mail: tish@thermo.isp.nsc.ru*

Submitted December 7, 1999; accepted for publication December 9, 1999

Abstract—The special features of redistribution of phosphorus implanted into silicon wafers with a high concentration of boron ($N_B = 2.5 \times 10^{20}$ cm^{-3}) were studied. It is shown that, in silicon initially doped heavily with boron, the broadening of concentration profiles of phosphorus as a result of postimplantation annealing for 1 h in the temperature range of 900–1150°C is significantly less than in the case of lightly doped silicon. The results are interpreted in terms of the impurity–impurity interaction with the formation of stationary boron–phosphorus pairs. The binding energy of boron–phosphorus complexes in silicon was estimated at 0.6–0.8 eV. © *2000 MAIK "Nauka/Interperiodica".*

INTRODUCTION

Experimental studies performed to date have shown that an annealing of silicon doped heavily with boron ($N_B \approx 2 \times 10^{20}$ cm^{-3}) and implanted with B^+ ions results in the formation of oscillating structures in the boron distribution [1–4]. It is the high initial level of doping with boron that represents one of the factors governing the formation of such pronounced features in the redistribution of boron both implanted and introduced into the starting samples by other methods [4].

In [1–4], both factors (a high level of doping and the effects related to implantation) were related to the same impurity, namely, by boron. In order to clarify the role of each of these factors in the redistribution of impurities, it is of indubitable interest to study the effects of implantation of other impurities (in particular, phosphorus) into silicon doped heavily with boron.

In this case, it should also be expected that specific features of redistribution of impurities would appear, because, as in [1–4], both factors related to a high initial doping level and to the effects of ion implantation are present. In addition, it is known [5, 6] that the acceptor and donor impurities implanted simultaneously into silicon interact with each other in the course of heat treatments, which causes the resulting impurity distribution to differ significantly from the distribution in the case where these impurities are introduced separately in the crystal. In certain cases, the corresponding impurity distribution may be described on the basis of the mechanism of formation of donor–acceptor pairs [5, 6]. It should be expected that such an interaction would also manifest itself in the case under consideration and would thus provide a better insight into the behavior of boron atoms in the course of formation of spatial structures.

The objective of this work was to study the special features of redistribution of implanted phosphorus against the background of a high concentration of boron dopant under the annealing conditions where the formation of the oscillatory structure in the boron distribution has been previously observed [1–4].

EXPERIMENTAL

In the main experiment, we used two sets of wafers. The first set included the KÉF-7.5 silicon wafers (*n*-Si:P, ρ = 7.5 Ω cm) with (100) orientation; boron was introduced into these wafers by diffusion from the surface source at a temperature of 1150°C so that the region with uniform background doping with a high concentration of 2.5×10^{20} cm^{-3} was formed in the near-surface layer with a thickness no less than 1.5 μm (Fig. 1). The second set included the KDB-10 silicon wafers (*p*-Si:B, ρ = 10 Ω cm) with (100) orientation and a low level of doping with boron and served as a reference with respect to the first set.

An HVEE-400 heavy-ion accelerator was used to implant P^+ ions with an energy of 300 keV and a dose of 10^{15} cm^{-2} into both sets of the wafers (Fig. 1). These sets of wafers were then annealed for 1 h at temperatures of 900, 950, 1000, 1075, and 1150°C in an inert-gas ambient.

In addition, we prepared two wafers, in one of which a high level of background doping with phosphorus impurity was attained by implanting P^+ ions with an energy of 300 keV and a dose of 10^{16} cm^{-2} into a KDB-10 (100) silicon wafer with subsequent annealing for 1 h at 1075°C in an inert-gas medium. As a result, a near-surface layer doped heavily with phosphorus was formed; the concentration of P in this layer

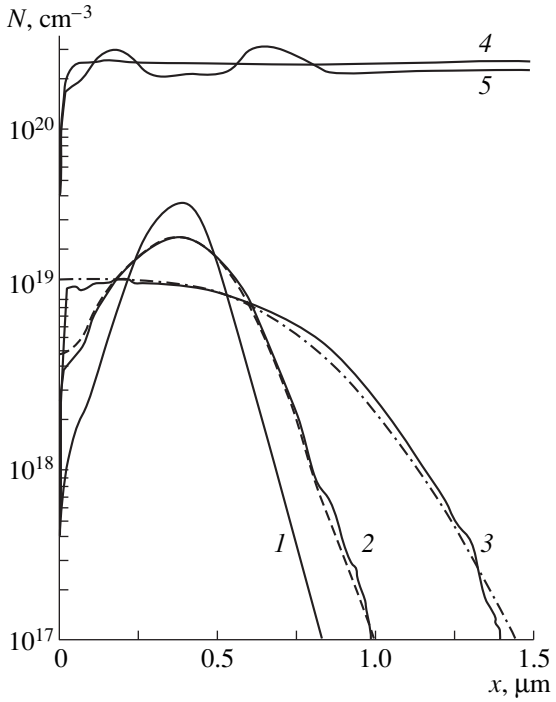

Fig. 1. Concentration profiles of (*1–3*) phosphorus and (*4, 5*) boron in silicon doped (*2, 4, 5*) heavily and (*3*) lightly with boron; the profiles were obtained after implantation of P^+ ions (E = 300 keV and $D = 10^{15}$ cm^{-2}) and subsequent annealing (T = 1075°C and t = 1 h). Curve *1* corresponds to the phosphorus concentration profile immediately after implantation, and curve *4* represents the initial boron distribution in heavily B-doped silicon. Solid lines are experimental, the dash-and-dot line corresponds to the result of the calculation of phosphorus diffusion in lightly doped silicon, and the dashed line represents the result of the calculation of the phosphorus diffusion in silicon doped heavily with boron with allowance made for the formation of P–B pairs.

decreased from about 10^{20} cm^{-3} at the surface to about 10^{19} cm^{-3} at a depth of 1.3 μm. The second wafer was cut from a KÉF-7.5 silicon ingot with (100) orientation and served as a reference for the first wafer.

Both wafers were implanted with $^{10}B^+$ ions with an energy of 100 keV and a dose of 10^{15} cm^{-2}; these wafers were then annealed in an inert medium for 1 h at 1075°C. This experiment was complementary to the main one, because the roles of boron and phosphorus atoms were changed to the opposite.

The depth distributions of P and B impurities was determined by secondary-ion mass spectroscopy (SIMS) using an MIQ-256 CAMECA-RIBER system; the yield of $^{10}B^+$, $^{11}B^+$, and $^{31}P^+$ secondary ions was measured using the beam of O_2^+ primary ions with an energy of 10 keV, and the yield of $(^{28}Si^{10}B)^-$, $(^{28}Si^{11}B)^-$, and $^{31}P^-$ secondary ions was measured using the primary beam of Cs^+ ions with an energy of 10 keV too. The constancy of the etching rate was checked by measuring the yield of ^{30}Si secondary ions.

EXPERIMENTAL RESULTS

For each annealing temperature, the initial spatial distribution of impurities after ion implantation was compared to that in heavily and lightly doped silicon after annealing under identical conditions.

It was found that, after annealing for 1 h at a temperature below 1000°C, the phosphorus profiles in silicon doped heavily with boron did not differ (to within the error of measurements) from the initial profiles obtained immediately after ion implantation. At the same time, a broadening of the profiles in lightly doped silicon as a result of annealing at the same temperature was clearly observed.

Broadening of phosphorus profiles in heavily doped samples becomes evident only at annealing temperatures above 1000°C. For such annealing temperatures, the phosphorus concentration profile in lightly doped silicon is still significantly broader than that in silicon doped heavily with boron (Fig. 1). Such behavior was observed not only for the phosphorus–boron pair of impurities [7] but also for other pairs of impurities, one of which acted as a donor and the other, as an acceptor [5, 6].

A qualitatively similar result was also obtained in the complementary experiment: the boron concentration profile was narrower in silicon doped heavily with phosphorus and subjected to ion implantation and annealing than that in the reference silicon sample doped lightly with phosphorus and subjected to the same implantation and annealing (Fig. 2).

Thus, as a result of preliminary high-concentration doping of the samples with either boron or phosphorus, the broadening of concentration profiles of the implanted impurity (phosphorus or boron) is less pronounced in the course of annealing than that in the lightly doped silicon.

In connection with this, it is of interest to compare the phosphorus concentration profiles in lightly doped silicon annealed at temperatures of 950 and 1075°C with those in silicon doped heavily with boron and annealed at temperatures of 1075 and 1150°C, respectively (Fig. 3). It can be seen that the aforementioned profiles coincide with each other to within the error of measurements. Thus, in the case of heavily doped silicon, an additional thermal activation is required to obtain the same diffusion flux that takes place in lightly doped silicon.

It is also worth noting that, in the cases where the background impurity is boron, its accumulation (in addition to the above processes) is observed in the form of peaks in the initially flat concentration profile in the ion-implanted layer (Fig. 1); these peaks are characteristic of oscillatory structures in the impurity distribution [1–4]. As shown previously [3], the depth positions of these peaks correspond to the boundaries of the implantation-damaged region, and the peaks themselves appear owing to the clusterization of excess (with respect to ultimate solubility) interstitial boron

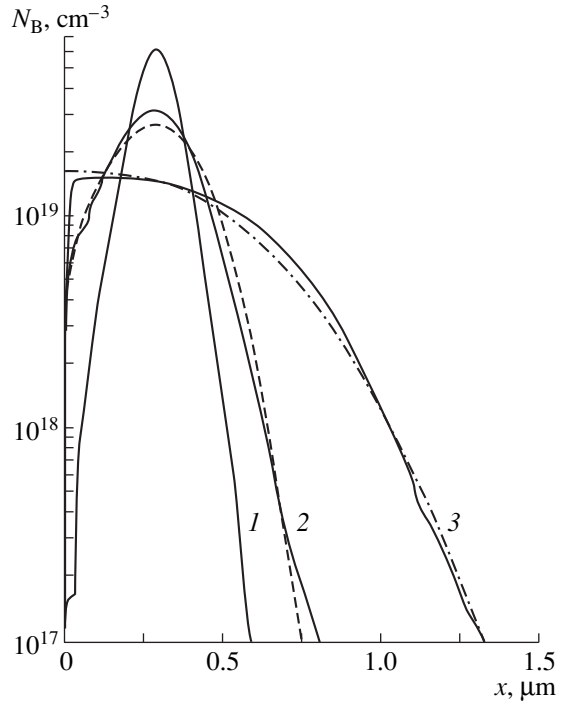

Fig. 2. The boron concentration profiles in silicon doped (*2*) heavily and (*3*) lightly with phosphorus; the profiles were obtained after implantation of B^+ ions (E = 100 keV and $D = 10^{15}$ cm^{-2}) and subsequent annealing (T = 1075°C and t = 1 h). Curve *1* was obtained immediately after implantation of B^+ ions. Solid lines are experimental, the dash-and-dot line corresponds to the calculation of the boron diffusion in lightly doped silicon, and the dashed line represents the result of the calculation of the boron diffusion in silicon doped heavily with phosphorus with allowance made for the formation of P–B pairs.

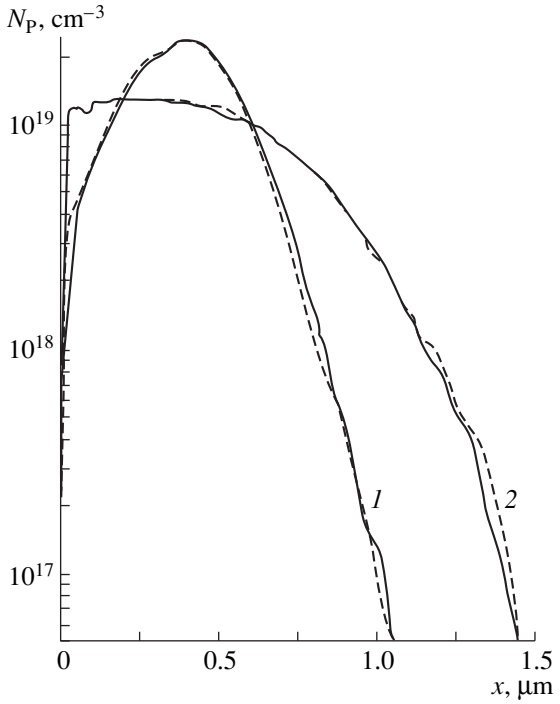

Fig. 3. Comparison of experimental phosphorus concentration profiles in silicon heavily (the dashed lines) and lightly (the solid lines) doped with boron; the profiles were measured after the implantation of P^+ ions (E = 300 keV and $D = 10^{15}$ cm^{-2}) and subsequent annealing for 1 h at temperatures (*1*) of 950 (lightly doped Si) and 1075°C (heavily doped Si) and (*2*) of 1075 (lightly doped Si) and 1150°C (heavily doped Si).

atoms and to the motion of mobile boron atoms to the formed clusters acting as sinks. The excess concentration of interstitial boron atoms at the above boundaries is due to the reaction of pushing the boron atoms out of the lattice sites by self-interstitials released from the damaged region. In this case (i.e., after the implantation of P^+ ions and subsequent annealing), formation of the peaks with the same magnitude as previously observed [1–4] requires annealing temperatures about 50–100°C higher than those used in the previous experiments, in which the implant and the impurity ensuring the high level of preliminary doping were the same (namely, boron).

It is also noteworthy that no special features are observed in the phosphorus concentration profiles in the regions where the peaks in boron distributions are formed (Fig. 1).

DISCUSSION OF RESULTS

Experimental concentration profiles of implanted impurities after annealing were compared with a solution to the following one-parameter boundary-value problem in diffusion:

$$\begin{cases} \dfrac{\partial C(x,t)}{\partial t} = D\dfrac{\partial^2 C}{\partial x^2}, \\ \dfrac{\partial C(0,t)}{\partial x} = 0, \\ C(x,0) = C_{\text{impl}}(x). \end{cases} \quad (1)$$

Here, $C(x, t)$ is the concentration, D is the diffusion coefficient (the parameter of simulation), $C_{\text{impl}}(x)$ is the concentration profile immediately after implantation, and x is the coordinate (depth). The boundary condition corresponds to the approximation of diffusion into a semi-infinite crystal.

The boundary-value problem given by (1) was solved numerically using an implicit difference scheme with enhanced accuracy [8]. The resulting diffusion coefficients are listed in the table, and the corresponding distributions are shown in Figs. 1 and 2 by the dash-and-dot lines. For silicon doped heavily with boron and

The values of parameters (diffusion coefficients) used in simulating the experimental concentration profiles of impurity in the lightly and heavily doped silicon

T, °C	D_P, 10^{-14} cm^2/s (KDB-10)	D_P, 10^{-15} cm^2/s (heavy doping with B)	D_B, cm^2/s (KÉF-7.5)	D_B, cm^2/s (heavy doping with P)
900	1.7	<1		
950	2.3	<1		
1000	3.7	<1		
1075	15	23	1.5×10^{-13}	1.5×10^{-14}
1150	57	150		

subjected to annealing at comparatively low temperatures (in which case the experimental concentration profiles of phosphorus are not broadened), we managed to estimate only the upper bound of the diffusion coefficient D (see table); if D exceeds this bound, the calculated profiles become appreciably broadened.

In lightly doped samples, the diffusion coefficients are in good agreement with available published data; however, in the lower half of the annealing-temperature range, the calculated values regularly exceed somewhat those obtained experimentally, which is conventionally explained by the influence of defects stored in complexes after implantation and released in the course of annealing.

In the heavily doped samples, the obtained values of effective diffusion coefficients are found to be much smaller than those in lightly doped silicon annealed under the same conditions. As in [5, 6], these discrepancies cannot be satisfactorily explained in terms of multiflux diffusion with allowance made for internal electric fields [9, 10].

In the case under consideration, distinctions between the diffusion-affected concentration profiles of the same impurity in the heavily and lightly doped samples (Figs. 1–3) can be explained in terms of the mechanism of formation of immobile impurity pairs (P–B). The effective formation of such pairs in heavily doped silicon diminishes the amount of the impurity that is mobile and is involved in the diffusion flux. According to what we assumed, the diffusion mechanism remains unchanged in this case, which is in qualitative agreement with the fact that the same concentration profile can be observed either for a higher doping level and at a higher annealing temperature or for a lower doping level and at a lower annealing temperature (Fig. 3). Consequently, in order to describe the simultaneously occurring processes of diffusion and pair formation (P–B), we can use the values of diffusion coefficient determined experimentally in lightly doped silicon. The problem of adequate description of the concentration profiles can then be reduced to a one-parameter problem for heavily doped silicon as well.

Indeed, for weak solid solutions (when the concentrations of P, B, and P–B pairs are much less than the number of lattice sites N) and in the approximation of local equilibrium, the concentration of pairs should be consistent with the mass action law; i.e.,

$$\frac{C_{P-B}}{C_P C_B} = K(T), \tag{2}$$

where $K(T)$ is the equilibrium constant of the quasi-chemical reaction, C_P is the concentration of phosphorus atoms, C_B is the concentration of boron atoms, and C_{P-B} is the concentration of P–B pairs. We can derive the explicit expression for the rate constant of quasi-chemical reaction (2) by minimizing the Gibbs thermodynamic potential with allowance made for variations in the configuration entropy in the case where the pairs are formed (see, for example, [11]); thus, we have

$$K(T) \approx \frac{4}{N}\exp\left(\frac{\Delta E}{kT}\right), \tag{3}$$

where $\Delta E = -(E_{P-B} - E_P - E_B)$ is the formation energy for a P–B pair; E_{P-B} is the variation in the crystal energy when two neighboring silicon atoms are replaced by a P–B pair; and E_P and E_B are variations in the crystal energy when silicon atoms are replaced by P and B atoms, respectively. Thus, the sole free parameter in simulation is the binding energy ΔE of a pair, because the diffusion coefficients for these impurities were already determined for lightly doped silicon.

When simulating the processes in heavily doped silicon, we first determined (in each time step) the spatial distribution of mobile impurity by subtracting the concentration of immobile pairs obtained at each point of the spatial mesh according to formulas (2) and (3) from the total concentration of the impurity. The diffusion-related redistribution of the mobile impurity was then determined at the next layer of the temporal mesh.

The calculated concentration profile that simulates the experimental profile of P in the presence of a high concentration of B background impurity with allowance made for the pair formation is shown in Fig. 1 by the dashed line. The corresponding values of binding energy were 0.6 eV for an annealing temperature of 1150°C and 0.7 eV for an annealing temperature of 1075°C. For annealing temperatures of 1000°C and below, in which case the concentration profile of P in silicon doped heavily with boron does not differ from

that after implantation, we can only determine the bound of the binding energy below which the concentration profiles start to be appreciably broadened. For 1000°C, this bound was found to be about 0.8 eV.

In a similar way (i.e., by simulation with allowance made for the pair formation), we also obtained the concentration profile of B in a crystal with a high background concentration of phosphorus (Fig. 2, the dashed line). In this case, the pair-formation energy was found to be equal to 0.8 eV.

Thus, a distinction between the concentration profiles of the same impurity in the heavily and lightly doped samples annealed under identical conditions can be interpreted using the mechanism of impurity–impurity interaction with the formation of immobile P–B pairs. The fact that the estimates of the pair-formation energy in the direct and complementary experiments agree closely suggests that the mechanism of this interaction is the same in both cases.

It has already been mentioned above that the peaks in the distribution of boron background impurity, which are initiated in the case under consideration by implantation of P^+ ions (Fig. 1), are formed at postimplantation-annealing temperatures higher by about 50–100°C than those in the case of B^+ implantation. This necessity of higher annealing temperatures is similar to the necessity of additional thermal activation of phosphorus diffusion in the presence of boron (Fig. 3). Therefore, this fact can also be explained in terms of the impurity–impurity interaction; i.e., a fraction of mobile boron atoms that was previously involved in the process of the formation of the oscillatory structure in the distribution [3] now becomes bound in immobile P–B pairs and drops out of the process. As the annealing temperature increases, the concentration of pairs decreases according to expressions (2) and (3), and a sufficient amount of boron is released to be accumulated in the peaks.

Except for the involvement in the pair-formation reaction, the redistribution of boron and phosphorus atoms in the same samples of silicon doped heavily with boron proceeds independently, judging from the fact that no specific features are observed in the portions of the phosphorus concentration profiles corresponding to the peaks in the boron concentration profiles. Consequently, sinks that trap boron atoms and are formed at the corresponding depths do not directly affect the diffusion-induced redistribution of phosphorus atoms.

CONCLUSION

Thus, the main results of this work consist in the following.

Broadening of concentration profiles of implanted phosphorus as a result of postimplantation annealing for 1 h in the temperature range of 900–1150°C is much less pronounced in silicon doped heavily with boron than in silicon doped lightly with boron. Similarly, preliminary doping of silicon with phosphorus to high concentrations appreciably reduces the broadening of boron concentration profiles in the course of annealing.

As a result of the implantation of P^+ ions into silicon doped heavily with boron and subsequent annealing, peaks are formed in an initially uniform distribution of background boron. This is similar to the boron-distribution oscillatory structure initiated by the implantation of B^+ ions and studied previously; however, in the former case, the annealing temperatures should be higher by 50–100°C.

The fact that the concentration profiles of the same impurity after implantation and annealing under identical conditions differ in shape in the heavily and lightly doped silicon can be explained using the concept of formation of immobile P–B pairs. We estimated the formation energy for P–B pairs at about 0.6–0.8 eV. On the basis of the impurity–impurity interaction, it is also possible to explain the necessity of higher annealing temperatures for the formation of an oscillatory structure in the boron distribution after the implantation of phosphorus ions as compared to those in the case of boron implantation: a fraction of boron atoms involved previously in the formation of the oscillatory structure is rendered immobile by forming the P–B pairs.

REFERENCES

1. A. M. Myasnikov, V. I. Obodnikov, V. G. Seryapin, *et al.*, Pis'ma Zh. Éksp. Teor. Fiz. **60**, 96 (1994) [JETP Lett. **60**, 102 (1994)].
2. A. M. Myasnikov, V. I. Obodnikov, V. G. Seryapin, *et al.*, Fiz. Tekh. Poluprovodn. (St. Petersburg) **31**, 338 (1997) [Semiconductors **31**, 279 (1997)].
3. A. M. Myasnikov, V. I. Obodnikov, V. G. Seryapin, *et al.*, Fiz. Tekh. Poluprovodn. (St. Petersburg) **31**, 703 (1997) [Semiconductors **31**, 600 (1997)].
4. V. I. Obodnikov and E. G. Tishkovskiĭ, Fiz. Tekh. Poluprovodn. (St. Petersburg) **32**, 417 (1998) [Semiconductors **32**, 372 (1998)].
5. B. Margesin, R. Canteri, S. Solmi, *et al.*, J. Mater. Res. **6**, 2353 (1991).
6. S. Solmi, S.Valmorri, and R. Canteri, J. Appl. Phys. **77**, 2400 (1995).
7. F. Wittel and S. Dunham, Appl. Phys. Lett. **66**, 1415 (1995).
8. A. A. Samarskiĭ, in *The Theory of Difference Schemes* (Nauka, Moscow, 1983), Chap. 3, p. 141.
9. C. P. Ho, J. D. Plummer, S. E. Hansen, and R. W. Dutton, IEEE Trans. Electron. Devices **ED-30**, 1438 (1983).
10. R. B. Fair and J. C. C. Tsai, J. Electrochem. Soc. **124**, 1107 (1977).
11. P. V. Kovtunenko, in *Physical Chemistry of Solid State: Crystals with Defects* (Vysshaya Shkola, Moscow, 1993), Chap. 1, p. 11.

Translated by A. Spitsyn

Semiconductors, Vol. 34, No. 6, 2000, pp. 634–640. Translated from Fizika i Tekhnika Poluprovodnikov, Vol. 34, No. 6, 2000, pp. 660–666.

ELECTRONIC AND OPTICAL PROPERTIES OF SEMICONDUCTORS

Multiphonon Capture of Charge Carriers by Deep-Level Centers in a Depletion Region of a Semiconductor

M. A. Dem'yanenko*, V. N. Ovsyuk, and V. V. Shashkin***

** Institute of Semiconductor Physics, Siberian Division, Russian Academy of Sciences, pr. Akademika Lavrent'eva 13, Novosibirsk, 630090 Russia;*

e-mail: byankin@thermo.isp.nsc.ru

*** Technological Institute of Applied Microelectronics, Siberian Division, Russian Academy of Sciences, Novosibirsk, 630090 Russia*

Submitted December 2, 1999; accepted for publication December 22, 1999

Abstract—Multiphonon field-assisted thermal capture of thermally equilibrium charge carriers by deep-level centers located in a depletion region of a semiconductor is analyzed. It is shown that, in the case of strong electron–phonon coupling (SEPC), the multiphonon capture with preliminary tunneling of an electron through a potential barrier in the depletion region occurs with a lower rate as compared to the direct multiphonon capture in the electrically neutral bulk of the semiconductor, whereas, in the case of weak electron–phonon coupling (WEPC), the capture rate in the depletion region of a semiconductor may exceed that in the electrically neutral bulk by several orders of magnitude. The results of experimental study of capture processes in AlGaAs doped with silicon indicate that electron–phonon coupling is strong in *DX* centers. © *2000 MAIK "Nauka/Interperiodica".*

1. INTRODUCTION

Multiphonon ionization of deep-level impurity centers in semiconductors and capture of charge carriers (henceforth, for definiteness, of electrons) by these centers can be adequately described on the basis of the concept of adiabatic potentials (terms) [1–4]. In the absence of an electric field, the capture occurs by tunneling transition of the "center" from the term U_2 that corresponds to an ionized center and a free electron with zero kinetic energy to the term U_1 that corresponds to the bound state of electron at the center (Fig. 1). In an electric field, a free electron being in the thermal equilibrium and having a negative kinetic energy $-\varepsilon$ tunnels preliminarily from the conduction band to the energy gap (this state corresponds to the term $U_{2\varepsilon}$), and then a tunneling transition of the "center" from the term $U_{2\varepsilon}$ to the term U_1 occurs. Ionization takes place in the reverse order.

Multiphonon ionization of deep-level centers in an electric field is found to be sensitive to the type of adiabatic potentials [5, 6]. The time τ_2 of tunneling through the adiabatic potential U_2 (the value of τ is experimentally determined from the field dependence of the emission rate) is found to exceed the value of $\hbar/2k_BT$ if the adiabatic potentials U_1 and U_2 are arranged on the same side of their intersection point (or tangency point, see [2]) and below it [this is the case of weak electron–phonon coupling (WEPC)]; by contrast, $\tau_2 < \hbar/2k_BT$ if U_1 and U_2 are found at opposite sides of the aforementioned point [this is the case of strong electron–phonon coupling (SEPC)]. Furthermore, the emission rate increases with an increasing electric field for both types of adiabatic potentials. In the above, $\hbar$ and k_B are the Planck and Boltzmann constants and T is temperature.

In this work, we analyzed theoretically the multiphonon field-assisted thermal capture of thermally equilibrium charge carriers by deep-level centers located in the depletion region of a semiconductor. It is shown that the rate of capture of an electron by a center located in the depletion region of a semiconductor may have a field dependence that differs radically from that of the emission rate. In the case of SEPC, the multiphonon capture of an electron with its preliminary tunneling through the potential barrier in the depletion region (see Fig. 2) occurs with a rate lower than the rate of direct multiphonon capture of an electron in the electrically neutral bulk of a semiconductor; in the case of WEPC, the above two rates can have a reverse relationship. Theoretical results are numerically illustrated by the examples of *DX* centers in AlGaAs doped with silicon and deep-level acceptors in germanium doped with gold. It is shown that, in the case of WEPC, the rate of electron capture in the depletion region of semiconductor may exceed by several orders of magnitude the corresponding rate in the electrically neutral bulk of a semiconductor at liquid-nitrogen temperature for the concentration of dopant equal to $N_d \approx 3 \times 10^{17}$ cm^{-3}.

The results of experimental studies of capture processes in AlGaAs doped with silicon indicate that we have a SEPC in the *DX* centers.

1063-7826/00/3406-0634$20.00

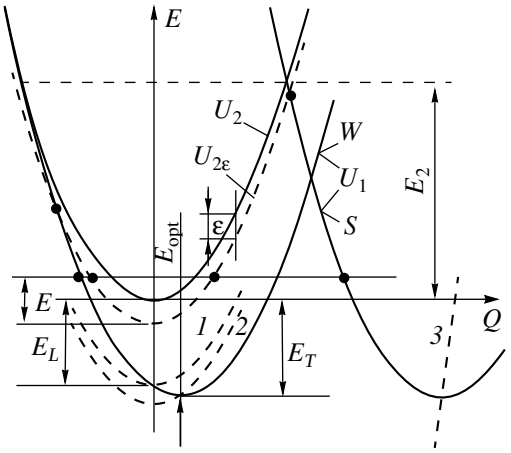

Fig. 1. Configuration diagrams for the cases of (*W*) weak and (*S*) strong electron–phonon coupling. U_1 corresponds to the state with an electron bound by the center; U_2 corresponds to an ionized center with an electron located at the conduction-band bottom; and $U_{2\varepsilon}$ corresponds to an ionized center, with an electron located below the conduction-band bottom by the tunneling energy ε. Dashed curve *1* represents $U_{2\varepsilon}$ for $\varepsilon = E_L$; curve *2* corresponds to $U_{2\varepsilon}$ for $\varepsilon = E_{opt}$; and curve *3* represents the same as curve *2* but in the case of strong electron–phonon coupling.

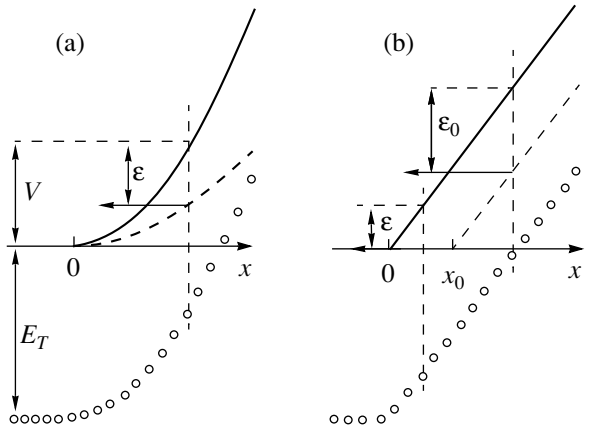

Fig. 2. Energy diagrams of depletion regions with (a) uniform doping and (b) a uniform electric field. The dashed lines represent the dependences of optimal electron-tunneling energy ε on the deep-center position *x*. Deep levels are represented by circles.

2. GENERAL RELATIONSHIPS FOR ELECTRON CAPTURE

Following [3], we represent the rate of emission from the center (the probability of ionization of the center per unit time) as $W \propto \exp(-\Phi_c)$, where Φ_c is the minimal value of the function $\Phi(E, \varepsilon, x) = \Theta(E, \varepsilon) + D(\varepsilon, x)$. Here,

$$\Theta(E, \varepsilon) = 2(S_2 \pm S_1) + \frac{(E_T + E - \varepsilon)}{k_B T}, \quad \left(\frac{S}{W}\right), \quad (1)$$

$D(\varepsilon, x)$ is the exponent in the expression for the probability of electron tunneling through the potential barrier, which, for an arbitrary shape of the latter, depends on the tunneling energy ε and the position of the center *x*; $S_i = (2M)^{1/2}|\int (U_i - E + \varepsilon)^{1/2} d\Theta|/\hbar$ are the modules of actions multiplied by $i/\hbar$ and gained in tunneling to the center with an energy $E - \varepsilon$ from the turn points to the intersection point for the terms U_1 and $U_{2\varepsilon}$; *M* is the effective mass of the center; E_T is the thermal binding energy; and *E* is the vibrational energy of the ionized center (see [3, 6]). The values of *E* and ε, for which $\Phi(E, \varepsilon, x)$ is minimized for a given *x*, are given by

$$2\tau_2 \pm 2\tau_1 = \hbar/k_B T, \quad \left(\frac{S}{W}\right) \quad (2)$$

$$2\tau_2 = \hbar \partial D/\partial \varepsilon, \quad (3)$$

where $\tau_i = \hbar|\partial S_i/\partial E|$ is the time of tunneling for the center under the corresponding adiabatic potential. In relationships (1) and (2), the upper sign corresponds to the case where the terms U_1 and $U_{2\varepsilon}$ are of the SEPC type and the lower sign corresponds to the case of WEPC. This is indicated by the fraction *S*/*W* on the right-hand side of formulas (1) and (2). It is noteworthy that, for the initial WEPC type of the terms U_1 and U_2, the type of the terms U_1 and $U_{2\varepsilon}$ changes to SEPC as the energy ε of electron tunneling increases and becomes higher than the luminescence-quantum energy E_L.

Following [2], we use the principle of detailed balancing to determine the capture rate (the probability of de-ionization of the center per unit time) as

$$R = W \exp\left(\frac{E_T - V + E_F}{k_B T}\right), \quad (4)$$

where E_F is the Fermi energy measured from the conduction-band bottom in the electrically neutral region of a semiconductor, and *V* is the potential energy of center with respect to its value in the electrically neutral region. Since relation (2) defines unambiguously the optimal value of *E* for any ε, we may assume that Θ, *W*, *R*, τ_1, and τ_2 are functions of ε whose optimal value is defined by relationship (3) and, in the general case, depends on the position of the center in the depletion region. For low electric fields, $\varepsilon \approx 0$ and the capture rate in the depletion region of a semiconductor is by $\exp(V/k_B T)$ times lower than that in the neutral region R_0. In the case of ultimately high electric fields (the criterion will be given below), the optimal $\tau_2 \longrightarrow 0$ [as follows from relation (3)], ε tends to the optical-ionization energy E_{opt} (see Fig. 1 and [3, 6]), and, consequently, the emission and capture rates are the highest for $\varepsilon = V$ provided that $V < E_{opt}$. In this case, the capture rate $R(V)$ attains its maximal value of $R_m(V) \propto \exp[-\Theta(V) + (E_T + E_F - V)/k_B T]$ (as for the pre-expo-

nential factor, see [2, 3]), and, for the derivative with respect to *V*, we have

$$\frac{d\ln(R_m)}{dV} = \mp\frac{2\tau_1}{\hbar}, \quad \left(\frac{S}{W}\right). \tag{5}$$

Consequently, in the case of WEPC, R_m first increases with increasing *V*, attains a maximum for $V = E_L$ (for which $\tau_1 = 0$), and then decreases. In the case of SEPC, *R* invariably decreases with increasing *V*.

For intermediate fields, we differentiate (4) with respect to *V* and find the differential form of the dependence of *R* on *V* (or on *x* because the dependence $V(x)$ is assumed to be known) as

$$\frac{d\ln(R)}{dV} = \frac{2\tau_2}{\hbar}\frac{d\varepsilon}{dV} - \frac{dD}{dV} - \frac{1}{k_BT}. \tag{6}$$

Here, the value of ε is determined from relationship (3) for any value of *V*. Without specifying the dependence $U_{1,2}(Q)$, we now consider the two most widely encountered cases: a parabolic increase in potential in the near-surface region of a uniformly doped semiconductor (Fig. 2a) and a linear increase in potential in a lightly doped region located between two heavily doped regions of a semiconductor (Fig. 2b).

Depletion region in a uniformly doped semiconductor. Let the concentration of doping impurity be N_d and let the permittivity be χ_s. The exponent in the expression for the electron-tunneling probability is then given by

$$D = \frac{V}{\hbar\omega_0}\phi\left(\frac{\varepsilon}{V}\right), \tag{7}$$

where $\omega_0^2 = q^2N_d/4m\chi_s$, $\phi(z) = \sqrt{z} - (1 - z)\ln[(1 + \sqrt{z})/\sqrt{1-z}]$, and *q* and *m* are the charge and effective mass of the tunneling electron. The relation between the potential energy *V* of the deep center and the optimal tunneling energy ε is defined by

$$V = \left(\frac{a(\varepsilon)+1}{a(\varepsilon)-1}\right)^2\varepsilon, \tag{8}$$

with the coordinate of the center given by $x = (2V\chi_s/q^2N_d)^{1/2}$. Here, $a(\varepsilon) = \exp(4\omega_0\tau_2(\varepsilon))$. For light doping, such that $4\omega_0\tau_2(\varepsilon) \ll 1$, the value of ε is defined by the field strength $F(x) = V(x)/2xq$ at the coordinate corresponding to the position of the deep center: $(\varepsilon/E_T)^{1/2} = 2(k_BT/\hbar)\tau_2(\varepsilon)(F(x)/F_0)$. Here, $F_0 = 2(2mE_T)^{1/2}k_BT/\hbar q$ (cf. [3]). If the doping level is sufficiently high, so that $4\omega_0\tau_2(\varepsilon) \gg 1$ (the inequality is violated for certain ε_c, because $\tau_2 \longrightarrow 0$ for $\varepsilon \longrightarrow E_{\text{opt}}$), then, for $\varepsilon < \varepsilon_c$, the value of ε is defined by the potential energy at the point of location of the center: $\varepsilon = V$. Furthermore, $D \approx V/\hbar\omega_0 \leq \varepsilon_c/\hbar\omega_0$, so that *D* may be ignored for $\hbar\omega_0 \gg \varepsilon_c$. In this case, for $V < \varepsilon_c$, the capture rate $R(V)$ attains its maximal value $R_m(V)$.

For small *V* and, consequently, small ε, we have $\varepsilon/V = A \equiv (a(0) - 1)^2/(a(0) + 1)^2$, and relation (6) can be rewritten as

$$\frac{d\ln(R)}{dV} = \mp\frac{2\tau_1(0)A}{\hbar} - \frac{\phi(A)}{\hbar\omega_0} - \frac{1-A}{k_BT}, \quad \left(\frac{S}{W}\right). \tag{9}$$

For a fairly high doping level (i.e., for $4\omega_0\tau_2(0) \gg 1$), $\varepsilon/V = A = 1$, $d\ln(R)/dV = \mp 2\tau_1(0)/\hbar - 1/\hbar\omega_0$, and, in the case of WEPC, the rate of capture by deep centers increases with increasing *V* for $2\omega_0\tau_1(0) > 1$. For light doping, such that $4\omega_0\tau_2(0) \ll 1$, we have $A \ll 1$ and $d\ln(R)/dV = -1/k_BT$.

Linearly increasing potential. Let the field strength be *F*; the exponent in the expression for the electron-tunneling probability is given by

$$D = \frac{4\sqrt{2m}\varepsilon^{3/2}}{3\hbar qF}. \tag{10}$$

Outside of the neutral region of a semiconductor, the optimal value of ε_0 is independent of *x* and is given by

$$\left(\frac{\varepsilon_0}{E_T}\right)^{1/2} = 2\frac{k_BT}{\hbar}\tau_2(\varepsilon_0)\frac{F}{F_0}. \tag{11}$$

For $x < x_0 = \varepsilon_0/Fq$, the values of $\varepsilon = V = xFq$ are optimal and relationship (6) takes the form

$$\frac{d\ln(R)}{dV} = \mp\frac{2\tau_1(V)}{\hbar} - \frac{2\sqrt{2mV}}{\hbar qF}, \quad \left(\frac{S}{W}\right). \tag{12}$$

According to (12), in the case of WEPC, the capture rate first increases with increasing *V*, attains a maximum for $\tau_1(V) = (2mV)^{1/2}/qF$, and then decreases. For $V > \varepsilon_0$, the optimal value of ε remains unchanged and the capture rate *R* continues to decrease according to the law $d\ln(R)/dV = -1/k_BT$. The maximum in *R* is attained for *V* smaller than ε_0, because, according to (3), $\tau_2(\varepsilon_0) = (2m\varepsilon_0)^{1/2}/qF$, and, according to (2), $\tau_2 > \tau_1$ in the case of WEPC.

According to (11), if $F \gg F_0$, then $\varepsilon_0 \longrightarrow E_{\text{opt}}$, because $k_BT\tau_2(\varepsilon = 0)/\hbar \sim 1$ is on the order of unity and tends to zero for $\varepsilon_0 \longrightarrow E_{\text{opt}}$. In the fields $F \gg F_0(2E_{\text{opt}}^{3/2}/3E_T^{1/2}k_BT)$, we also have $D \ll 1$, and, consequently, in such fields, $\varepsilon = V$ and the capture rate attains its maximal value $R_m(V)$ for $V < \varepsilon_0$.

The above relationships involve the functions $\tau_{1,2}(\varepsilon)$ and $\Theta(\varepsilon)$ that are undefined so far. In order to calculate these functions, we have to specify the form of adiabatic potentials $U_{1,2}(Q)$.

3. THE RELATIONSHIPS FOR CAPTURE IN THE MODEL BY HUANG AND RHYS

In the context of the model suggested by Huang and Rhys, adiabatic potentials have the form of two identical shifted parabolas: $U_2 = M\omega^2Q^2/2$ and $U_1 = M\omega^2(Q -$

$Q_0)^2/2 - E_T$; thus, the emission and capture rates can be calculated exactly. Following [1, 3], we determine the corresponding dependences in parametric form; these dependences are valid for both WEPC and SEPC and are given by

$$\frac{\hbar\omega}{E_T}\Theta(y) = |1-y|\left[\pm 2\omega\tau_2(y) - \sqrt{1+\xi^2} + \xi\cosh\frac{\vartheta}{2}\right], \quad \left[\begin{matrix} y<1 \\ y>1 \end{matrix}\right]; \tag{13}$$

$$2\omega\tau_2(y) = \frac{\vartheta}{2} \pm \ln\frac{+\sqrt{1-\xi^2}}{\xi}, \quad \left[\begin{matrix} y<1 \\ y>1 \end{matrix}\right]; \tag{14}$$

$$\left[\begin{matrix} y>1-\beta \\ y<1-\beta \end{matrix}\right], \quad 2\omega\tau_1(y) = \mp\left(\pm\ln\frac{1+\sqrt{1+\xi^2}}{\xi} - \frac{\vartheta}{2}\right), \quad \left[\begin{matrix} y<1 \\ y>1 \end{matrix}\right]. \tag{15}$$

In this case, the optimal vibrational energy of an ionized center is equal to

$$E(y) = E_T|1-y| \times \frac{\cosh(\vartheta/2)\sqrt{1+\xi^2} - \xi \mp \sinh(\vartheta/2)}{2\sinh(\vartheta/2)}, \quad \left[\begin{matrix} y<1 \\ y>1 \end{matrix}\right]. \tag{16}$$

Here, $y = \varepsilon/E_T$, $\vartheta = \hbar\omega/k_BT$, $\xi = \beta/|1-y|\sinh(\vartheta/2)$, and $\beta = E_{opt}/E_T - 1$. The upper and lower signs are chosen according to the inequalities written in the square brackets; in equality (15), the left-hand inequalities are used for the signs at the brackets and the right-hand inequalities determine the sign within the brackets.[1]

The largest excess of the capture rate for WEPC in the depletion region over the capture rate in the neutral region $(R_m/R_0)_{max}$ is attained for $y = 1 - \beta$ and is defined by

$$\frac{\hbar\omega}{E_T}\ln\left(\frac{R_m}{R_0}\right)_{max} = \xi_0\cosh\frac{\vartheta}{2} + \ln\frac{1+\sqrt{1+\xi_0^2}}{\xi_0} - \sqrt{1+\xi_0^2} - \frac{\vartheta}{2}, \tag{17}$$

where $\xi_0 \equiv \xi(y = 0)$. For $\vartheta \gg 1$ and $\beta \ll 1$, we have $(\hbar\omega/E_T)\ln(R_m/R_0)_{max} = \ln(1/\beta) - 1$.

The exponents D in the expression for the tunneling probability and the values of y at a given point in a semiconductor for parabolic (Fig. 2a) and linear (Fig. 2b) laws of an increase in the potential with increasing x are given by expressions (7) and (8) (for D) and (10) and (11) (for y).

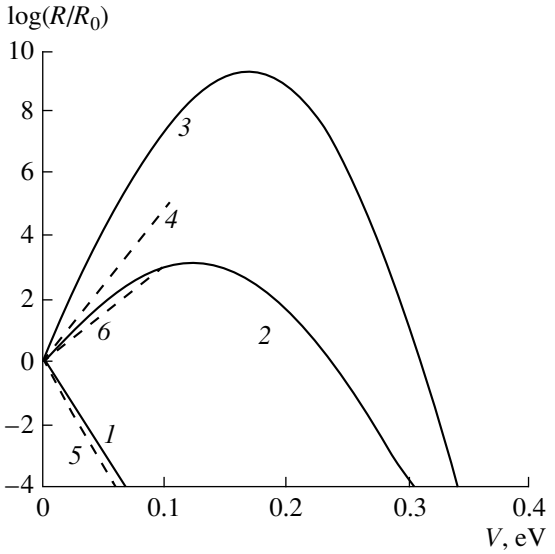

Fig. 3. Relative rates of electron capture by deep centers located in the depletion region of a uniformly doped semiconductor in relation to the potential energy of the centers at $T = 77$ K. Curve *1* is for *DX* centers in AlGaAs:Si in the case of strong electron–phonon coupling; curves *2–4* are for *DX* centers in AlGaAs:Si in the case of weak electron–phonon coupling; curve *5* is for any deep centers in the absence of tunneling ($\varepsilon = 0$); and curve *6* is for Au acceptors in *p*-Ge. The parameters are given in the text.

We now offer some numerical examples. Figure 3 shows the capture rates (the probabilities of de-ionization) R in the depletion region of an uniformly doped semiconductor in relation to the potential energy V for *DX* centers in $Al_{0.4}Ga_{0.6}As$ doped with silicon (curves *1–4*) and for deep-level acceptors in germanium doped with gold (curve *6*); the quantities R are rendered dimensionless by dividing them by the corresponding values R_0 in the electrically neutral region. In the case of *DX* centers in AlGaAs, we used both models discussed previously: the SEPC (curve *1*) [7] and WEPC (curves *2–4*) [8]. Dependences *1–3* were calculated to the Huang–Rhys approximation using formulas (4), (7), (8), (13), and (14). We used the following values of the parameters: $T = 77$ K, $\hbar\omega = 5.5$ meV [9], $E_T = 0.2$ eV, $E_2 = 0.2$ eV [8, 10], $m = 0.1m_0$ [11, 12], and $N_d = 3 \times 10^{17}$ cm^{-3} (for dependences *1* and *2*). Here, E_2 is the energy corresponding to the intersection point for the potentials U_1 and U_2 (see Fig. 1) and m_0 is the mass of the free electron. Curve *3* represents the dependence of R_m/R_0 on V for the aforementioned values of the parameters. Dependences *4* and *6* are plotted using formula (9) for *DX* centers in $Al_{0.4}Ga_{0.6}As$ doped with silicon and deep acceptors in germanium doped with gold, respectively. In the latter case, we used the experimentally measured value of the tunneling time $\tau_2 = 10^{-13}$ s, the value of τ_1 was determined from formula (2), and

[1] Relationships (13) and (14) coincide completely with the relations derived in [3] where adiabatic potentials corresponding to the case of WEPC were considered. However, taking into account that no direct indications of applicability of these relations to the case of SEPS were reported in [3] and for the sake of completeness of presentation, we consider it desirable to write them down here.

the mass of charge carriers involved in tunneling was assumed equal to the mass of light holes [6]. It can be seen that, in the case of SEPC, the capture rate in the depletion region (curve *1*) decreases with increasing V and differs only slightly from the dependence $R/R_0 = \exp(-V/k_BT)$ shown by curve *5* in Fig. 3. In the case of WEPC, the capture rate in the depletion region may increase by several orders of magnitude with increasing V. The aforementioned distinction can be used to identify the type of adiabatic potentials of deep centers, in particular, *DX* centers in AlGaAs doped with silicon, in which case a SEPC should be expected by analogy with studied *DX* centers in AlGaAs doped with tellurium [6].

4. EXPERIMENT

In order to be able to study the process of capture by deep centers in the same sample both in the presence of a depletion region and in the case of flat bands, we used molecular-beam epitaxy (a RIBER 32P system) to grow structures that included

—an *i*-GaAs(100) substrate;

—an n^+-GaAs 0.5-μm-thick layer doped with silicon to the concentration of $N_d = 10^{18}$ cm^{-3} (a nonrectifying contact);

—an *n*-$Al_xGa_{1-x}As$ 0.4-μm-thick layer doped with silicon to the design concentration of $N_d = 3 \times 10^{17}$ cm^{-3} (a layer containing *DX* centers);

—an insulating *i*-$Al_xGa_{1-x}As$ 0.45-μm-thick layer; and

—a passivating *i*-GaAs 250-Å-thick layer.

By varying the voltage across the Schottky barrier from 1 to –10 V, we could form both flat bands and a well-defined depletion region in the layer with *DX* centers at the boundary with an insulating layer with a near-surface potential of ≈0.2 V. The Schottky barrier was produced by depositing an Au / Ti film that was circular in shape and had an area of 1.26×10^{-3} cm^2. The composition of $Al_xGa_{1-x}As$ was given by $x = 0.385$ and 0.45 and was chosen close to the composition corresponding to the direct-gap–indirect-gap transition; in this case, the minimums of three valleys approximately coincide [11, 12]. This makes it possible to use the configuration diagram for two adiabatic potentials, no matter which valleys contribute their wave functions to formation of the wave function of a *DX* center; i.e., we may assume that the term U_2, to which the transition from the term U_1 occurs, coincides with the conduction-band bottom. In this case, the relative mass m/m_0 of electron tunneling along an electric field varies insignificantly: it is equal to 0.1 for the Γ valley, 0.125 for the *L* valley, and 0.2 for the *X* valley [11]. Furthermore, for the above values of x, the dependence of the barrier height for the electron transition from the conduction-band bottom E_c to the *DX* center on x has a minimum [11] and, consequently, depends only slightly on the error in determining the value of x.

In order to enhance the reliability of the results, we performed three types of measurements:

(i) We measured the magnitude of variation in high-frequency capacitance ΔC (f = 100 kHz) with periodic illumination of the sample (f_m = 8 Hz with the filling factor equal to 2) with the light with $\lambda \approx 1$ μm and the intensity of ~10^{17} photon/(cm^2 s) as a function of the bias voltage V_b applied to the Schottky barrier (V_b was varied from 1 to –10 V) at various temperatures (from 80 to 140 K). For the samples with $x = 0.385$ and 0.45, the magnitude of variation in the high-frequency capacitance ΔC was smaller than 0.1 pF (the modulation of the depletion-region thickness was much less than its average value) and remained virtually unchanged for all V_b; it decreased only slightly if the value of V_b varied so that it contributed to the depletion of the *n*-AlGaAs layer. Consequently, the capture rate in the depletion layer does not exceed the capture rate in the neutral region of a semiconductor, because an excess of the former would cause the quantity ΔC to decrease as the depletion region in the *n*-AlGaAs layer is formed. As the temperature was raised, ΔC decreased with an activation energy equal to 0.11 and 0.14 eV for the samples with $x = 0.385$ and 0.45, respectively. Taking also into account that, during illumination and immediately afterwards, electron concentration in the conduction band (as measured by the *CV* method) decreased as the temperature increased with activation energies of 0.085 and 0.09 eV in the temperature range under consideration for the samples with $x = 0.385$ and 0.45, we obtain the barrier height for the transition of electrons from the conduction-band bottom E_c to *DX* centers equal to 0.2 and 0.23 eV, respectively. Such a temperature dependence of electron concentration n is observed if the dominant processes are (I) optical ionization of *DX* centers with transfer of electrons to the conduction band and (II) the back capture of electrons by *DX* centers; since $n \ll N_d$, we have $n \approx (N_d P\sigma_0/v_T\sigma_c)^{1/2}$. Here, N_d is the concentration of *DX* centers; P is the flux of radiation quanta; v_T is the thermal velocity of electrons; and σ_0 and $\sigma_c = \sigma_{c0}\exp(-E_c/k_BT)$ are the cross sections for optical ionization of a *DX* center and for the capture of an electron from the conduction band by this center, respectively.

(ii) We measured the parameters of deep centers by the modulation-spectroscopy method [13]. In the case under consideration, the studied deep level is the level ensuring the major doping effect, which required the further development of this method. However, we will not dwell on this here; we only report that, in the temperature range of 77–300 K and for the modulation frequencies ranging from 8 Hz to 2 kHz, a single level with the parameters of $E_e = 0.41$ eV and $\sigma_{e0} = 1.2 \times 10^{-14}$ cm^2 was dominant; these parameters determine the emission cross section $\sigma_e = \sigma_{e0}\exp(-E_e/k_BT)$. The obtained values for the parameters E_c, E_e, and σ_{e0} agree well with the known parameters of *DX* centers in AlGaAs doped with silicon. This indicates that, in the

samples we studied, the processes of capture are in fact governed by *DX* centers.

(iii) We measured the *C–V* characteristics to determine the concentration profile of ionized impurities after electron capture in the dark for a specified time by the *DX* centers ionized preliminarily by optical radiation for various states of the *n*-AlGaAs layer: from the flat bands to well-developed depletion. For each fixed bias voltage applied to the Schottky barrier V_b, the *DX* centers were completely ionized by optical radiation with $\lambda \approx 1$ μm. The sample was then kept in the dark for a certain fixed time (15 and 60 s for the samples with $x = 0.385$ and 0.45, respectively) under the same bias V_b; afterwards, the dependence of the concentration N_{CV} determined by the *C–V* method on the depth of depletion layer with V_b varying from –10 to 1 V was rapidly (in 5 s) measured. Figure 4 shows the obtained dependences for a sample with $x = 0.45$ (for a sample with $x = 0.385$, the dependences were similar). The concentration profile measured directly under constant illumination of the sample (curve *L* in Fig. 4) indicates that the actual concentration of impurity is close to the expected one and is constant over the depth of the doped AlGaAs layer. For $V_b = 0$, the band bending V_s at the boundary of *n*-AlGaAs is approximately equal to –10 mV (the bands are almost flat) and the rate of electron capture by *DX* centers is independent of *x*. As the potential V_b decreases to –10 V, the depletion layer is formed at the boundary with *n*-AlGaAs and V_s increases to –200 mV; in this case, the rate of capture of electrons by *DX* centers located in the depletion region decreases virtually to zero as the distance between the *DX* centers and the neutral region of the semiconductor increases.

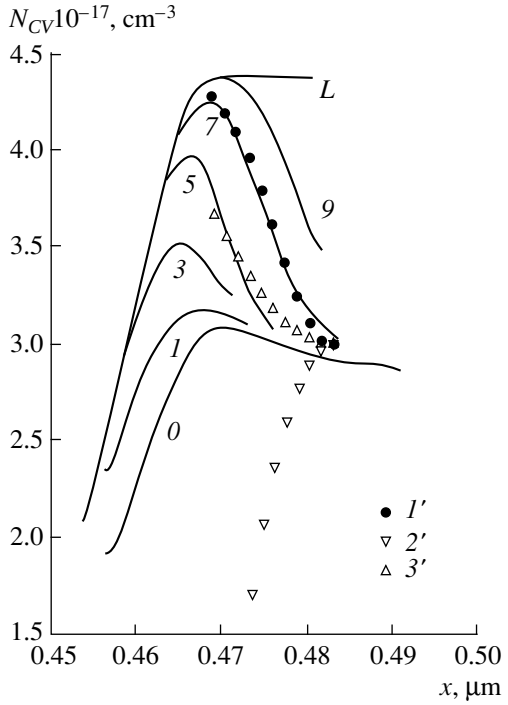

Fig. 4. The solid lines represent the dependences of the ionized-impurity concentration N_{CV} on the depth *x* in $Al_{0.45}Ga_{0.55}As$ doped with silicon. The dependences were measured in the dark 60 s after the illumination was switched off; the depleting voltages (in V) applied to the Schottky barrier are indicated at each corresponding curve. Curve *L* represents the concentration profile measured during illumination. The circles and triangles correspond to the dependences $N_{CV}(x)$ calculated for the case of (*1*') strong electron–phonon coupling with $\hbar\omega = 5.5$ meV and (*2*' and *3*') weak electron–phonon coupling with $\hbar\omega = 5.5$ and 36 meV, respectively. $T = 78$ K.

Figure 4 shows the concentration profiles calculated to the Huang–Rhys approximation in the cases of the weak and strong electron–phonon couplings for $V_b = -7$ V with the same parameters as used in calculating the dependences shown in Fig. 3. It was assumed that a change in the dependence of potential energy *V* of the center on the coordinate *x* may be ignored if a variation in the ionized-center concentration is small. In this case, the concentration of ionized *DX* centers depends on the time elapsed after the switching-off of illumination as $N_{CV}(x, t) = N_d \exp(-R(x)t)$. It can be seen that good agreement with experimental data is obtained only if SEPC is assumed. In the case of WEPC, for the local-vibration phonons having an energy of $\hbar\omega = 5.5$ meV [9] and governing the trend of adiabatic potential in the configuration space, the capture rate increases with increasing distance from the neutral bulk of the semiconductor (Fig. 4). As $\hbar\omega$ increases, the tunneling time τ_1 decreases, which can bring about the sign reversal of dR/dV [see formula (9)]; however, even if $\hbar\omega$ increases up to 36 meV (the energy of LO phonons [11]), there is still no good agreement between the theory and experiment within the WEPC context. Furthermore, for $\hbar\omega$ as large as above and at $T = 78$ K, the tunneling between the adiabatic potentials U_1 and U_2 becomes so promoted that the magnitude of the optimal vibrational energy of the center equals $E < 1$ meV; in addition, the temperature dependence of the capture rate depends only slightly on the energy E_2 and exhibits an activation energy of ≈20 meV, which is lower by a factor of 10 than the known experimental data [10]. Thus, we may conclude that the *DX* centers in AlGaAs doped with silicon exhibit strong electron–phonon coupling.

5. CONCLUSION

We analyzed the multiphonon field-assisted thermal capture of thermally equilibrium charge carriers by deep-level centers located in the depletion region of a semiconductor. It is shown that the rate of electron capture by the deep center may have radically different field dependences. In the case of strong electron–phonon coupling, the multiphonon capture with preliminary tunneling of an electron through the potential barrier in the depletion region occurs with a lower rate than direct multiphonon capture in the electrically neutral

bulk of a semiconductor; conversely, in the case of weak electron–phonon coupling, the capture rate in the depletion region of a semiconductor may exceed by several orders of magnitude the capture rate in the neutral bulk.

The results of experimental studies of the capture processes in AlGaAs doped with silicon indicate that there is a strong electron–phonon coupling in *DX* centers.

ACKNOWLEDGMENTS

We thank A.I. Toropov for supplying us with AlGaAs structures.

REFERENCES

1. T. Markvart, J. Phys. C: Solid State Phys. **14**, L895 (1981).
2. V. N. Abakumov, I. A. Merkulov, V. I. Perel', and I. N. Yassievich, Zh. Éksp. Teor. Fiz. **89**, 1472 (1985) [Sov. Phys. JETP **62**, 853 (1985)].
3. V. Karpus and V. I. Perel', Zh. Éksp. Teor. Fiz. **91**, 2319 (1986) [Sov. Phys. JETP **64**, 1376 (1986)].
4. V. N. Abakumov, V. I. Perel', and I. N. Yassievich, in *Nonradiative Recombination in Semiconductors* (Inst. Yad. Fiz. Ross. Akad. Nauk, St. Petersburg, 1997), Chap. 9, p. 10.
5. S. D. Ganichev, I. N. Yassievich, W. Prettl, *et al.*, Phys. Rev. Lett. **75**, 1590 (1995).
6. S. D. Ganichev, I. N. Yassievich, and V. Prettl, Fiz. Tverd. Tela (St. Petersburg) **39**, 1905 (1997) [Phys. Solid State **39**, 1703 (1997)].
7. D. V. Lang and R. A. Logan, Phys. Rev. B **19**, 1015 (1979).
8. J. C. M. Henning and I. P. M. Ansems, Semicond. Sci. Technol. **2**, 1 (1987).
9. P. M. Mooney, G. A. Northrop, T. N. Morgan, and H. G. Grimmeiss, Phys. Rev. B **37**, 8298 (1988).
10. P. M. Mooney, J. Appl. Phys. **67**, R1 (1990).
11. S. Adachi, J. Appl. Phys. **58**, R1 (1985).
12. L. Pavesi and M. Guzzi, J. Appl. Phys. **75**, 4779 (1994).
13. B. A. Bobylev, V. N. Ovsyuk, S. B. Sevast'yanov, and V. I. Usik, Fiz. Tekh. Poluprovodn. (Leningrad) **23**, 1932 (1989) [Sov. Phys. Semicond. **23**, 1197 (1989)].

Translated by A. Spitsyn

Semiconductors, Vol. 34, No. 6, 2000, pp. 641–643. Translated from Fizika i Tekhnika Poluprovodnikov, Vol. 34, No. 6, 2000, pp. 667–669.

ELECTRONIC AND OPTICAL PROPERTIES OF SEMICONDUCTORS

Temperature Dependences of Electrical Properties of *n*-type PbSe Single-Crystalline Films Subjected to α-Particle Bombardment

Ya. P. Saliĭ* and R. Ya. Saliĭ**

** Near-Carpathians University, Ivano-Frankivsk, 284000 Ukraine*

*** Kiev State University, ul. Glushkova 6, Kiev, 252127 Ukraine*

Submitted December 6, 1999; accepted for publication December 21, 1999

Abstract—The effect of a low-energy α-particle bombardment (5.5 MeV) on the electrical properties of *n*-PbSe is studied. It is found that the bombardment increases the carrier density. The samples with an initial electron concentration lower than 10^{17} cm^{-3} change their properties after an α-particle dose of up to approximately 10^{12} cm^{-2}. The change is not steady for the samples with higher initial carrier densities. The mobilities of charge carriers decrease in samples with a lower initial carrier density and do not change in those with a high carrier density. © *2000 MAIK "Nauka/Interperiodica".*

PbSe is a narrow-band semiconductor of particular interest for application in infrared optoelectronics. Radiation treatment is widely used to control the electrical properties of semiconductors [1–3]. However, there is still a lack of information at present concerning the effect of α-particle bombardment on the temperature variations of electrical properties of the single-crystalline *n*-PbSe films.

In this work, we studied the effect of the bombardment with α-particles with an energy of 5.5 MeV and doses up to 4×10^{12} cm^{-2} on the temperature dependences of the electrical parameters (the concentration n and the mobility of charge carriers μ) for single-crystal films of *n*-type semiconductors. The samples of the *n*-PbSe were films 12–15 μm in thickness deposited in vacuum on the (111) cleavage surface of BaF_2 by a hot wall epitaxy. The concentration and mobility of charge carriers in single-crystalline films were $n \approx 10^{17}$ cm^{-3} and $\mu \approx 3 \times 10^4$ cm^2/(V s). Electrical parameters were measured in the temperature range of 77–320 K. The samples were irradiated with an isotropic flux of low-energy α-particles (5.5 MeV, ^{238}Pu source). The flux was determined by the exposure time using the known flux density 5×10^7 cm^{-2} s^{-1} [4].

Isochronous annealing was performed in air for the samples with electrical parameters varying under the bombardment. The duration of each stage of annealing was 6–10 min. The temperature dependence of the electrical properties at 77–300 K was measured after each annealing. The main stage of the annealing occurs in the range of 90–140°C, within which the concentration and mobility of charge carriers regain their initial values. This apparently restricts the applicability of α-bombardment in manufacturing the reliable thermally stable devices. The parameters of *n*-PbSe samples prior to and after the α-particle bombardment are listed in the table.

The results can be divided into two groups. Samples 30 and 31 belonging to the first group had a relatively low concentration of the charge carriers prior to the bombardment: 1.09×10^{17} and 0.86×10^{17} cm^{-3}, respectively. The concentration of the carriers for this group of samples increased by a factor of 1.5, and the mobility decreased by a factor of 3 under the irradiation with comparatively low doses of α-particles (1.8×10^{11} cm^{-2}). The second group included samples 29 and 32 with higher initial electron concentrations: 1.46×10^{17} and 1.79×10^{17} cm^{-3}, respectively. These samples exhibited no changes in the concentration and mobility even for the α-particles doses equal to 4.32×10^{12} cm^{-2}.

Experimental temperature variations of the concentrations of charge carriers for the samples of the first group prior to and after the bombardment are shown in Fig. 1a. In the low-temperature range of 77–200 K, the concentration of charge carriers is almost constant, and impurity conduction takes place. At higher temperatures, the conductivity slightly increases. The α-particle irradiation causes the curves to shift to higher concentrations with a subsequent stabilization at a level of about 1.6×10^{17} cm^{-3}. The main change in concentration occurs at small doses of up to 10^{11} cm^{-2}; the further increase of dose virtually does not affect the concentration.

1063-7826/00/3406-0641$20.00 © 2000 MAIK "Nauka/Interperiodica"

Sample characteristics

Sample	Thickness h, μm	α-particle flux Φ, 10^{11} cm^{-2}	Concentration N_D^+, 10^{17} cm^{-3}	Adjustable parameters of mobility μ, cm^2/(V s)	
				A, 10^{-3} cm^{-2} V s K$^{3/2}$	B, 10^{-9} cm^{-2} V s K$^{-5/2}$
30	14	0	1.09 ± 0.04	2 ± 1	0.6 ± 0.1
		1.8	1.65 ± 0.05	13 ± 1	1.2 ± 0.1
31	12	0	0.86 ± 0.04	5 ± 1	0.6 ± 0.1
		10.8	1.51 ± 0.06	40 ± 10	1.3 ± 0.1
29	15	0	1.46 ± 0.13	5 ± 1	0.65 ± 0.05
		43.2	1.73 ± 0.08	5 ± 1	0.65 ± 0.05
32	12	0	1.79 ± 0.05	15 ± 1	0.50 ± 0.05
		37.8	1.80 ± 0.08	18 ± 1	0.50 ± 0.05

The obtained temperature dependences of the concentration of charge carriers can be explained by the change in concentrations of donor levels N_D^+ in the course of bombardment and by the contribution of intrinsic conductivity at high temperatures. The temperature dependence of the concentration $n(T)$ can be determined from the equation of electroneutrality

$$n(T) = N_D^+ + n_i^2(300) \times \exp\{-[E_g(T) - E_g(300)]/kT\}/n, \quad (1)$$

where the band gap

$$E_g(T) = E_g(300) - 0.00004(300 - T)\ \text{eV},$$

$E_g(300) = 0.29$ eV, and the preexponential factor of the concentration of intrinsic charge carriers is assumed to depend only weakly on temperature, $n_i(300) = 3 \times 10^{16}$ cm^{-3}. The concentration of donor levels N_D^+ determined from the experimental temperature dependence of the concentration of charge carriers is given in the table. From the table it follows that, as a result of irradiation, the concentration of donor levels for the samples of the first group becomes two times higher, and for the samples of the second group it remains almost unchanged. The limiting value of the concentration $n \approx 1.7 \times 10^{17}$ cm^{-3}, which corresponds to pinning of the Fermi level at the level of a defect with the energy $E_D^+ = E_{FC} = -0.024$ eV determined from the relation

$$n = N_C \exp(E_{FC}/kT), \quad (2)$$

where $N_C = 8.2 \times 10^{18}$ cm^{-3}, $T = 77$ K, and $E_{FC} = E_F - E_C$.

The temperature dependences of mobility for the samples with a low initial concentration of charge carriers are shown in Fig. 1b. The mobility is reduced after the irradiation by a factor of 2–3 within the entire temperature range. At low temperatures, this reduction is caused by scattering by an increased number of ionized defects and, at high temperatures, by the acoustic phonons with modified phonon energy spectrum, probably due to the formation of defects, which results in an increase in the effective interaction of the charge carriers with phonons.

In the samples with a high initial concentration of charge carriers and, consequently, defects, the mobility does not change in the course of bombardment.

The temperature dependence of mobility of charge carriers may be approximated by the following function

$$\mu = \frac{1}{(A/T^{3/2} + BT^{5/2})}, \quad (3)$$

chosen according to Matthiessen rule. Here, the first term in the denominator accounts for the scattering by ionized defects, and the second term, for the scattering by acoustic phonons. It is known that $B \propto E_{ac}^2/C_1$, where E_{ac} is a constant of the deformation potential, C_1 is an averaged velocity of propagation of acoustic vibrations; and $A \propto N_I$, where N_I is the total number of ionized impurities (both donors and acceptors) [5, 6].

The obtained values of coefficients A and B are given in the table. It is seen that, for samples 30 and 31 with a low initial concentration of charge carriers, the coefficients A and B increase with bombardment by factors of 6–8 and 2, respectively. For the samples with a high initial concentration of charge carriers, the coefficients A and B do not change, the coefficient B being equal to the value for the samples of the first group prior to the bombardment. This is indicative of the different nature of the dominant defects in both groups after the bombardment. The prevailing defects in the samples of the first group are the radiation-induced defects, for the

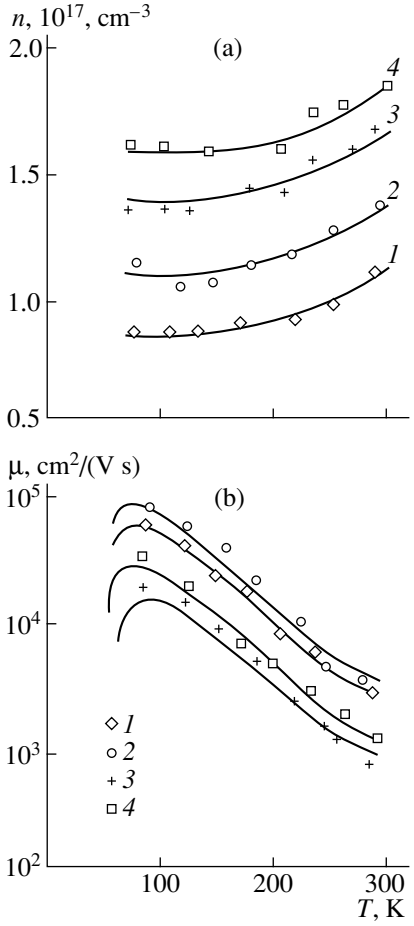

Temperature variations of (a) concentration and (b) mobilities of charge carriers for the *n*-PbSe films (*1*, *2*) prior to α-particle bombardment and (*3*, *4*) after the bombardment; numbers *1* and *3* refer to sample 31; *2* and *4*, to sample 30.

samples of the second group they are native defects. The interstitial atoms formed during the bombardment in the samples of the first group become stabilized, and in the samples of the second group, they recombine with native vacancies. The concentration of the native defects prior to the bombardment in the samples of the first group is twice as high as for the second group.

The temperature dependence of the concentration of charge carriers is affected by the variation of the vacancy concentration; the temperature dependence of carrier mobility, by the variation in the concentration of interstitial atoms.

REFERENCES

1. D. M. Zayachuk and V. A. Shenderovskiĭ, Ukr. Fiz. Zh. **36** (11), 1692 (1991).
2. Ya.P. Saliĭ, Ukr. Fiz. Zh. **43** (8), 968 (1998).
3. D. M. Freik, V. V. Prokopiv, and Ya. P. Saliĭ, Neorg. Mater. **32** (5), 546 (1996).
4. D. M. Freik, A. K. Shkol'nyĭ, and Ya. P. Saliĭ, Ukr. Fiz. Zh. **34** (9), 1392 (1989).
5. D. M. Zayachuk, Fiz. Tekh. Poluprovodn. (St. Petersburg) **31** (2), 281 (1997) [Semiconductors **31** (2), 173 (1997)].
6. F. J. Blatt, *Physics of Electronic Conduction in Solids* (McGraw-Hill, New York, 1968; Mir, Moscow, 1971).

Translated by A. Zalesskiĭ

Semiconductors, Vol. 34, No. 6, 2000, pp. 644–649. Translated from Fizika i Tekhnika Poluprovodnikov, Vol. 34, No. 6, 2000, pp. 670–676.

ELECTRONIC AND OPTICAL PROPERTIES OF SEMICONDUCTORS

Charge Carrier Mobility in *n*-$Cd_xHg_{1-x}Te$ Crystals Subjected to Dynamic Ultrasonic Stressing

A. I. Vlasenko, Ya. M. Olikh, and R. K. Savkina*

Institute of Semiconductor Physics, National Academy of Sciences of Ukraine, Kiev, 252028 Ukraine

** e-mail: savkina@class.semicond.kiev.ua*

Submitted December 9, 1999; accepted for publication December 23, 1999

Abstract—The Hall mobility was studied in the *n*-$Cd_xHg_{1-x}Te$ crystals subjected to dynamic ultrasonic stressing ($W_{US} \le 10^4$ W/m^2, f = 5–7 MHz). It was found that, in field of the ultrasonic deformation, an increase in the carrier mobility in the impurity conduction region (T < 120 K) and a decrease in the intrinsic conduction region (T > 120 K) occurred in all tested samples. In this case, the magnitude of the sonic-stimulated variation in μ_H increases with decreasing structural perfection of a crystal. Different mechanisms of ultrasonic influence on μ_H with regard to scattering by optical phonons, ionized impurities, and alloy potential are analyzed, with the current flow conditions in the crystal taken into account. It is shown that, in the impurity conduction region, the main cause of the sonic-stimulated increase of the Hall mobility is the smoothing of the macroscopic intracrystalline potential that results from the inhomogeneity of the crystals. In the intrinsic conduction region, a decrease in mobility is caused by an increase in the intensity of scattering by the optical phonons. © *2000 MAIK "Nauka/Interperiodica".*

1. INTRODUCTION

Previously, it was found that transport coefficients of the $Cd_xHg_{1-x}Te$ crystals are sensitive to the effect of the intense high-frequency alternating deformation, that is, to the ultrasonic effect both in the mode of ultrasound treatment [1, 2] and in the course of dynamic stressing [3–5]. Different mechanisms of acoustically stimulated irreversible variations of the electrical parameters (concentration and mobility) of the $Cd_xHg_{1-x}Te$ crystals, including thermoacoustic annealing [1], destruction of the defect clusters [2], and so on, have been proposed. Processes of the ultrasound-induced transformation of the crystal defects in $Cd_xHg_{1-x}Te$ were studied in [4, 5]. In this paper, we analyze mechanisms of the carrier mobility variations in the n-$Cd_xHg_{1-x}Te$ crystals that have different degrees of structural perfection and are subjected to dynamic ultrasonic stressing.

2. EXPERIMENTAL RESULTS

Temperature dependences of the Hall mobility $\mu_H(T)$ in the *n*-$Cd_xHg_{1-x}Te$ crystals ($0.2 \le x \le 0.22$ and 3×10^{14} cm^{-3} < n < 10^{15} cm^{-3}) in the intense field of the ultrasound-induced deformation ($W_{US} \le 10^4$ W/m^2, f = 5–7 MHz) in the temperature range T = 77–300 K were studied. The experimental technique was described in [5].

Experimental curves of $\mu_H(T)$ for several samples with different μ_H^0 values at T = 77 K are shown in Fig. 1 (curves *1–4*). The initial $\mu_H^0(T)$ dependences in the intrinsic conduction region (T > 120 K) are similar to the corresponding dependence in the structurally perfect crystals (dashed line), but, in the impurity conduction region, the mobility is lower. For samples 3 and 4, the slope of the $\mu_H^0(T)$ curve inverts at T < 120 K and the mobility has anomalously low values. This can be explained by the variation of the scattering mechanism that is observed in the $Cd_xHg_{1-x}Te$ crystals at lower temperatures (T < 50 K) [6, 7]. Apparently, these trends in μ_H(T) are related to the variation of the current flow conditions due to the bulk inhomogeneity of the crystals, which is confirmed by the form of the resistivity dependences on the magnetic field. In high magnetic fields ($B \ge 0.2$ T), the resistivity does not saturate and magnetoresistance $\Delta\rho_\perp/\rho_0(B)$ increases linearly with B. It should be noted that, in sample 1, the magnetoresistance dependence on B is weak and the μ_H(T) dependence is the most similar to the mobility behavior in the structurally perfect crystal. In addition, in sample 4, the Hall coefficient R_H strongly depends on B (>20% for $B \le 0.55$ T). Apparently, at lower temperatures (<77 K), conduction in the sample becomes of the *p*-type.

Under ultrasound stressing, an increase in μ_H^{US}/μ_H^0 = 1.1–1.8 in the impurity conduction region (T < 120 K) and a decrease in the Hall mobility μ_H^{US}/μ_H^0 = 0.83–0.93 in the intrinsic conduction region are observed in all investigated samples (Fig. 1, curves *1'–4'*). In this case, the magnetoresistance dependences $\Delta\rho_\perp/\rho_0(B)$ are saturated in high magnetic fields. Henceforth, the index *US* indicates that the parameter is mea-

sured in the field of the ultrasound-induced deformation, and the index 0 corresponds to the measurements in the absence of ultrasonic stressing (except for ρ_0, which is the resistivity at $B = 0$). It should be noted that all observed acoustically stimulated variations have a reversible character. After switching off the ultrasound, mobility in the impurity conduction region returns to the initial values in the same time as the carrier concentration $(eR_H)^{-1}$. The conditions of our experiment do not allow us to say the same about mobility in the intrinsic conduction region.

The Raman spectra are shown in Fig. 2 for samples 3 and 4 with the largest influence of ultrasound on mobility. Curves *1*' and *2*' correspond to the ultrasonic stressing at room temperature. Curves *1* and *2* correspond to the measurements at the same temperature with an absence of ultrasonic stressing. The caption to Fig. 2 describes the conditions under which the spectra were measured.

The mobility dependences on the intensity of the ultrasonic stressing $\mu_H(\sigma_{US})$ at different temperatures are shown in Fig. 3. It can be seen that the form of the amplitude dependences $\mu_H(\sigma_{US})$ is governed by temperature. At $T = 83$ K (curve *1*), μ_H increases linearly under the influence of the ultrasonic vibrations. At higher temperatures ($T = 93$ K, curve *2* and $T = 103$ K, curve *3*), the mobility μ_H levels off after a small linear increase. As the temperature is further increased, an acoustically stimulated decrease in $\mu_H(\sigma_{US})$ ($T = 125$ K, curve *4*) is observed.

3. DISCUSSION

Analyzing the experimental data, it should be noted that the acoustically stimulated variation of the Hall mobility can be related, first of all, to the variation in the conditions of charge-carrier scattering in the crystal in the presence of ultrasonic stressing. Another possible reason is the changing of the current flow conditions in an inhomogeneous crystal. Let us analyze these possible reasons in detail.

As has been established previously, for proper analysis of the μ_H(T) dependence in $Cd_xHg_{1-x}Te$ at T = 4–300 K, it is sufficient to consider three scattering mechanisms: by polar optical phonons (μ_{op}), by alloy potential (μ_{al}), and by ionized impurities (μ_{ion}) [8]. Such mechanisms as acoustic phonon scattering and electron–electron scattering do not provide a noticeable contribution to the total scattering process. Let us assume that, in the presence of ultrasonic stressing, the carrier scattering is determined by the same mechanisms:

$$(\mu_H^{US})^{-1} = (e/m^*)^{-1}\sum(\tau_i^{US})^{-1} = (\mu_{op}^{US}) + (\mu_{al}^{US})^{-1} + (\mu_{ion}^{US})^{-1}. \quad (1)$$

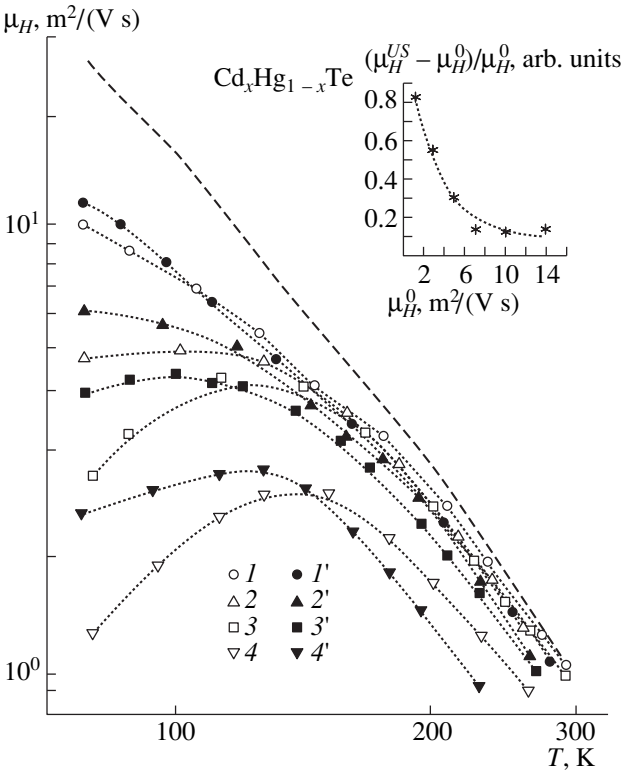

Fig. 1. Temperature dependences of the Hall mobility μ_H in the $Cd_xHg_{1-x}Te$ crystals. Curves *1, 2, 3,* and *4* were measured in the absence of ultrasound stressing, and curves *1*', *2*', *3*', and *4*' correspond to the samples subjected to ultrasound stressing ($\sigma_{US} = 4.8 \times 10^5$ Pa, $f = 6.5$ MHz). The $\mu_H(T)$ dependence for a structurally perfect crystal is given by the dashed line [6]. The dependence of the sonic-stimulated increase in the Hall mobility $\Delta\mu_{H,77}^{US} = (\mu_H^{US} - \mu_H^0)/\mu_H^0$ on the value of $\mu_{H,77}^0$ at $T = 77$ K and $\sigma_{US} = 4.8 \times 10^5$ Pa is shown in the insert.

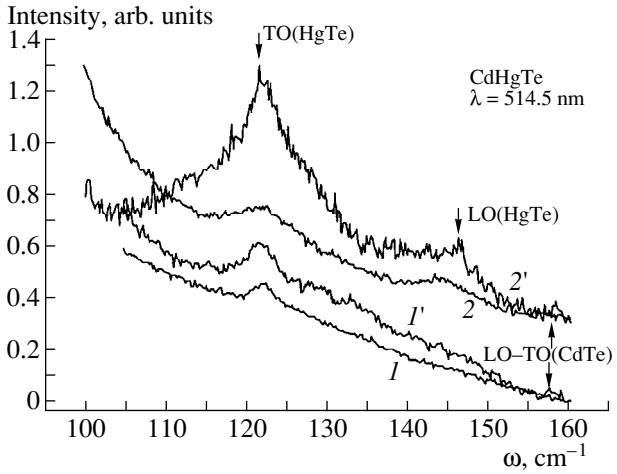

Fig. 2. Raman spectra of the $Cd_xHg_{1-x}Te$ crystals (curves *1* and *1*' correspond to sample 3; curves *2* and *2*' correspond to sample 4). Curves *1*' and *2*' correspond to the sample subjected to ultrasound stressing, $T = 300$ K, $\sigma_{US} = 4.8 \times 10^5$ Pa.

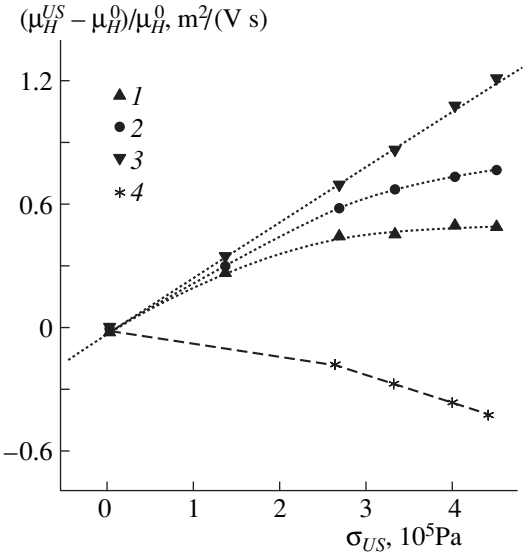

Fig. 3. Dependence of the carrier mobility on the amplitude of the ultrasound stressing of the $Cd_xHg_{1-x}Te$ crystal (sample 3) at temperatures of (*1*) 83, (*2*) 93, (*3*) 103, and (*4*) 125 K.

Let us consider separately each of these mechanisms from the standpoint of its ultrasound-induced modification.

3.1. Ionized-Impurity Scattering

Ionized impurity scattering is dominant in $Cd_xHg_{1-x}Te$ crystals at T < 50 K. Nevertheless, it is necessary to consider this mechanism at higher temperatures. The relaxation time for this mechanism can be given by [8]

$$\tau_{\text{ion}} = (\varepsilon_s \hbar^3/2\pi e^4 N_i)(k^3/m^*)(1/F_{\text{ion}}), \qquad (2)$$

where F_{ion} is a function accounting for the symmetry of the electron wave functions and for the screening of the scattering center potentials by the free carriers, N_i is the concentration of the ionized impurities, $\varepsilon_s = \varepsilon_L + \varepsilon_\infty$, ε_L is the dielectric constant of the CdTe and HgTe sublattices, and ε_∞ is the high-frequency dielectric constant. Other designations are as generally accepted.

It is well known that the essence of the processes that occur in $Cd_xHg_{1-x}Te$ crystals under the influence of external factors, such as laser irradiation [9], deformation [10], γ-irradiation [11], ultrasonic treatment [1], etc., consists in the redistribution of the initial (native) defects or newly formed point defects between matrix and sinks (dislocations, small-angle boundaries, boundaries of subblocks, and so on). This process is governed by the initial state of the defects and causes variation of the material properties. One can assume that a similar situation takes place also in the case of dynamic below-threshold ultrasonic stressing of $Cd_xHg_{1-x}Te$ crystals [4, 5]. In accordance with general mechanisms of the defect transformation in $Cd_xHg_{1-x}Te$ in the field of intense ultrasound-induced deformation, a temporary (during the ultrasound action) detachment of the point defects (for example, Hg or background-impurity atoms) from dislocations and small-angle boundaries to the interstices of matrix and (or) capture of vacancies by the linear defects are possible. In this case, the concentration of donors $N_d^0 + N_d^{US}$ should increase and the concentration of acceptors $N_a^0 - N_a^{US}$ should decrease. Therefore, in the presence of ultrasonic stressing, the concentration of the scattering centers N_i should be changed. Let us express N_i^{US}, without consideration of the ionization degree of the defects, as

$$N_i^{US} = N_i^0 + \Delta N_i = N_i^0 + (N_d^{US} - N_a^{US}). \qquad (3)$$

At $T = 77$ K and $\sigma_{US} = 4.8 \times 10^5$ Pa, ultrasound-induced variation of carrier concentration from $n_0 = 7.5 \times 10^{14}$ cm^{-3} to $n_{US} = 8.5 \times 10^{14}$ cm^{-3} is observed for sample 1, from $n_0 = 3.2 \times 10^{14}$ cm^{-3} to $n_{US} = 4 \times 10^{14}$ cm^{-3} for sample 2, from $n_0 = 3 \times 10^{14}$ cm^{-3} to $n_{US} = 6 \times 10^{14}$ cm^{-3} for sample 3, and from $n_0 = 9 \times 10^{14}$ cm^{-3} to $n_{US} = 1.5 \times 10^{15}$ cm^{-3} for sample 4. Concentration variation $(n_{US} - n_0)$ corresponds to the ΔN_i value. In the tested samples, N_i^0 does not exceed 5×10^{15} cm^{-3}. Taking into account (3), we easily derive the relation between μ_{ion}^0 and μ_{ion}^{US} as

$$(\mu_{\text{ion}}^{-1})^{US} = (\mu_{\text{ion}}^{-1})^0(1 + \Delta N_i/N_i^0), \qquad (4)$$

from which, considering the aforementioned estimates of ΔN_i and N_i^0, we obtain the ratio $\mu_{\text{ion}}^{US}/\mu_{\text{ion}}^0 = (0.99–0.89)$. This shows that the intensity of scattering by the ionized impurities increases due to an acoustically stimulated increase in the concentration of scattering centers. Therefore, this mechanism does not allow us to explain an increase in the mobility μ_H, which is observed in the experiment.

As one can see from (2), another cause of mobility variation in the case of scattering by the ionized impurities may be an increase in the free carrier concentration *n* in the crystal. This results, first, in more effective screening of the Coulomb potential of scattering centers, and, therefore, in a decrease in the contribution of this mechanism to the total scattering. This assumption is confirmed by calculations of the $F_{\text{ion}}(n)$ dependence: an increase in *n* from 10^{14} to 10^{15} cm^{-3} leads to $F_{\text{ion}}^{US}/F_{\text{ion}}^0 = 0.95$ and, as a result, to an insignificant increase in the mobility ratio $\mu_{\text{ion}}^{US}/\mu_{\text{ion}}^0 = 1.05$. Furthermore, an increase in the carrier concentration causes also an increase in mobility μ_{ion} due to an increase in the average electron energy [12]. However, although

this mechanism results in an increase in mobility, it does not enable us to explain quantitatively the experimental results for all tested samples, in particular, for the dependence of the ultrasound-induced mobility increase on the $\mu^0_{H,77}$ value measured in the absence of the ultrasonic deformation. Dependence of the acoustically stimulated increase in the Hall mobility $\Delta\mu^{US}_{H,77}$ on the $\mu^0_{H,77}$ value is presented in Fig. 1 (see the inset). The larger the value of $\mu^0_{H,77}$, the less pronounced the ultrasound effect (that is, $\Delta\mu^{US}_{H,77}$) for equal values of the intensity of the ultrasound stressing.

3.2. Scattering by the Alloy Potential

Scattering by the alloy potential arises from the disturbance in periodicity of the crystal potential in $A_xB_{1-x}C$ solid solutions due to disorder in the arrangement of the A and B atoms in the sites of the crystal lattice. Study of this mechanism is based on the assumption that the difference between the A and B atomic potentials $U_{AB}(r) = U_A - U_B$ is a small perturbation. In addition, the U_{AB} potential is localized: $U_{AB} = \Delta E$ for $r < r_0$ and $U_{AB} = 0$ for $r > r_0$, where r_0 is the distance between the nearest neighbors [13].

The relaxation time for alloy scattering may be expressed as [14]

$$\tau_{al} = (\pi N_0/\hbar x(1-x)\Delta E^2)(k^{-3}(d\varepsilon/dk)^2), \qquad (5)$$

where ΔE is the alloy scattering potential, N_0 is the number of atoms in the unit volume, and x is the composition parameter. The value of ΔE is assumed, in the first approximation, to be equal to the difference between the band gaps of the AC and BC crystals [15, 16]. It is proposed in [14] to choose ΔE as the difference between the A and B atomic screened potentials. In this case, the value of the alloy potential for $Cd_xHg_{1-x}Te$ is $\Omega\Delta E = 9 \times 10^{-29}$ eV cm^3, $\Delta E = 1$ eV [14, 17] and Ω is the volume of the unit cell. A much smaller value $\Delta E = 0.23$ eV obtained from calculations in the coherent potential approximation [18] was successfully used in [19] in calculations of the mobility temperature dependences. It should be noted that, most often, ΔE is used as an adjustable parameter determined from a comparison of the calculated and experimental data.

As in the above case of the ionized impurity scattering, it is possible to assume the existence of several mechanisms of the ultrasound-induced modification of scattering by the disorder of the crystal lattice. First, due to the μ_{al} dependence on the electron energy ($\sim\varepsilon^{-1/2}$) [14], an acoustically stimulated increase in the carrier concentration should enhance scattering by the alloy potential. Calculations at $T = 10$ K show that the contribution of this mechanism increases from 5% for $n = 4 \times 10^{14}$ cm^{-3} to 25% for $n = 2 \times 10^{16}$ cm^{-3} [20]. A similar result was obtained in [12] at $T = 77$ K. Thus, due to the acoustically stimulated increase of n, the mobility limited by the alloy scattering should decrease, which excludes this mechanism from consideration, because it does not correspond to the experimentally observed effect.

The deformation mechanism of the ultrasound influence on the alloy potential is quite possible if we choose the latter as the difference between the CdTe and HgTe band gaps. However, calculations show that, at the intensities of ultrasound-stressing used in the experiment, the value of the effective pressure P generated by the ultrasonic wave in crystal does not exceed 5×10^5 Pa. In this case, the alloy potential in the field of the ultrasound-induced deformation $\Delta E^{US} = [\varepsilon_g^0 + (d\varepsilon_g/dP)P]_{CdTe} - [\varepsilon_g^0 - (d\varepsilon_g/dP)P]_{HgTe}$ decreases by a negligible value (no more than $\sim 5 \times 10^{-5}$ eV). Finally, since the carrier concentration increases in the ultrasound field, it is possible to assume that the alloy potential has additional screening. However, in the case of alloy scattering, it is not clear if screening significantly changes the localized potential ΔE [14].

Thus, the analysis shows that it is impossible to explain the effect of the ultrasound-induced increase of the Hall mobility in the impurity conduction region only on the basis of variation of the scattering conditions.

3.3. Ultrasound-Stimulated Modification of the Large-Scale Crystal Potential

Another possible cause of the acoustically stimulated increase in mobility μ_H is variation of the current flow conditions in the sample due to the ultrasound-induced modification of the intracrystalline potential. We have in mind the large-scale potential, whose specific dimension exceeds the carrier free path, and, therefore, we do not consider the influence of this potential on the electron scattering processes. It is well known that reduced (in comparison with the theoretical values) carrier mobilities and the anomalous decrease of $\mu_H(T)$ in the impurity conduction region at $T <$ 120 K, which we observed in the tested samples, cannot be explained by additional scattering mechanisms. This shows that there are drift barriers in the crystal related to the covariant and contravariant modulation of the crystal energy bands in the inhomogeneous samples [21, 22]. At the same time, the larger the size of inhomogeneity, the greater the difference between the Hall mobility and the drift mobility. The presence of the bulk inhomogeneities in the samples is confirmed, as we mentioned above, by the linear dependence of $\Delta\rho_\perp/\rho_0(B)$ in the high magnetic fields.

In our opinion, the intracrystalline potential is smoothed in the field of the ultrasound-induced deformation. The point defects localized at (or near) the extended defects absorbing the ultrasound wave are

transferred to the matrix under the effect of the acoustic field and cause the hillocks in the potential relief to flatten. In this case, a larger crystal volume is involved in conduction at the percolation level. The increase of the Hall mobility in the impurity conduction region ($T <$ 120 K) and the saturation of the magnetoresistance $\Delta\rho_\perp/\rho_0(B)$ in the high magnetic fields in the samples subjected to ultrasonic stressing confirm these assumptions.

It is necessary to make clear that, by inhomogeneities, which give rise to the large-scale potential, we mean dislocations with the surrounding impurities, the dislocation clusters, the low-angle boundaries, inclusions of the second phase of the basic components of the solid solution, impurities which appear near dislocations, and other defects. Considering the sonic-dislocation mechanism as dominant in the ultrasound-wave interaction with crystal and absorption of the ultrasonic energy near such macrodefects, we can also assume that smoothing of the large-scale potential is governed by the ultrasound-initiated deionization of the levels localized at the dislocation line. In the initial state, these levels capture the majority carriers and form impermeable inclusions. The acoustically stimulated increase in the electron concentration in the impurity conduction region supports this assumption [5]. However, study of the relaxation time of the acoustically stimulated processes in *n*-CdHgTe show that, after relief of the ultrasound stressing, concentration and mobility return to the initial values in ~10^2–10^3 s. This suggests that the ultrasound-stimulated transformations involve diffusion rather than recombination, because, in the latter case, the typical relaxation time is ~10^{-6}–10^{-7} s.

It should be also noted that, in spite of the key role of dislocations in the ultrasonic effects in the CdHgTe crystals, we do not consider scattering by dislocations, because the contribution of this mechanism becomes appreciable at temperatures < 50 K for a dislocation density of $N_d > 10^6$ cm^{-2} [23]. However, in the investigated samples, N_d does not exceed 10^5 cm^{-2}. In addition, we do not exclude the possibility of the ultrasound-induced formation, under certain conditions, of a parallel conduction channel with carrier mobility higher than that in the matrix. However, further studies are needed to confirm this conclusion.

3.4. Optical Phonon Scattering

We now attempt to explain the decrease of the carrier mobility in the intrinsic conduction region. It has been established that scattering by the optical phonons is dominant in the CdHgTe crystals in the temperature range of 77–300 K. Therefore, a decrease in the carrier mobility in the field of the ultrasound-induced deformation in the intrinsic conduction region, which we observed in all tested samples, can be explained by the ultrasound-induced modification of the CdHgTe phonon spectrum. Actually, in the field of the ultrasound-induced deformation, an increase in the band intensity of the Raman spectra occurs (Fig. 2). We may relate this result to an increase in the crystal's effective temperature, which causes the rate of scattering by optical phonons to increase. Attention is attracted to the fact that the ultrasound influence on the Raman spectra correlates with the magnitude of the acoustically stimulated variation of mobility in these samples. Further studies are necessary for quantitative estimations. We only note that, both in the impurity conduction and intrinsic conduction regions, an increase in the rate of scattering by optical phonons also occurs.

The competition of the scattering processes mentioned above gives an adequate explanation of the Hall mobility dependences on the intensity of the ultrasound stressing $\mu_H(\sigma_{US})$ at different temperatures (Fig. 3). At lower temperatures, the form of the $\mu_H(\sigma_{US})$ dependence is determined by the acoustically induced smoothing of the intracrystalline potential, i.e., by variation of the current flow conditions under ultrasound stressing due to an increase in the effective crystal volume at the percolation level. As temperature increases, the concentration distribution over the crystal becomes uniform and the space-charge regions disappear. In this case, the contribution of the crystal lattice vibrations increases and the efficiency of this mechanism in the field of the ultrasound-induced deformation also increases. This accounts for the fact that the curve $\mu_H(\sigma_{US})$ first levels off and then descends. Now the dependence of the ultrasound-induced increase of μ_H on the value of $\mu^0_{H,77}$ becomes quite clear. The least pronounced effect is observed in sample 1, which has the most perfect structure and the highest value of $\mu^0_{H,77}$. It is reasonable to assume that, in the uniform CdHgTe crystal in which it is possible to neglect the influence of the large-scale potential, the ultrasound-induced decrease in the carrier mobility would occur in the temperature range of 77–300 K due to an increase in the rate of scattering by optical phonons and alloy potential.

CONCLUSION

Thus, we observed an increase in the Hall mobility in the impurity conduction region ($T <$ 120 K) in $Cd_xHg_{1-x}Te$ crystals subjected to dynamic ultrasound stressing. The magnitude of the sonic-stimulated variation in μ_H increases with the decreasing structural perfection of a crystal. We also observed a mobility decrease in the intrinsic conduction region ($T >$ 120 K) for all investigated samples. We analyzed the possible mechanisms of the ultrasound influence on the μ_H taking into account scattering by optical phonons, ionized impurities, alloy potential, and the conditions of the current flow in the crystal. In the impurity conduction region, the principal cause of the ultrasound-induced

increase in the Hall mobility is the smoothing of the macroscopic intracrystalline potential determined by the inhomogeneity of the tested crystals. In the intrinsic conduction region, a decrease in mobility is attributed to an increase in the rate of scattering by optical phonons.

REFERENCES

1. K. A. Myslivets and Ya. M. Olikh, Fiz. Tverd. Tela (Leningrad) **32**, 2912 (1990) [Sov. Phys. Solid State **32**, 1692 (1990)].
2. P. I. Baranskiĭ, A. E. Belyaev, S. M. Komirenko, and N. V. Shevchenko, Fiz. Tverd. Tela (Leningrad) **32**, 2159 (1990) [Sov. Phys. Solid State **32**, 1257 (1990)].
3. A. V. Lyubchenko and Ya. M. Olikh, Fiz. Tverd. Tela (Leningrad) **37**, 2505 (1985) [Sov. Phys. Solid State **27**, 1500 (1985)].
4. O. I. Vlasenko, Ya. M. Olikh, and R. K. Savkina, Ukr. Fiz. Zh. **44**, 618 (1999).
5. A. I. Vlasenko, Ya. M. Olikh, and R. K. Savkina, Fiz. Tekh. Poluprovodn. (St. Petersburg) **33**, 410 (1999) [Semiconductors **33**, 398 (1999)].
6. A. I. Vlasenko, A. V. Lyubchenko, and E. A. Sal'kov, Ukr. Fiz. Zh. **25**, 1318 (1980).
7. Y. Y. Dubowski, T. Dietl, W. Szymanska, and R. R. Galaska, J. Phys. Chem. Solids **42**, 351 (1981).
8. W. Szymanska and T. Dietl, J. Phys. Chem. Solids **39**, 1025 (1978).
9. A. I. Vlasenko, K. R. Kurbanov, A. V. Lyubchenko, and E. A. Sal'kov, Ukr. Fiz. Zh. **25**, 1392 (1980).
10. S. G. Gasan-zade, Optoélektron. Poluprovodn. Tekh. **33**, 91 (1998).
11. A. I. Vlasenko, V. V. Gorbunov, and A. V. Lyubchenko, Ukr. Fiz. Zh. **29**, 423 (1984).
12. I. R. Gorokhovskiĭ, A. K. Laurinavichyus, Yu. K. Pozhela, *et al.*, Fiz. Tekh. Poluprovodn. (Leningrad) **21**, 1998 (1987) [Sov. Phys. Semicond. **21**, 1211 (1987)].
13. P. N. Gorleĭ and V. A. Shenderovskiĭ, *Variational Methods in the Kinetic Theory* (Naukova Dumka, Kiev, 1992).
14. J. Kossut, Phys. Status Solidi B **86**, 593 (1978).
15. D. Chattopadhyay and B. R. Nag, Phys. Rev. B **12**, 5676 (1975).
16. L. Makowski and M. Glicksman, J. Phys. Chem. Solids **34**, 487 (1973).
17. Y. Y. Dobowski, Phys. Status Solidi B **85**, 663 (1978).
18. K. C. Hass, H. Ehrenreich, and B. Velicky, Phys. Rev. B **27**, 1088 (1983).
19. P. Moravec, R. Grill, J. Franc, *et al.*, Proc. SPIE **3890**, 307 (1999).
20. F. J. Bartoli, C. A. Hoffman, and J. R. Meyer, J. Vac. Sci. Technol. A **1**, 1669 (1983).
21. M. A. Kinch, M. J. Brau, and A. Simmons, J. Appl. Phys. **44**, 1649 (1973).
22. M. K. Sheĭnkman and A. Ya. Shik, Fiz. Tekh. Poluprovodn. (Leningrad) **10**, 209 (1976) [Sov. Phys. Semicond. **10**, 128 (1976)].
23. H. Oszwaldowski, J. Phys. Chem. Solids **46**, 791 (1985).

Translated by I. Kucherenko

Semiconductors, Vol. 34, No. 6, 2000, pp. 650–654. Translated from Fizika i Tekhnika Poluprovodnikov, Vol. 34, No. 6, 2000, pp. 677–681.

ELECTRONIC AND OPTICAL PROPERTIES OF SEMICONDUCTORS

On the Origin of the Thermal–Field Asymmetry in Ionic Polarization/Depolarization of Oxide in Si-MOS Structures

E. I. Gol'dman, A. G. Zhdan, and G. V. Chucheva

Institute of Radio Engineering and Electronics (Fryazino Branch), Russian Academy of Sciences, pl. Vvedenskogo 1, Fryazino, Moscow oblast, 141120 Russia

Submitted December 20, 1999; accepted for publication December 28, 1999

Abstract—Based on the concepts of the significant role of the surface neutralization of positive ions at the boundaries of the oxide layer in the processes of ion transport in an insulating gap of MOS structures, the origin of a well-pronounced asymmetry in the temperature and temporal characteristics of the volume–charge ionic polarization/depolarization of an insulator are analyzed. The neutralization of ions occurs owing to the tunneling capture of electrons from semiconducting and metallic contacts. Experimental data obtained in a wide range of variations in the gate potential V_g and related to the thermally stimulated and isothermal polarization of oxide in Si-MOS structures consistently support the asymmetry model that accounts for a higher degree of neutralization of ions and a higher coupling of ions to electrons at the metal surface (gate) than at the semiconductor surface. The transients exhibit three stages during polarization. The first of these is related to the transport of unneutralized (free) ions; in the initial stages of thermally stimulated and isothermal polarization for V_g = const, the ions move in the oxide ballistically. In the second stage, a transition from the mode of free-ion drift to the modes of hyperbolic and (or) exponential kinetics of relaxation is observed; in the latter case, the current becomes virtually independent of the field, temperature, and the rates of the field or temperature scans and becomes a single-valued function of actual time. In this case, the law of relaxation is defined by the rate of tunneling ionization of neutral associations of ion + electron and (or) by their diffusion and thermal decomposition in the bulk of the insulator. *© 2000 MAIK "Nauka/Interperiodica".*

The observations of pronounced asymmetry in the processes of the bulk–charge ionic polarization and depolarization of the gate oxide in Si-MOS structures are well known [1–6]; however, these observations have not been adequately interpreted so far. At the same time, the determination of the physical origin of such distinctions is very important both from the cognitive standpoint and from the standpoint of solving the practical MIS-microelectronics problems requiring a substantial reduction in the level of ionic contamination of the insulator so that the optical-active range could be extended to the submicron region [7–11]. Other factors being the same, the polarization of SiO_2 proceeds much slower than the depolarization and sets in for depolarizing gate potentials $V_{gd} < 0$. These circumstances clearly manifest themselves in both the isothermal dynamic current–voltage (*I–V*) characteristics of polarization and depolarization and in the measurements of thermally stimulated polarization; for values of V_g close in magnitude, the polarization currents are observed at appreciably higher temperatures than the depolarization currents [4, 6] (Fig. 2).

We are going to show that the analysis of the field and temperature characteristics of thermally stimulated and isothermal polarization and depolarization of the insulating layer in MIS structures makes it possible to clarify the cause of the asymmetry observed.

We studied an Al–SiO_2–*n*-Si(100) system similar to those investigated in [5, 6, 12]. The technique and the data-processing algorithms of experiments and also the measurement procedure were described in detail in [13]. The structure was completely depolarized at a high temperature ($T \simeq 423$ K) with a voltage of V_{gd} = –10 V, was cooled to 295 K, and the potential of the field electrode was then changed abruptly to that corresponding to polarization ($V_{gp} > 0$); in the course of subsequent heating at a constant rate of $\beta_T \simeq 0.4$ K/s, we measured the current of thermally stimulated polarization (TSP) $I = jS$, where j is the current density and S is the area of the field electrode. A family of TSP curves obtained for several values of V_{gp} = const is shown in Fig. 2. It follows from Fig. 2 that the curves $I(T)$ shift to lower temperatures as V_{gp} increases and, in the region of the initial increase, the TSP current follows the Arrhenius law with the activation energy E virtually independent of the polarizing field (see the insert in Fig. 2).[1] In a wide range of V_g ($1.0 \le V_g \le 10$ V), the value of E is almost constant and equals 0.82 ± 0.05 eV; i.e., within the limits of experimental accuracy, E coin-

[1] In the case of *a priori* unknown kinetics of thermally stimulated relaxation, the "method of initial increase in current," in which the relationship $I \propto \text{const}\exp(-E/kT)$ is used, yields the most reliable data on the value of E [14–16].

cides with the activation energy of thermally stimulated depolarization, which is equal to 0.87 ± 0.05 eV [6]. According to [6], this indicates that the initial stages of an increase in the TSP current are related to the thermal activation of the time of transit τ_d of free ions through the oxide layer. Under the condition of the drift of small charge [17], i.e., if the inequality

$$4\pi q N_S \kappa_{SiO_2} \ll V_{gp}/h \qquad (1)$$

is valid, the TSP current is given by

$$I = \frac{qSN_S}{\tau_d} = \frac{qSN_S\tilde{V}_{gp}\mu_0\exp(-E_\mu/kT)}{h^2}. \qquad (2)$$

Here, q is the elementary charge; N_S is the density of free ions at the oxide/gate contact, which are not neutralized and are involved in the transit; κ_{SiO_2} is the oxide permittivity; h is the oxide thickness; $\tilde{V}_{gp} = V_{gp} + V_c$ is the voltage drop across the oxide; $V_c \cong 0.5$ V is the contact potential difference for Al–Si (it was calculated according to [18] for Si with a free-electron concentration of 10^{13} cm^{-3} [5, 6, 12] at a temperature of 350 K, which corresponds to the middle of the temperature range used; see Fig. 3, curve *1*); $\tau_d = h^2/\mu\tilde{V}_{gp}$, where $\mu = \mu_0\exp(-E_\mu/kT)$ is the ion mobility; E_μ is the activation energy of mobility; and k is the Boltzmann constant. According to (2), the corresponding Arrhenius curves plotted as $\log(I/\tilde{V}_{gp}) = f(T^{-1})$ are expected to be represented by a common straight line whose slope is defined by the value of E_μ. Such a plot constructed on the basis of the data shown in Fig. 2 is in complete agreement with the above concepts (Fig. 3, curve *1*). The value of E_μ determined by the method of least squares is 0.82 ± 0.05 eV. Extrapolating the straight line $\log(I/\tilde{V}_{gp}) = f(T^{-1})$ to the point $T^{-1} = 0$, we estimate that $N_S \simeq 3.3 \times 10^8$ cm^{-2} ($S = 2.4 \times 10^{-2}$ cm^2, $\mu_0 = 3.2$ cm^2 V^{-1} s^{-1} [6], and $h = 1.7 \times 10^5$ cm) from the portion $\log(qSN_S\mu_0/h^2)$ intercepted on the T^{-1} axis by this line [see (2)]. Substituting this value of N_S into the left-hand side of (1), we obtain (for $\kappa_{SiO_2} = 3.9$) $4\pi qN_S/\kappa_{SiO_2} \simeq 1.5 \times 10^2$ V cm^{-1}, and, as can be easily verified, the condition for the small-charge drift is met for all experimental values of $\tilde{V}_{gp}$ (Figs. 2, 3). Relying on the above consideration, identifying E with E_μ, and taking into account that the determined value of E_μ agrees well both with the known values [17, 19–22] and with the values obtained previously by us using other methods [5, 12], we conclude that the initial stages in an increase in the TSP current are definitely related to the thermal activation of the free-ion transit.

Comparison of the data obtained here on TSP with the results of studies of thermally stimulated depolarization [6] makes it possible to clarify the origin of the

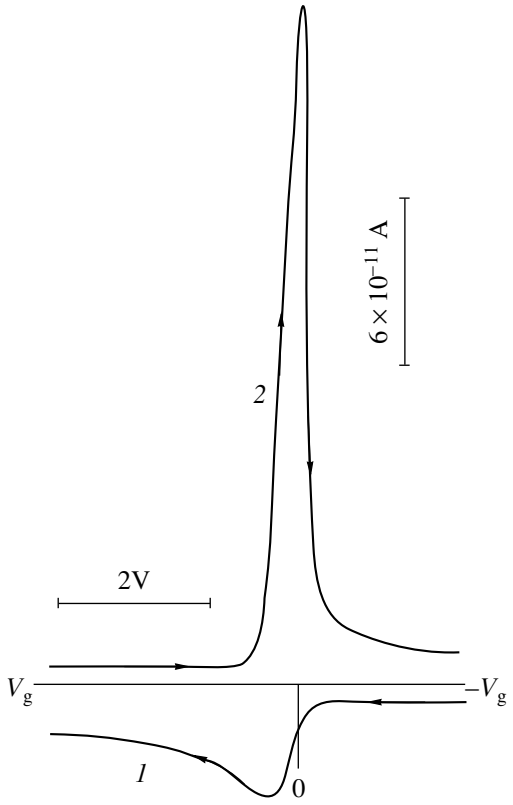

Fig. 1. Dynamic current–voltage characteristics of an Al–SiO_2–Si MOS structure. A pronounced asymmetry in the processes of ionic (*1*) polarization and (*2*) depolarization is evident. The temperature of measurements was $T = 423$ K, and the field-sweep rate was $\beta_V = 0.02$ V s^{-1} [5].

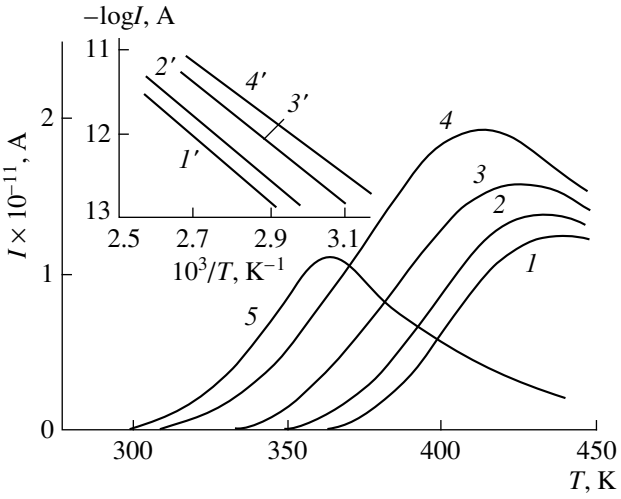

Fig. 2. Thermally stimulated polarization of a Si-MOS structure for the polarizing voltages V_{gp} = (*1*) 0.5, (*2*) 1.4, (*3*) 5, and (*4*) 10 V. Curve *5* (the scale on the vertical axis is 1.5×10^{-10} A) represents the thermally stimulated depolarization for $V_{gd} = -1$ V [6] and $\beta_T \simeq 0.4$ K/s. The Arrhenius curves for the stages of an initial increase in the current (curves *1*'–*4*', see the inset) are plotted on the basis of curves *1*–*4*.

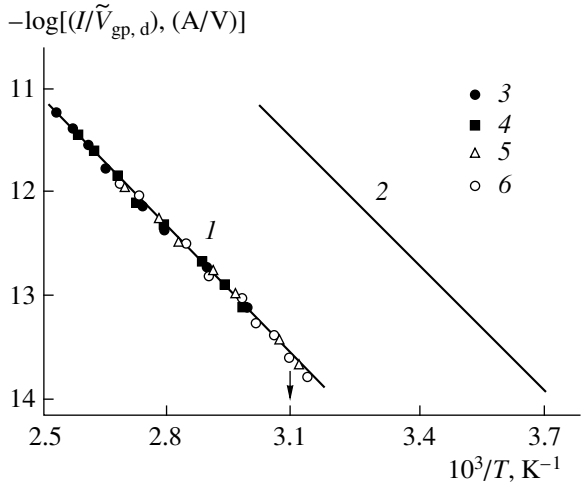

Fig. 3. Straight line *1* represents the temperature dependences of effective ionic electrical conductivity $\log(I/V_{gp}) = f(T^{-1})$ for the regions of initial rise of the current ($T_0 < T < T_m$) in the curves of thermally stimulated polarization (curves *1–4* in Fig. 2) for the voltages V_{gp} = (*3*) 0.5, (*4*) 1.4, (*5*) 5, and (*6*) 10 V. Straight line *2* represents the dependence $\log(I/|\tilde{V}_{gd}|) = f(T^{-1})$ (taken from [6]) characteristic of effective ionic electrical conductivity normalized to the common value of $N_S = 4.5 \times 10^{10}$ cm^{-2} for various depolarizing voltages in the range of $0.6 \le |V_{gd}| \le 11.2$ V.

asymmetry observed. To this end, we show in Fig. 3 the universal straight line (*2*) $\log(I|\tilde{V}_{gd}|) = f(T^{-1})$, where $\tilde{V}_{gd} \equiv V_{gd} + V_c$, which characterizes the initial stages of an increase in the depolarization current for various values of V_{gd} [6]. Straight lines *1* and *2* are virtually parallel in accordance with the aforementioned activation energies of corresponding processes. Therefore, a difference in the values of "polarization" $(I/\tilde{V}_{gp})$ and "depolarization" $(I/|\tilde{V}_{gp}|)$ electrical conductivities at the same temperature may be due only to a difference in the preexponential factors in the expression that describes the initial stages of an increase in the polarization and depolarization currents (see footnote 1) or, for all other parameters being equal (the same sample),

$$(I/|\tilde{V}_{gd}|)/(I/\tilde{V}_{gp})_{T = \text{const}} = \Delta = N_{ss}/N_{sg},$$

where N_{ss} and N_{sg} are the densities of free (not neutralized) ions at the contacts of the oxide/silicon and oxide/gate, respectively. According to [6], $N_{ss} = 4.5 \times 10^{10}$ cm^{-2}. Determining the value of Δ for a certain given temperature (indicated by the arrow in Fig. 3; $\Delta = 132$), we have $N_{sg} = N_{ss}/\Delta = 3.4 \times 10^8$ cm^{-2}, which is quite close to the value obtained previously by extrapolating the straight line $\log(I/\tilde{V}_{gp}) = f(T^{-1})$, $N_{sg} = 3.3 \times 10^8$ cm^{-2} (Fig. 3, straight line *1*). The inequality $N_{sg} \ll N_{ss}$ can be easily accounted for [6, 12] by a difference in the degree of neutralization of the ions present in the oxide at its boundaries with metal (gate) and silicon. In the course of depolarization, due to the depletion of the surface, an accumulation of ions occurs owing to the fact that tunneling decomposition of neutral associations (ion + electron) occurs simultaneously with the transit of the ion-charge front; at a later time, these ions also become incorporated into the transit–time packet [12]. The Fermi level position is fixed at the insulator–metal contact, so that any realistic electric field cannot perturb the balance between the tunneling processes of neutral-association ionization and the ion neutralization. Therefore, charging of the ions formed as a result of decomposition of neutral associations inhibits the process of accumulation of mobile charge in the insulator, because the rate of this process is much lower in the case of polarization than in the case of depolarization. In addition, the state (possibly virtual) of an electron bound by neutral associations at the boundary with the metal may occur to be deeper than that at the boundary with the semiconductor owing to the distinctions in the type of its hybridization with the wave functions of electrons in the metal and semiconductor. Therefore, the initial stages of TSP would be governed by the transport of free (not neutralized) ions with a density much lower than in the case of thermally stimulated depolarization. This fact manifests itself quantitatively in the value of $\Delta \gg 1$. After the transit of free ions, the TSP rate is limited by slower tunneling processes of neutral-association ionization and neutralization of ions separated more and more from the metal surface and also by the decomposition of neutral associations that diffuse from the gate to the semiconductor in the bulk of the insulator. This is naturally accompanied by a drastic decrease in the rate of the current increase and by the emergence of its peak and the region of slow decrease (see Figs. 1, 2); in this region, like in the case of thermally stimulated depolarization [6], the current becomes virtually independent of the polarizing field, temperature, and the heating rate β_T; i.e., the current becomes a single-valued function of the actual time *t*. In the context of the model [6, 12], only the descending portions of the thermally stimulated current can be quantitatively interpreted; unfortunately, they cannot be studied in detail because of a loss of reproducibility of experimental data if the samples are heated to temperatures higher than 460 K.

We now consider the results of studies of isothermal polarization, which is also widely used to gain insight into the phenomena of ion transport in insulators of MIS structures [1–3, 5, 12]. The results of observations at T = const are generally easier to interpret, because, in this case, there is no need to consider the poorly known temperature dependences of preexponential factors. It follows from the theory [23] that the initial stages of polarization in the dynamic *I–V* characteristics are defined by the free-ion transport through the barrier formed by external voltage V_g and occur under the con-

ditions of a quasi-balance between the processes of ionization and neutralization. The corresponding problem of depolarization was solved in [5]; according to the experimentally verified model developed in [5], the current in these stages is proportional to $N_S\exp(V_g/kT)$ and is independent of the field-sweep rate $\beta_V = dV_g/dt$ = const < 0.05 if $\beta_V < 0.05$ V s^{-1}. As in the case of TSP, the peaks and tails of the current in the *I–V* characteristics of polarization (Fig. 1) correspond to a transition from the quasi-steady condition of the free-ion drift to nonsteady conditions of tunneling ionization of neutral associations (with a characteristic time of τ_i), their diffusion from the metal surface, and eventual decomposition (with characteristic time τ) in the bulk of the insulator layer. The value of τ is expected to increase with increasing time *t* as a result of a broad spatial distribution of tunneling distances. This causes the current to fall off hyperbolically and to be independent of an electric field in the insulator: $I \propto t^{-\gamma}$, where $\gamma \simeq 1$ [12]. Diffusion of neutral associations is described by the power-law dependences with $\gamma = 1.5$ [23], and the decomposition of neutral associations in the bulk of the insulator obeys a classical exponential law [12] $I \propto \exp(-t/\tau)$. These dependences can be easily distinguished if $\tau \gg \tau_i$ or $\tau \ll \tau_i$. In particular, the hyperbolic kinetics of isothermal relaxation of the field-independent depolarization current for V_g = const was clearly observed experimentally [12]; contrariwise, the exponential region of depolarization kinetics corresponding to the decomposition of neutral associations in the bulk of the insulator has not been observed within an actual time range.[2] Thus, a drastic decrease in the rate of rise in the polarization current beyond the initial region of the dynamic *I–V* characteristic, which is accompanied by the appearance of a peak with an extended tail in the $I[V_g(t)]$ curve (cf. curves *1* and *2* in Fig. 1), should be treated as evidence of a transition from the quasi-steady thermal-emission mechanism of the free-ion transport [5] to the relaxation that is limited by tunneling ionization, diffusion, and eventual decomposition of neutral associations in the bulk of the insulator. Since the polarization current in the final stage of relaxation is found to be comparable to the displacement current $I \simeq C_i\beta_V$ (Fig. 1), where C_i is the geometric capacitance of the insulator layer, it is difficult to clarify the mechanism of the current fall-off in the dynamic *I–V* characteristics; the situation is further complicated by the fact that both the tunneling-related ionization of neutral associations and their diffusion with eventual thermal decomposition in the bulk of the insulator are virtually independent of the electric field.

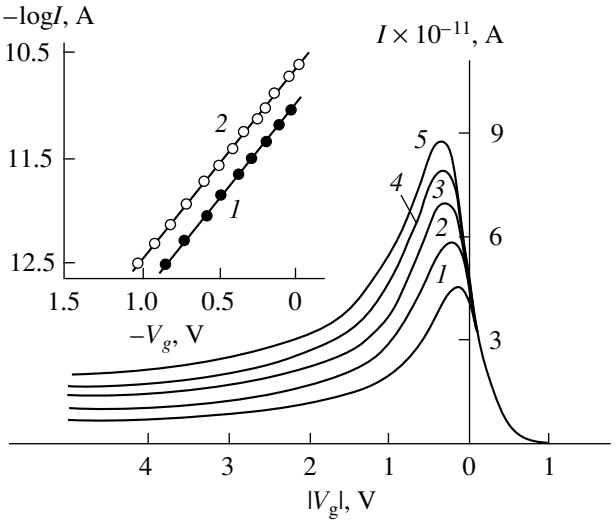

Fig. 4. Dynamic current–voltage characteristics of polarization at T = 423 K that demonstrate the independence of the polarization current at the initial stages of its rise on the values of β_V = (*1*) 0.02, (*2*) 0.03, (*3*) 0.04, (*4*) 0.05, and (*5*) 0.06 V s^{-1}. Dynamic current–voltage characteristics of polarization at (*1*) 423 and (*2*) 453 K are shown in the inset ($\beta_V = 0.02$ V s^{-1}).

In connection with this, it would be reasonable to complement the method of dynamic *I–V* characteristics with observations of kinetics of the isothermal polarization-current relaxation with a stepped switching of depolarizing voltage to the voltage ensuring the polarization, because, under these conditions, it is the initial transit-time effect that may be difficult to measure.[3] At the same time, new opportunities open up for the measurements of long-term relaxation of the polarization current. Following the transit of the free-ion packet from the gate to the semiconductor, a transition region is bound to appear in the dependence $I(t)$; this region is physically similar to that observed in the TSP curves and the dynamic *I–V* characteristics of polarization. At longer times, the relaxation kinetics would follow the hyperbolic law $I \propto t^{-\gamma}$ and, further, the exponential law $I \propto \exp(-t/\tau)$.

Figures 4 and 5 show experimental data that illustrate the main laws of isothermal-relaxation kinetics of the oxide's ionic polarization and support the aforementioned concepts. Figure 4 demonstrates that the initial stages of polarization are independent of the value of β_V, that the current depends exponentially on V_{gp} (see the insert), and that a transition between the expo-

[2] As a consequence of very large values of τ (~3.6×10^3 and 2.2×10^7 s at 423 and 333 K, respectively) and a small diffusion coefficient of neutral associations (at 423, this coefficient is by eight orders of magnitude smaller than the diffusion coefficient of free ions), the evidence for the existence of the corresponding transport mechanism was only obtained using a special method for measurements of steady current, which involved thermal modulation [12].

[3] This is due to the small magnitude of the transit-time signal, which is caused by small values of N_S at the gate surface. It is difficult to measure this signal against the background of the current that arises owing to differentiation of the polarizing-voltage step by the geometric capacitance of the sample and the lead capacitance.

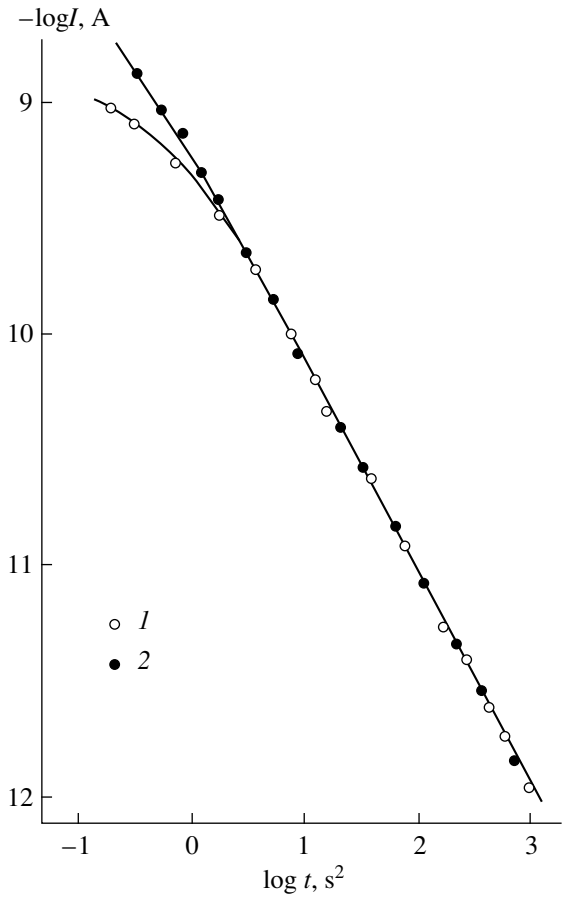

Fig. 5. Kinetics of isothermal relaxation of the polarization current at a temperature of 453 K. The polarization voltages V_{gp} were equal to (*1*) 1 and (*2*) 5 V.

nential and the very slowly descending portions of the $I[V_g(t)]$ curves is gradual. It follows from Fig. 5 that the polarization-current relaxation follows a hyperbolic law with $\gamma \simeq 1$ and that I is independent of V_{gp}. A comparison of these data and the laws of isothermal depolarization indicates that the tails in polarization curves are relatively protracted. This may indicate that the electron is bound more tightly by an ion in neutral associations located close to the gate than in the case of neutral associations located at the semiconductor surface. The considered origin of asymmetry in the ionic polarization/depolarization of an insulator in a MOS structure is independently verified by the absence of such asymmetry in a Si–SiO_2–Si system [24]. On this basis, we may state that the regularly observed temperature and time asymmetry in the ionic polarization/depolarization of the oxide is caused by asymmetry in the degree of neutralization of ions, which are present in the oxide layer at the semiconductor and metal surfaces.

REFERENCES

1. M. Yamin, IEEE Trans. Electron Devices **12**, 88 (1965).
2. M. Kuhn and D. J. Silversmith, J. Electrochem. Soc. **118**, 966 (1971).
3. A. G. Tangena, N. F. de Rooij, and J. Middelhock, J. Appl. Phys. **49**, 5576 (1978).
4. T. Hino and K. Yamashita, J. Appl. Phys. **50**, 4879 (1979).
5. E. I. Gol'dman, A. G. Zhdan, and G. V. Chucheva, Fiz. Tekh. Poluprovodn. (St. Petersburg) **31**, 1468 (1997) [Semiconductors **31**, 1268 (1997)].
6. E. I. Gol'dman, A. G. Zhdan, and G. V. Chucheva, Fiz. Tekh. Poluprovodn. (St. Petersburg) **33**, 962 (1999) [Semiconductors **33**, 877 (1999)].
7. G. S. Horner, M. Kleefstra, T. G. Miller, and M. A. Peters, Solid State Technol., No. 6, 79 (1995).
8. G. Ya. Krasnikov, Élektron. Tekh., Ser. 3, No. 1, 67 (1996).
9. T. Shimatani, S. Pidin, and M. Koyanagi, Jpn. J. Appl. Phys., Part 1 **36** (3B), 1659 (1997).
10. G. V. Chucheva, Candidate's Dissertation (Moscow, 1998).
11. E. H. Nicollian and J. R. Brews, *MOS (Metal Oxide Semiconductor) Physics and Technology* (New York, Wiley, 1982).
12. E. I. Gol'dman, A. G. Zhdan, and G. V. Chucheva, Fiz. Tekh. Poluprovodn. (St. Petersburg) **33**, 933 (1999) [Semiconductors **33**, 852 (1999)].
13. E.I. Gol'dman, A. G. Zhdan, and G. V. Chucheva, Prib. Tekh. Éksp., No. 6, 110 (1997).
14. K. H. Nickolas and J. Woods, Br. J. Appl. Phys. **15**, 783 (1964).
15. L. I. Grossweiner, J. Appl. Phys. **24**, 1306 (1953).
16. A. G. Zhdan and N. A. Lushnikov, Fiz. Tekh. Poluprovodn. (Leningrad) **16**, 793 (1982) [Sov. Phys. Semicond. **16**, 509 (1982)].
17. M. A. Lampert and P. Mark, *Current Injection in Solids* (Academic, New York, 1970; Mir, Moscow, 1973).
18. S. Sze, *Physics of Semiconductor Devices* (Wiley, New York, 1981; Mir, Moscow, 1984).
19. T. W. Hickmott, J. Appl. Phys. **46**, 2583 (1975).
20. M. R. Boudry and J. P. Stagg, J. Appl. Phys. **50**, 942 (1979).
21. S. R. Hofstein, IEEE Trans. Electron. Devices **ED-13**, 222 (1966).
22. G. Greeuw and J. F. Verwey, J. Appl. Phys. **56**, 2218 (1984).
23. E. I. Gol'dman, Fiz. Tekh. Poluprovodn. (St. Petersburg) **34** (2000) (in press) [Phys. Solid State **34** (2000) (in press)].
24. K. Vanhensden, W. L. Warren, R. A. B. Devine, *et al.*, Nature (London) **368**, 587 (1997).

Translated by A. Spitsyn

Semiconductors, Vol. 34, No. 6, 2000, pp. 655–657. Translated from Fizika i Tekhnika Poluprovodnikov, Vol. 34, No. 6, 2000, pp. 682–684.

ELECTRONIC AND OPTICAL PROPERTIES OF SEMICONDUCTORS

Equilibrium Energy Distribution of Localized Carriers in Disordered Semiconductors Subjected to an External Electric Field at Low Temperature

D. V. Nikolaenkov, V. I. Arkhipov, and V. R. Nikitenko

Moscow Engineering Physics Institute, Kashirskoe sh. 31, Moscow, 125080 Russia

Submitted December 23, 1999; accepted for publication December 28, 1999

Abstract—An equilibrium energy distribution of charge carriers is possible in the 3D case in disordered semiconductors with a sufficiently rapidly decreasing density of localized states at low temperatures when the contribution of thermally activated hops of charge carriers to the hopping transport is negligible. A Boltzmann exponential with a field-dependent effective temperature describes the asymptotic behavior of this distribution.

Processes of carrier transport in amorphous semiconductors with conduction via delocalized states have been successfully described in terms of the multiple-trapping model [1–3]. This model implies that two carrier fractions exist in the material, occupying at any given instant of time delocalized and localized states. However, in the materials with all carriers in localized states, e.g., in most polymers, charge transport is due to carrier hopping. Many interesting and important features of the hopping transport in disordered semiconductors have been observed experimentally in fairly high electric fields [4–6]. It has been shown both analytically [7–10] and by Monte Carlo simulations [11, 12] that the energy distribution of localized carriers and the carrier mobility in a disordered semiconductor can be described both by the ordinary temperature T and by some effective temperature $T_F(F)$ dependent on the magnitude of the applied external electric field F. Analytical calculations [7, 9] of this effective temperature yield

$$T_F = \frac{eF}{2\gamma k}, \tag{1}$$

while numerical simulation yields

$$T_F = 0.67\frac{eF}{\gamma k}$$

(see [11]) or

$$T_F = (0.69 \pm 0.03)\frac{eF}{\gamma k}$$

(see [12]), where e is the elementary charge, γ is the reciprocal localization radius, and k is the Boltzmann constant. The equilibrium energy distribution of injected carriers in an amorphous semiconductor subjected to an external electric field at low temperatures, when the contribution of thermally activated hops to the transport process is negligible, has been found [9] for the 1D case, which, in fact, corresponds to high electric fields. In this paper, we demonstrate that the equilibrium energy distribution of localized carriers is also possible in the 3D case at low temperatures in an external electric field. We show that this distribution can be described by the Boltzmann exponential with an effective temperature given by (1).

As an equation describing the kinetics of the hopping transport, we use the well-known balance equation

$$\frac{\partial f_i}{\partial t} = \sum_{j \neq j} \nu_{ij} f_j - f_i \sum_{j \neq j} \nu_{ij}, \tag{2}$$

written for the case of low occupancy of localized states, $f_i \ll 1$. Here, f_i is the mean occupation number of the ith state and ν_{ij} is the probability of transition from the state i to the state j. Let us assume that in the quasi-equilibrium transport regime, when the density of states is time-independent, a great number of carriers can avoid unlikely jumps that take a very long time $t_R \gg \hbar/\Delta E$, i.e., jumps that do not contribute significantly to the transport process [13]. (Here, $\hbar$ is Planck's constant and ΔE is the characteristic energy change in carrier transition from one localized state to another.) This assumption makes it possible to take advantage of the concept of the distribution function $f(\mathbf{r}, E, t)$ averaged over continuous variables: energy E (deeper states have higher energies E) and radius vector $\mathbf{r}$. Let us use the Miller–Abrahams expression for the transition rate

$$\nu(|\Delta\mathbf{r}|, R) = \nu_0 \exp\left[-2\gamma|\Delta\mathbf{r}| - H(\mathscr{E})\frac{\mathscr{E}}{kT}\right], \tag{3}$$

where $\mathscr{E} \equiv E - e\mathbf{F}\Delta\mathbf{r} - E'$, $H(\mathscr{E})$ is the Heaviside function, ν_0 is the characteristic rate of tunneling carrier hops, and $\Delta\mathbf{r} = \mathbf{r} - \mathbf{r}'$. Then, we use equation (2) to

derive the following kinetic equation for the distribution function f,

$$\frac{\partial f(\mathbf{r}, E, t)}{\partial t} = \nu_0 \int d\mathbf{r}' \exp(-2\gamma|\Delta\mathbf{r}|) \left[\int_{-\infty}^{E - e\mathbf{F}\Delta\mathbf{r}} dE' f(\mathbf{r}, E', t) + \int_{E - e\mathbf{F}\Delta\mathbf{r}}^{\infty} dE' \exp\left(\frac{E - e\mathbf{F}\Delta\mathbf{r} - E'}{kT} \right) f(\mathbf{r}', E', t) \right] g(E) \quad (4)$$

$$- \nu_0 \int d\mathbf{r}' \exp(-2\gamma|\Delta\mathbf{r}|) \left\{ \int_{E - e\mathbf{F}\Delta\mathbf{r}}^{\infty} dE' g(E') + \int_{-\infty}^{E - e\mathbf{F}\Delta\mathbf{r}} dE' \exp\left[\frac{-(E - e\mathbf{F}\Delta\mathbf{r} - E')}{kT} \right] g(E') \right\} f(\mathbf{r}, E, t),$$

normalized by the condition

$$\int d\mathbf{r} \int_{-\infty}^{\infty} f(\mathbf{r}, E, t) dE = 1, \quad (5)$$

where t is time, and $g(E)$ is the energy distribution of localized states normalized by the condition

$$\int_{-\infty}^{\infty} g(E) dE = 1. \quad (6)$$

The zero energy $E = 0$ corresponds to the maximum of the function $g(E)$. Equation (4) is written on the assumption that the position and energy of localized states are uncorrelated, which corresponds to the case of completely disordered materials.

At low temperatures, when the contribution of thermally activated hops can be neglected subject to the condition of the hypothetical equilibrium, kinetic equation (4) for the equilibrium distribution function averaged over the space coordinates

$$f_{\text{eq}}(E) = \int f(\mathbf{r}, E, \infty) d\mathbf{r} \quad (7)$$

takes the form

$$0 = \nu_0 \int d\mathbf{r}' \exp(-2\gamma|\Delta\mathbf{r}|) \int_{-\infty}^{E - e\mathbf{F}\Delta\mathbf{r}} dE' f_{\text{eq}}(E') g(E) - \nu_0 \int d\mathbf{r}' \exp(-2\gamma|\Delta\mathbf{r}|) \int_{E - eF\Delta\mathbf{r}}^{\infty} dE' g(E') f_{\text{eq}}(E). \quad (8)$$

We use equation (8) and formulas (5) and (6) to derive the following integral equation:

$$f_{\text{eq}}(\varepsilon) = \frac{g(\varepsilon) \int_{-\infty}^{\infty} d\varepsilon' A(\varepsilon, \varepsilon') f_{\text{eq}}(\varepsilon')}{4 - \int_{-\infty}^{\infty} d\varepsilon' A(\varepsilon, \varepsilon') g(\varepsilon')}. \quad (9)$$

Here, we introduced the kernel

$$A(\varepsilon, \varepsilon') = 4H(\varepsilon - \varepsilon') - (2 + |\varepsilon - \varepsilon'|) e^{-|\varepsilon - \varepsilon'|} \quad (10)$$

and the dimensionless variables $\varepsilon = E/kT_F$ and $\varepsilon' = E'/kT_F$, where T_F is the effective temperature defined by (1). The appearance of this effective temperature is associated with the fact that, during transport, the electric field transfers carriers into states with a higher energy, similarly to the thermodynamic effects described by the ordinary temperature T.

This equation can be solved by the iteration method; as the first approximation, we use the density of localized states

$$f_{\text{eq}}^{(0)}(E) = g(E). \quad (11)$$

Substituting (11) into (9), we obtain

$$\int_{-\infty}^{\infty} d\varepsilon' A(\varepsilon, \varepsilon') g(\varepsilon') \approx \begin{cases} \exp(E/kT_F)/E, & E \gg E_0 + E_m(T_F); \\ 1, & E \ll -E_0 - E_m(T_F). \end{cases} \quad (12)$$

Here, the quantity $E_m(T_F)$ depends on the particular form of the density of states $g(E)$. In particular, in the case of a Gaussian distribution

$$g(E) = g_0 \exp[-(E/E_0)^2],$$

we have $E_m(T_F) = E_0^2/2T_F$, while in the case of an exponential distribution

$$g(E) = g_0 \exp(-|E/E_0|)$$

we obtain $E_m(T_F) = E_0^2/(T_F - E_0)$. Hence,

$$f_{\text{eq}}^{(1)} \approx |E|^{-\text{sgn}(E)} g(E) \exp\left(\frac{E}{kT_F} \right), \quad |E| \gg E_0 + E_m(T_F). \quad (13)$$

Thus, to a first approximation, the equilibrium energy distribution is described by the Boltzmann function.

To calculate the distribution function $f_{\text{eq}}(E)$ more precisely, we substitute, in accordance with (13), the function $g(E)\exp(E/kT_F)$ into the right-hand side of equation (9). The resulting solution $f_{\text{eq}}^{(2)}(E)$ has the

same asymptotic form as the function $f_{eq}^{(1)}(E)$, since the asymptotic form (12) of the function $\int d\varepsilon' A(\varepsilon, \varepsilon')g(\varepsilon')$ appearing in equation (9) is not changed. Thus, if the density of localized states $g(E)$ is sufficiently "shallow," so that the equilibrium can be established,

$$Eg(E)\exp\left(\frac{E}{kT_F}\right) \longrightarrow 0, \quad |E| \longrightarrow \infty, \qquad (14)$$

then the asymptotic form of the occupancy of localized states $\varphi(E) = f(E)/g(E)$ is the exponential $\exp(E/kT_F)$. The quantity $E_m(T_F)$ appearing in equations (12) and (13) is the characteristic energy of the peak in the distribution function $f_{eq}(E)$.

Thus, we showed the following. First, in the 3D case, as also in the 1D one [9], the spatially uniform equilibrium energy distribution of localized charge carriers may occur even in the limiting case $T \longrightarrow 0$, when the contribution from thermally activated hops to the kinetic equation (4) can be completely neglected. Second, this distribution can be approximated by the Boltzmann distribution function with the effective temperature (1) instead of the ordinary temperature. It should be noted that this effective temperature coincides with previous analytical estimations [9, 10].

REFERENCES

1. A. I. Rudenko and V. I. Arkhipov, Philos. Mag. B **45**, 177 (1982).
2. A. I. Rudenko and V. I. Arkhipov, Philos. Mag. B **45**, 189 (1982).
3. V. I. Arkhipov, A. I. Rudenko, A. M. Andriesh, *et al.*, *Transient Injection Currents in Unordered Solids* (Shtiintsa, Kishinev, 1993).
4. L. B. Schein, Philos. Mag. B **65**, 795 (1992).
5. H. Bässler, Phys. Status Solidi B **175**, 15 (1993).
6. C. E. Nebel and R. A. Street, Int. J. Mod. Phys. B **7**, 1207 (1993).
7. B. I. Shklovskiĭ, E. I. Levin, H. Fritzsche, and S. Baranovskiĭ, in *Advances in Disordered Semiconductors*, Ed. by H. Fritzsche (World Scientific, Singapore, 1990), Vol. 1, p. 161.
8. V. I. Arkhipov and H. Bässler, Philos. Mag. Lett. **67**, 343 (1993).
9. V. I. Arkhipov and H. Bässler, Philos. Mag. Lett. **69**, 241 (1994).
10. V. I. Arkhipov and H. Bässler, Philos. Mag. B **68**, 425 (1993).
11. S. Marianer and B. I. Shklovskiĭ, Phys. Rev. B **46**, 13100 (1992).
12. S. D. Baranovskiĭ, B. Cleve, R. Hess, *et al.*, J. Non-Cryst. Solids **164/166**, 437 (1993).
13. M. Pollak, Philos. Mag. **36**, 1157 (1977).

Translated by S. Goupalov

Semiconductors, Vol. 34, No. 6, 2000, pp. 658–661. Translated from Fizika i Tekhnika Poluprovodnikov, Vol. 34, No. 6, 2000, pp. 685–688.

ELECTRONIC AND OPTICAL PROPERTIES OF SEMICONDUCTORS

Photoelectric Phenomena in *a*-Si:H/*p*-$CuInSe_2$ Heterostructures

Yu. A. Nikolaev*, V. Yu. Rud', Yu. V. Rud'*, and E. I. Terukov****

** Ioffe Physicotechnical Institute, Russian Academy of Sciences, Politekhnicheskaya ul. 26, St. Petersburg, 194021 Russia*

*** St. Petersburg State Technical University, ul. Politekhnicheskaya 29, St. Petersburg, 195251 Russia*

Submitted December 29, 1999; accepted for publication December 29, 1999

Abstract—The photosensitive *a*-Si:H/*p*-$CuInSe_2$ heterostructures were obtained for the first time by the deposition of hydrogenated amorphous silicon on polycrystalline *p*-$CuInSe_2$ substrates. The photoelectric properties of the new system were studied. The conclusion was drawn on the prospects of the application of this system for solar and linearly polarized radiation photoconvertors. © *2000 MAIK "Nauka/Interperiodica".*

The development of solar power is mainly directed towards the efficiency increase and cost reduction of the solar cells [1–3]. The use of the $CuInGaSe_2$ chalcopyrite materials in the production of thin-film solar cells is recognized to be one of the most promising avenues for accomplishing these ends [4]. In recent years, several research teams have reported photoconversion efficiencies higher than 17% for the chalcopyrite materials and higher than 10% in the case of the modules fabricated from these materials [5–7]. The photoconversion in such devices is generally defined by the ZnO/CdS/$CuInGaSe_2$/Mo/glass structure. However, in an effort to increase the production efficiency and because of environmental considerations, a demand arose to replace the CdS buffer layers with an alternative material. The potentialities of various semiconductors had already been analyzed as such materials [8–10]. In this paper, the potentialities of the high-resistivity layers of amorphous hydrogenated silicon (*a*-Si:H) as a buffer material for the preparation of the photosensitive heterostructures on the basis of *p*-$CuInSe_2$ bulk crystals were first studied.

1. The electrically homogeneous polycrystalline $CuInSe_2$ wafers with a free hole concentration $p \simeq 3 \times 10^{17}$ cm^{-3} at $T = 300$ K were used as the substrates for the deposition of *a*-Si:H films. The typical dimensions of the wafers were about $5 \times 5 \times 1$ mm^3. After mechanical polishing, the surface of the wafers was treated in the polishing etchant. The *a*-Si:H films were deposited onto the surface of $CuInSe_2$ wafers at a temperature of 230°C by the RF glow discharge method. The gas mixture $SiH_4 : H_2$ (9 : 1) was used in the film growth. The process described provides the deposition of ~1 μm-thick *a*-Si:H films with a mirror surface. The *a*-Si:H films exhibited a good adhesion to the $CuInSe_2$ surface. The dark resistivity of *n*-type *a*-Si:H films amounts to ~10^9 Ω cm at $T = 300$ K.

2. All the *a*-Si:H/*p*-$CuInSe_2$ heterostructures obtained exhibited a pronounced rectification. A steady-state current–voltage characteristic typical of such heterostructures is shown in the inset in Fig. 1. Conduction of heterostructures is initiated, as a rule, by the positive external bias applied to the *p*-$CuInSe_2$ substrate. As the forward bias voltage increases ($U \gtrsim 2$ V), the current–voltage characteristic of the heterostructures considered is typically defined by the relationship

$$I = (U - U_0)/R_0, \quad (1)$$

where $U_0 \simeq 1.8$–2 V is the cutoff voltage and $R_0 \simeq 10^5$ Ω is the residual resistance at $T = 300$ K. In view of the electrical properties of the substrates, we may assume that the main contribution to the R_0 is provided by the series resistance of the *a*-Si:H film. The reverse current in the structures under study typically obeys the power law $I \propto U^\alpha$, where $\alpha = 0.6$–1. Such behavior can primarily be caused by the imperfections at the periphery of the heterostructures obtained.

The photovoltaic effect is reproducibly observed when the *a*-Si:H/*p*-$CuInSe_2$ heterostructures are exposed to light. The sign of the photoelectric voltage in all such heterostructures corresponds to the negative polarity at the *a*-Si:H film and appears to be independent of the energy of incident photons $\hbar\omega$ and the position of the light probe at the heterostructure surface. This allows us to attribute the photovoltaic effect observed to separation of photogenerated pairs in the single active region resulting from the formation of such a heterostructure. The photosensitivity of all the heterostructures obtained is found to be higher in the case of illumination from the side of their wide-gap component (*a*-Si:H). The best heterostructures of this type are characterized by the open-circuit photoelectric voltage $U_{ir} = 0.3$ V and short-circuit current $i_{sc} = 0.1$ mA when exposed to unfocused radiation from an incandescent lamp ($L \simeq 100$ W). The maximum voltage

and current photosensitivities of the structures studied are S_U = 150 V/W and S_i = 25 μA/W, respectively, at T = 300 K. It is evident that the mentioned parameters of the first structures are still far from the ultimate values for this system. The optimization of the properties of its components will be the next stage in these studies.

3. Figure 1 shows the representative spectral dependences of the relative quantum efficiency of photoconversion η, which is defined as the ratio of the short-circuit photocurrent to the number of incident photons, for one of the heterostructures studied. The long-wavelength edge of the dependence $\eta(\hbar\omega)$ for the heterostuctures is defined by the photoactive absorption in their $CuInSe_2$ narrow-gap layer and appears to be the same at $\hbar\omega \lesssim 1$ eV for two different geometric layouts of the illumination (Fig. 1, curves *1, 2*). The maximum of η in the case of a heterostructure illuminated from the $CuInSe_2$ side and the step at $\hbar\omega$ = 1.01 eV, which arises for a heterostructure illuminated from the side of the *a*-Si:H, are consistent with the bandgap E_g of the ternary compound [11, 12]. The exponential increase in the heterostructure photosensitivity for $\hbar\omega < 1$ eV is described by a high slope $S = \delta(\ln i_{sc})/\delta(\hbar\omega) \simeq 30$ eV^{-1} corresponding to the direct optical transitions in $CuInSe_2$ [11]. Therefore, as soon as the photon energy $\hbar\omega > 1.01$ eV, a dramatic drop in photosensitivity occurs in the short-wavelength region for the heterostructure illuminated from the side of the substrate. This drop is due to the absorption of radiation in the bulk of the $CuInSe_2$ layer adjacent to the active region of the heterostucture. The pronounced feature at $\hbar\omega <$ 0.95 eV with a peak near 0.9 eV in the spectra $\eta(\hbar\omega)$ of the heterostuctures is characteristic of the initial crystals. This feature results from the photoactive absorption involving the defect levels in $CuInSe_2$ with the energy position of E_v + 0.11 eV [11, 13].

When the heterostructures are illuminated from the side of the *a*-Si:H films, their photosensitivity spectra become rather wide (Fig. 1, curve *1*). In this case, the FWHM of the photosensitivity band $\delta_{1/2}$ increases steeply from 50 to 900–950 meV. In the broadband mode of photodetection, two bands can be revealed in the spectral region of high photosensitivity. The energy positions of the peaks of these bands are indicated by the arrows in Fig. 1 (curve *1*). These features are associated with the interference of the incident radiation in the *a*-Si:H film. Actually, the estimate of the thickness of this film based on the energy position of the extrema in the $\eta(\hbar\omega)$ spectra and refractive index of *a*-Si:H correlates with that obtained from the optical transmission spectra of the film deposited onto the glass in the same process.

We note that the attainment of the broadband mode of photodetection in the *a*-Si:H/*p*-$CuInSe_2$ heterostructures can be indicative of the rather perfect (at least as regards the photosensitivity processes) interface of amorphous *a*-Si:H and crystalline $CuInSe_2$ in spite of the large difference in their structures. The short-wavelength dip of the $\eta(\hbar\omega)$ dependence in the photosensitivity spectra of *a*-Si:H/*p*-$CuInSe_2$ heterostructures in the vicinity of 2 eV corresponds to the onset of the interband absorption in *a*-Si:H and thus can be assigned to the optical absorption in the hydrogenated amorphous silicon layer adjacent to the active region of the heterostructure.

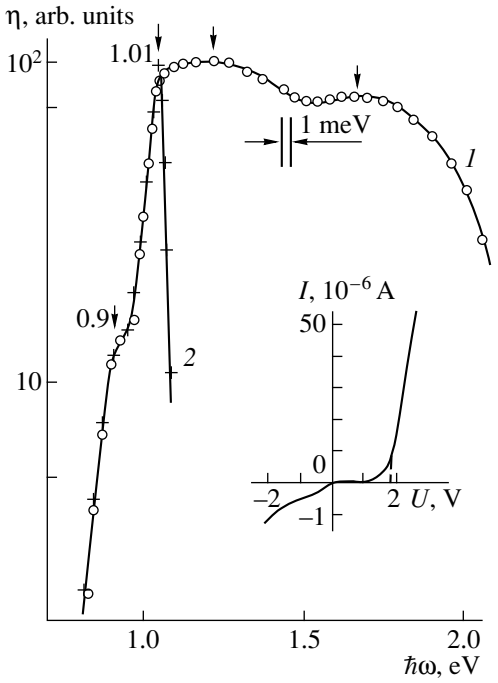

Fig. 1. Spectral dependences of the relative quantum efficiency of photoconversion for the *a*-Si:H/*p*-$CuInSe_2$ heterostructure (sample 3) at T = 300 K. The structure is exposed to light from the *a*-Si:H side (curve *1*) and from the *p*-$CuInSe_2$ side (curve *2*). The current–voltage characteristic is shown in the inset. The forward direction corresponds to the positive polarity of the external bias at the *p*-$CuInSe_2$.

4. When exposed to linearly polarized radiation, these heterostructures behave as typical isotropic substances. Actually, the short-circuit photocurrent is independent of the orientation of the electric-field **E** of the light wave at normal incidence. Thus, the natural photopleochroism of these structures [14] is virtually zero (P_N = 0) in the entire photosensitivity region. This is just an indication of the isotropic behavior of the photoactive absorption by the *a*-Si:H amorphous film and $CuInSe_2$ polycrystalline substrate.

As soon as the angle of incidence of linearly polarized radiation onto the *a*-Si:H film of the heterostructure becomes distinct from zero (θ > 0°), the photocurrent appears to be dependent on the azimuth angle φ between the **E** vector and plane of incidence according to the formula

$$i_\varphi = i^p \cos^2\varphi + i^s \sin^2\varphi. \qquad (2)$$

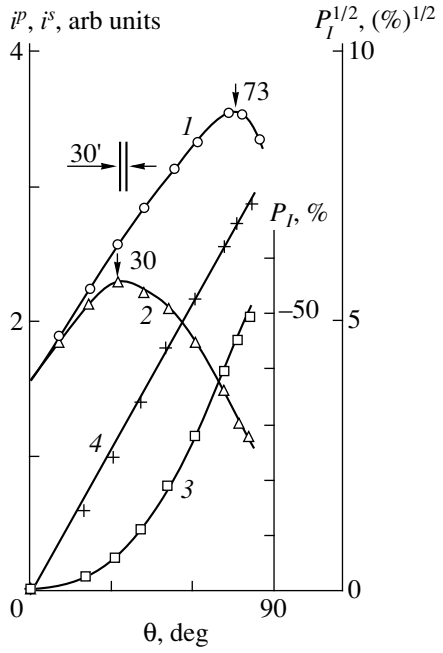

Fig. 2. Dependences of the short-circuit photocurrent (*1*) i^p and (*2*) i^s and induced-photopleochroism coefficient (*3*) $P_I = f(\theta)$ and (*4*) $P_I^{1/2} = f(\theta)$ on the angle of incidence of linearly polarized radiation onto the receiving plane *a*-Si:H of a *a*-Si:H/*p*-$CuInSe_2$ heterostructure at T = 300 K. The data for sample 6 at λ = 1.1 μm are presented.

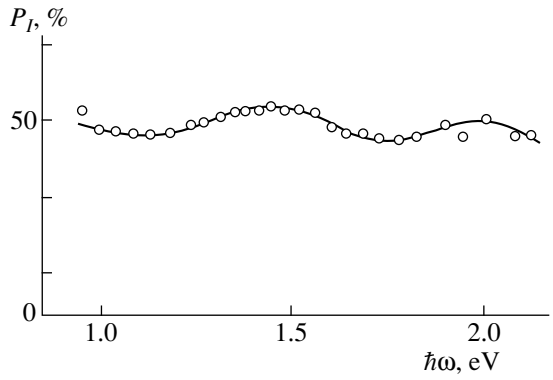

Fig. 3. Spectral dependence of the induced-photopleochroism coefficient P_I of the *a*-Si:H/*p*-$CuInSe_2$ heterostructure at T = 300 K. The data are shown for sample 6 exposed to light from the side of *a*-Si:H, θ = 75°.

Here, i^p and i^s are the photocurrents for the polarizations, which are parallel to the plane of incidence and normal to it, respectively. The polarization ratio i^p/i^s increases with θ.

The typical dependences of i^p and i^s on the angle of incidence of linearly polarized radiation for $\hbar\omega$ = const are shown in Fig. 2 (curves *1*, *2*). With regard to the criteria of polarization photoelectric spectroscopy [15, 16], the increase in i^p and i^s with θ observed, as well as the appearance of the peaks in the dependences $i^p(\theta)$ and $i^s(\theta)$, are indicative, on the one hand, of the high optical quality of *a*-Si:H films deposited on $CuInSe_2$ and, on the other hand, of the interference of linearly polarized radiation in these films [15].

The angular dependences of the induced-photopleochroism coefficient P_I for the *a*-Si:H/*p*-$CuInSe_2$ heterostructures in the entire photosensitivity region are characterized by an increase in P_I with the angle of incidence under the parabolic law $\sqrt{P_I} \propto \theta$ (see Fig. 2, curves *3*, *4*). For all these dependences, $P_I = 0$ for $\theta = 0$. The latter is defined by the isotropic character of the photoactive absorption. It follows from the experimental curves $P_I = f(\theta)$ (Fig. 2, curve *3*) that the abrupt transition from the isotropic mode to the polarization-sensitive mode of photoconversion in *a*-Si:H/*p*-$CuInSe_2$ heterostructures is possible merely by increasing the angle of incidence.

The typical spectral dependence of the induced-photopleochroism coefficient for one of the heterostructures exposed to light from the side of an *a*-Si:H film for $\theta \simeq 75°$ is shown in Fig. 3. It follows from this figure that the P_I coefficient in such heterostructures oscillates throughout the entire photosensitivity region and maintains its large average value. Consequently, the "spectral window" effect also manifests itself for polarization photosensitivity on exposure of the heterostructure to light from the side of the wide-gap material. With regard to [15], the manifestation of P_I oscillations can be assigned to the interference of the linearly polarized radiation in the "wide-gap spectral window" of the heterostructure. The assessment of the refractive index based on the induced-photopleochroism coefficient yields a value which agrees satisfactorily with the known value for *a*-Si:H.

In conclusion, it has been found in the present study that heterostructures based on chalcopyrite semiconductors of the $CuInSe_2$ type and amorphous hydrogenated silicon can find application in the development of high-efficiency cadmium-free solar cells and photoanalysers of linearly polarized radiation.

REFERENCES

1. K. Takahashi and M. Konagai, in *Amorphous Silicon Solar Cells* (North Oxford Academic, London, 1986), p. 141.
2. B. Sang, K. Dairiki, A. Yamada, and M. Konagai, Jpn. J. Appl Phys. **38**, 4983 (1999).
3. B. Dimmler and H. W. Schock, Prog. Photovoltaics **4**, 425 (1996).
4. H. W. Schock, Appl. Surf. Sci. **92**, 606 (1996).
5. J. R. Tuttle, J. S. Ward, A. Duda, *et al.*, Mater. Res. Soc. Symp. Proc. **426**, 143 (1996).
6. T. Negami, M. Nishitani, N. Kohara, *et al.*, Mater. Res. Soc. Symp. Proc. **426**, 1451 (1996).

7. H. S. Ullal, K. Zweibel, and B. von Reodern, in *Proceedings of the 26th IEEE Photovoltaic Specialists Conference, 1997*, p. 301.
8. Y. Ohtake, K. Kushiyama, M. Ishikawa, *et al.*, Jpn. J. Appl. Phys. **34**, 5949 (1995).
9. Y. Ohtake, S. Chaisitsak, A. Yamada, and M. Konagai, Jpn. J. Appl. Phys. **37**, 3220 (1998).
10. S. Chaisitsak, T. Segiyama, A. Yamada, and M. Konagai, Jpn. J. Appl. Phys. **38**, 4989 (1999).
11. T. J. Coutts, L. L. Kazmerski, and S. Wagner, *Copper Indium Diselenide for Photovoltaic Applicatons* (Elsevier, Amsterdam, 1986).
12. *Physicochemical Properties of Semiconductors: A Reference Book* (Nauka, Moscow, 1979).
13. N. N. Konstantinova, M. A. Magomedov, V. Yu. Rud', and Yu.V. Rud', Fiz. Tekh. Poluprovodn. (Leningrad) **26**, 558 (1992) [Sov. Phys. Semicond. **26**, 317 (1992)].
14. F. P. Kesamanly, V. Yu. Rud', and Yu. V. Rud', Fiz. Tekh. Poluprovodn. (St. Petersburg) **30**, 1921 (1996) [Semiconductors **30**, 1001 (1996)].
15. F. P. Kesamanly, V. Yu. Rud', and Yu. V. Rud', Fiz. Tekh. Poluprovodn. (St. Petersburg) **33**, 513 (1999) [Semiconductors **33**, 483 (1999)].
16. V. Yu. Rud', Yu. V. Rud', and H. W. Schock, Solid State Phenom. **67/68**, 421 (1999).

Translated by Yu. Aleshchenko

Semiconductors, Vol. 34, No. 6, 2000, pp. 662–664. Translated from Fizika i Tekhnika Poluprovodnikov, Vol. 34, No. 6, 2000, pp. 689–691.

SEMICONDUCTOR STRUCTURES, INTERFACES, AND SURFACES

Thermoelectric and Photoelectric Properties of the *p–n* $CuInSe_2$/CdS Heterostructures Obtained by the Quasi-Equilibrium Deposition Method

M.-R. A. Magomedov, Sh. M. Ismailov, Dzh. Kh. Magomedova, and P. P. Khokhlachev

Institute of Physics, Dagestan Scientific Center, Russian Academy of Sciences, ul. 26 Bakinskikh Komissarov 94, Makhachkala, 367003 Dagestan, Russia

Submitted March 18, 1999; accepted for publication August 18, 1999

Abstract—Through deposition of $CuInSe_2$ films on CdS substrates in a quasi-closed-circuit "hot-wall" reactor, *p–n* $CuInSe_2$/CdS heterostructures were obtained. The thermoelectric power, current–voltage characteristics, and photosensitivity spectra of the structures were investigated. © *2000 MAIK "Nauka/Interperiodica".*

The $CuInSe_2$-based solar cells and optoelectronic devices are competitive with the best devices fabricated from silicon and gallium arsenide [1]. $CuInSe_2$/CdS heterostructures provide electrical characteristics corresponding to device applications [2, 3]. Data on heterostructures that include the $CuInSe_2$ film deposited on the bulk CdS crystal are lacking in the literature. A method for obtaining these structures, as well as their electrical and spectral characteristics, is described in this paper for the first time. The specific features of obtaining the photosensitive single-phase films of $CuInSe_2$ with an electron mobility of 50 $cm^2/(V\ s)$ and a hole mobility of 6 $cm^2/(V\ s)$ were reported in [4, 5].

To obtain heterostructures, *n*-CdS bulk crystals grown from the melt were used. First, wafers of cadmium sulfide with an average size of $8 \times 5 \times 0.4$ mm^3 and a resistivity of 10^2–10^3 Ω cm at 290 K were mechanically polished. Second, they were etched in a 1% solution of bromine in methanol for 20 s and in a chromium etchant for 5 min. The CdS substrates were then placed in a quasi-closed-circuit "hot-wall" reactor that was mounted within the operating volume of the vacuum system, which was designed for deposition of the $CuInSe_2$ films. The structures were obtained by sputtering a fine powder prepared from polycrystals and single crystals of $CuInSe_2$, which were grown by the vertical Bridgman method [6] in vacuum at a residual pressure of 10^{-4} Pa. The temperatures of the source and substrate were 1450–1650 K and 550–650 K, respectively. The "hot-wall" method with an autonomously controlled temperature (up to 800 K) of the screen was used. The use of the "hot wall" provided operating conditions close to quasi-equilibrium ones and reduced diffusion at the heterointerface, while the low rates of deposition (1–5 nm/s) were favorable for a good adhesion.

Nonrectifying contacts to CdS were formed by indium deposition at 500 K, and thin gold layers were deposited on the surface of the $CuInSe_2$ film. The linearity of contacts was tested based on current–voltage (*I–V*) characteristics. The electrical conductivity and the Hall effect were measured using the four-probe method. The charge-carrier concentration for CdS and $CuInSe_2$ was 10^{15}–10^{16} and 4×10^{17}–1×10^{18} cm^{-3} at 300 K, respectively.

The $CuInSe_2$ films 4–5 μm in thickness were deposited on the CdS bulk crystals with a resistivity of 10^2 Ω cm and a mobility of 70 $cm^2/(V\ s)$. The steady-state thermoelectric power of 150 μV/K, which was measured along the normal to the layers, corresponded to *n*-type conduction, while the thermoelectric power for CdS and $CuInSe_2$ was 230 and 450 μV/K at 300 K, respectively. The barrier thermoelectric power was measured in planar geometry [7] using electronic-flash thermal pulses with an energy of 0.05 J and a duration of 2 μs. The temperature was measured on the surface of the sample, which was placed into a cell with an orifice plate. The emf values at a large temperature gradient ($\sim 2 \times 10^2$ K/cm) were more than one order of magnitude larger compared to the emf for the samples without barriers.

Typical *I–V* characteristics of the *p*-$CuInSe_2$/*n*-CdS heterostructure at 290 K that were measured in the dark and under illumination are shown in Fig. 1. In the region of low biases, the *I–V* characteristics obtained in the dark are symmetric and coincide with those obtained under illumination; i.e., the current density is defined by the equilibrium conduction rather than by injection. The forward *I–V* characteristic remains virtually unchanged under the influence of illumination, while the resistance of CdS decreases and the slope of the *I–V* characteristic increases at reverse biases. The nonrectifying region of the *I–V* curve is defined by the

temperature dependence of conduction (Fig. 1, the inset). For biases up to 0.7 V, the exponential region of the *I–V* curve is adequately described by the diode equation $I = I_s \exp(eV/nkT)$, where n = 1.1–2.6. This indicates that generation–recombination processes occur in the space charge region. The calculated barrier height 0.97 eV, which was obtained from the energy model of an ideal heterojunction, is close to the published data [8], while the experimental barrier height from the cutoff-voltage estimate is 0.65 eV.

The saturation-current values for the asymmetric *p–n* junction were calculated from the diode equation

$$I_s = eN_d \frac{D_n}{L_n} \exp\left(-\frac{V_d - \Delta E_c}{kT}\right) \quad (1)$$

and were $\leq 10^{-7}$ A/cm^2. The quantity $\Delta E \longrightarrow 0$ if the electron affinities for constituents are identical. The electron affinity for $CuInSe_2$ and CdS is about 4.5 eV. The diffusion coefficient and diffusion length for electrons in $CuInSe_2$, D_n = 4.2 cm^2/s and L_n = 0.6 μm, are obtained from the capacitance–voltage curves and photovoltage measurement. Since the majority charge carrier concentration in the $CuInSe_2$ region is two order of magnitude larger than that in the CdS region, the parameters of the *p*-material are included in equation (1).

The experimental saturation dark current, which was determined from linear forward *I–V* characteristics in the zero bias region, does not exceed 10^{-6} A/cm^2. This points both to a low equilibrium concentration of the holes involved in conduction at the contact and to separation of the electron–hole pairs across the generation region thickness if edge effects are insignificant.

On illuminating the heterostructure in the CdS absorption region (wavelengths of 500–900 nm), the photovoltage is observed. The spectral dependences of the photosensitivity in the mode of short-circuit current $I_{ph}(\hbar\omega)$ for various geometric conditions of illumination are shown in Fig. 2. The setup for measuring the spectral characteristics was designed on the basis of an MDR-2 monochromator. An incandescent lamp with a power of 150 W served as the radiation source. The spectra were normalized to the constant photon flux. For the modulation frequency of 400 Hz, in which case the thermal generation processes are insignificant, the photoresponse increases steadily with an increase in the radiation intensity. It can be seen from Fig. 2 that, if the heterostructure is illuminated from the side of the CdS substrate, the maximum sensitivity is observed (as distinct from the case of thin films) at the wavelength of 0.6 μm ($\hbar\omega \approx 2$ eV). If the $CuInSe_2$ film is illuminated, the photosensitivity is low and manifests itself in a low-energy region only. For illumination in the longitudinal geometry (from the end plane), in which case the radiation is absorbed close to the heterojunction active region, a plateau is observed between the bandgap energies of corresponding components.

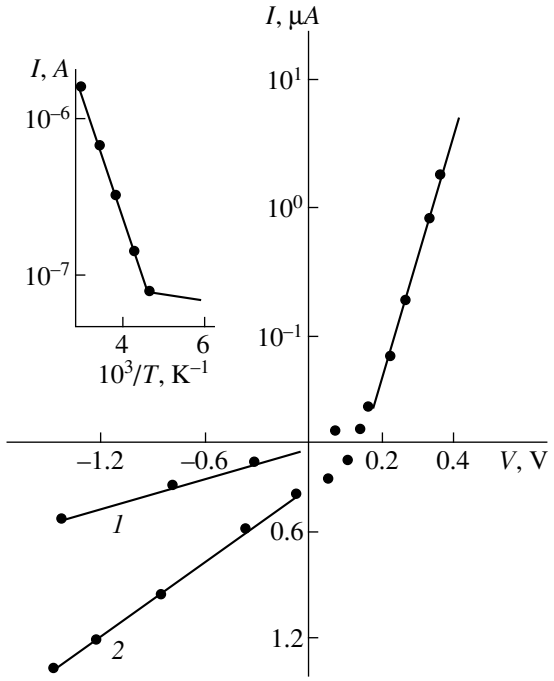

Fig. 1. Typical *I–V* characteristics of the $CuInSe_2$/CdS heterostructure at T = 290 K (*1*) in the dark and (*2*) with an illumination intensity of 20 mW/cm^2. The temperature dependence of the forward current at the constant voltage is shown in the inset.

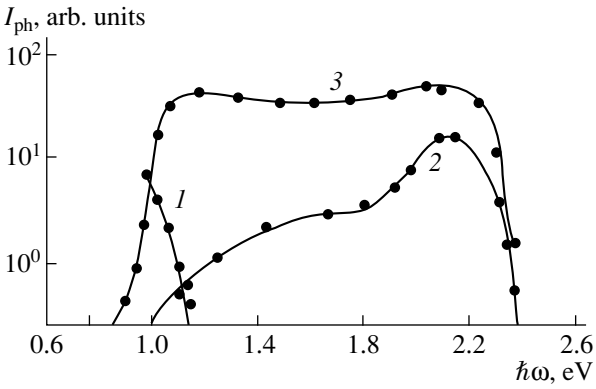

Fig. 2. Spectral dependence of the short circuit current *i* in the *p*-$CuInSe_2$/*n*-CdS structure in the case of illumination of (*1*) the $CuInSe_2$ film, (*2*) the CdS crystal, and (*3*) in parallel geometry.

The short-circuit photocurrent density I_{ph} depends on the relation between two terms [9]:

$$I_{ph} = e\beta N\left[1 - \exp(-kd) + \exp(-kd)\frac{k'L}{k'L + 1}\right], \quad (2)$$

where β is the quantum efficiency; $N = N_0 f(k, l, R)$; N_0 is the number of incident photons; k' and k are the absorption coefficients; l is the *p*-layer thickness; d is the space charge layer thickness; and R and L are the

reflectivity and diffusion length of the charge carriers, respectively, in the *p*-layer. The plateau observed in the spectral dependence of the photocurrent is due to the fact that the second term is predominant in formula (2) if $l > L$ and the collection of photocarriers is slightly weakened by recombination. The maximum depending on the k'/l ration is observed if the absorption in the *n*-region is weak and $l > L\exp(-k'l) \sim 1$. The selective character of photosensitivity in the case of illumination from the $CuInSe_2$ side can be explained by a small diffusion length of the minority carriers. The highest voltage sensitivity is 5×10^2 V/W, and the highest current sensitivity is 5 mA/W.

Thus, the obtained data on thermoelectric and photoelectric properties of the structures consisting of *p*-$CuInSe_2$ and *n*-CdS bulk crystal indicate that these heterostructures can be used to solve applied problems.

REFERENCES

1. V. Yu. Rud', Yu. V. Rud', I. V. Bondar', and V. F. Gremenyuk, Fiz. Tekh. Poluprovodn. (St. Petersburg) **32** (4), 432 (1998) [Semiconductors **32** (4), 385 (1998)].
2. *Current Topics in Photovoltaics*, Ed. by T. Coutts and J. Meakin (Academic, London, 1985; Mir, Moscow, 1988).
3. M. A. Magomedov and Yu. V. Rud', Fiz. Tekh. Poluprovodn. (St. Petersburg) **27** (2), 245 (1993) [Semiconductors **27** (2), 137 (1993)].
4. M.-R. A. Magomedov, Dzh. Kh. Amirkhanova, Sh. M. Ismailov, *et al.*, Zh. Tekh. Fiz. **67** (3), 34 (1997) [Tech. Phys. **42**, 282 (1997)].
5. M.-R. A. Magomedov, J. Kh. Amirchanova, Sh. M. Ismailov, and P. P. Khokhlachev, in *Proceedings of the 4th Asian Thermophysical Properties Conference, Tokyo, 1995*, A1 d3, p. 55.
6. M. A. Abdullaev, R. M. Gadzhieva, Dzh. Kh. Magomedova, and P. P. Khokhlachev, Izv. Ross. Akad. Nauk, Neorg. Mater. **33** (3), 411 (1997).
7. I. I. Balmush, Z. I. Dashevskiĭ, and A. I. Kasiyan, in *Thermoelectric Effects in Semiconductor Heterostuctures* (Shtiintsa, Kishinev, 1992), p. 144.
8. S.-H. Wei and A. Zunger, Appl. Phys. Lett. **63**, 2549 (1993).
9. S. Sze, *Physics of Semiconductor Devices* (Wiley, New York, 1981; Mir, Moscow, 1984).

Translated by N. Korovin

Semiconductors, Vol. 34, No. 6, 2000, pp. 665–667. Translated from Fizika i Tekhnika Poluprovodnikov, Vol. 34, No. 6, 2000, pp. 692–694.

SEMICONDUCTOR STRUCTURES, INTERFACES, AND SURFACES

Critical Voltage Growth Rate when Initiating the Ultrafast Impact Ionization Front in a Diode Structure

A. M. Minarskiĭ and P. B. Rodin

Ioffe Physicotechnical Institute, Russian Academy of Sciences, Politekhnicheskaya ul. 26, St. Petersburg, 194021 Russia

Submitted October 4, 1999; accepted for publication December 9, 1999

Abstract—The threshold of the voltage-rise rate was estimated; this threshold should be achieved in a reversely biased diode structure to excite an impact ionization front propagating with a velocity higher than saturated carrier drift velocities. © *2000 MAIK "Nauka/Interperiodica".*

The ultrafast impact ionization wave in the reversely biased diode structure [1–3] corresponds to the most interesting scenario of the p–n junction avalanche breakdown, in many respects similar to the streamer-type breakdown in a gas and a solid [4–7]. The impact ionization front propagates in a p^+–n–n^+ structure (the typical n–base length is 100–250 μm, its doping level is $N_d = 10^{14}$ cm^{-3}) from the cathode to the anode (see figure) with a velocity a few times exceeding the saturated drift velocity $v_s \approx 10^7$ cm/s of carriers, leaving behind it a dense electron–hole plasma with concentration $N \gg N_d$. The front propagation can modulate a structure conductance in a shorter time than the drift time W/v_s and is sufficiently uniform over the area [2, 3, 8] as distinct from the streamer [5]. The front is excited as follows [2, 3]: first, back bias U_0 lower than the steady avalanche breakdown voltage but close to it (see figure, curve *1*) is applied to the diode and series load resistance R. Then, the applied voltage is increased (curves *2* and *3*) according to the law

$$U(t) = U_0 + At, \quad (1)$$

which can be considered with good accuracy as linear at the initiation stage. The front is initiated only at a sufficiently fast voltage rise, $A > A_{\text{th}}$, with the voltage applied to the structure at the initiation instant much exceeding the steady breakdown voltage.[1] The threshold $A_{\text{th}} \approx 10^{12}$ V s^{-1} only slightly depends on the material (Si or GaAs) and device design. The existence of this threshold was previously qualitatively explained as follows (see [2, 3]). It is necessary to form a so-called overvoltage region near the p^+–n junction, in which the electric field strength E substantially exceeds the impact ionization threshold. This should be done so fast that thermal carriers would not have time to appear in this region, initiate the avalanche breakdown and, thus, prevent a further voltage increase due to the device current growth. As far as we know, the value of A_{th} was not estimated quantitatively. In this paper, we point to an alternative cause of the threshold A_{th} and estimate its value.

Leaving aside the urgent problem of plane front transverse stability [11–13] and wave initiation uniformity [14], we assume that the front is excited and then propagates uniformly over the entire structure area.

First of all, we consider the basic mechanisms of the ultrafast front propagation by the example of a quasi-steady stable mode (see figure, curve *4*). The electric field E somewhat exceeds the impact ionization threshold E_{th} ahead of the front, and there exists a low initial concentration of free electrons and holes, n_0, $p_0 \ll N_d$. The wave propagation is characterized by electron–hole plasma generation with a concentration N sufficient for the almost complete screening of the electric field. Carrier generation due to the impact ionization and field displacement (screening) from newly formed conductive regions are two main processes responsible for wave propagation, while the electron drift is not important in conductance modulation. In this respect, the wave propagates analogously to the threadlike streamer under the conditions of preionization [7]. In the simplest case of threshold dependence of impact ionization coefficients on the field, $\alpha(E) = \alpha_0\Theta(E - E_{\text{th}})$, where $\Theta(E)$ is the Heaviside function (unit step), the wave velocity v_f and the impact ionization region size l_f (where $E > E_{\text{th}}$) can be approximately related by formulas [11] completely similar to those [7] for a streamer; i.e.,

$$v_f = \frac{l_f}{\tau_f}, \quad \tau_f = \frac{1}{\alpha_0 v_s}\ln\frac{N}{n_0}, \quad N = \frac{\alpha_0 \varepsilon \varepsilon_0 E_{\text{th}}}{q}, \quad (2)$$

where ε is the semiconductor permittivity and q is the elementary charge. The quantity τ_f stands for the field displacement time and is controlled only by material parameters. The size of the impact-ionization region l_f

[1] The wave initiation and propagation are described in [2, 3] in detail, a descriptive pattern is also presented by the numerical simulation data in [8–10].

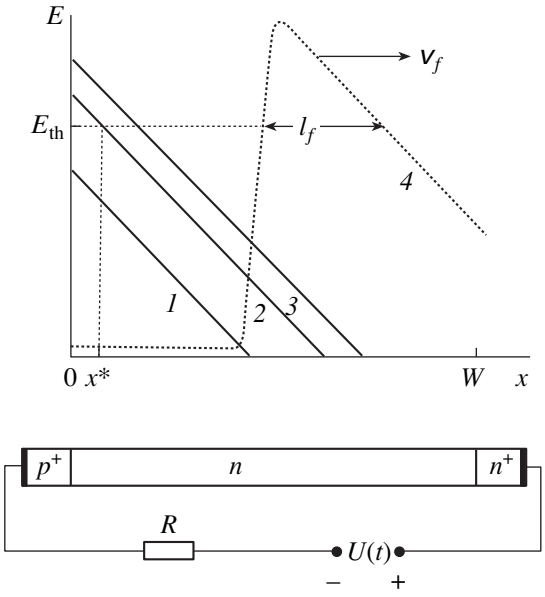

Diagram of the p^+–n–n^+ structure (bottom) and electric field distributions in the n–base (top) at various instants: (*1*) $t_1 = 0$, the initial field distribution; (*2*, *3*) $t_2 < t_3$, the front was not yet initiated; and (*4*) the field in the traveling wave. E_{th} is the impact ionization threshold, and x^* is the boundary of the region in which the impact ionization can occur at time t_2.

depends on the external applied voltage, ionization front position, doping level N_d, and, at large base lengths, also on the neutral (not depleted) region size ahead of the front [11].[2]

The velocity of a quasi-steadily propagating wave always exceeds the drift velocity, $v_f > v_s$ [15]: the front cannot move with a velocity lower than v_s since the drift-induced spreading of carriers destroys the space charge region behind the wave front. According to (2), the condition $v_f > v_s$ is equivalent to $l_f > v_s\tau_f$; i.e., the external voltage applied to the diode should be sufficiently high during the wave propagation for the ionization region size to exceed the critical size.

The overall objective of this paper is to indicate the critical role of drift-induced spreading at the wave initiation stage when electron (n) and hole (p) concentrations are low (n, $p < N_d$), while the applied voltage increases (see figure, curves *2*, *3*). In this case, the generation region size is necessary small over a certain time, and the condition $l_f > v_s\tau_f$ is not satisfied and should be substituted with the condition imposed onto the generation-region expansion rate. The boundary x^* of the region where $E > E_{th}$ is determined from $E(x^*, t) = E_{th}$. If the generation zone expands faster than the drift velocity, $dx^*/dt > v_s$, all carriers produced by impact ionization certainly remain in the ionization zone and contribute to the field screening as their concentration increases. Thus, the drift spreading ceases to be a factor preventing the front formation. The field in the structure can be approximately defined as

$$E(x, t) = E_{max}(t) - \frac{qN_d}{\varepsilon\varepsilon_0}x,$$
$$E_{max}(t) = \sqrt{\frac{2qN_dU(t)}{\varepsilon\varepsilon_0}}. \quad (3)$$

When deriving (3), we assume the field distribution to be triangular (see figure, curves *1–3*), neglecting the voltage drop in the quasi-neutral region near the n^+ contact. The voltage $U(t)$ is believed to be totally applied to the diode, which is valid for a small current through the load at the initiation stage. It follows from (1) and (3) that the boundary x^* moves with the velocity

$$\frac{dx^*}{dt} = \frac{A}{E_{max}(t)}. \quad (4)$$

Taking into account that $E_{max}(t) \approx E_{th}$ at the initiation stage, we estimate the critical rate of voltage growth as

$$A_{th} \approx E_{th}v_s. \quad (5)$$

Assuming that $E_{th} \approx 2 \times 10^5$ V s^{-1} and $v_s = 10^7$ cm s^{-1}, we find $A_{th} \approx 2 \times 10^{12}$ V s^{-1}, which is close to the experimentally observed value of 10^{12} V s^{-1} [2, 3]. We emphasize that A_{th} depends only on material parameters and is identical for structures with various dopant concentrations N_d.

The approximativeness of (5) is caused by a steplike dependence of impact ionization coefficients $\alpha(E)$. The inequality $A > A_{th}$ is equivalent to a sufficient, redundantly strong condition for wave initiation. Actually, the impact ionization is implicitly assumed to proceed uniformly in the entire range $E > E_{th}$. In fact, the most intense generation proceeds at the left edge of this region (see figure), where the field is at its maximum and exceeds the threshold one for a long time. Under these conditions, drifting carriers need an additional time to leave the ionization region; that is, the condition $dx^*/dt > v_s$ can be weakened. Hence, formula (5) represents an upper bound of the critical field-rise rate.

The threshold voltage-rise rate exists also when initiating the streamer that propagates from a tip in a semiconductor [5] and has the same typical value of 10^{12} V s^{-1}. Condition (5) coincides with the critical voltage-rise rate estimated in [7] as

$$\left(\frac{dU}{dt}\right)_{th} \approx \frac{E_0v_s}{\ln(\alpha_0R)}, \quad (6)$$

(where R is the tip radius and it is assumed that $\alpha(E) = \alpha_0\exp(-E_0/E)$) within a factor accounting for the three-dimensional nature of streamer initiation.

[2] A comparison with the theory of front self-similar propagation in the TRAPATT diode [15] shows that dependences (2) are accurate to within logarithmic corrections.

The condition $A > E_{th}v_s$ is equivalent to the known condition for the field rise rate in a diode structure in the case of wave initiation

$$\varepsilon\varepsilon_0\frac{\partial E}{\partial t} < qN_d v_s. \quad (7)$$

This condition was derived for a TRAPATT diode in [15] on the assumption that the wave is initiated and propagates in the mode of current J = const. The left-hand side of (7) corresponds to the density of bias current $J = \varepsilon\varepsilon_0\partial E/\partial t$ flowing through the structure prior to the front initiation. Since J = const, this bias current coincides with the conduction current flowing through the conductive region after the wave initiation. This current $J = qN_d v_f$ ensures the compensation for charged donors in the depletion region. Condition (7) represents a formal consequence of the condition $v_f > v_s$ and the model assumption J = const [15]. The equivalence of (5) and (7) can be verified by direct substitution, choosing $E(x, t) = E(0, t) = E_{max}(t)$ and taking into account that $dE_{max}/dt = (qN_d/\varepsilon\varepsilon_0)dx^*/dt$.

If condition (5) is satisfied, the origin of carriers initiating the impact ionization is unimportant. On the one hand, any carrier found in the zone $E > E_{th}$ generates new carriers without leaving the impact ionization region. There are two carrier sources: thermal generation directly in the region of high field and drift of holes from the diode neutral region [2, 3]. We note that the characteristic time τ_f of concentration rise from the initial value $n_0 = 10^5$–10^6 cm^{-3} to the final one $N > 10^{16}$–10^{18} cm^{-3} depends logarithmically on n_0 and, for given typical values, a change in n_0 by a few orders of magnitude leads to a change in τ_f merely by tens of percents. This can be substantial for understanding the low sensitivity of basic switching characteristics (in particular, delay-time stability) to a specific initiation mechanism.

REFERENCES

1. I. V. Grekhov and A. F. Kardo-Sysoev, Pis'ma Zh. Tekh. Fiz. **5**, 950 (1979) [Sov. Tech. Phys. Lett. **5**, 395 (1979)].
2. V. M. Tuchkevich and I. V. Grekhov, *New Methods for High-Power Switching by Semiconductor Devices* (Nauka, Leningrad, 1988).
3. I. V. Grekhov, Solid-State Electron. **32**, 923 (1989).
4. L. B. Loeb, Science **148**, 1417 (1965).
5. N. G. Basov, A. G. Molchanov, A. S. Nasibov, *et al.*, Zh. Éksp. Teor. Fiz. **70**, 1751 (1976) [Sov. Phys. JETP **43**, 912 (1976)].
6. S. K. Dhali and P. F. Willams, J. Appl. Phys. **62**, 4696 (1987).
7. M. I. D'yakonov and V. Yu. Kocharovskiĭ, Zh. Éksp. Teor. Fiz. **94** (10), 321 (1988) [Sov. Phys. JETP **67**, 1049 (1988)].
8. R. J. Focia, E. Schamiloglu, C. B. Fleddermann, *et al.*, IEEE Trans. Plasma Sci. **25**, 138 (1997).
9. Yu. D. Bilenko, M. E. Levishteĭn, M. V. Popova, *et al.*, Fiz. Tekh. Poluprovodn. (Leningrad) **17**, 1812 (1983) [Sov. Phys. Semicond. **17**, 1156 (1983)].
10. A. F. Kardo-Sysoev and M. V. Popova, Fiz. Tekh. Poluprovodn. (St. Petersburg) **30**, 803 (1996) [Semiconductors **30**, 431 (1996)].
11. A. M. Minarskiĭ and P. B. Rodin, Fiz. Tekh. Poluprovodn. (St. Petersburg) **31**, 433 (1997) [Semiconductors **31**, 366 (1997)].
12. A. M. Minarskiĭ and P. B. Rodin, Solid-State Electron. **41**, 813 (1997).
13. H. Jalali, R. Joshi, and J. A. Gaudet, IEEE Trans. Electron Devices **45**, 1761 (1998).
14. S. N. Vaĭnshteĭn, Yu. V. Zhilyaev, and M. E. Levinshteĭn, Pis'ma Zh. Tekh. Fiz. **14**, 1552 (1988) [Sov. Tech. Phys. Lett. **14**, 664 (1988)].
15. V. S. Deloach and D. L. Scharfetter, IEEE Trans. Electron Devices **ED-20**, 9 (1970).

Translated by A. Kazantsev

Semiconductors, Vol. 34, No. 6, 2000, pp. 668–670. Translated from Fizika i Tekhnika Poluprovodnikov, Vol. 34, No. 6, 2000, pp. 695–697.

SEMICONDUCTOR STRUCTURES, INTERFACES, AND SURFACES

Special Features of Generation–Recombination Processes in the *p–n* Junctions Based on HgMnTe

L. A. Kosyachenko*, S. É. Ostapov*, and Sun Weiguo**

** Chernovtsy University, Chernovtsy, 274012 Ukraine*

*** Luoyang Optoelectronics Institute, PO Box 030, Luoyang, Henan, 471009 People's Republic of China*

Submitted November 12, 1999; accepted for publication December 9, 1999

Abstract—New experimental data on the charge transport in *p–n* junctions based on $Hg_{1-x}Mn_xTe$ ($x \approx 0.11$) are reported. The experimental *I–V* characteristics are interpreted in terms of the Sah–Noyce–Shockley theory with allowance made for special features of recombination of the charge carriers in a narrow-gap semiconductor. © *2000 MAIK "Nauka/Interperiodica".*

As is known, electrical properties and, correspondingly, detectability of a photodiode based on narrow-gap semiconductors (such as HgCdTe and HgMnTe) are primarily defined by the generation–recombination processes in a *p–n* junction [1–3]. We report here the data indicating that recombination processes in such diodes have distinctive features.

The diode structures were produced by ion etching of *p*-$Hg_{0.89}Mn_{0.11}Te$ structures. The bandgap E_g determined from the optical-transmission spectra was equal to ~0.18 eV at 77 K. The electron concentration in the near-surface n^+-layer (1–2 μm thick) was close to $\sim 10^{18}$ cm^{-3}, whereas the hole concentration p in the substrate was $(2–3) \times 10^{16}$ cm^{-3}. The dimensions of active regions were defined by photolithography, and a three-layer Au/Cr/Pd metallization was used to form the nonrectifying contacts [4].

Figure 1 shows typical electrical characteristics of n^+–p junctions based on $Hg_{1-x}Mn_xTe$ and formed on the same substrate. The feature common to the shown current–voltage (*I–V*) characteristics is the presence of the portions corresponding to the dependence $I \propto \exp(eV/2kT)$ for the voltages $V < 0.1$ V; this is characteristic of the recombination mechanism of the current. The diode's differential resistance R_{dif} varies appreciably from diode to diode for low *V*, decreases rapidly with increasing voltage, and finally approaches the value that is independent of V and is the same for different diodes for $V > 0.3$ V. This lowest value of resistance that is equal to ~270 Ω in the case under consideration (with the diode area being 5×10^{-5} cm^2) obviously corresponds to the substrate resistance R_s. If the voltage drop across R_s is taken into account, the curve $I(V)$ becomes steeper for the currents ≳10 μA (points *2* in Fig. 1) and now represents the dependence $I \sim \exp(eV/kT)$ rather than the dependence $I \sim \exp(eV/2kT)$. Thus, the recombination current that is dominant in the region of low bias voltages gives way to the above-barrier diffusion current as *V* increases. This interpretation seems to be quite plausible, because the diffusion current depends on *V* more heavily than does the recombination current.

However, taking into account the voltage drop across the substrate resistance (i.e., plotting the dependence of *I* on $V - IR_s$), we virtually do not change the curves in the region of $V < 0.2$ V. For the voltage drop across R_s to be significant for the voltage $V \approx 0.08$ V, the value of R_s should be at least by two orders of magnitude larger than the determined value of R_s. In [5], it was assumed that the diode structure formed by ion etching incorporated a high-resistivity layer between the n^+ and p regions; this is similar to what is observed in the n^+–p^-–p junctions formed by ion implantation in $Hg_{1-x}Cd_xTe$ [6]. In order to interpret a drastic weakening of the influence of R_s on $I(V)$ for $V > 0.3$ V, we have to assume in addition that the electrical conductivity of the high-resistivity layer is modulated by electrons injected into this layer from the n^+-layer to such an extent that its resistance becomes much less than the substrate resistance for large forward currents. Apparently, another interpretation based on the consideration of special features of recombination itself in the *p–n* junction that does not include a high-resistivity p^- layer and is formed in a narrow-gap semiconductor (like $Hg_{0.89}Mn_{0.11}Te$) appears more realistic.

According to the Sah–Noyce–Shockley theory [7], the most effective recombination centers are located below the conduction-band bottom by the energy [8]

$$E_t = \frac{E_g}{2} + \frac{kT}{2}\ln\left(\frac{\tau_{p0}N_c}{\tau_{n0}N_v}\right), \qquad (1)$$

where N_c and N_v are the effective densities of states in the conduction and valence bands, respectively, and are proportional to $m_e^{3/2}$ and $m_h^{3/2}$ (m_e and m_h are the effec-

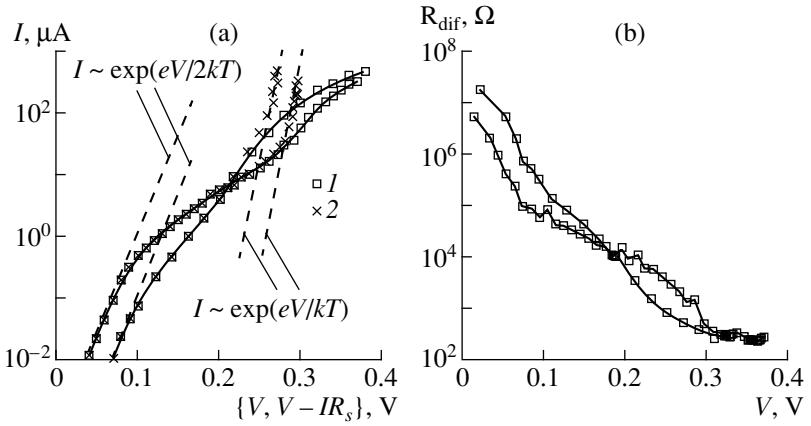

Fig. 1. (a): (*1*) The current–voltage characteristics of n^+–p junctions based on $Hg_{0.89}Mn_{0.11}Te$ and (*2*) the dependences of I on $V - IR_s$; (b): the voltage dependences of differential resistance for the same diodes.

tive masses of electron and hole); and τ_{n0} and τ_{p0} are the lifetimes of electron and hole, respectively.

It follows from (1) that, in the case of a wide-gap semiconductor, the recombination centers may be assumed to be located virtually in the middle of the forbidden band. However, for a narrow-gap semiconductor ($m_e \ll m_h$ and $N_c \ll N_v$), the second term on the right-hand side of (1) becomes comparable to $E_g/2$. In addition, the position of the Fermi level $\Delta\mu$ in the p and n regions ($\Delta\mu$ in the substrate is defined by the equality $p = N_v\exp(-\Delta\mu/kT)$) becomes close to $E_g/2$, and for $p = 2 \times 10^{16}$ cm^{-3}, amounts to ~0.03 eV at $T = 77$ K. It is this circumstance that brings about appreciable changes in the voltage dependence of the recombination current, which is defined by the following formula [7]:

$$I = A\frac{en_i}{\sqrt{\tau_{n0}\tau_{p0}}}\sinh\left(\frac{eV}{2kT}\right)\int_0^W f(x)dx. \qquad (2)$$

Here, A is the diode area, n_i is the intrinsic concentration of charge carriers; W is the width of the depletion layer; and $f(x)$ is a function that depends not only on the coordinate x but also on τ_{n0}, τ_{p0}, N_c, N_v, and E_t. For an asymmetric n^+–p junction, the expression for $f(x)$ can be written [8] as

$$f(x) = \left[\exp\left(-\frac{eV}{kT}\right)\cosh\left(\frac{E_g^* - 2E_t^*}{2kT}\right) + \cosh\left(\frac{E_g^* - eV - 2\varphi(x)}{2kT}\right)\right]^{-1}, \qquad (3)$$

where $E_t^* = E_t - \Delta\mu$, $E_g^* = E_g - 2\Delta\mu + kT(\tau_{p0}N_c/\tau_{n0}N_v)$, $\Delta\mu$ is the aforementioned position of the Fermi level in the bulk of a semiconductor, and $\varphi(x)$ is the distribution of the charge-carrier energy in the depletion layer. In this case, we deal with an abrupt asymmetric n^+–p junction, with the depletion layer being located in a lightly doped p-region; i.e., we have $\varphi(x) = (\varphi_0 - eV)(1 - x/W)^2$, where φ_0 is the barrier height in the case of equilibrium.

Figure 2 shows the results of calculating the current with formulas (2) and (3). If we assume that $m_e = m_h$, $E_t = E_g/2$, and $\tau_{n0} = \tau_{p0}$, the calculated curve virtually coincides with that defined by the expression

$$I = A\frac{en_iW}{\sqrt{\tau_{n0}\tau_{p0}}}\frac{2kT}{\varphi_0 - eV}\left[\exp\left(\frac{eV}{2kT}\right) - 1\right], \qquad (4)$$

which can be obtained from (2) by replacing the integration with respect to x with multiplication of the maximal value of the integrand by its half-width [8].

If we then assume that $m_e = 0.01m_h$ for $Hg_{0.89}Mn_{0.11}Te$ [9] and that the position of the recombi-

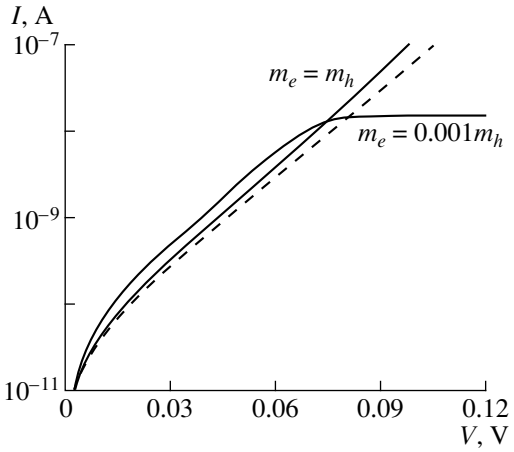

Fig. 2. The recombination currents calculated with formulas (2) and (3) for $m_e = m_h$ and $m_e = 0.01m_h$. The dashed line corresponds to the current calculated with formula (4). $T = 80$ K.

nation level E_t is defined by expression (1), the calculated dependence of the current deviates significantly from (4); this is similar to what is observed in experimental curves in the range of $0.08 < V < 0.2$ V (Fig. 1), in which case the diffusion current is negligibly small. A quantitative analysis of the results of calculations for $V < 0.08$ V does not make much sense, because we do not take into account the difference between τ_{n0} and τ_{p0}, i.e., between the lifetimes of electrons and holes under the condition that the recombination centers (traps) are either completely empty or completely filled with electrons [7]. We may only assume that consideration of a difference between τ_{n0} and τ_{p0} cannot radically affect the trend of the dependence $I(V)$ for $V < 0.08$ V.

We note that, in order to quantitatively compare the calculated curves with experimental data for $V <$ 0.08 V, we should assume that the effective lifetime $\tau_0 = \sqrt{\tau_{n0}\tau_{p0}}$ is equal to 10^{-5}–10^{-6} s (for different diodes), which is consistent with the results reported previously [2, 9]. It is also worth noting that the value of such an important characteristic as the product R_0A [1, 2, 9] can be as high as ~500 Ω cm^2 for the diodes under investigation (with the long-wavelength cutoff of ~7 μm).

REFERENCES

1. A. Rogalski, Infrared Phys. **28**, 139 (1988).
2. A. Rogalski and J. Rutkowski, Infrared Phys. **29**, 887 (1989).
3. P. Brogowski, M. Mucha, and J. Piotrowski, Phys. Status Solidi **114**, K37 (1989).
4. K. A. Kosyachenko, I. M. Rarenko, O. O. Bodnaruk, *et al.*, Sci. Bull. Chernovtsy University, Physics **40**, 59 (1998).
5. L. A. Kosyachenko, I. M. Rarenko, O. A. Bodnaruk, and Sun Weiguo, Fiz. Tekh. Poluprovodn. (St. Petersburg) **33**, 1438 (1999) [Semiconductors **33**, 1293 (1999)].
6. L. O. Budulac, J. Cryst. Growth **86**, 723 (1988).
7. C. Sah, R. Noyce, and W. Shockley, Proc. IRE **45**, 1228 (1957).
8. L. A. Kosyachenko, V. P. Makhniy, and I.V. Potykevich, Ukr. Phys. J. **23**, 279 (1978).
9. A. Rogalski, Infrared Phys. **31**, 117 (1991).

Translated by A. Spitsyn

Semiconductors, Vol. 34, No. 6, 2000, pp. 671–676. Translated from Fizika i Tekhnika Poluprovodnikov, Vol. 34, No. 6, 2000, pp. 698–703.

SEMICONDUCTOR STRUCTURES, INTERFACES, AND SURFACES

Influence of SiO_2 Protective Films on the Diffusion of Atomic Hydrogen during the Hydrogenation of Epitaxial *n*-GaAs

A. V. Panin* and N. A. Torkhov**

** Institute of Strength Physics and Material Science, Siberian Division, Russian Academy of Sciences, Akademicheskiĭ pr. 2/1, Tomsk, 634055 Russia*

e-mail: pav@ispsms.tsc.ru

*** Research Institute of Semiconductor Devices, Tomsk, 634045 Russia*

e-mail: tna@ic.tsu.ru

Submitted December 20, 1999; accepted for publication December 21, 1999

Abstract—The surface relief of SiO_2 films and the influence of these films on the in-diffusion of atomic hydrogen in a semiconductor in the course of hydrogenation were investigated by atomic-force microscopy and scanning tunneling microscopy. The mesostructures appearing as a corrugation on the semiconductor surface are shown to be formed during the deposition of the SiO_2 film. This fact causes an increase in the amount of hydrogen penetrating into a semiconductor in the course of hydrogenation. The deposition of the dielectric film on the *n*-GaAs surface results in its reconstruction consisting in forming a quasi-periodic relief. The treatment of the *n*-GaAs surface covered with the SiO_2 protective film in atomic hydrogen modifies the surface relief of the epitaxial layer. *© 2000 MAIK "Nauka/Interperiodica".*

1. INTRODUCTION

Hydrogenation is one of the efficient methods of treating semiconductor structures to considerably modify their electrophysical characteristics [1–3]. As a rule, the modifications observed are caused by the fact that hydrogen atoms passivate various electrically active centers located on the surface and in the bulk of a semiconductor [4, 5]. At the same time, atomic hydrogen obtained from molecular hydrogen by decomposition in the hydrogen plasma can cause the stoichiometry of the surface layer of a semiconductor to be violated [6]. Therefore, in the case of treatment in the hydrogen plasma, the semiconductor surface is covered with a SiO_2 protective film 5–10 nm thick [7, 8]. In this case, the efficiency of penetration of atomic hydrogen into the semiconductor can be even higher in the presence of a SiO_2 surface layer than without it [8].

This study is devoted to investigating the influence of the SiO_2 film on the diffusion of atomic hydrogen in a semiconductor. Using scanning tunneling microscopy and atomic-force microscopy, we investigated the surface structure of the GaAs layers and SiO_2 films and also the influence of the hydrogenation of the SiO_2–*n*-GaAs structures on the relief of the semiconductor surface.

2. EXPERIMENTAL PROCEDURE

The samples were produced on the basis of *n*-GaAs(100) epitaxial layers grown by metalloorganic hydride epitaxy on n^+-GaAs:Te substrates with a concentration of 2×10^{18} cm^{-3}. A charge-carrier concentration in epitaxial *n*-GaAs:Sn amounted to 4×10^{16} cm^{-3}, and the thickness of the layers was 0.5 μm. The nonrectifying contact was formed on the n^+-GaAs side by means of electrochemical deposition of GeNi/Au with subsequent annealing at a temperature of 450°C in nitrogen for 5 min.

To remove the native oxide, the *n*-GaAs surface was treated in an ammonia etchant ($NH_3OH : H_2O = 1 : 5$). According to the ellipsometry data, the thickness of residual oxide amounted to ~6 Å. The SiO_2 films were deposited on the *n*-GaAs surface by the plasma-chemical method. The temperature of deposition of the SiO_2 layers was lower than 300°C, which rules out the migration of atoms of the crystal matrix over the surface of the *n*-GaAs epitaxial layer. The thickness of the SiO_2 films estimated from the data of ellipsometry varied from 5 to 170 nm.

The treatment of the SiO_2–*n*-GaAs structures in the atomic-hydrogen flow was carried out at a temperature of 200°C for 5 min. A residual pressure in the vacuum chamber amounted to 3.7×10^{-4} Pa, and the pressure of hydrogen in the treatment zone was 1.3×10^{-2} Pa. The atomic-hydrogen flow was produced by the generator based on the Penning discharge with a hollow cathode and a self-incandescent element [8] spaced at 12 cm from the sample holder. The discharge voltage was 170–190 V for a current of 2 A. An input flow rate of hydrogen to the generator was kept constant by the electronic gas-flow-rate controller at a level of 700 atm cm^3/h.

A layer-by-layer elemental analysis of SiO_2 films and the near-surface regions of GaAs layers was per-

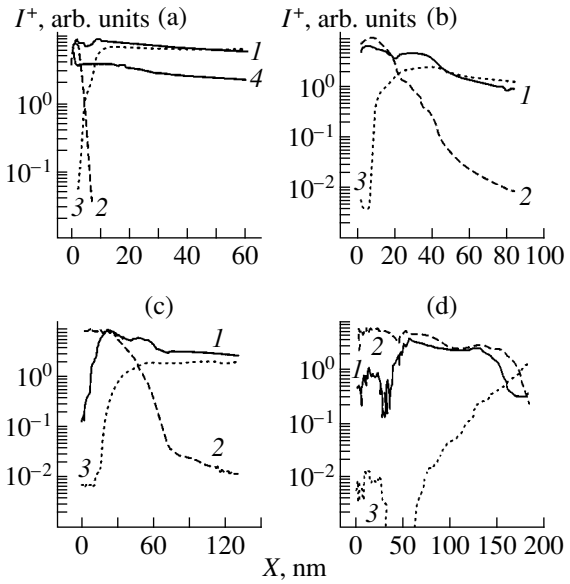

Fig. 1. Concentration profiles for positive ions (*1*) H^+, (*2*) Ga^+, and (*3*) Si^+ in the SiO_2–*n*-GaAs structures with a SiO_2-film thickness of (a) 5, (b) 38, (c) 93, and (d) 170 nm; (*4*) is the concentration profile for H^+ in *n*-GaAs.

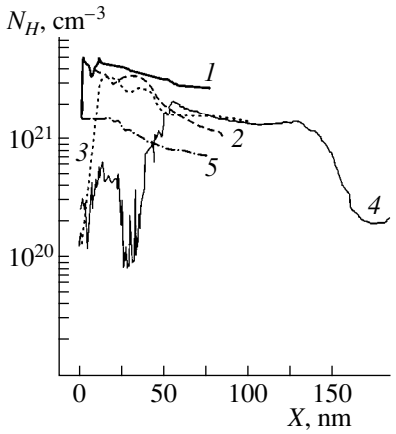

Fig. 2. Concentration profiles for the positive ions H^+ in the SiO_2–*n*-GaAs structure with a SiO_2-film thickness of (*1*) 5, (*2*) 38, (*3*) 93, and (*4*) 170 nm; (*5*) is the concentration profile for H^+ in *n*-GaAs.

formed using an MS-7201M secondary-ion mass spectrometer with a depth resolution of 30 Å. Dependences of the signals corresponding to H^+, Si^+, and Ga^+ secondary ions on the sputtering time were measured.

The surface morphology of SiO_2 films and GaAs layers was studied using an SMM-2000TA scanning multimicroscope produced in quantity by ZAO "KPD" (Moscow Institute of Electronic Engineering) and operating both in the scanning tunneling microscope (STM) and atomic-force microscope (AFM) modes. The images of the surface for nonconducting films of silicon dioxide were obtained in the AFM mode. We used standard cantilevers made of Si_3N_4 (Park Scientific Instruments, USA). The cantilever was scanned over the surface, and the photodiode current was kept constant using a feedback; this corresponds to the scanning in the constant-force mode of the probe–substrate interaction. The GaAs surface before depositing the SiO_2 films and also following their etching-off was investigated in the STM mode. The silicon-oxide film was removed by means of etching the structure in a solution of hydrofluoric acid ($HF : H_2O = 1 : 10$). The STM measurements were performed using a platinum tip (Pt of 99.99% purity) in the direct-current mode. The voltage between the tip and the semiconductor surface was chosen to be 1.5 V. All the measurements were performed under atmospheric-air conditions at room temperature.

3. EXPERIMENTAL RESULTS

According to the data of secondary-ion mass spectrometry, the SiO_2 films are transparent for atomic hydrogen. In Fig. 1, we show the distribution profiles for a concentration of positive ions H^+, Si^+, and Ga^+ in the SiO_2–*n*-GaAs structures. The thickness of the SiO_2 layers amounts to 5, 38, 93, and 170 nm. In the process of hydrogenation, the hydrogen atoms penetrate freely to the SiO_2–*n*-GaAs interface and diffuse further, deep into the semiconductor. This fact is evidenced by the presence of hydrogen in the surface region of GaAs in all the samples irrespective of the silicon-oxide thickness (see curve *1* in Figs. 1a–1d). As follows from the analysis of distribution profiles for the H_+ concentration in the SiO_2–*n*-GaAs structures (Fig. 2), the amount of hydrogen penetrating both in the dielectric film and in the surface region of the semiconductor depends on the SiO_2-layer thickness. The greater the thickness of SiO_2, the lower the maximum hydrogen concentration (Fig. 2, curves *1–4*). Thus, the presence of the SiO_2 layer leads to a more efficient accumulation of hydrogen in the near-surface region of *n*-GaAs.

The maximum concentration of hydrogen (5.2×10^{21} cm^{-3}) in the samples with the thinnest SiO_2 layer probably stems from the presence of pores in the film of thin dielectrics. In Fig. 3, we show an AFM image of the surface of the SiO_2 film 10 nm thick; the image was obtained with the magnification of 4×10^6. As can be seen in Fig. 3, the film is porous. The sizes of pores are comparable with the magnitude of the crystal-lattice constant of the semiconductor. A similar porous structure of the insulator film favors the unimpeded penetration of hydrogen in GaAs during hydrogenation. With increasing silicon-oxide thickness, the pores disappear and the amount of hydrogen in the SiO_2 and *n*-GaAs layers decreases.

In Figs. 4a–4d, we present AFM images of the surfaces of the SiO_2 films 10, 38, 93, and 170 nm thick, respectively; the images were obtained at a magnifica-

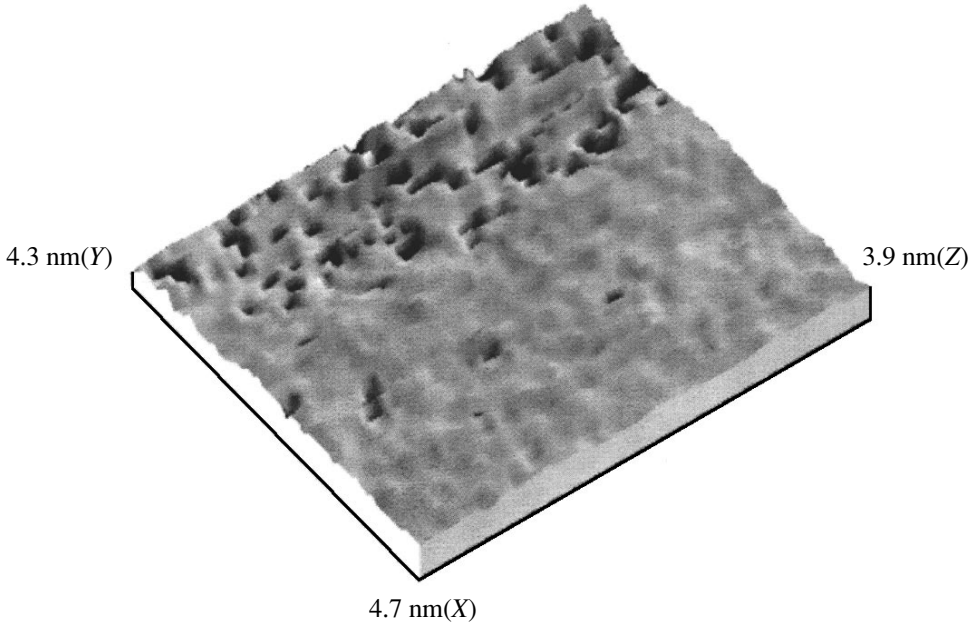

Fig. 3. STM image of the surface for the SiO_2 film 10 nm thick. Magnification is 4×10^6.

tion of 1.6×10^4. As a result of the investigations, it was discovered that periodic mesostructures appearing as a surface corrugation are formed on the surface following the deposition of dielectrics. The analysis of the images showed that the SiO_2 films have a quasi-periodic undulatory surface relief, with the characteristic period and amplitude depending on the thickness of the deposited layer. With increasing the SiO_2 thickness from 10 to 170 nm, geometric dimensions (period) of the hillocks first increase from 200 to 400 nm according to the logarithmic law and then level off. The height of the hillocks (amplitude) is independent of the film thickness and remains within the range of 4–8 nm.

It should be noted that the appearance of a similar relief when depositing a SiO_2 thin film (Fig. 4) is not related to the initial surface of the semiconductor substrate. The STM images of the *n*-GaAs initial surface before and after etching off the native oxide are shown in Figs. 5 and 6, respectively. According to the ellipsometry data, the native-oxide thickness amounts to 3.5 nm. From a comparison of Figs. 5 and 6, it can be seen that the roughness caused by the presence of the native oxide on the surface disappears following the treatment of *n*-GaAs in the ammonia etchant and the semiconductor surface turns out to be flat. The peak-to-peak value defined as $S_y = Z_{max} - Z_{min}$ [9] amounts to 23 nm (Fig. 6).

The treatment of the SiO_2–*n*-GaAs structures in the atomic-hydrogen flow leads to a considerable modification of the morphology of the *n*-GaAs surface. To verify this assumption, the SiO_2 film was etched off in a buffer etchant and the GaAs-surface relief was investigated by means of the scanning tunneling microscope. The STM images of the semiconductor surface before and after the treatment with atomic hydrogen are shown in Figs. 7 and 8, respectively.

As a result of the investigations performed, it was established that, after etching off the SiO_2 layer 10 nm thick, the *n*-GaAs surface turns out to be rougher compared to the initial one (before depositing the insulator). The maximum peak-to-peak value is more than doubled (S_y = 403 nm), while the surface shape becomes quasi-periodic (Fig. 7). Conversely, after treatment in atomic hydrogen and etching off the SiO_2 film, the *n*-GaAs surface turns out to be smooth. The peak-to-peak value amounts to S_y = 196 nm (Fig. 8).

4. DISCUSSION OF EXPERIMENTAL RESULTS

As is known, the structural basis for all the crystalline and amorphous modifications of silicon dioxide is the oxygen tetrahedron SiO_4. It is assumed that, as in amorphous modifications of SiO_2, annular structures oriented predominantly parallel to the surface of the semiconductor substrate arise in silicon-dioxide films. In a three-dimensional structure, the windows of these rings form submicrocrystalline channels 0.5 nm in radius [10]. A marked penetrability of hydrogen and helium atoms into the SiO_2 layers is associated with these channels. In this case, the distinctions in structures of the SiO_2 films obtained by plasma oxidation and by the standard thermal oxidation [11] are not detected by X-ray photoelectron spectroscopy.

A possible cause of the more efficient accumulation of hydrogen in the surface region of the semiconductor

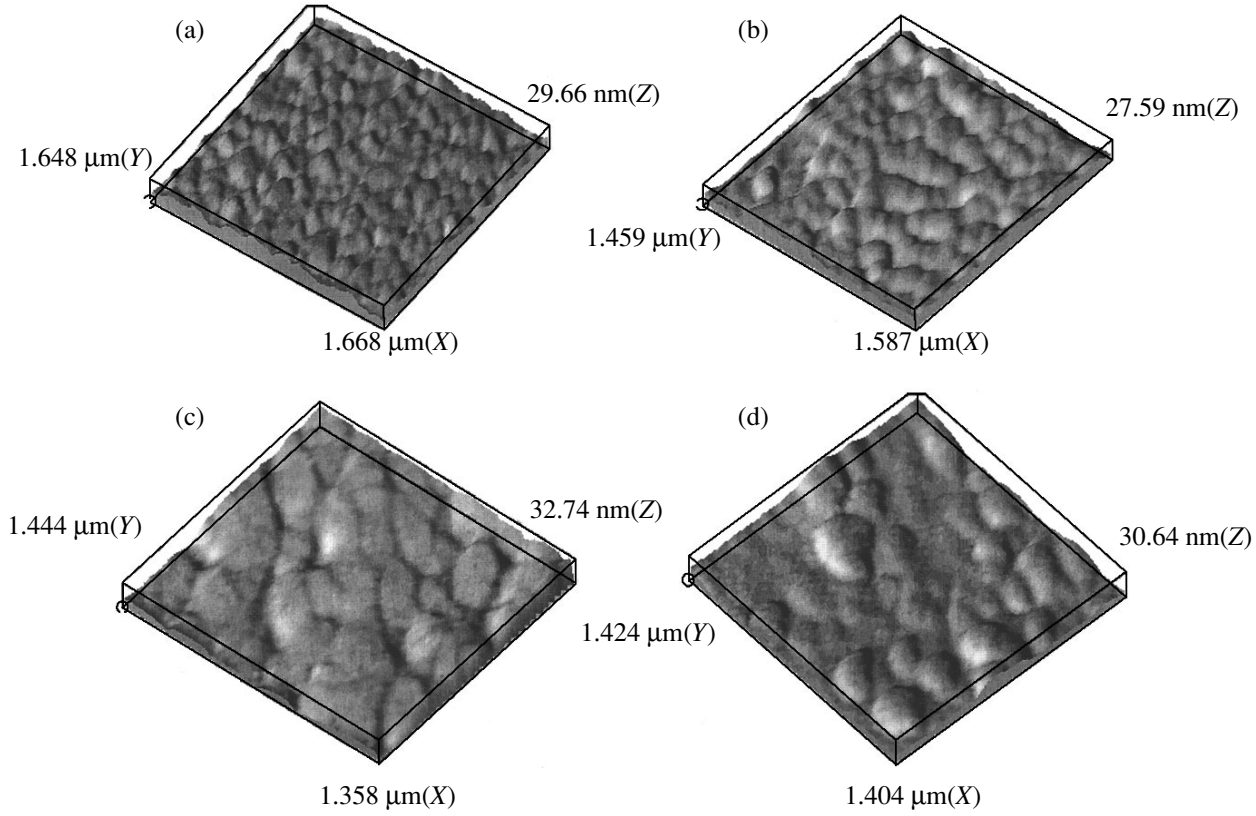

Fig. 4. AFM image of the surface of the SiO_2 film with a thickness of (a) 10, (b) 38, (c) 93, and (d) 170 nm. Magnification is 1.6×10^4.

in the presence of the SiO_2 film and also of the highest amount of hydrogen in samples with the smallest thickness of silicon oxide may be an increase in the film-surface area. As follows from Fig. 4, the film 10 nm thick has the most irregular surface and the largest surface area. As a result, a larger amount of atomic hydrogen is chemisorbed on such a SiO_2 film, which leads to an increase in the atomic-hydrogen flow deep in the SiO_2 layer.

The causes of the appearance of corrugation on the surface of the SiO_2 films are unclear. It can be caused both by the nucleation nature of the layer growth and by the internal stresses arising in thin films and at the film–substrate interface. However, we may state with confidence that the thermal stresses arising in thin films owing to a difference in the coefficients of thermal expansion of SiO_2 (0.48×10^{-6} K^{-1}) and GaAs (5.3×10^{-6} K^{-1}) [12] and also the stresses caused by a mismatch between the lattice parameters of interfacing materials lead to strains in the crystal lattice of the deposited insulator film. The presence of the strains in the SiO_2–*n*-GaAs structures, similarly to the SiO_2–Si structures [13], results in formation of microscopic voids, which are transformed into macroscopic pores in the course of cooling the structure. Some of these pores may be holes, which leads to an increased sensitivity of the interface to adsorption processes [10]. It is evident that the number of pores decreases with increasing film thickness and, simultaneously, the amount of hydrogen in the SiO_2 layers also decreases.

From the analysis of Si and Ga concentration profiles shown in Fig. 1, it follows that there is no abrupt interface between the SiO_2 film and the *n*-GaAs substrate; rather, there is certain boundary layer containing chemical components of SiO_2 and GaAs. It is known that, in the case of thermally oxidized silicon, the thickness of the SiO_2–Si transition layer with a violated stoichiometry is approximately the same both for thick (~200 nm) and ultrathin (2.3–4.5 nm) SiO_2 films and amounts to 2–3 nm [10]. In our case, when using the SiO_2 films obtained by the plasma-chemical method, the thickness of the transition layer turns out to be much larger. Simultaneously, a dependence of the transition-layer extension on the silicon-oxide thickness is observed.

The penetration of Si atoms into the surface region of GaAs and Ga atoms in the SiO_2 film is probably related to chemical reactions of interaction between surface atoms of the semiconductor and the products of a reaction during the plasma-chemical deposition of the

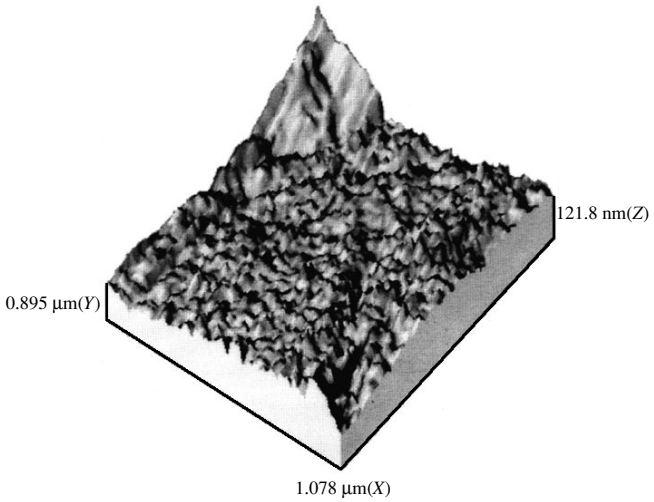

Fig. 5. STM image of the *n*-GaAs surface with a native oxide. Magnification is 1.6×10^4.

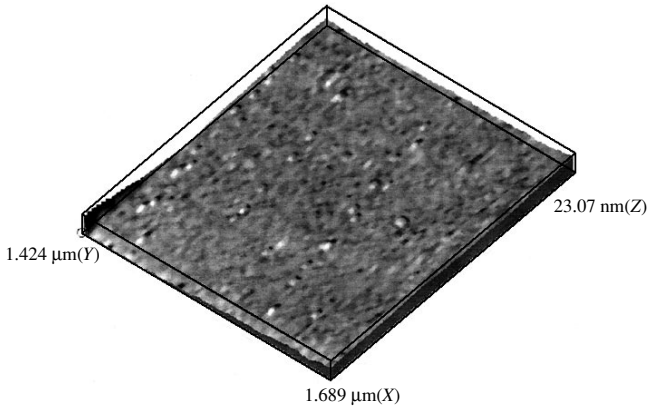

Fig. 6. STM image of the *n*-GaAs surface after etching off the native oxide. Magnification is 1.6×10^4.

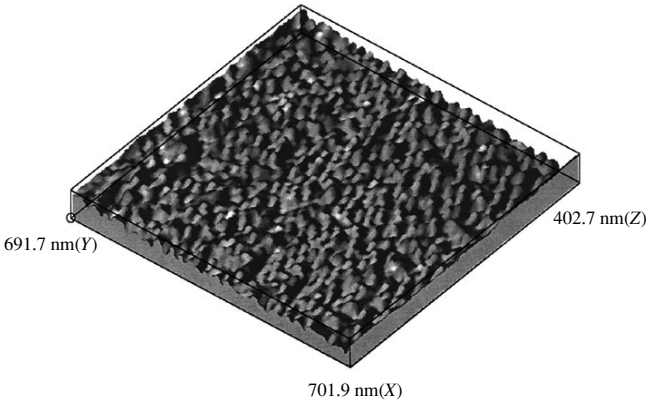

Fig. 7. STM image of the *n*-GaAs surface after etching off the SiO_2 film. Magnification is 3.2×10^4.

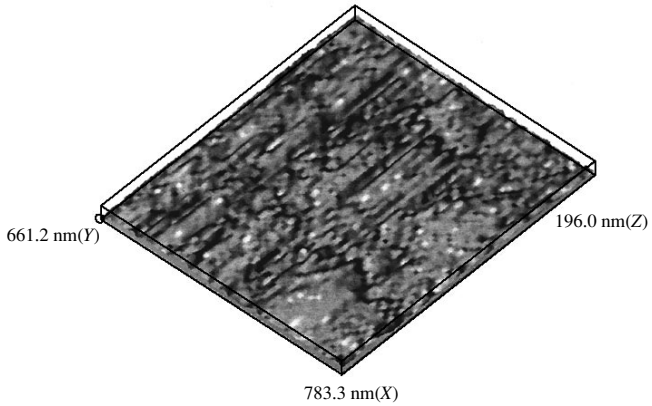

Fig. 8. STM image of the *n*-GaAs surface after etching off the SiO_2 film treated in atomic-hydrogen flow. Magnification is 3.2×10^4.

silicon-oxide film [14] on the *n*-GaAs surface, rather than to the diffusion of Si (due to the fairly low temperature maintained while depositing the SiO_2 layers). This assumption is confirmed by a modification of the surface relief of the semiconductor substrate following the deposition of the SiO_2 layers.

It is known that the buffer etchant (a solution of hydrofluoric acid) does not etch GaAs. Therefore, after the SiO_2 film is removed, the remaining relief of the GaAs surface must reflect the nature of the interaction between active elements of plasma and the semiconductor surface during the synthesis of the SiO_2 film. As can be seen from Fig. 7, the relief of the GaAs surface is appreciably roughened and acquires a certain quasi-periodicity that is indicative of a considerable reconstruction of the semiconductor surface during the process of synthesis of the SiO_2 film.

The smoother surface of GaAs following the treatment of the SiO_2–GaAs structures in the atomic-hydrogen flow (Fig. 8) can be explained by the formation of a thin layer with a high concentration of hydrogen at the insulator–semiconductor interface and in the near-surface region of GaAs [15]. This thin layer of hydrogenated GaAs has physical and chemical properties different from those of deeper layers. In particular, the rate of its chemical etching is lower than the GaAs etching rate. This surface layer, formed from low-mobility hydrogen molecules at interstitial sites of the GaAs lattice, acts as the diffusion barrier and can simultaneously interfere with the diffusion of hydrogen atoms both to the semiconductor and to the surface. This assumption is confirmed by the presence of peaks in the hydrogen distribution in the vicinity of the interface on the *n*-layer side.

5. CONCLUSION

On the basis of the analysis of experimental results, it was established that the presence of the SiO_2 film leads to a more efficient accumulation of hydrogen near the surface of the *n*-GaAs layer. The amount of hydrogen penetrating both into the insulator film and into the near-surface region of the semiconductor during the hydrogenation is determined by the relief of the protective film and decreases with increasing SiO_2-layer thickness. It was shown that the presence of the SiO_2 protective film leads to an appreciable modification of the morphology of the GaAs surface during treatment in the atomic-hydrogen flow. The deposition of the SiO_2 layer on the GaAs surface results in surface reconstruction consisting in the formation of a quasi-periodic relief on the semiconductor surface. However, in the course of treatment in atomic hydrogen, the GaAs surface covered by the SiO_2 protective film becomes smooth.

ACKNOWLEDGMENTS

We thank V.G. Bozhkova for assistance in carrying out the experiments and V.A. Kagadeĭ for treating the samples in atomic-hydrogen flow.

REFERENCES

1. A. Paccagnella, A. Callegari, E. Latta, and M. Gasser, Appl. Phys. Lett. **55**, 259 (1989).
2. U. K. Chakrabarti, S. J. Pearton, W. S. Hobson, *et al.*, Appl. Phys. Lett. **57**, 887 (1990).
3. S. J. Pearton, J. Electron. Mater. **14a**, 737 (1985).
4. V. L. Gurtovoĭ, V. V. Dremov, V. A. Makarenko, *et al.*, Fiz. Tekh. Poluprovodn. (St. Petersburg) **29**, 1888 (1995) [Semiconductors **29**, 986 (1995)].
5. J. Chevallier and M. Aucouturier, Annu. Rev. Mater. Sci. **18**, 219 (1988).
6. J. A. Schafer, V. Persch, S. Stock, *et al.*, Europhys. Lett. **12**, 563 (1990).
7. S. Balasubramanian, V. Kumar, and N. Balasubramanian, J. Appl. Phys. **74**, 4521 (1993).
8. V. G. Bozhkov, V. A. Kagadeĭ, and N. A. Torkhov, Fiz. Tekh. Poluprovodn. (St. Petersburg) **32**, 1343 (1998) [Semiconductors **32**, 1196 (1998)].
9. P. A. Arutyunov and A. L. Tolstikhina, Mikroélektronika **26**, 426 (1997).
10. V. S. Vavilov, V. F. Kiselev, and B. N. Mukashev, *Defects in the Bulk and at the Surface of Silicon* (Nauka, Moscow, 1990).
11. K. Suda and T. Hattory, Surf. Sci. **168**, 652 (1986).
12. Z. Yu. Gotra, *Reference Book on the Technology of Microelectronic Devices* (Kamenyar, Lvov, 1986).
13. S. A. Litvinenko, V. G. Litovchenko, and V. I. Sokolov, Optoélektron. Poluprovodn. Tekh., No. 9, 39 (1985).
14. L. V. Khramova, T. P. Smirnova, and E. G. Eremina, Neorg. Mater. **28**, 1662 (1992).
15. N. A. Torkhov and S. V. Eremeev, Fiz. Tekh. Poluprovodn. (St. Petersburg) **33**, 1209 (1999) [Semiconductors **33**, 1100 (1999)].

Translated by V. Bukhanov

Semiconductors, Vol. 34, No. 6, 2000, pp. 677–679. Translated from Fizika i Tekhnika Poluprovodnikov, Vol. 34, No. 6, 2000, pp. 704–706.

SEMICONDUCTOR STRUCTURES, INTERFACES, AND SURFACES

Photosensitivity of *a*-Si:H/*n*-InSe Heterocontacts

Yu. A. Nikolaev*, V. Yu. Rud', Yu. V. Rud'*, and E. I. Terukov***

** Ioffe Physicotechnical Institute, Russian Academy of Sciences, ul. Politekhnicheskaya 26, St. Petersburg, 194021 Russia*

*** St. Petersburg State Technical University, ul. Politekhnicheskaya 29, St. Petersburg, 195251 Russia*

Submitted December 21, 1999; accepted for publication December 21, 1999

Abstract—Rectifying photosensitive structures were obtained for the first time by bringing the surfaces of thin films of amorphous hydrogenated silicon deposited onto the silica-glass substrates into direct optical contact with the InSe natural-cleavage surface. Spectral dependences of the quantum efficiency of the obtained heterocontacts were studied, and the prospects for the use of the new *a*-Si:H/*n*-InSe heterocontacts in solar cells were assessed. © *2000 MAIK "Nauka/Interperiodica".*

Studies of the photoconversion processes in the structures based on amorphous hydrogenated silicon are motivated by hopes to reduce the cost of silicon solar cells [1]. At present, a selection of effective technologies for formation of thin films of amorphous and polycrystalline silicon (as well as the films of binary and ternary semiconductor compounds) with the aim of producing efficient photoconversion structures is under way [1–6]. This work pursues the above objective and is devoted to pioneering studies of photosensitivity of a contact between amorphous hydrogenated silicon (*a*-Si:H) and the InSe direct-gap semiconductor compound, the band gap of which is $E_g = 1.21$ eV at a temperature of $T = 300$ K [7].

In order to produce photosensitive structures based on *a*-Si:H films and InSe bulk crystals, we brought the surfaces of the above materials into direct optical contact [8, 9]. This method makes it possible to use semiconductors with the required characteristics; to eliminate any additional technological operations in forming the contact itself; and, thus, to avoid the changes in physical properties of the starting phases.

The *a*-Si:H films were prepared by the method of radio-frequency glow discharge. As an operating gas medium, we used a mixture of silane (12%) and hydrogen. The substrates were chemically cleaned silica-glass wafers ~0.1 mm thick; in the course of the film deposition, the substrate temperature was ~260°C. This temperature ensured that homogeneous *a*-Si:H films with a dark resistivity of $\rho \approx 10^9\ \Omega$ cm at room temperature were obtained. The actual parameters made it possible to obtain reproducibly the *a*-Si:H films that were homogeneous over the depth and had a specular surface with an area of $\sim 15 \times 15$ mm^2. For the thickness of ~1 μm, the *a*-Si:H films had a bright-red uniform coloring under the conditions of daylight illumination.

InSe single crystals were grown by planar crystallization of the melt that had a composition close to stoichiometric for the binary compound; in the case where there was no intentional doping, the films were of *n*-type, with a free-carrier concentration of $n \approx 10^{15}$ cm^{-3} and a resistivity of $\rho \approx 10^2\ \Omega$ cm at $T = 300$ K. A plane-parallel plate with perfect specular surfaces was obtained from the *n*-InSe single-crystal ingots by cleaving in atmospheric air [9, 10]. Average dimensions of the *n*-InSe platelets used in forming the heterocontacts were ~5 mm × 5 mm × 0.1 mm.

The heterocontacts are typically obtained by bringing one of the surfaces of the *n*-InSe platelet into direct contact with the outer as-grown surface of *a*-Si:H film. With the use of a special holder, this contact is fixed in such a way that a high stability of its photoelectric properties is attained. Schematic representation of the *a*-Si:H/*n*-InSe heterocontacts is shown in Fig. 1. A typical steady-state current–voltage characteristic of one of the heterocontacts obtained is shown in Fig. 2. It follows from Fig. 2 that the method of bringing the as-grown surface of *a*-Si:H film into direct contact with the *n*-InSe natural-cleavage surface makes it possible to produce rectifying structures. In such a type of heterocontact, the forward (conducting) direction corresponds to the negative polarity of external bias voltage applied to the *n*-InSe platelet. It also follows from

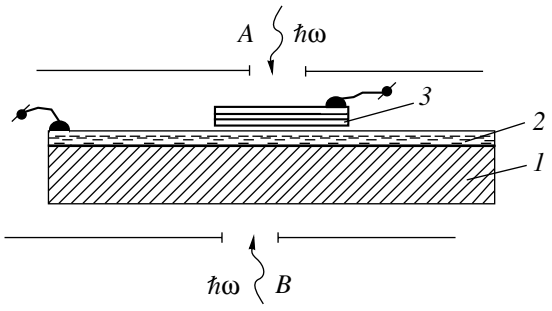

Fig. 1. Schematic representation of a *a*-Si:H/*n*-InSe heterocontact: (*1*) the silica-glass substrate, (*2*) the *a*-Si:H film, and (*3*) InSe.

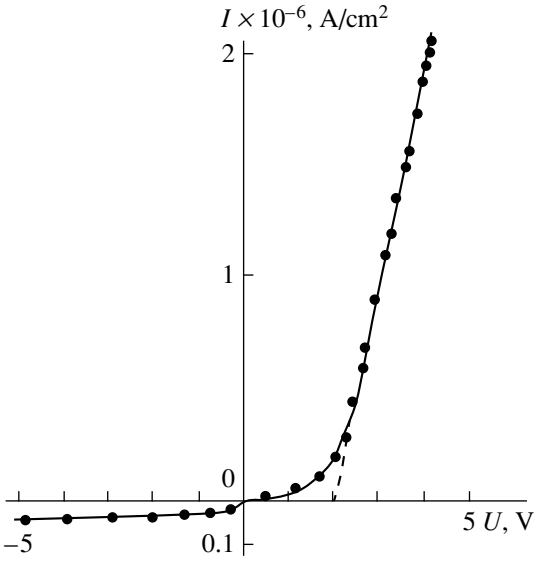

Fig. 2. A steady-state current–voltage characteristic of an *a*-Si:H/*n*-InSe heterocontact. T = 300 K. The heterocontact area is ~0.25 cm^2, and the conducting (forward) direction corresponds to the positive polarity of the external-bias voltage applied to *a*-Si:H.

Fig. 2 that, for the forward-bias voltages of $U > 2.5$ V, the current–voltage characteristic $I(U)$ of *a*-Si:H/*n*-InSe structures is described by the law $U = U_0 + R_0 I$. For all the structures obtained, the value of the cutoff voltage is $U_0 \approx 2$ V and the on resistance is $R_0 \approx 10^7$ Ω at T = 300 K. It follows from the comparison of electrical properties of the contacting materials that the high value of R_0 is largely defined by electrical properties of *a*-Si:H films. For all the heterocontacts obtained, the reverse current–voltage characteristic typically follows the power law $I \sim U^m$ (m = 0.7–1); the reverse current increases with increasing bias voltage, which can be due to imperfections at the heterocontact periphery and to the corresponding influence of the leakage currents. It is noteworthy that the parameters of the current–voltage characteristics are fairly stable in time; i.e., there are no pronounced processes of degradation.

The photovoltaic effect was observed in the obtained *a*-Si:H/*n*-InSe heterostructures if they were illuminated from the sides of either of the two materials (Fig. 1, configurations *A* and *B*). In this case, the sign of photovoltage was found to be the same under both conditions of illumination of these structures, did not change if the light probe ~0.2 mm in diameter was moved over the surface, and was retained in the entire range of photosensitivity. The aforementioned special features suggest that the separation of photogenerated charge carriers in such structures occurs in a single active region that originates as a result of the formation of the optical contact between *a*-Si:H and *n*-InSe. In all such heterocontacts, the polarity of photovoltage corresponds to the sign "+" at *a*-Si:H, which is consistent with the direction of rectification. The photosensitivity of *a*-Si:H/*n*-InSe structures is higher if the structure is illuminated from the side of the wide-gap material and amounts to 1–5 V/W at T = 300 K in samples of the highest quality. The above value is well reproduced if the position of the InSe platelet ~1 × 1 mm^2 in area is shifted over the *a*-Si:H surface, which indicates that the *a*-Si:H films are fairly homogeneous. It is also important that, in such structures, the photovoltaic effect (like the current–voltage characteristics) does not exhibit any indications of degradation.

Typical spectral dependences of relative quantum efficiency of photoconversion η determined from the ratio of the short-circuit photocurrent to the number of incident photons are shown in Fig. 3 for two different geometrical characteristics of illuminating an *a*-Si:H/*n*-InSe structure. Only the long-wavelength edge of the spectrum is insensitive to the geometry of illumination, which is caused by the fact that the light is absorbed in the bulk in this spectral region. The spectral position of the long-wavelength exponential edge of η and a feature in the form of a peak (Fig. 3, curve *2*) or a step (Fig. 3, curve *1*) are consistent with the InSe band gap [6, 8]; in addition, a steep slope of the edge $S = \delta(\ln\eta)/\delta(\hbar\omega) \approx 40$ eV^{-1} in various structures is related to direct band-to-band optical transitions in the above compound. In the case where the heterostructure is illuminated from the side of InSe, we observe a sharp falloff of photosensitivity with increasing energy of incident photons ($\hbar\omega > 1.21$ eV), which is caused by the influence of the radiation absorption in the narrow-gap material; at the same time, in the case of illumination from the side of the wide-gap material (*a*-Si:H), this falloff of η is found to be appreciably shifted to shorter wavelengths (deep within the fundamental-absorption region of InSe; see Fig. 3, curves *1*, *2*).

In geometry *B* of illumination (Fig. 1), the full width of the photosensitivity spectra at half maximum is $\delta_{1/2} \approx$ 50–60 meV for the thickness range of the structures used, whereas a transition to geometry *B* is accompanied with a substantial increase in $\delta_{1/2}$ to the values of 700–750 meV. In this case, the sharp short-wavelength falloff of the photosensitivity is located in the vicinity of 2 eV, which corresponds to band-to-band transitions in *a*-Si:H [2]. Consequently, the photosensitivity of *a*-Si:H/*n*-InSe heterocontacts illuminated from the side of the wide-gap material remains at a high level in the spectral range limited by the band gaps of the phases in contact; this is similar to what is observed in the case of ideal abrupt heterojunctions [11, 12]. In turn, this suggests that the differences between the structures of contacting semiconductors are noncritical under conditions of direct contact; in this case, we consider the contact between amorphous hydrogenated silicon and the natural-cleavage surface of InSe crystal with the wurtzite structure [6].

A special feature of *a*-Si:H/*n*-InSe heterostructures studied is a distinct series of six equidistant peaks in the

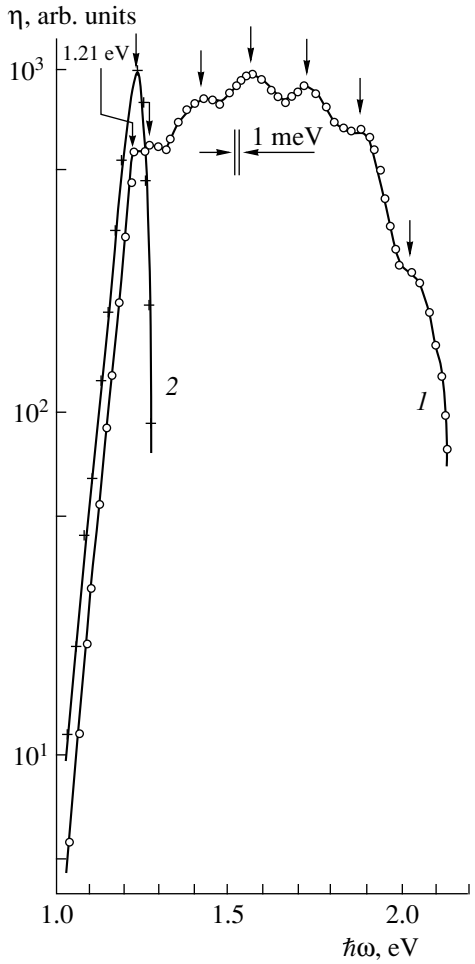

Fig. 3. Spectral dependences of relative quantum efficiency of photoconversion for an *a*-Si:H/*n*-InSe heterocontact: (*1*) illumination from the side of *a*-Si:H (geometry *A*) and (*2*) illumination from the side of InSe (geometry *B*). T = 300 K.

region of high photosensitivity of heterocontacts. If we relate these peaks to the interference of radiation in the *a*-Si:H wide-gap film, the estimation of the film thickness on the basis of positions of the peaks yields the value of ~1 μm, which is consistent with the results of measurements of the film thickness by other methods. The very presence of the structure in the photosensitivity spectra, along with the fact that the dependence $\eta(\hbar\omega)$ is broadband, should be considered as an indication of the fairly high structural perfection of photosensitive structures based on *a*-Si:H films brought into direct contact with InSe. This result makes it possible to consider as promising, from the standpoint of the study of the new heterocontacts, the quick-procedure approach to the formation of new heterocontacts by bringing the semiconductor materials into direct contact. In the case that certain practical potentialities are found on the basis of these results, efforts could be made to develop the technology for formation of permanent heterostructures based on such materials. In this case, it is obvious that technological development of permanent heterostructures based on *a*-Si:H as a wide-gap semiconductor and on InSe as a narrow-gap material with high absorptivity of radiation within the entire solar spectrum may result in the development of high-efficiency thin-film solar cells.

REFERENCES

1. *Polycrystalline Semiconductors V–Bulk Materials, Thin Films and Devices*, Ed. by J. H. Werner, H. P. Strunk, and H. W. Schock (Scitec. Publ., Zuerich, 1999).
2. *Amorphous and Microcrystalline Semiconductor Devices*. Vol. 2: *Materials and Devices Physics*, Ed. by J. Kanicki (Artech House, Boston, 1992).
3. W. Wang and K. Liao, Mater. Res. Soc. Symp. Proc. **70**, 359 (1986).
4. R. DeRosa, M. L. Grilli, G. Sosikala, *et al.*, Solid State Phenom. **67/68**, 565 (1999).
5. B. Sang, K. Daiziki, A. Yamada, and M. Konagai, Jpn. J. Appl. Phys. **38**, 4983 (1999).
6. *Physicochemical Properties of Semiconductors: A Reference Book* (Nauka, Moscow, 1979).
7. I. V. Bodnar, V. Yu. Rud', and Yu. V. Rud', Cryst. Res. Technol. **31**, 261 (1996).
8. V. Yu. Rud', V. F. Gremenok, Yu. V. Rud', *et al.*, Fiz. Tekh. Poluprovodn. (St. Petersburg) **33**, 1205 (1999) [Semiconductors **33**, 1097 (1999)].
9. F. Adduci, M. Ferrara, P. Tantalo, and A. Cingolani, Phys. Status Solidi A **15**, 303 (1973).
10. N. M. Mekhtiev, Yu. V. Rud', and É. Yu. Salaev, Fiz. Tekh. Poluprovodn. (Leningrad) **12**, 1566 (1978) [Sov. Phys. Semicond. **12**, 924 (1978)].

Translated by A. Spitsyn

Semiconductors, Vol. 34, No. 6, 2000, pp. 680–685. Translated from Fizika i Tekhnika Poluprovodnikov, Vol. 34, No. 6, 2000, pp. 707–711.

SEMICONDUCTOR STRUCTURES, INTERFACES, AND SURFACES

Surface Magnetoplasma Waves in a Ferromagnetic Semiconductor and their Excitation by a Magnetic Dipole

V. L. Fal'ko, S. I. Khankina, and V. M. Yakovenko

Usikov Institute of Radio Physics and Electronics, National Academy of Sciences of Ukraine, ul. Proskury 12, Kharkov, 310085 Ukraine

Submitted November 26, 1999; accepted for publication December 29, 1999

Abstract—Natural oscillations of an electromagnetic field at the boundary of free space with a ferromagnetic semiconductor are studied. The corresponding dispersion law and the domain of existence are determined. It is shown that these oscillations can be excited by a magnetic dipole located above the surface of the conducting medium. The fields and energy-flux density of surface waves in free space are calculated. © *2000 MAIK "Nauka/Interperiodica".*

1. For many years, consistent attention has been drawn to magnetic conducting materials, in particular, to ferromagnetic semiconductors [1–4], because of their unique properties. Many of these properties can be used and are already used in practical applications, such as those related to various systems for data processing, delay lines, filters, and new components for integrated circuits. Undoubtedly, magnetic semiconductors deserve attention also from the general physical standpoint, because, in these materials, quasiparticles of a new type are formed, phase separation occurs in the ground state, magnetoresistance exhibits specific properties, and so on. Physical processes occurring at the surface should be taken into account when microstructures are formed on the basis of the materials under consideration. These processes include also the effects related to special features of excitation and propagation of the surface electromagnetic waves.

2. In a series of works (see references in [5]), it was theoretically and experimentally shown that the slow magnetoplasma waves existed in a magnetic field at the boundary between the conducting medium and free space; these are surface helicons. They come into existence in strong magnetic fields if the electrical conductivity of a semiconductor is the highest along the magnetic field. It is assumed that the total current (composed of the displacement and conduction currents) in the direction transverse to the magnetic field is small compared to the longitudinal total current. In the reference frame with the *OZ*-axis parallel to the magnetic-field vector $\mathbf{H}_0$ and the *OY*-axis directed along the normal to the interface between the media (the semiconductor occupies the half-space with $y < 0$), the following inequalities hold for the components of the permittivity tensor $\varepsilon_{ik}(\omega)$ of the semiconductor:

$$|\varepsilon_{zz}| \gg |\varepsilon_{xy}| \gg |\varepsilon_{xx}|, \tag{1a}$$

$$|\varepsilon_{zz}\varepsilon_{xx}| \gg |\varepsilon_{xy}^2|. \tag{1b}$$

Here, ω is the wave frequency. Such conditions are met, for example, in a two-component plasma if the density and mass of electrons differ appreciably from those of holes. The spectrum of the surface helicons $\omega(\mathbf{k})$ is defined by the Hall component of the permittivity ε_{xy} and is determined from the equation

$$k_z^2 = -\frac{i\varepsilon_{xy}}{2}\operatorname{sgn} k_x \frac{\omega^2}{c^2} \quad (k_x^2 \gg k_z^2). \tag{2}$$

Evidently, the wave propagates only if

$$(+i\varepsilon_{xy}\operatorname{sgn} k_x) < 0, \tag{3}$$

and its frequency is given by

$$\omega = 2\frac{k_z^2 c^2 |\omega_{H\alpha}|}{\omega_{0\alpha}^2}, \tag{4}$$

where $\omega_{0\alpha}$ and $\omega_{H\alpha}$ are the plasma and cyclotron frequencies of the charge carrier that gives the largest contribution to the Hall conduction.

Attenuation of the surface helicons is caused by the permittivity component ε_{xx} and, as follows from conditions (1a), is much less than the frequency defined by (4).

In these waves, the magnetic-field components are larger than the electric-field components, with $E_z \cong 0$. We note that surface helicons exist in a limited range of angles given by

$$1 < \tan^2\vartheta \sin^2\vartheta \cos^2\vartheta \gg \frac{\omega_0^4}{c^4 k^4}\frac{\omega^2}{\omega_H^2}, \tag{5}$$

where ϑ is the angle of the vector $\mathbf{H}_0$ with the vector $\mathbf{k}_\perp = (k_x, 0, k_z)$. The first condition in (5) specifies the angle range of $\pi/4 + n\pi < \vartheta < 3\pi/4 + n\pi$ ($n = 0, 1$), and the second condition excludes the vicinities of the angles $\vartheta = \pi/2 + n\pi$ from consideration.

1063-7826/00/3406-0680$20.00

Since the slowly attenuated surface helicons exist in a wide range of frequencies

$$\omega_{H\alpha} \gg \omega, \quad (6)$$

and their phase velocities are controlled by the magnitude of external magnetic field $\mathbf{H}_0$, these helicons can interact with various waves (such as the spin and sonic waves) and also with electron beams.

It is noteworthy that the characteristics of propagation of these waves are defined not only by the properties of the semiconductor but also by those of the bordering medium. In [6], coupled surface helicon–spin waves that originated at the interface between the semiconductor and ferrite were observed. An interaction of helicons with an electron subsystem of ferrite near the interface causes the frequency of generated oscillations to change appreciably; this frequency is found to depend on both the Hall component ε_{xy} and the components of the ferrite's permeability tensor $\mu_{ik}(\omega)$. The equation for the surface waves at the semiconductor–ferrite boundary is written as [6]

$$k_z^2 = -i\varepsilon_{xy}\frac{\omega^2}{c^2}\operatorname{sgn}k_x\frac{\mu_{xx} + i\operatorname{sgn}k_x\mu_{xy}}{1 + \mu_{xx} + i\operatorname{sgn}k_x\mu_{xy}}, \quad (7)$$

where the components $\mu_{ik}(\omega)$ are given by

$$\mu_{xx} = \mu_{yy} \equiv \mu = 1 + \frac{\omega_g\omega_M}{\omega_g^2 - \omega^2}; \quad \mu_{zz} = 1;$$
$$\mu_{xy} = -\mu_{yx} = \frac{i\omega\omega_M}{\omega_g^2 - \omega^2}, \quad (8)$$
$$\mu_{xz} = \mu_{zx} = \mu_{yz} = \mu_{zy} = 0.$$

Here,

$$\omega_g = g(H_0 + \beta M); \quad \omega_M = 4\pi g M;$$

g is the magnetomechanical ratio; and β is the anisotropy constant. The magnetic field $\mathbf{H}_0$ is aligned with the anisotropy axis and coincides with the direction of the equilibrium magnetic moment $\mathbf{M}$ of the ferromagnet.

It can be shown that the domain of existence of wave (7) differs from that of surface helicon (4). Indeed, substituting expression (8) into equation (7), we arrive at

$$k_z^2 = -\frac{i\varepsilon_{xy}}{2}\operatorname{sgn}k_x\frac{\omega^2}{c^2}\frac{\omega_g + \omega_M + \operatorname{sgn}k_x\omega}{\omega_g + \frac{\omega_M}{2} + \operatorname{sgn}k_x\omega}. \quad (9)$$

We now consider a semiconductor for which the inequality $i\varepsilon_{xy} < 0$ is valid. In the configuration where $k_x > 0$, surface wave (9) exists for any frequencies $\omega < \omega_H$. In the case where $k_x < 0$, the transparency band for these waves is specified as

$$\omega_g + \frac{\omega_M}{2} < \omega < \omega_g + \omega_M \quad (i\varepsilon_{xy} < 0, k_x < 0) \quad (10)$$

(outside this band, we have $k_z^2 < 0$). In n-type semiconductors ($i\varepsilon_{xy} < 0$), a surface wave cannot exist for $k_x > 0$. In such semiconductors, the wave exists for k_x outside the frequency range (10), i.e., for the frequencies satisfying the following inequalities:

$$\omega < \omega_g + \frac{\omega_M}{2} \text{ and } \omega < \omega_g + \omega_M \quad (i\varepsilon_{xy} > 0, k_x < 0). \quad (11)$$

Attenuation of the surface wave (7), like that of surface helicon (2), is related to the component ε_{xx}.

3. In this paper, we consider a structure composed of a magnetic semiconductor with two types of charge carriers (medium 1, $y < 0$) and free space (medium 2, $y > 0$). Propagation of the waves in medium 1 is described by a system of equations including the Maxwell equations and constitutive equations that define the relation between the fields $\mathbf{E}^{(1)}$ and $\mathbf{H}^{(1)}$ and the inductions $\mathbf{D}^{(1)}$ and $\mathbf{B}^{(1)}$. In terms of the Fourier components, the constitutive equations (without considering the spatial dispersion) have the following form: $D_i^{(1)} = \varepsilon_{ik}(\omega)E_k^{(1)}$ and $B_i^{(1)} = \mu_{ik}(\omega)H_k^{(1)}$. The permittivity-tensor components of a ferromagnetic semiconductor are given by

$$\varepsilon_{xx} = \varepsilon_{yy} = \varepsilon - \sum_\alpha \frac{\omega_{0\alpha}^2(\omega + i\nu_\alpha)}{\omega[(\omega + i\nu_\alpha)^2 - \omega_{H\alpha}^2]},$$
$$\varepsilon_{xy} = -\varepsilon_{yx} = -\sum_\alpha \frac{i\omega_{0\alpha}^2\omega_{H\alpha}}{\omega[(\omega + i\nu_\alpha)^2 - \omega_{H\alpha}^2]}, \quad (12)$$
$$\varepsilon_{zz} = \varepsilon_0 - \sum_\alpha \frac{\omega_{0\alpha}^2}{(\omega + i\nu_\alpha)\omega};$$

the permeability-tensor components are given by formulas (8). If conditions (1a) are met, two waves propagate in the magnetic semiconductor; normal components of the wave vector for these waves are defined as

$$k_{y1}^2 = -k_x^2 - \frac{k_z^2}{\mu} - \frac{\omega^4}{c^4k_z^2}\varepsilon_{xy}^2\frac{\mu^2 + \mu_{xy}^2}{\mu} - 2\frac{\mu_{xy}}{\mu}\frac{\omega^2}{c^2}\varepsilon_{xy}, \quad (13)$$

$$k_{y2}^2 = -\frac{\varepsilon_{zz}}{\varepsilon_{xx}}\left(k_z^2 - \frac{\omega^2}{c^2}\varepsilon_{xx}\frac{\mu^2 + \mu_{xy}^2}{\mu}\right) \quad (14)$$

(if we assume that $\mu = 1$ and $\mu_{xy} = 0$ in (13) and (14), we obtain the magnitudes of normal components of the wave vectors for the ordinary and extraordinary waves in a conventional semiconductor). The components of the fields in these waves are related by the following formulas.

For wave 1 (13), we have

$$H_{x1} = \frac{H_{y1}}{\Delta}\Big[-k_x(k_x\mu_{xy}+k_{y1}\mu)+\frac{\omega^2}{c^2}(\mu_{xy}\varepsilon_{xx}+\mu\varepsilon_{xy}) + \frac{k_x}{\varepsilon_{zz}}(k_{y1}\varepsilon_{xx}-k_x\varepsilon_{xy})\Big],$$

$$H_{z1} = \frac{H_{y1}}{k_z\Delta}\Big\{-k_z^2(k_x\mu_{xy}+k_{y1}\mu)+(k_{y1}\varepsilon_{xx}-k_x\varepsilon_{xy}) \times\Big[\frac{\omega^2}{c}(\mu^2+\mu_{xy}^2)-\frac{\mu}{\varepsilon_{zz}}(k_x^2+k_{y1}^2)\Big]\Big\},$$

$$E_{z1} = -\frac{c}{\omega\varepsilon_{zz}}(k_xH_{y1}-k_{y1}H_x), \quad (15)$$

$$E_{x1} = -\frac{k_xc(k_xH_{y1}-k_{y1}H_{x1})}{k_z\omega\varepsilon_{zz}}+\frac{\omega}{k_zc}(-\mu_{xy}H_{x1}+\mu H_{y1}),$$

$$E_{y1} = -\frac{k_yc(k_xH_{y1}-k_{y1}H_{x1})}{k_z\omega\varepsilon_{zz}}-\frac{\omega}{k_zc}(\mu H_{x1}+\mu_{xy}H_{y1}),$$

$$\Delta = k_x(k_x\mu-k_{y1}\mu_{xy})+k_z^2 - \frac{\omega^2}{c^2}(\mu\varepsilon_{xx}-\mu_{xy}\varepsilon_{yy})+\frac{k_{y1}}{\varepsilon_{zz}}(k_{y1}\varepsilon_{xx}-k_x\varepsilon_{xy}).$$

It is noteworthy that we may ignore ε_0 in the diagonal components of tensor ε_{ik} in view of the smallness of the displacement current compared to the conduction current.

For wave 2 (14), we have

$$H_{x2} = -\frac{k_{yz}}{k_x}H_{y2}, \quad H_{z2} = -\frac{\varepsilon_{xy}}{\varepsilon_{xx}}\frac{k_z}{k_x}H_{y2},$$

$$E_{x2} = \frac{k_zc}{\omega\varepsilon_{xx}}H_{y2}, \quad E_{y2} = \frac{k_{y2}}{k_x}E_{x2}, \quad (16)$$

$$E_{z2} = \frac{k_z^2-\frac{\omega^2}{c^2}\varepsilon_{xx}}{k_x\varepsilon_{xx}}\frac{c}{\omega}H_{y2}.$$

In free space, the waves split into *H*-waves ($E_z = 0$) and *E*-waves ($H_z = 0$).

For an *H*-wave, we have

$$E_{x1}^{(2)} = \frac{k_x}{k_{y0}}H_{y1}^{(2)}, \quad H_{z1}^{(2)} = -\frac{k_x^2+k_{y0}^2}{k_{y0}k_z}H_{y1}^{(2)},$$
$$E_{z1}^{(2)} = 0, \quad E_{x1}^{(2)} = \frac{\omega}{ck_z}H_{y1}^{(2)}, \quad E_{y1}^{(2)} = -\frac{k_x}{k_zk_{y0}}\frac{\omega}{c}H_{y1}^{(2)}. \quad (17)$$

For an *E*-wave, we have

$$H_{z2}^{(2)} = 0, \quad H_{x2}^{(2)} = -\frac{k_{y0}}{k_x}H_{y2}^{(2)},$$

$$E_{z2}^{(2)} = -\frac{c}{\omega}\frac{(k_x^2+k_{y0}^2)}{k_x}H_{y2}^{(2)}, \quad E_{x2}^{(2)} = -\frac{k_zc}{\omega}H_y^{(2)}, \quad (18)$$

$$E_{y2}^{(2)} = -\frac{k_zk_{y0}}{k_x}\frac{c}{\omega}H_{y2}^{(2)}, \quad k_{y0}^2 = -k_x^2-k_z^2+\frac{\omega^2}{c^2}.$$

For the boundary conditions at the plane $y = 0$, we choose the conditions for continuity of tangential components of magnetic and electric fields and also for continuity of the normal component of the magnetic-induction vector. Substituting formulas (15)–(18) into the boundary conditions, we obtain expressions that define the spectrum and attenuation of the surface waves at the interface between the magnetic semiconductor and free space. The surface waves propagating in the *XOZ* plane come into existence if the following conditions are satisfied:

$$k_x^2 > \frac{k_z^2}{\mu}, \quad \frac{\omega^4}{c^4k_z^2}\varepsilon_{xy}^2\frac{\mu^2+\mu_{xy}^2}{\mu}, \quad \frac{\mu_{xy}}{\mu}\frac{\omega^2}{c^2}\varepsilon_{xy}. \quad (19)$$

The spectrum of uncoupled "oblique" surface waves is defined by the following equation:

$$k_z^2 = k_{z0}^2 \equiv -i\frac{\omega^2}{c^2}\varepsilon_{xy}\operatorname{sgn}k_x \times\frac{(\mu-i\mu_{xy}\operatorname{sgn}k_x)(1-i\mu_{xy}\operatorname{sgn}k_x)}{1+\mu-i\mu_{xy}\operatorname{sgn}k_x}. \quad (20)$$

Attenuation of a coupled helicon–spin wave [as in the case of surface helicon (4)] is proportional to the effective collision frequency of charge carriers. Substituting the values of tensor components μ_{ik} (8) into (20), we have

$$k_z^2 = k_{z0}^2 \equiv i\frac{\omega^2}{c^2}\frac{\varepsilon_{xy}}{2}\operatorname{sgn}k_x \times\frac{(\omega_g+\omega_M-\omega\operatorname{sgn}k_x)(\omega-\omega_1)(\omega+\omega_2)}{\Big(\omega_g+\frac{\omega_M}{2}-\omega\operatorname{sgn}k_x\Big)(\omega_g^2-\omega^2)}, \quad (21)$$

where $\omega_{1,2} = \sqrt{\omega_g^2+\frac{\omega_M^2}{4}} \pm \frac{\omega_M}{2}\operatorname{sgn}k_x$. In *p*-type semiconductors ($i\varepsilon_{xy} < 0$), the waves with the following frequencies propagate along the *OX*-axis ($k_x < 0$ and, consequently, $\omega_1 < \omega_g$):

$$\omega_1 < \omega < \omega_g\Big(\frac{5\pi}{4} < \vartheta < \frac{7\pi}{4}\Big), \quad (i\varepsilon_{xy} < 0). \quad (22)$$

For $k_x > 0$, the conditions $\omega_g + \frac{\omega_M}{2} < \omega_1 < \omega_g + \omega_M$ are met for ω_1; thus, hybrid waves (21) can exist in the three frequency ranges; i.e.,

$$\begin{gathered} 0 < \omega < \omega_g; \quad \omega_g + \frac{\omega_M}{2} < \omega + \omega_1; \\ \omega > \omega_g + \omega_M\left(\frac{\pi}{4} < \vartheta < \frac{3\pi}{4}\right), \quad (i\varepsilon_{xy} < 0). \end{gathered} \tag{23}$$

In *n*-type semiconductors ($i\varepsilon_{xy} > 0$), the following transparency bands appear for the surface waves:

for $k_x < 0$,

$$\begin{gathered} 0 < \omega < \omega_1 \quad \text{and} \quad \omega > \omega_g, \\ \left(i\varepsilon_{xy} > 0, \quad \frac{5\pi}{4} > \vartheta > \frac{7\pi}{4}\right), \end{gathered} \tag{24}$$

and for $k_x > 0$,

$$\begin{gathered} \omega_g < \omega < \omega_g + \frac{\omega_M}{2}, \quad \omega_1 < \omega < \omega_g + \omega_M, \\ \left(i\varepsilon_{xy} > 0, \quad \frac{\pi}{4} < \vartheta < \frac{3\pi}{4}\right). \end{gathered} \tag{25}$$

Thus, the magnetic properties of a semiconductor affect the surface-wave frequency. As a result, a coupled helicon–spin wave originates and (as distinct from the surface silicon) propagates in certain transparency bands within the frequency region of $\omega \ll \omega_H$ rather than in the entire frequency region. The characteristics of the coupled helicon–spin waves in the semiconductor–ferrite structures differ from those in the structures composed of a magnetic semiconductor and free space.

In the former structure, the interaction of the magnetic subsystem in the ferrite with conduction electrons in the semiconductor occurs in a narrow region in the vicinity of the boundary $y = 0$. In the latter structure, the interaction between the magnetic and electronic subsystems occurs in the entire volume of the semiconductor (in the half-space defined by $y < 0$).

We now dwell briefly on the magnetic semiconductors for which condition (1) is valid for the tensor components $\varepsilon_{ik}(\omega)$ and for which the following equality also holds:

$$\varepsilon_{xx}\varepsilon_{zz} = \varepsilon_{xy}^2. \tag{26}$$

We note first of all that the surface helicon-spin waves do not exist if equality (26) is valid. However, "oblique" pseudosurface waves appear if the following inequalities are valid:

$$\varepsilon_0\omega_H^2 < \omega_0^2 < \frac{|\omega_H k_x k_z|}{\omega}c^2. \tag{27}$$

The dispersion relation for these waves is defined by the equation

$$\begin{gathered} 1 + \mu - \mu_{xy}\operatorname{sgn}k_x = -i\frac{\omega^2}{c^2} \\ \times \frac{|\varepsilon_{xy}|(\mu - i\mu_{xy}\operatorname{sgn}k_x)(1 - i\mu_{xy}\operatorname{sgn}k_x)}{k_z|k_x|}. \end{gathered} \tag{28}$$

The solution to equation (28) exists only for $k_x > 0$. The wave frequency coincides with the frequency of the Damon–Eshbach surface waves [4]

$$\omega_{\mathrm{DE}} = \omega_g + \frac{\omega_M}{2}, \tag{29}$$

while attenuation is noncollisional and is caused by propagation time lag in the semiconducting medium:

$$\gamma = \frac{\omega_M^2\omega_0^2}{|k_x k_z|c^2|\omega_H|}\frac{\omega_{\mathrm{DE}}}{16\left(\omega_g + \frac{\omega_M}{4}\right)}. \tag{30}$$

The mechanism of origination of this attenuation is related to the following factors. In the semiconductor, one of the partial waves, namely, the wave with the wave-number component k_{y2} ($\mathrm{Re}\,k_{y1} < 0$ and $\mathrm{Im}\,k_{y2} < 0$), is a bulk wave in the region of high frequencies $\omega > \nu$ if conditions (26) and (27) are satisfied. This wave carries away a part of the wave energy from the surface to the bulk of the conducting medium. A similar effect was predicted in [7], in which a ferrodielectric–semiconductor structure was considered.

4. In this section, we consider the excitation of hybrid helicon–spin waves (20) and (21) by an emitter located at a finite distance from the planar interface between two media (free space and a ferromagnetic semiconductor). Since we are interested in waves of the magnetic type (in such waves, the electric-field components are small), a magnetic dipole should be chosen as the emitter. The latter is located in free space ($y > 0$) at a distance a from the surface $y = 0$. In fact, all the known magnetic dipoles belong to the above type and constitute a current loop whose size is small compared to the wavelength. The current $\mathbf{J}^{\nu}(\mathbf{r}, t)$ in the loop can be defined as

$$\mathbf{J}^{(\nu)}(\mathbf{r}, t) = \mathbf{j}_0\delta(x)\delta(y - a)\delta(z)e^{-i\omega t}, \tag{31}$$

$$\mathbf{j}_0 = (j_{0x}, j_{0y}, 0). \tag{32}$$

The magnetic moment of the dipole under consideration is directed along the *OZ*-axis.

A system of field equations for free space is written as

$$\operatorname{curl}\mathbf{E} = 0, \quad \operatorname{curl}\mathbf{H} = \frac{4\pi}{c}\mathbf{J}^{(\nu)}; \quad \operatorname{div}\mathbf{H} = 0 \tag{33}$$

and can be reduced to the following inhomogeneous field equation:

$$\Delta \mathbf{H} = -\frac{3\pi}{c}\mathrm{curl}\mathbf{J}^{(\mathrm{v})}. \tag{34}$$

A solution to equation (34) is given by the sum of two terms; i.e.,

$$H_i^{(\mathrm{v})} = \int_{-\infty}^{\infty}\int dk_x dk_z A_i(k_x, k_z) e^{i(k_x x + k_{y0} y + k_z z - \omega t)}$$

$$-\frac{1}{2\pi^2}\int_{-\infty}^{\infty}\int\int dk_x dk_y dk_z e^{i[k_x x + k_y (y-a) y + k_z z - \omega t]} \tag{35}$$

$$\times \frac{F_i(\mathbf{k})}{k_x^2 + k_y^2 + k_z^2} \quad (i = x, y, z),$$

where $k_{y0} = ik_\perp$, $k_\perp = \sqrt{k_x^2 + k_z^2}$;

$$F_x = \frac{ik_z}{c} j_{0y}, \quad F_y = -\frac{ik_z}{c} j_{0x},$$
$$F_z = -\frac{i}{c}(k_x j_{0y} - k_y j_{0x}). \tag{36}$$

The first term in (35) is a solution to a homogeneous Laplace equation, whereas the second term is a solution to an inhomogeneous equation and defines the waves that propagate from the source. In the second term in (35), the major contribution to the integral of k_y is given by the poles $k_y = ik_\perp$ for $y > a$ and $k_y = -ik_\perp$ for $y < a$ (the poles are chosen from the condition for attenuation of the field at $y = \pm\infty$). The components of the vector $\mathbf{A}$ are related by the formulas

$$A_x = \frac{k_x}{k_{y0}} A_y, \quad A_z = \frac{k_z}{k_{y0}} A_y. \tag{37}$$

We can use the boundary conditions for $y = 0$ to express the unknown coefficients $A_i(k_x, k_z)$ in terms of the given parameters of the dipole and to determine the field of the electromagnetic wave reflected to free space H_i^{ref} [the first term in (35)]. In the general form, these expressions are very cumbersome. The vanishing determinant of a system of equations for A_i corresponds to the dispersion relation for natural surface waves in a system of free space and a ferromagnetic semiconductor (see (20) and (21)). For these waves, we have

$$A_y(k_x, k_z) = -\frac{i}{2\pi} e^{-k_{\perp a}} \frac{P(k_x, k_z)}{k_\perp^2 - k_{\perp 0}^2}, \tag{38}$$

$$P(k_x, k_z) = P(k_\perp, \vartheta)$$

$$= \frac{i}{\cos\vartheta \sin^2\vartheta k_\perp c[1 + (\mu - i\,\mathrm{sgn}\,k_x \mu_{xy})]}$$

$$\times \left\{ -\mu(k_x j_{0y} + ik_\perp j_{0x})\left[k_x^2 + \frac{\omega^2}{c^2}\varepsilon_{xy}\frac{\mu_{xy}}{\mu + i\,\mathrm{sgn}\,k_x \mu_{xy}}\right] \right. \tag{39}$$

$$\left. + \frac{\omega^2}{c^2}\varepsilon_{xy} k_x (\mu - i\,\mathrm{sgn}\,k_x \mu_{xy})(\mu_{xy} j_{0y} - j_{0x}) \right\},$$

where $k_{\perp 0}^2 = k_{z0}^2/\cos^2\vartheta$.

It is convenient to calculate the field $H_i^{(\mathrm{ref})}(\mathbf{r})$ in a cylindrical coordinate system (ρ, ϑ, y), in which case $x = \rho\sin\vartheta$ and $z = \rho\cos\vartheta$. The field $H_y^{(\mathrm{ref})}(\mathbf{r})$ can be then given by

$$H_y^{(\mathrm{ref})}(\mathbf{r}, t) = -\frac{ie^{-i\omega t}}{2\pi}\int_0^\infty k_\perp dk_\perp \int_0^{2\pi} \frac{d\vartheta' P(k_{\perp,\vartheta'})}{k_\perp^2 - k_{\perp 0}^2(\vartheta')} \tag{40}$$
$$\times \exp\{-k_\perp(y + a) + ik_\perp \rho\cos(\vartheta' - \vartheta)\}.$$

In what follows, we are interested in the fields of reflected wave (40) in the wave zone, i.e., at distances from the emitter larger than the wavelength. In integrating with respect to $k_\perp$, the major contribution to the integral is given by small values of $k_\perp$ such that $k_\perp \rho \ll 1$. In this case, the stationary-phase approximation can be used to calculate the integral for ϑ'. Within the interval $[0, 2\pi]$, there are two stationary-phase points; they are $\vartheta_1' = \vartheta$ and $\vartheta_2' = \vartheta + \pi$. Field (40) can be represented as the sum of the two terms

$$H_y^{(\mathrm{ref})} = -i\sqrt{\frac{2}{\pi\rho}}\int_0^\infty \sqrt{k_\perp} dk_\perp e^{-k(y+a)}$$
$$\times \left\{ \frac{P_1(k_{\perp,\vartheta})}{k_\perp^2 - k_{\perp 1}^2} e^{ik_\perp \rho - i\frac{\pi}{4}} + \frac{P_2(k_{\perp,\vartheta})}{k_\perp^2 - k_{\perp 2}^2} e^{-ik_\perp \rho + i\frac{\pi}{4}} \right\}, \tag{41}$$

where $P_1 = P(\vartheta' = \vartheta)$, $P_2 = P(\vartheta' = \vartheta + \pi)$, $k_{\perp 0}^2 = k_{\perp 0}^2(\vartheta' = \vartheta)$, and $k_{\perp 2}^2 = k_{\perp 2}^2(\vartheta' = \vartheta + \pi)$. The integrands in (41) have singularities in the form of poles at the points $k_\perp = \pm k_{\perp 1, 2}$ ($P_{1,2}(k_\perp)\sqrt{k_\perp}$ are smooth functions). The poles $k_{\perp 1, 2}$ are located within the first and third quadrants of the complex plane of $k_\perp$. In integrals (41), we pass on to integration along contours. In the first term, this contour consists of the semi-axis $(0, \infty)$, an arc with the radius $R \longrightarrow \infty$, and the semi-axis $(0, i\infty)$; in the second term, the contour includes the semi-axis $(0, \infty)$, an arc with infinitely large radius, and the semi-axis $(0, -i\infty)$. It can be easily verified that the pole with $\mathrm{Re}\,k_\perp \gg \mathrm{Im}\,k_\perp > 0$ contributes largely to the expression

for $H_y^{(\mathrm{ref})}$; at the same time, the value of the integral along the arcs and the imaginary axis is exponentially small. For $H_y^{(\mathrm{ref})}(\rho, \vartheta, y)$, we have

$$H_y^{(\mathrm{ref})}(\rho, \vartheta, y) = -\sqrt{\frac{\pi}{2\rho k_{\perp 1}}}e^{-k_{\perp 1}(y+a)+ik_{\perp 1}\rho+i\pi/4}\Phi(k_{\perp 1}, \vartheta),$$

$$\Phi(k_{\perp 1}, \vartheta) = \frac{k_{\perp 1}^2[\omega_g - \omega\,\mathrm{sgn}(\sin\vartheta)]}{\cos\vartheta\left[\left(\omega_g + \frac{\omega_M}{2}\right) - \omega\,\mathrm{sgn}(\sin\vartheta)\right]c} \times [\sin\vartheta j_{0y} + i j_{0x}]. \quad (42)$$

Formula (42) defines the field located in free space and generated as a result of excitation of the surface wave by the magnetic dipole. For this wave, the density of energy flux through the cylindrical surface element $ds = \rho d\vartheta dy$ [$S_\rho = \frac{dW}{ds} = \mathbf{S}\mathbf{n}_\perp$, where $S = \frac{c}{4\pi}[\mathbf{E}\mathbf{H}^*]$] and $n_\perp = (\sin\vartheta, \cos\vartheta)$ is given by

$$S_\rho = \frac{\omega}{4\pi k_{\perp 1}}|H_y|^2 = \frac{\omega k_{\perp 1}^2 e^{-2k_{\perp 1}(y+a)}(\sin^2\vartheta j_{0y}^2 + j_{0x}^2)}{\rho c^2 c\cos^2\vartheta} \times \frac{[\omega_g - \omega\,\mathrm{sgn}(\sin\vartheta)]^2}{\left[\omega_g + \frac{\omega_M}{2} - \omega\,\mathrm{sgn}(\sin\vartheta)\right]^2}. \quad (43)$$

The flux density of the radiation under consideration is largest if the dipole and the detector are arranged at the interface between the media. Thus, the surface hybrid wave defined by (21)–(25) can be observed if this wave is excited using a magnetic dipole and if the detector is located in the plane $y = 0$ within the ranges of angles of $\frac{\pi}{4} < \vartheta < \frac{3\pi}{4}$ in the cases of (23) and (25) or within $\frac{5\pi}{4} < \vartheta < \frac{7\pi}{4}$ in the cases of (22) and (24).

REFERENCES

1. É. A. Nagaev, *Physics of Magnetic Semiconductors* (Nauka, Moscow, 1979).
2. É. A. Nagaev, V. V. Osipov, and A. A. Samokhvalov, Usp. Fiz. Nauk **166** (6), 685 (1996) [Phys. Usp. **39**, 861 (1996)].
3. É. A. Nagaev, Usp. Fiz. Nauk **168** (8), 917 (1997) [Phys. Usp. **41**, 831 (1997)].
4. M. I. Kaganov, N. B. Pustyl'nik, and T. I. Shalaeva, Usp. Fiz. Nauk **167** (2), 191 (1997) [Phys. Usp. **40**, 181 (1997)].
5. N. N. Beletskiĭ, A. A. Bulgakov, S. I. Khankina, and V. M. Yakovenko, *Plasma Instabilities and Nonlinear Phenomena in Semiconductors* (Naukova Dumka, Kiev, 1984).
6. I. N. Oleĭnik and V. M. Yakovenko, Ukr. Fiz. Zh. **26** (1), 19 (1981).
7. V. L. Fal'ko, S. I. Khankina, and V. M. Yakovenko, Fiz. Nizk. Temp. **25** (2), 195 (1999) [Low Temp. Phys. **25** (2), 144 (1999)].

Translated by A. Spitsyn

Semiconductors, Vol. 34, No. 6, 2000, pp. 686–692. Translated from Fizika i Tekhnika Poluprovodnikov, Vol. 34, No. 6, 2000, pp. 712–718.

LOW-DIMENSIONAL SYSTEMS

Reflection Coefficient of a Semiconductor Superlattice Subjected to a Magnetic Field

A. A. Bulgakov* and O. V. Shramkova

Institute for Radiophysics and Electronics, National Academy of Sciences of Ukraine, Khar'kov, 310085 Ukraine

** e-mail: bulgakov@ire.kharkov.ua*

Submitted May 25, 1999; accepted for publication August 18, 1999

Abstract—Propagation of magnetoplasma waves in a structure formed by periodically alternating semiconductor and dielectric layers is studied for the case where an external magnetic field is applied parallel to the layers; the waves traveling in the plane normal to the field are considered. Dispersion characteristics are calculated with the finiteness of the speed of light accounted for, and the features of the structure reflectivity are analyzed. It is demonstrated that the physical parameters and thicknesses of the layers composing the superlattice can be obtained from the frequency, angle of incidence, and magnetic-field dependences of the reflection coefficient. © *2000 MAIK "Nauka/Interperiodica".*

1. INTRODUCTION

The problem of studying physical properties and technological parameters of such structures as semiconductor superlattices presents considerable experimental difficulties. Analysis of the dependence of electromagnetic-wave reflection or transmission coefficients on various external parameters like frequency, angle of incidence, or static magnetic field is one of the contactless methods for examining the superlattice characteristics.

We demonstrated in [1] that, in a layered medium, frequency and magnetic-field dependences of the permittivity tensor results in the formation of a specific band structure of the spectrum and the appearance of "collective surface magnetoplasmon" modes (surface waves propagating over the semiconductor–insulator layer interfaces). The fields of such a wave penetrate, or "tunnel," through the layers of the structure and are, thus, coupled by the boundary conditions. Under certain conditions, it is possible to excite these modes with an external field and investigate the related superlattice properties.

In this paper, we obtain analytical formulas and perform numerical calculations of the reflection $\mathcal{R}$ and transmission $\mathcal{T}$ coefficients for the electromagnetic wave incident on a semiinfinite periodically layered structure composed of the semiconductor and insulator layers and subjected to an external magnetic field. It is shown that by analyzing the frequency, angle of incidence, and magnetic field dependences of the above coefficients one can determine the geometrical as well as physical parameters of the layers composing the structure.

One should be aware of a specific point in the calculation of the reflection and transmission coefficients of the periodic medium. It is related to the fact that the group velocity of the spatial harmonics in different transmission bands can be either positive or negative. This was pointed out by L. Mandel'shtam as far back as in 1945 [2].

A lot of publications have been devoted to theoretical and experimental investigations of the reflection and transmission coefficients in homogeneous media (see, e.g., [3]). One of the most comprehensive studies of the process of the plane wave reflection from a dielectric medium was presented in Fedorov's monograph [4].

The problem of reflection from a periodic dielectric structure was considered previously by A. Yariv and P. Yeh [5]. However, considerable interest in such studies has not been shown until recently [6].

2. THE PROBLEM FORMULATION AND THE BAND STRUCTURE OF THE SPECTRUM

We consider the reflection and transmission of light through the semiinfinite periodically layered structure composed of alternating semiconductor layers of thickness d_1 and insulator layers of thickness d_2. Let the z-axis be oriented perpendicularly to the layers. We assume that an external magnetic field H_0 oriented along the y-axis is applied to the structure. In this paper, we consider the magnetoplasma waves propagating in the xz-plane, perpendicular to the magnetic field. We use the Maxwell equations written for the semiconductor and dielectric layers and also the boundary conditions at the layer interfaces; these conditions ensure the continuity of the electric- and magnetic-field tangential components. For the configuration considered, the Maxwell equations are decoupled into two sets: that for the *TE* waves with the nonzero field components E_y, H_x, and H_z (ordinary wave); and that for the *TM* waves with

1063-7826/00/3406-0686$20.00

the nonzero field components E_x, E_z, and H_y (extraordinary wave). Only the *TM* waves are considered below, since the external magnetic field has no effect on the properties of the *TE* waves. The material equations result in the following expression for the permittivity tensor of the semiconductor [7]:

$$\varepsilon_{xx} = \varepsilon_{zz} = \varepsilon_{\parallel} = \varepsilon_0\left\{1 - \frac{\omega_p^2(\omega + i\nu)}{\omega[(\omega + i\nu)^2 - \omega_H^2]}\right\},$$

$$\varepsilon_{xz} = -\varepsilon_{zx} = \varepsilon_{\perp} = -i\varepsilon_0\frac{\omega_p^2\omega_H}{\omega[(\omega + i\nu)^2 - \omega_H^2]},$$

where ω_p is the plasma frequency, ε_0 is the lattice-related part of the permittivity, ω_H is the cyclotron frequency, and ν is the effective collision rate.

For the insulator layers, we have

$$\mathbf{D}_2 = \varepsilon_2\mathbf{E}_2, \quad \varepsilon_2 = \text{const}.$$

For the plane wave $\exp(-i\omega t + ik_x x + ik_z z)$, the transverse wavenumber in each layer is given by

$$k_{z1} = \sqrt{\frac{\omega^2}{c^2}\varepsilon_{f1} - k_x^2}, \quad k_{z2} = \sqrt{\frac{\omega^2}{c^2}\varepsilon_2 - k_x^2}, \qquad (1)$$

where ε_f is the so-called Voigt permittivity:

$$\varepsilon_f = \varepsilon_{\parallel} + \frac{\varepsilon_{\perp}^2}{\varepsilon_{\parallel}}. \qquad (2)$$

In formula (1), subscripts 1 and 2 correspond to the semiconductor and insulator layers, respectively.

To describe the periodically layered medium, we use the transfer matrix technique [8]: the fields at the beginning and at the end of each structure period are related by

$$\begin{pmatrix} H_{y1}(0) \\ E_{x1}(0) \end{pmatrix} = \hat{m}\begin{pmatrix} H_{y2}(d) \\ E_{x2}(d) \end{pmatrix},$$

where $d = d_1 + d_2$ is the period of the structure. The fields in a periodic structure should comply with the Floquet theorem; thus,

$$H_{y2}(d) = H_{y1}(0)e^{i\bar{\mathbf{k}}d}, \quad E_{x2}(d) = E_{x1}(0)e^{i\bar{\mathbf{k}}d}. \qquad (3)$$

The wavenumber $\bar{\mathbf{k}}$, the so-called Bloch wavenumber, is the transverse wavenumber averaged over the structure period; it replaces the transverse numbers k_{z1} and k_{z2}, which characterize separate layers. The Bloch wavenumber is defined by the following relation, resulting from the Floquet theorem:

$$\cos\bar{\mathbf{k}}d = \frac{m_{11} + m_{22}}{2} = \cos k_{z1}d_1\cos k_{z2}d_2$$

$$-\frac{\varepsilon_{f1}\varepsilon_2}{2k_{z1}k_{z2}}\left[\left(\frac{k_{z1}}{\varepsilon_{f1}}\right)^2 + \left(\frac{k_{z2}}{\varepsilon_2}\right)^2 - k_x^2\left(\frac{\varepsilon_{\perp 1}}{\varepsilon_{\parallel 1}\varepsilon_{f1}}\right)^2\right] \qquad (4)$$

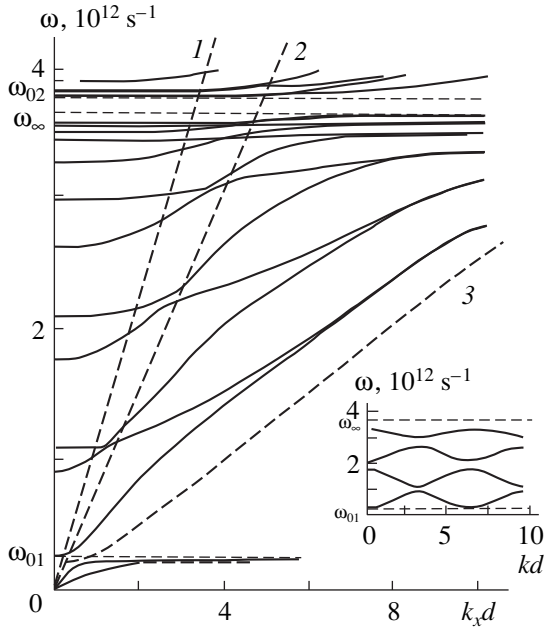

Fig. 1. The band structure of the spectrum.

$$\times \sin k_{z1}d_1\sin k_{z2}d_2.$$

Here, m_{11} and m_{22} are the elements of the transfer matrix $\hat{m}$:

$$m_{11} = \cos k_{z1}d_1\cos k_{z2}d_2 - \left[\frac{k_{z1}\varepsilon_2}{k_{z2}\varepsilon_{f1}} - \left(\frac{\varepsilon_{\perp 1}}{\varepsilon_{\parallel 1}}\right)^2\frac{k_x^2\varepsilon_2}{k_{z1}k_{z2}\varepsilon_{f1}}\right]$$

$$\times \sin k_{z1}d_1\sin k_{z2}d_2 + i\frac{\varepsilon_{\perp 1}k_x}{\varepsilon_{\parallel 1}k_{z1}}\sin k_{z1}d_1\cos k_{z2}d_2,$$

$$m_{22} = \cos k_{z1}d_1\cos k_{z2}d_2 - \frac{k_{z2}\varepsilon_{f1}}{k_{z1}\varepsilon_2}\sin k_{z1}d_1\sin k_{z2}d_2$$

$$-i\frac{\varepsilon_{\perp 1}k_x}{\varepsilon_{\parallel 1}k_{z1}}\sin k_{z1}d_1\cos k_{z2}d_2.$$

We note that, for an infinite periodic medium, this formula represents the dispersion equation, which gives the relation between ω, k_x, and $\bar{\mathbf{k}}$.

The eigenmode spectrum is shown in Fig. 1. The plots were calculated by formula (4); it was assumed that the structure is composed of an InSb semiconductor layer ($\varepsilon = 17.8$, $\omega_p = 10^{12}$ s^{-1}, $d_1 = 0.02$ cm) and an insulator layer ($\varepsilon_2 = 2$, $d_2 = 0.005$ cm), and a magnetic field $H_0 = 159.2 \times 10^3$ A/m (which corresponds to 2000 Oe) is applied.[1] The effective collision rate ν was assumed to be zero. One can see that the spectrum has a band structure. The bands related to the propagating waves (the allowed bands) lie between the Bloch wave-

[1] The same parameters were used in the calculations whose results are represented in the other figures.

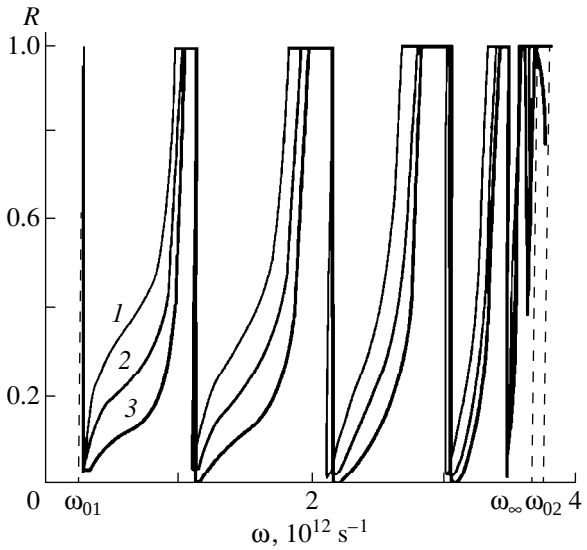

Fig. 2. The reflection coefficient for θ = (*1*) 0°, (*2*) 45°, and (*3*) 60° for $k_x = 0$.

numbers $\bar{\mathbf{k}}d = 2\pi N$ and $\bar{\mathbf{k}}d = \pi(2N + 1)$, where $N = 0, 1, 2, \ldots$; the corresponding band boundaries are plotted by thick and thin solid lines, respectively. Straight line *1* corresponds to the light line of the homogeneous half-space: $k_{zg} = \sqrt{(\omega/c)^2\varepsilon_g - k_x^2} = 0$ (here, ε_g is the permittivity of the homogeneous half-space). Straight line *2* corresponds to $k_{z2} = 0$. Points to the left of this line describe the waves with the waveguide-type field configuration in the second layer ($k_{z2}^2 > 0$), while, in the waves corresponding to the points to the right of this line, the field penetrates, or "tunnels," through the second layer ($k_{z2}^2 < 0$). The following characteristic frequencies are important [8]:

$$\omega_{01,\,02} = \pm\frac{\omega_H}{2} + \sqrt{\frac{\omega_H^2}{4} + \omega_{ps}^2}, \qquad (5)$$

where $\omega_{ps} = \omega_p\sqrt{\varepsilon_{01}/(\varepsilon_{01} + \varepsilon_2)}$ is the frequency of the surface plasmon at the semiconductor–insulator interface. The hybrid frequency is given by

$$\omega_\infty = \sqrt{\omega_p^2 + \omega_H^2}. \qquad (6)$$

Finally, formula

$$\omega_{cr} = \omega_{ps}\frac{\varepsilon_2}{\varepsilon_{01}}\sqrt{\frac{\varepsilon_{01}}{\varepsilon_{01} - \varepsilon_2}} \qquad (7)$$

defines the "critical frequency," whose significance will become clear below.

Let us consider the different regions of the bandstructure.

(i) $\omega < \omega_{01}$. In this region, $\varepsilon_f < 0$, k_{z1} and k_{z2} are purely imaginary quantities, and the fields of the waves propagating through the structure decay exponentially away from the interfaces. Such waves can be called the "collective surface magnetoplasmons." It can be seen from Fig. 1 that, for any Bloch wavenumber $\bar{\mathbf{k}}$, the dispersion curves approach the horizontal asymptote $\omega = \omega_{01}$, and the transmission band width tends to zero with increasing $k_x d$. We note that there is only one transmission band.

(ii) In the region between ω_∞ and ω_{02} (assuming that $\omega_H > \omega_{cr}$) a second "collective" wave band appears. If $\omega_{02} < \omega_\infty$ ($\omega_H < \omega_{cr}$), the second band of "collective surface magnetoplasmons" does not exist.

(iii) For $\omega_{01} < \omega < \omega_{02}$ (in the case $\omega_H < \omega_{cr}$) or for $\omega_{01} < \omega < \omega_\infty$ (in the case $\omega_H > \omega_{cr}$) the wavenumber k_{z1} is real, while k_{z2} can be either real or imaginary. This region is specific in that the permittivity $\varepsilon_f \longrightarrow \pm\infty$ for $\omega \longrightarrow \omega_\infty$; consequently, the argument $k_{z1}d_1$ of the trigonometric functions in the dispersion equation (4) also tends to infinity. Any transmission band is characterized by an integer number of half-waves that fit across each layer, i.e., the formation of the transmission and no-transmission bands is governed by the conditions of geometrical resonance over the thickness of one of the layers. Thus, with increasing $k_{z1}d_1$, the number of transmission and no-transmission bands also becomes infinitely large. The curve *3*, corresponding to $k_{z1} = 0$, is an asymptotic line for the boundaries of all bands in this region; its shape is determined by the frequency dependence of the Voigt permittivity. This also explains the shape of the transmission bands: their width vanishes with increasing $k_z d$, and their frequency approaches ω_∞. This feature of the magnetoplasma wave spectrum is described in our paper [1].

(4) Finally, when ω exceeds both ω_{02} and ω_∞, the magnetic field dependence of the permittivity tensor components wanes with increasing frequency, the spectral bandstructure becomes similar to that of an insulator superlattice, and the boundaries of the bands approach the asymptote $k_{z1} = 0$, which is a straight line in this region.

3. REFLECTION AND TRANSMISSION COEFFICIENTS

The periodic structure spectrum can be investigated, among other ways, by studying the dependence of the electromagnetic wave reflection coefficient on the related experimental parameters. In addition, the energy of the incident wave can be expended to excite the eigenmodes of the periodic structure, e.g., the "collective surface magnetoplasmons," which are responsible for the specific transmission bands in a periodic medium. Thus, the rest of the paper is devoted to the theoretical study of the reflection and transmission coefficients.

The problem of reflection from a homogeneous medium is well known in the literature [9]. The reflection coefficient for a periodic dielectric layer was calculated in [5]. However, certain difficulties related to the proper choice of the sign of the Bloch wavenumber arise in the problem of reflection from a semiinfinite periodic structure. It is known [9] that the reflected and transmitted waves must carry energy away from the interface. The choice of the solution for the reflected wave in the form of the wave propagating into the homogeneous medium is straightforward. However, inside the periodic structure, the sign of the wave group velocity along the z-axis varies as a function of the band and the spatial-harmonic number. This can be seen from the $\omega(\bar{\mathbf{k}}\,d)$ dependence for $k_x d$ = const, plotted in the inset of Fig. 1. It follows from (4) that

$$e^{i\bar{\mathbf{k}}d} = \frac{m_{11}+m_{22}}{2} \pm i\sqrt{1-\left(\frac{m_{11}+m_{22}}{2}\right)^2} = \cos\bar{\mathbf{k}}d \pm \sin\bar{\mathbf{k}}d. \quad (8)$$

The sign of the Bloch wavenumber and, consequently, the sign of the group velocity $\bar{\mathbf{v}}_{gr} = \partial\omega/\partial\bar{\mathbf{k}}$ are determined by the sign of the second term in this expression. If $\sin\bar{\mathbf{k}}\,d > 0$, then the positive sign corresponds to the positive group velocity and energy flux along the z-axis, while the negative sign means that the energy flows towards the interface with the homogeneous medium. If $\sin\bar{\mathbf{k}}\,d < 0$, then the negative sign corresponds to the energy flux in the positive direction. Thus, the sign of the radical term (or of the $\sin\bar{\mathbf{k}}\,d$) corresponding to the wave carrying energy from the interface into the periodic medium should be chosen in the following way (see Fig. 1): plus for the first transmission band; minus for the second; plus for the third; minus for the fourth; etc. It is this specifity in the problem of reflection from a periodic medium that was noted by L. Mandel'shtam [2].

Taking these considerations into account, let us define the reflection coefficient as the ratio of the time-averaged energy flux in the wave reflected from the surface to the incident flux; and the transmission coefficient, as the ratio of the averaged transmitted energy flux to the incident flux.

It is convenient to represent the electric field in a homogeneous medium as

$$E_{xg} = E^i_{xg}(e^{ik_{zg}z} + E^r e^{-ik_{zg}z}), \quad (9)$$

where E^i_{xg} and E^r are the incident- and reflected-wave amplitudes, respectively. The magnetic field in the homogeneous half-space can be found using the Maxwell equations:

$$H_{yg} = \frac{\omega\varepsilon_g}{k_{zg}c}E^i_{xg}(e^{ik_{zg}z} - E^r e^{-ik_{zg}z}).$$

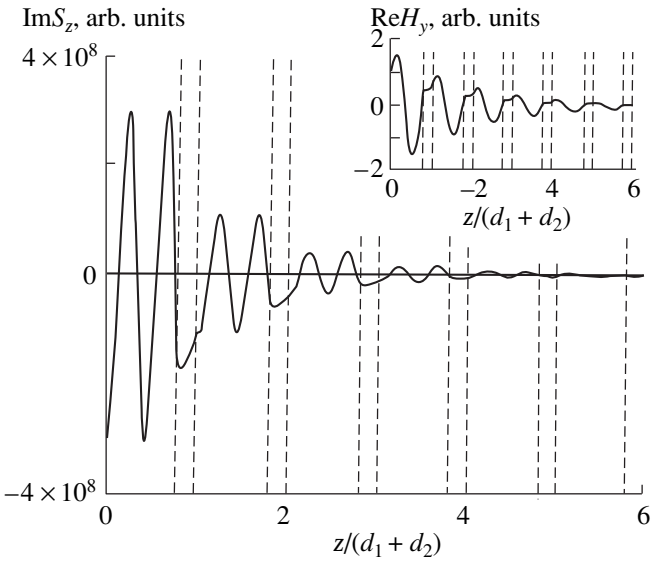

Fig. 3. Electromagnetic energy flux in the forbidden bands; $k_x = 10$.

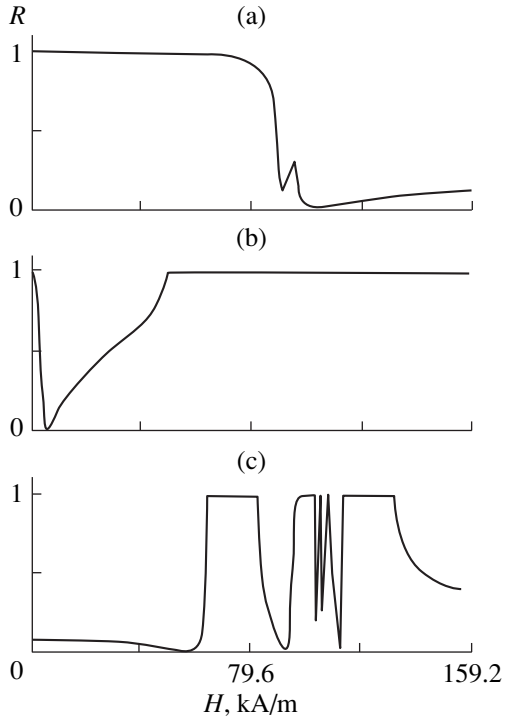

Fig. 4. Magnetic-field dependence of the reflection coefficient for w = (a) 4.1×10^{11}, (b) 9.5×10^{11}, and (c) 2.5×10^{12} s^{-1}; $k_x = 10$.

The magnetic field in the structure can be expressed as

$$H_{y1} = A_1 e^{ik_{z1}z} = A_2 e^{-ik_{z1}z} \quad (10)$$

in the range of 0–d_1; similarly, we have

$$H_{y2} = B_1 e^{ik_{z2}z} + B_2 e^{-ik_{z2}z} \quad (11)$$

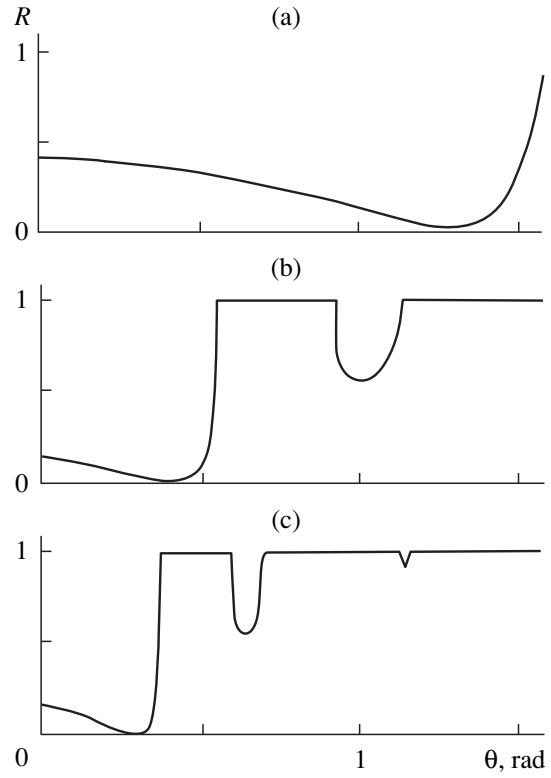

Fig. 5. The reflection coefficient as a function of the angle of incidence for the permittivity of the homogeneous medium ε_g = (a) 1, (b) 10, and (c) 20; $\omega = 2.5 \times 10^{12}$ s^{-1}.

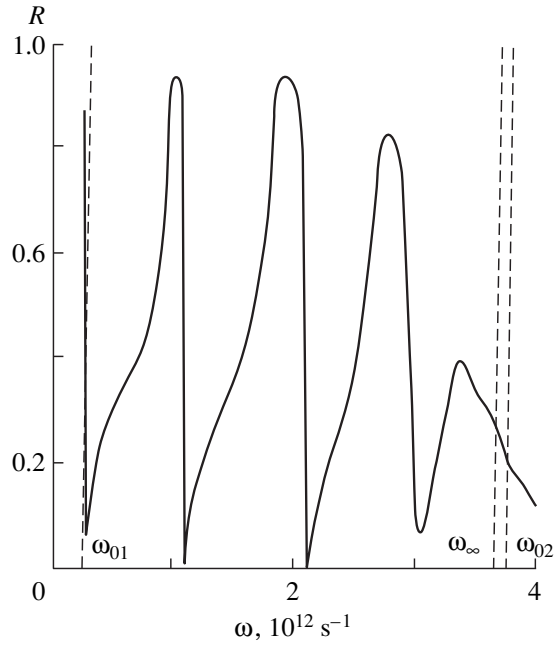

Fig. 6. Reflection coefficient calculated with the dissipation taken into account; $k_x = 0$ and $\nu = 2 \times 10^{11}$ s^{-1}.

in the range of d_1–d_2.

Substituting H_{y1} and H_{y2} in the Maxwell equations, we obtain

$$E_{x1} = \frac{ck_{z1}}{\omega\varepsilon_{f1}}\left[A_1 e^{ik_{z1}z}\left(\frac{\varepsilon_{\perp 1}k_x}{\varepsilon_{\parallel 1}k_{z1}} + 1\right) + A_2 e^{-ik_{z1}z}\left(\frac{\varepsilon_{\perp 1}k_x}{\varepsilon_{\parallel 1}k_{z1}} - 1\right)\right],$$

$$E_{x2} = \frac{ck_{z2}}{\omega\varepsilon_2}(B_1 e^{ik_{z2}z} - B_2 e^{-ik_{z2}z}).$$

The boundary conditions at the interface between the homogeneous half-space and the structure call for the continuity of the tangential components of the fields:

$$E_{xg}(0) = E_{x1}(0), \quad H_{yg}(0) = H_{y1}(0).$$

At the interface between the layers of the structure, the following boundary conditions must be satisfied:

$$E_{x1}(d_1) = E_{x2}(d_1), \quad H_{y1}(d_1) = H_{y2}(d_1).$$

The reflection and transmission coefficients can be obtained using these conditions. Introducing for the sake of convenience the designation $\alpha = m_{12}/[\exp(-i\bar{\mathbf{k}}\,d) - m_{11}]$, we obtain

$$\mathcal{R} = \left|\left(1 - \frac{k_{zg}c}{\omega\varepsilon_g}\right)\Big/\left(1 + \frac{k_{zg}c}{\omega\varepsilon_g}\alpha\right)\right|^2, \tag{12}$$

for the reflection coefficient, and

$$\mathcal{T} = \frac{4k_{zg}c}{\omega\varepsilon_g}\left\{\alpha\Big/\left|1 + \frac{k_{zg}c}{\omega\varepsilon_g}\alpha\right|^2\right\}, \tag{13}$$

for the transmission coefficient. In the above expressions,

$$m_{12} = -i\frac{c}{\omega}\left\{\frac{k_{z2}}{\varepsilon_2}\cos k_{z1}d_1 \sin k_{z2}d_2 + \left[\frac{k_{z1}}{\varepsilon_{f1}} - \left(\frac{\varepsilon_{\perp 1}}{\varepsilon_{\parallel 1}}\right)^2 \frac{k_x^2}{k_{z1}\varepsilon_{f1}}\right]\sin k_{z1}d_1 \cos k_{z2}d_2 + i\frac{\varepsilon_{\perp 1}}{\varepsilon_{\parallel 1}\varepsilon_2}\frac{k_x k_{z2}}{k_{z1}}\sin k_{z1}d_1 \sin k_{z2}d_2\right\},$$

where $k_x = (\omega/c)\sqrt{\varepsilon_g}\sin\theta$, $k_{zg} = (\omega/c)\sqrt{\varepsilon_g}\cos\theta$, and θ stands for the angle of incidence of the electromagnetic wave from the homogeneous half-space. This angle is measured from the negative z-axis direction.

The structure of the spectral bands can be studied in a number of ways: one can measure the frequency dependence of the reflection coefficient $\mathcal{R}$ for the constant magnetic field H_0 = const and the angle of incidence θ = const, or $\mathcal{R}(\theta)$ for H_0 = const and ω = const,

or, finally, the magnetic field dependence of the reflection coefficient $\mathcal{R}(H)$ for ω = const and θ = const.

The $\mathcal{R}(\omega)$ dependence in the frequency range $\omega_{01} < \omega < \omega_\infty$ for $H = 159.2 \times 10^3$ A/m (2000 Oe) for three different angles of incidence is shown in Fig. 2. Comparing Figs. 1 and 2, one can see that the reflection coefficient takes the value $\mathcal{R} = 1$ in the forbidden bands. In the transmission bands, the dependence $\mathcal{R}(\omega)$ is not monotonic, but the curves in the different bands are similar to each other. Note that any transmission band may feature an "absolute transmission" frequency, where the reflection coefficient exactly equals zero, i.e., the incident wave energy is fully transmitted inside the periodic structure. A similar phenomenon may also take place in the case of reflection from a homogeneous medium, the corresponding angle of incidence being called the Brewster angle [9]. In contrast with this case, in the periodic structure, a set of frequencies from different transmission bands corresponds to a single angle.

It is interesting to find the field distribution within the structure if the frequency belongs to a forbidden band. The point is that the wavenumbers in the structure layers are still real. Consequently, the field oscillates within each layer, while its amplitude decays with depth inside the structure. However, the field oscillations do not result in the energy transfer, since the z-component of the flux is a pure imaginary quantity. Thus, the penetration of the field inside the periodic medium is caused by the reactive component of the energy flux. In Fig. 3, we present the distribution of the imaginary part of the energy flux $\mathrm{Im}S_z$ in a periodic medium. The flux oscillations occur because the field oscillates in each layer, which is clearly demonstrated by the inset in the upper part of Fig. 3. Note that the field can penetrate into the structure to a depth of many periods, depending on the value of $|\bar{\mathbf{k}}|^{-1}$. Since $\bar{\mathbf{k}}$ is defined by (4) and depends both on the structure parameters (d_1 and d_2) and the physical properties of the layers, it is possible to control the penetration depth in a number of ways. It would be of interest to compare the phenomenon of the field penetration inside a periodic structure with the case of electromagnetic wave reflection from an insulator half-space with large ε [4].

In Fig. 4, the $\mathcal{R}(H)$ dependences are plotted for several frequencies at a fixed $k_x d = 10$. One can see that the transmission bands and no-transmission bands appear in the magnetic field dependences as well. Note that the width and shape of the transmission bands depend in an intricate manner on the frequency and magnetic field. We believe that this feature of the magnetoplasma wave spectrum can be used to develop special band filters.

Next, let us study the influence of the permittivity ε_g of the homogeneous half-space on the reflection coefficient. The point is that the maximum value of the longitudinal wavenumber at grazing incidence ($\theta = 90°$) equals $k_x = (\omega/c)\sqrt{\varepsilon_g}$. Hence, the entire dispersion region to the right of the light line (Fig. 1) is inaccessible when the incident wave comes from the vacuum. Meanwhile, it is of considerable interest to study the propagation of the waves in the regions adjacent to the characteristic frequencies ω_{01}, ω_{02}, and ω_∞, where the phase velocity is low. Evidently, such modes can be excited by the wave incident from a medium with high permittivity. From Fig. 5, one can see that, for $\varepsilon_g = 1$, only part of a single transmission band can be spanned by variation of the angle of incidence. For $\varepsilon_g = 10$, two bands are accessible for penetration of the incident wave; there are three such bands for $\varepsilon_g = 20$.

Consider the situation when an integer number of the half-waves fit over the thickness of the first layer and, thus, the Bragg resonance condition is satisfied: $k_{z1}d_1 = n\pi$. It follows from (4) that in this case $\bar{\mathbf{k}}\,d = k_{z2}d_2$ for odd n and $\bar{\mathbf{k}}\,d = k_{z2}d_2 + \pi$ for even n. Substituting these values in (12) we find that the reflection coefficient is given by

$$\mathcal{R} = \left|\frac{\varepsilon_g k_{z2} - \varepsilon_2 k_{zg}}{\varepsilon_g k_{z2} + \varepsilon_2 k_{zg}}\right|^2 \qquad (14)$$

and is equal to the reflection coefficient of the second layer only [9]. Thus, the parameters of one of the layers can be found from the observation of the Bragg resonance, provided that the parameters of the other layer are known.

The effect of damping in the semiconductor layer on the reflection coefficient can be seen from Fig. 6. Comparing Figs. 2 and 6, one can see that, with the damping accounted for, the reflection coefficient in the forbidden bands is no more equal to unity; thus, the energy of the incident wave is transmitted inside the superlattice even if its frequency falls within a forbidden band. This occurs due to the fact that the wavenumbers k_{z1} and k_{z2}, as well as the Bloch wavenumber $\mathbf{k}$, are now complex quantities. This means that the z component of the energy flux is also a complex quantity, and $\mathrm{Re}S_z \neq 0$.

It should also be noted that the reflection coefficient in the vicinity of $\omega = \omega_\infty$ is smaller that 0.5, and the bands discussed above in connection with the argument $k_{z1}d_1$ going into infinity in formula (4) disappear. This means that the frequency width of the allowed and forbidden bands cannot be smaller than the effective damping rate.

4. CONCLUSION

Thus, features of the reflection coefficient of a semiconductor periodic structure subjected to a magnetic field have been studied. It was demonstrated that information about the physical parameters and thicknesses of the layers comprising the superlattice can be obtained from an analysis of the dependences of the reflection coefficient on frequency, angle of incidence, and magnetic field. Hence, such measurements can be

used as contactless methods for examining the parameters of periodic structures.

We suppose that the specific properties of the reflection coefficient can be utilized to develop devices such as filters, attenuators, etc., in the wavelength range from centimeters to micrometers. For instance, any transmission band features a Brewster frequency, for which the energy of the incident wave penetrates into the superlattice without losses ($\mathcal{R} = 0$). These frequencies vary with the magnetic field and angle of incidence. Also, the transmission and no-transmission bands over the magnetic field appear when the field strength is varied. The depth at which the external field in the forbidden-band frequency region penetrates into the structure depends on the ratio of the layer thicknesses.

Finally, studying the features of the reflection coefficient, one can obtain information on the spectral properties of the periodic structure and also excite slow waves like collective magnetic polaritons.

REFERENCES

1. A. A. Bulgakov and O. V. Shramkova, Radiotekh. Élektron. (Moscow) (1999) (in press).
2. L. Mandel'shtam, Zh. Éksp. Teor. Fiz. **15** (9), 475 (1945).
3. Yu. K. Grigulis, *Electromagnetic Methods for Analysis of Layered Semiconductor and Metal Optics of Anisotropic Media* (Zinatne, Riga, 1970).
4. F. I. Fedorov, *Optics of Anisotropic Media* (Izd. Akad. Nauk BSSR, Minsk, 1958).
5. A. Yariv and P. Yeh, *Optical Waves in Crystals: Propagation and Control of Laser Radiation* (Wiley, New York, 1984; Mir, Moscow, 1987).
6. A. V. Danilov and S. A. Il'chenko, in *Proceedings of the 4th International Conference on Electron Transport and Optical Phenomena in Inhomogeneous Media, 1991* (St. Petersburg, 1991).
7. V. P. Silin and A. A. Rukhadze, *Electromagnetic Properties of Plasma and Plasmalike Media* (Atomizdat, Moscow, 1961).
8. F. G. Bass, A. A. Bulgakov, and A. P. Tetervov, *High-Frequency Properties of Semiconductors with Superlattices* (Nauka, Moscow, 1989).
9. L. D. Landau and E. M. Lifshitz, *Course of Theoretical Physics. Vol. 8. Electrodynamics of Continuous Media* (Nauka, Moscow, 1982; Pergamon Press, Oxford, 1984).

Translated by M. Skorikov

Semiconductors, Vol. 34, No. 6, 2000, pp. 693–699. Translated from Fizika i Tekhnika Poluprovodnikov, Vol. 34, No. 6, 2000, pp. 719–725.

LOW-DIMENSIONAL SYSTEMS

Low-Temperature Photoluminescence and X-ray Diffractometry Study of $In_xGa_{1-x}As$ Quantum Wells

S. V. Evstigneev*, R. M. Imamov, A. A. Lomov**, Yu. G. Sadof'ev*, Yu. V. Khabarov***, M. A. Chuev****, and D. S. Shipitsin***

** Lebedev Institute of Physics, Russian Academy of Sciences, Leninskiĭ pr. 53, Moscow, 117924 Russia*
e-mail: sadofyev@sci.lebedev.ru
*** Shubnikov Institute of Crystallography, Russian Academy of Sciences, Leninskiĭ pr. 59, Moscow, 117333 Russia*
**** Institute of Radio Engineering and Electronics, Russian Academy of Sciences, Mokhovaya ul. 11, Moscow, 103907 Russia*
***** Institute of Physics and Technology, Russian Academy of Sciences, ul. Krasikova 25a, Moscow, 117218 Russia*
Submitted July 14, 1999; accepted for publication November 25, 1999

Abstract—The structures grown by molecular-beam epitaxy with $In_xGa_{1-x}As$ quantum wells (QWs) in GaAs were studied by X-ray diffractometry and low-temperature photoluminescence techniques. The inhomogeneity of the QW composition along the growth direction was established. Energy positions of the exciton recombination lines in the QWs with step-graded In distribution were calculated, and good agreement with the experimental data was obtained. *© 2000 MAIK "Nauka/Interperiodica".*

1. INTRODUCTION

Most of the work devoted to the fabrication and investigation of the structures with single and multiple heterojunctions, such as heterostructures with selective doping, quantum wells (QWs), and superlattices, was based on the gallium and aluminum arsenides [1]. The lattice constants of these two materials match almost perfectly, which enables one to obtain high-quality structures. However, employment of other materials may result in a considerable improvement in the characteristics of existing devices and the enhancement of their functional capabilities. Recently, structures with strained $In_xGa_{1-x}As$ layers confined by GaAs or AlGaAs barriers have become widely used. Employment of $In_xGa_{1-x}As$ layers as QWs opens the way to achieving better confinement of the charge carriers in the size-quantization states and to varying the optical characteristics of the heterostructures [2, 3]. To take an example, the use of an $In_xGa_{1-x}As$ layer as the channel of a high electron mobility transistor (HEMT) enabled the authors of the recent publication [4] to obtain the maximum transconductance of 1510 mS/mm and the cutoff frequency of 220 GHz, which is one of the best results for HEMTs. The use of a near-contact graded-gap $In_xGa_{1-x}As$ layer makes it possible to form nonalloyed ohmic contacts, which considerably simplifies the fabrication of large-scale integrated circuits [5]. An unconventional method for the formation of independent contacts to the isotype QWs of a double-well heterostructure has been proposed by us [6]; it is based on the use of QWs of different composition, including $In_xGa_{1-x}As$ ones.

In connection with this wide usage of the strained $In_xGa_{1-x}As$ heterostructures, wide-scale investigations of the samples being obtained are required to optimize the technological regimes for the formation of In-containing layers and interfaces. Another problem is related to the identification of the band diagram of the structures with InGaAs–AlGaAs heterojunctions and QWs, which is necessary for developing devices with the required characteristics. In particular, to elaborate the growth technology for InGaAs quantum-scale layers one needs to know such parameters as the indium molar fraction and the layer thickness. The photoluminescence (PL) technique is commonly used for *ex situ* control of these parameters of the quantum-scale heterostructures. In the spectrum of the PL originating from the electron–hole pair recombination in the QW, the position of the main line corresponds to the energy difference between the ground quantum-scale levels E_{e1} and E_{hh1} of electrons in the conduction band and heavy holes in the valence band, respectively, with the correction for the exciton binding energy. This position depends on the well width, composition, and the QW exciton binding energy. Thus, information on the configuration of a given QW cannot be unambiguously obtained from the PL data. Broadening of the PL lines is often observed, and detailed knowledge of the factors that determine the linewidth is required. Besides, the generally accepted estimates for the band-diagram parameters of the InGaAs–AlGaAs structures are lacking. This problem has not been solved until now, since these structures are strained because of the large lattice mismatch of the materials involved (7% mismatch between InAs and GaAs). Complete information on the $In_xGa_{1-x}As$ elastic constants and their dependence on

Table 1. The QW parameters set by the technological conditions and determined from X-ray diffractometry data

Sample	MBE			DRC							
	d, nm	x	T_s, °C	d_1, nm	x_1	d_2, nm	x_2	d_3, nm	x_3	Σd_i, nm	$\langle x \rangle$
A	13.5	0.08	580	3.3 ± 0.1	0.037 ± 0.004	10.0 ± 0.3	0.071 ± 0.001	1.3 ± 0.2	0.043 ± 0.003	14.6 ± 0.6	0.061 ± 0.002
B	13.5	0.17	555	3.38 ± 0.08	0.10 ± 0.03	10.0 ± 0.1	0.165 ± 0.005	–	–	13.4 ± 0.2	0.149 ± 0.005
C	11.5	0.17	535	Calculation was not performed							
	3.0	0.17	535	Calculation was not performed							
	6.0	0.25	500	Calculation was not performed							

the In content and temperature cannot be found in the literature, which makes a theoretical calculation of the band gap of a strained-layer QW impossible. To calculate the free-carrier properties in such heterostructures one also needs to know the conduction- and valence-band discontinuities at the heterojunction ΔE_c and ΔE_v and their dependence on the QW composition. Usually, the value being taken for the band gap of the $In_xGa_{1-x}As$ QW is based on the assumption that it is linearly dependent on the In content, with the coefficient equal to the band-gap difference of the bulk materials at a fixed temperature. The value adopted in different publications for the $\Delta E_c/\Delta E_g$ ratio varies from 0.55 to 0.85 [7–9]. In this context, it is desirable to use the other nondestructive control techniques to complement the PL data.

Combined studies by the PL and double-crystal X-ray diffractometry techniques were performed in this work to determine the main parameters of $In_xGa_{1-x}As$ QWs that were grown by molecular-beam epitaxy (MBE) and had different widths and In content and were confined by the GaAs barriers. In addition, calculations of the $e1$–$hh1$ transition energies for the grown QWs were carried out using an empirical expression for the indium-content dependence of the InGaAs/GaAs QW band gap. The PL spectra calculated in this way [taking into account the binding energy of the exciton in the two-dimensional (2D) layer] and using the QW parameters determined from the X-ray diffraction reflection curves (DRCs) agree well with the experimental results.

2. GROWTH OF THE SAMPLES

Samples with the QWs were grown by MBE in a Tsna-18 setup on the semiinsulating GaAs(001) substrates misoriented by 3° in the [110] direction. Two structures with a single QW (samples *A* and *B*) and a structure with three QWs (sample *C*) were grown. The designed indium molar fraction x and the QW widths varied from 0.08 to 0.25 and from 3 to 13.5 nm, respectively. These values were determined from the measured dependences of the Ga and In molecular beam equivalent pressures on the temperatures of the corresponding molecular sources and on the source calibrations based on the growth rates of GaAs and InAs layers. The study was largely focused on the wide QWs with $x \approx 0.2$, which can be used in various types of field-effect transistors. In this connection, the growth temperatures of the In-containing layers exceeded their usual values by 30–40°C to achieve a higher conductivity of the 2D channels obtained. In the pseudomorphous HEMT structures (with a single doped barrier layer above the In-containing QW) grown under these conditions, the 2D electron gas mobilities of 5700 and 37000 $cm^2/(V\,s)$ were obtained at temperatures of T = 300 and 77 K, respectively, and the 2D electron density $n_s = 2.4 \times 10^{12}$ cm^{-2}.

To prevent the diffusion of impurities and defects from the substrate into the active region of the heterostructure, a 0.5-μm-thick GaAs buffer layer was first deposited on all of the samples. Similar GaAs layers were also used to separate the InGaAs QWs from the film surface and from each other. The structures were not intentionally doped during the growth. A substrate temperature of 610°C was held during the GaAs deposition; the GaAs growth rate was 0.6 μm/h, and the ratio of the As and Ga beam equivalent pressures was 20 : 1. In the case of formation of both $In_xGa_{1-x}As$ layer interfaces, the growth was interrupted for 90 s with the arsenic flux being maintained. This was done to reduce the interface roughness and to change the substrate temperature, which was first decreased to a certain value depending on the QW composition and then increased to 610°C after the deposition of an $In_xGa_{1-x}As$ layer. The rodlike high-energy electron diffraction patterns with no pronounced intensity modulation along the reflections were observed at all stages of the growth process. To prevent thermal desorption from the near-surface region and to minimize possible thermally stimulated indium segregation, three GaAs monolayers were deposited in samples *A* and *C* over the QW layer before the growth interruption at its upper interface and raising of the substrate temperature. This operation was not performed in the growth of sample *B*. The designed $In_xGa_{1-x}As$ QW parameters, along with the corresponding growth temperatures T_s, are given in Table 1 in the column marked as "MBE."

3. X-RAY DIFFRACTION STUDIES

The layer structural parameters were studied by the techniques of double-crystal X-ray diffractometry. We employed a TRS-1 triple-crystal X-ray spectrometer operating in automated mode controlled by a personal computer and the MATEX controller. The DRCs were recorded in the (004) reflection in the $\omega/(1 + \beta)\theta$-scanning mode (here, β is the asymmetry coefficient) with a narrow (8') slit placed in front of the detector. The same layout was also used in the θ-scanning mode to measure the contribution of the diffuse scattering in the DRCs. A 1.1-kW X-ray tube with a copper anode served as a radiation source. The X-ray beam incident on the sample was formed by a slit triple-reflection monochromator made of a high-quality Ge(004) crystal. The DRCs were recorded in a step-by-step regime; the signals at each point were accumulated until the desired signal statistics was achieved. Other details of the experimental setup are similar to those described in [10].

The DRCs recorded for samples *A* and *C* are shown in Figs. 1a and 1b, respectively. Qualitatively, the features observed in the curves are readily understood. One can see that, in addition to the main diffraction maximum at $\Delta\theta = \theta - \theta_B = 0$ (where θ_B is the Bragg angle), a complicated interference pattern resulting from the superposition of the two waves with different oscillation periods is observed in the tails of the DRCs. The smaller period oscillations indicate that a film of thickness

$$L = (\lambda \sin\theta_0)/\Delta\theta \sin 2\theta_B \approx 0.1\ \mu\text{m} \qquad (1)$$

exists on the sample surface (here, λ is the X-ray wavelength and θ_0 is the grazing angle).

The larger period oscillations exhibit a clearly pronounced maximum, which indicates that a single-crystal layer of thickness ~0.01 μm with the lattice constant different from that of the substrate is formed near the surface of the sample, the lattice constant difference being equal to $\Delta a = -\alpha_0(\cot\theta_B)\Delta\theta$ (where a_0 is the substrate lattice constant). Analyzing the DRCs recorded from the asymmetric reflections, we found that the grown layers are pseudomorphous. Taking this into account, we estimated the In content in the QWs to be $x = 0.07$ and 0.17 in samples *A* and *B*, respectively.

To carry out a quantitative analysis of the DRCs and to obtain detailed information on the structure parameters of separate layers and interfaces, the method developed in [11] was used. The parameters estimated from the technological settings were taken as an initial approximation. Next, the models that give the best agreement between the theoretical and experimental DRCs were searched for. Note that not only the proper model can be selected by this method but also the errors for the parameters being determined can be found for each layer of the sample. Fitting of a calculated curve to the one recorded experimentally was terminated when the rms errors of the parameters obtained exceeded their average values.

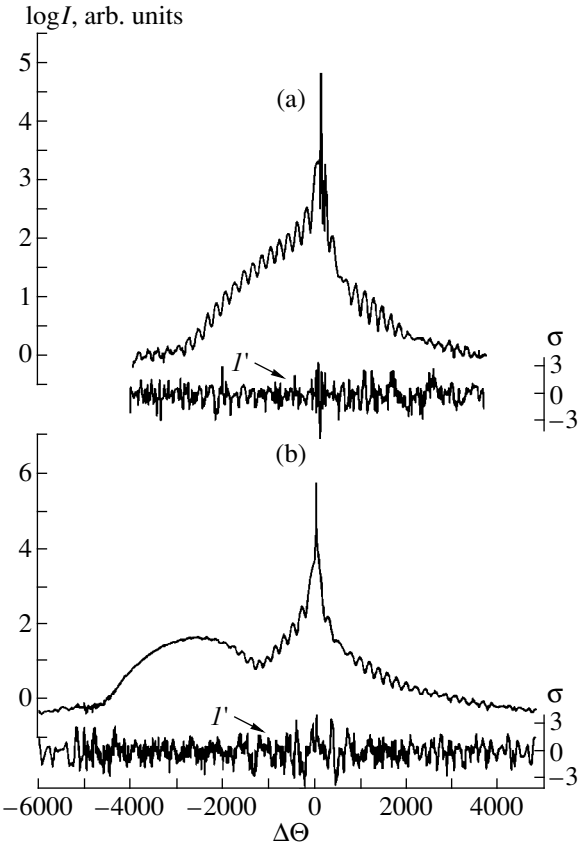

Fig. 1. Diffraction reflection curves for the $In_xGa_{1-x}As/GaAs$ heterostructures: (a) sample *A* ($\chi^2 = 1.28$) and (b) sample *B* ($\chi^2 = 1.33$). Curves *1* and *1*' represent the standard error σ. *I* stands for intensity.

The DRCs calculated in the model with abrupt interfaces are visually similar to the experimental ones. However, the agreement achieved is not satisfactory, since the values obtained for the χ^2 functional [10] differed greatly from unity. Thus, the model with additional sublayers, characterizing the heterojunction broadening, was introduced at the next stage of the analysis. This yielded χ^2 values of 1.28 and 1.33 for samples *A* and *B*, respectively. Virtually no visual difference between the theoretical and experimental curves can be found in this case. This result is illustrated by the standardized residuals δ shown in the bottom of Figs. 1a and 1b; almost all of them fall well within the theoretically predicted range from –3 to 3.

In Figs. 2a and 2b, the distributions of lattice deformation $\Delta a_\perp/a$ and amorphization f_i over the distance from the surface are shown for samples *A* and *B*, respectively.

The structure of the QW layer is characterized by an abrupt top interface with the GaAs layer and a bottom interface broadened by about 3 nm inside the sample.

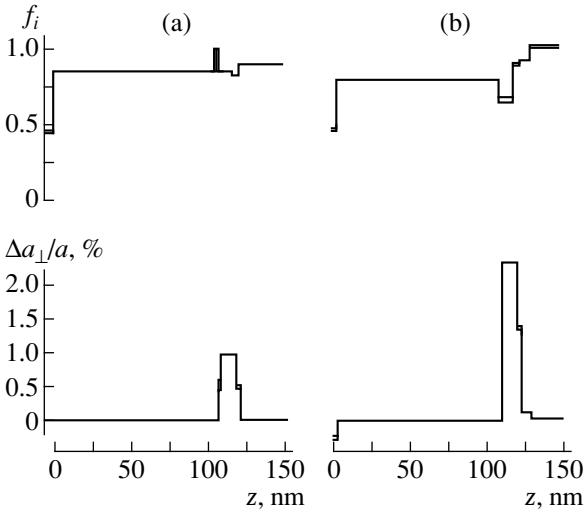

Fig. 2. Distribution profiles of the statistical Debye–Waller factor f_i and lattice constant change in the axial direction $\Delta a_\perp/a$ over the thickness of the samples (a) *A* and (b) *B*.

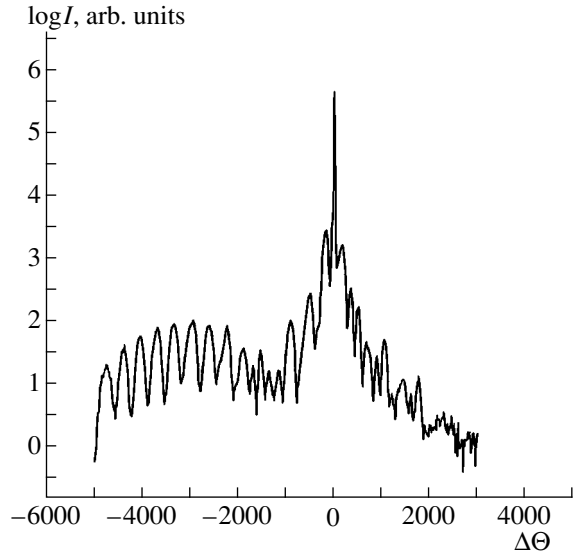

Fig. 3. Diffraction reflection curve for sample *C*. *I* stands for intensity.

The In content (or the change in the interplanar spacing) in the transition regions is reduced by about 1.5 and 2 times for samples *A* and *B*, respectively, as compared to the main part of the QW. The thicknesses and indium content in the $In_xGa_{1-x}As$ layers determined from the X-ray diffraction data are given in Table 1 in the column headed "DRC." One can see that the QW layer is effectively composed of three and two sublayers in samples *A* and *B*, respectively. Subscripts 1, 2, and 3 in Table 1 enumerate the corresponding QW regions sequentially from the substrate to the surface of the epitaxial film. The total thickness and average In content in the $In_xGa_{1-x}As$ layer are given in the two rightmost columns in Table 1. The obtained values agree well with those corresponding to the technological settings.

The models obtained for samples *A* and *B* differ most significantly in the average value of the atomic ordering in the crystal lattice f_i characterizing the main region of the QW. The values f_i = 0.85 and 0.62 obtained for samples *A* and *B*, respectively, differ by more than 30% (see Fig. 2b). This means that the In-containing layer in sample *A* is more perfect than that in sample *B*. This is corroborated by the fact that the diffuse scattering intensity in the angle range corresponding to the reflection from the $In_xGa_{1-x}As$ lattice is higher and the interference oscillations at $\Delta\theta < 0$ (Fig. 1b) decay more rapidly in sample *B*.

The DRC of sample *C* is shown in Fig. 3. A large number of oscillations can be observed here, which confirms the existence of the clearly developed multilayer structure near the surface. Using the technique of the χ^2 functional minimization [10], one can obtain, if need be, extensive information on the layer parameters in the sample.

4. PHOTOLUMINESCENCE

The PL measurements were carried out at liquid-nitrogen temperature. An Ar^+ laser emitting at λ = 488 nm was used as an excitation source. The laser radiation was focused at a ~50-μm-diameter spot, and the maximum excitation intensity was 200 W/cm^2. The spectra were recorded with an MDR-23 monochromator equipped with a cooled FEU-62 photomultiplier operating in the photon-counting mode.

The PL $I_{PL}(E)$ spectra of samples *A*, *B*, and *C* are demonstrated in Figs. 4a and 4b. Intense and, at the same time, rather broad bands related to the $e1$–$hh1$ excitonic recombination in the QWs are observed. The PL band energy positions and widths at half-maximum are given in Table 2 in the column headed as "PL." Broadening of the PL bands may be caused both by the QW–barrier interface imperfections, resulting in the fluctuations of the QW width, and compositional inhomogeneity over the QW thickness. The appearance of such imperfections is confirmed by the X-ray diffraction data, which indicate that the bottom interface is broadened (and depleted in indium) to a greater extent.

One should note that the intensity of the radiative recombination in the $In_xGa_{1-x}As$ layers is very high. Even the signal corresponding to the smallest peak (related to the 3-nm well in sample *C*) exceeds the barrier-layer signal by two orders of magnitude.

Table 2. Parameters of the quantum wells determined from the photoluminescence data

Sample	PL		Calculation 1		Calculation 2						
	E_{e1-hh1}, eV	Peak width, meV	d, nm	x	d_1, nm	x_1	d_2, nm	x_2	d_3, nm	x_3	Σd_i, nm
A	1.4391	9	14.6	0.064	3.3	0.033	10.0	0.07	1.3	0.04	14.6
B	1.3306	21	13.4	0.175	3.4	0.01	10.0	0.17			13.4
C	1.3272	12	11.0	0.17	1.6	0.11	10.0	0.175			11.6
	1.4459	13	3.0	0.14	1.6	0.11	1.4	0.175			3.0
	1.2999	25	6.0	0.24	1.0	0.17	5.0	0.25			6.0

5. CALCULATION OF THE PHOTOLUMINESCENCE TRANSITION ENERGY $E_{e1–hh1}$ AND DETERMINATION OF THE QUANTUM WELL PARAMETERS

Most of the QWs in the samples under consideration are wide, i.e., the ground quantum-confined levels are located near the edges of the corresponding allowed bands. In this case, the potential barrier heights and, consequently, the specific choice of the $\Delta E_c/\Delta E_g$ ratio are of little importance for calculation of the PL peak energy position. For definiteness, we chose for this parameter the average value among those cited in the literature, equal to 0.7. The QW exciton transition energy was determined by adding the $In_xGa_{1-x}As$ band gap at 77 K to the energy of the *e*1 and *hh*1 quantum confinement levels measured from the corresponding band edges and subtracting the exciton-binding energy. Dependence of the $In_xGa_{1-x}As$ band gap E_g on the indium content is largely determined by a second-degree polynomial [12–14]. The coefficients of the first- and second-order terms were taken from [15], and the value of the GaAs band gap at 77 K, equal to 1.508 eV, was taken as the origin:

$$E_g\ [\text{eV}] = 1.508 - 1.214x + 0.264x^2. \qquad (2)$$

The energies of the first electron and heavy-hole quantum confinement levels were calculated numerically from the Schrödinger equation, which was solved in the one-electron approximation in the frame of the envelope-function method. It is assumed that the electron and heavy-hole effective masses do not vary throughout the structure and are equal to the values calculated for the QW layer using the following relationships:

$$\begin{aligned} m_e^* &= 0.0665 - 0.0642x, \\ m_{hh}^* &= 0.62 - 0.22x. \end{aligned} \qquad (3)$$

The transfer matrix technique was used to solve the Schrödinger equation. The rectangular QW shape with abrupt interfaces was assumed. For samples *A* and *B*, QW parameters determined from the DRCs (total $In_xGa_{1-x}As$ layer width and indium content calculated as an average over all QW regions) were taken as a first approximation for the calculation of the PL transition energies. For sample *C*, the parameters were taken from the "MBE" column of Table 1.

The exciton-binding energy in the QWs considered varies in the range of 6–9 meV, the maximum value corresponding to the 3-nm-thick $In_xGa_{1-x}As$ layer [16, 17]. For most of the wells, this value is 7 ± 1 meV. Thus, the average value of the exciton-binding energy, equal to 7 meV, is a good approximation for the calculation of all PL peaks.

In Fig. 5, experimental data and theoretical results for the transition energies $E_{e1–hh1}$ in samples *A*, *B*, and *C* are shown by closed and open symbols, respectively. The errors in the calculated QW parameters for samples *A* and *B* correspond to the errors in the weight-average parameters determined from the DRCs. One can see that satisfactory agreement between the results of calculations and the energy position of the PL peaks is achieved for sample *A* and the wide QW of sample *C*. For sample *B* and the narrow (3-nm) QW of sample *C*, the disagreement is quite appreciable. This is probably caused by the nonuniformity of the indium distribution in the QWs. Note that experimentally obtained energies of the *e*1–*hh*1 transition correspond to lower values of the indium molar fraction than the expected ones. In Fig. 5, we indicate the values of the indium molar fraction determined from the fit of the results of calculations for the rectangular QWs to the experimental data. The QW parameters thus obtained from the $E_{e1–hh1} = f(d, x)$ dependences are given in Table 2 ("Calculation 1").

To clarify the causes of such a disagreement between the theory and experiment, we calculated the luminescence transition energies for the step-graded QWs. As stated above, it follows from the DRC analysis that in the ~3-nm-thick bottom boundary region of the QW layers in samples *A* and *B* the indium content is lower than in the rest of the layer (Fig. 2a). This depleted region is formed due to the surface segregation of indium atoms in the process of the QW growth. The increased growth temperatures that we use to obtain high conductivity of the In-containing channels favors this effect. The excess indium atoms accumulating in the near-surface region of the QW either desorb during the growth interruption at the upper interface or

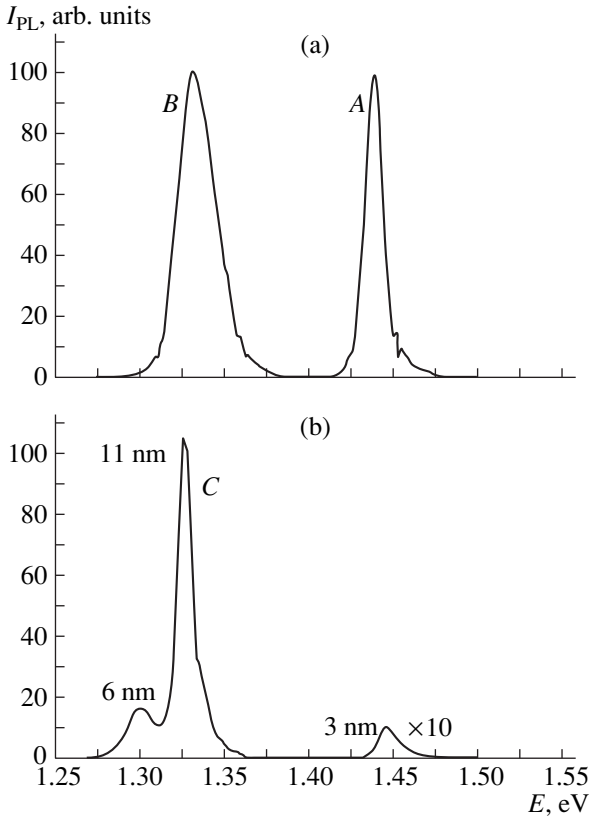

Fig. 4. Photoluminescence spectra of the samples under study at T = 77 K: (a) single-QW structures *A* and *B* and (b) triple-QW structure *C*.

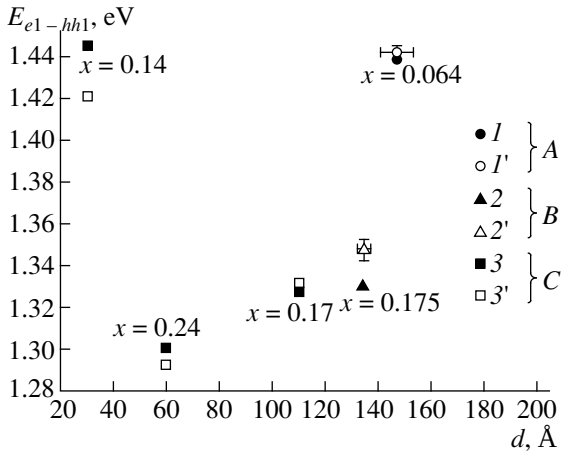

Fig. 5. The *e*1–*hh*1 QW exciton recombination energies in the samples under study: (*1*)–(*3*) experimental data and (*1*')–(*3*') results of calculations.

diffuse in the adjacent GaAs layer. The evidence for the latter mechanism of the indium redistribution is found from the DRC analysis in sample *A* (Table 1). In this case, the depletion region is formed by the In atom diffusion in the adjacent 3-monolayer-thick region of the GaAs barrier deposited to prevent indium evaporation during the growth interruption. For sample *B*, which is not coated with the GaAs protective film during the growth interruption at the top interface, excess indium desorption takes place.

Taking all this into account, we calculated the energy position of the PL peaks for the QWs composed of several regions differing in indium content. For samples *A* and *B*, the parameters were taken from Table 1 ("DRC" column). For sample *C*, it was assumed that the InGaAs layers consist of two regions: an indium-depleted region formed due to the surface segregation and the "core" of the QW, whose composition nearly corresponds to the technological settings. It was assumed that the indium molar fraction in these regions differs by a factor of 1.5. The *e*1–*hh*1 transition energies calculated with the parameters given in Table 2 agree with the experimental values measured for the grown QWs (with regard to the averaged exciton binding energy of 7 meV).

Note the good agreement between the simulated parameters of the QWs in samples *A* and *B* and the X-ray diffraction data. It follows from the results presented that the inhomogeneous QW composition profile should be taken into account, which is especially important for the thin wells (thinner than 6 nm) and increased epitaxy temperatures, since in this case the thickness of the indium-depleted region is comparable to the thickness of the QW core.

6. CONCLUSION

Combined X-ray diffraction and PL studies of the $In_xGa_{1-x}As$ heterostructures carried out in this work enabled us to establish the relation between the energy position of the QW PL lines and the composition inhomogeneity over the QW thickness. Calculation performed in the frame of the rectangular QW model (using an empirical formula for the $In_xGa_{1-x}As$ band gap in the presence of strain) gives satisfactory agreement with the experiment for relatively thick QWs (thicker than 6 nm) with a low indium molar fraction (below 0.17). Application of the model corrected by introducing the step-graded profile of the QW composition revealed by the X-ray diffraction studies results in better agreement between the theoretical and experimental values both for the wide and narrow QWs. With the epitaxy regimes used, the vertical compositional inhomogeneity of the QWs near the bottom interface is caused by the surface segregation effects and, near the top interface, by the indium diffusion into the adjacent GaAs layer. Further refinement of the model for the calculation of the narrow QW PL spectra requires precise information on the ratio $\Delta E_c/\Delta E_g$ of the conduction-band to the full band-gap discontinuity.

ACKNOWLEDGMENT

This work was supported by the Russian Foundation for Basic Research (project no. 98-02-1758) and the Russian State Program "Physics of the Solid-State Nanostructures" (project nos. 97-2019 and 98-3009).

REFERENCES

1. M. H. Herman, D. Bimberg, and J. Christen, J. Appl. Phys. **70**, R1 (1991).
2. H. Jurgen, T. P. E. Broekaert, and C. C. Fonstad, J. Appl. Phys. **71**, 2475 (1992).
3. N. N. Ledentsov, V. A. Shchukin, M. Grundmann, *et al.*, Phys. Rev. B **54**, 8743 (1996).
4. F. Diette, D. Langrez, J. L. Codron, *et al.*, Electron. Lett. **32**, 848 (1996).
5. Y. Shiraishi, N. Furuhata, and A. Okamoto, J. Appl. Phys. **76**, 5099 (1994).
6. S. V. Evstigneev, Yu. V. Kopaev, Yu. G. Sadof'ev, *et al.*, Mikroélektronika **27**, 317 (1998).
7. S. Kuroda, N. Harada, T. Katakami, *et al.*, IEEE Trans. Electron. Devices **ED-36**, 2196 (1989).
8. M. Wojtowicz, D. Pascua, A.-C. Han, *et al.*, J. Cryst. Growth **175/176**, 930 (1997).
9. T. G. Andersson, Z. G. Chen, V. D. Kulakovskiĭ, *et al.*, Phys. Rev. B **37** (8), 4032 (1988).
10. A. M. Afanas'ev, M. A. Chuev, R. M. Imamov, *et al.*, Kristallografiya **42** (3), 514 (1997) [Crystallogr. Rep. **42** (3), 467 (1997)].
11. A. M. Afanas'ev, M. A. Chuev, R. M. Imamov, and A. A. Lomov, Kristallografiya **45** (3) (2000) (in press) [Crystallogr. Rep. **45** (3) (2000) (in press)].
12. E. Kuphal, A. Pocker, and A. Eisenbach, J. Appl. Phys. **73**, 4599 (1993).
13. K. H. Goetz, D. Bimberg, H. Jurgensen, *et al.*, J. Appl. Phys. **54**, 4543 (1983).
14. T. Y. Wang and G. B. Stringfellow, J. Appl. Phys. **67** (1), 344 (1990).
15. I. V. Bradley, W. P. Gillin, K. P. Homewood, and R. P. Webb, J. Appl. Phys. **73**, 1686 (1993).
16. M. J. L. S. Haines, N. Ahmed, S. J. A. Adams, *et al.*, Phys. Rev. B **43**, 11944 (1991).
17. K. J. Moore, G. Duggan, K. Woodbridge, and C. Roberts, Phys. Rev. B **41**, 1090 (1990).

Translated by M. Skorikov

Semiconductors, Vol. 34, No. 6, 2000, pp. 700–711. Translated from Fizika i Tekhnika Poluprovodnikov, Vol. 34, No. 6, 2000, pp. 726–736.

LOW-DIMENSIONAL SYSTEMS

Self-Ordered Microcavities Embedded in Ultrashallow Silicon *p–n* Junctions

N. T. Bagraev*, A. D. Buravlev*, L. E. Klyachkin*, A. M. Malyarenko*, and S. A. Rykov**

** Ioffe Physicotechnical Institute, Russian Academy of Sciences, Politekhnicheskaya ul. 26, St. Petersburg, 194021 Russia*

*** St. Petersburg State Technical University, Politekhnicheskaya ul. 29, St. Petersburg, 195251 Russia*

Submitted December 30, 1999; accepted for publication 30 December, 1999

Abstract—Scanning tunneling spectroscopy was used to obtain topographic images of the (100) surface of ultrashallow diffusion profiles of boron in silicon. This method makes it possible to study the influence of fluctuations of the surface deformation potential, which depend on the thickness of the preliminary deposited oxide layer and on the crystallographic orientation of the fluxes of nonequilibrium vacancies and self-interstitials that stimulate the exchange mechanisms of impurity diffusion. The existence of self-assembled systems of quantum anti-dots, which are formed due to fluctuations in the surface deformation potential and which are microdefects that penetrate through the diffusion profile of the dopant, is demonstrated for the first time. It is established that a spread in the sizes of quantum anti-dots is reduced with increasing temperature of the impurity diffusion. In addition, the sizes of quantum anti-dots are found to be interrelated to their spatial distribution, which is indicative of a fractal mechanism of formation of self-assembled zero-dimensional systems under conditions of strong interaction of the flux of impurity atoms with that of primary defects. Self-assembled quantum anti-dots embedded into a system of silicon quantum wells make it possible to design microcavities with distributed negative feedback; the existence of such microcavities is confirmed by spectral dependences of the reflection and transmission coefficients in the visible and infrared regions of the spectrum, respectively. © *2000 MAIK "Nauka/Interperiodica".*

1. INTRODUCTION

The formation of all currently known nanostructures in semiconductors is based on processes of local self-ordering of atoms in the matrix [1]. At the same time, the self-ordered nanostructures can also originate due to anisotropy in the diffusion of impurity atoms and ions in the course of their introduction to the semiconductor lattice by ion implantation and diffusion [2, 3]. Such a self-organization of impurity atoms is enhanced drastically if nonequilibrium impurity diffusion is used under the conditions of controlled injection of vacancies or self-interstitials [3, 4]. In this case, planar technology is preferable. This technology makes it possible to implement the mechanism of enhanced diffusion of the dopant by stimulating the exchange interaction of the impurity atom with the self-interstitial [the kick-out (KO) mechanism of interstitial impurity diffusion] or the vacancy (the substitutional mechanism of the impurity diffusion); it is also possible to retard drastically the impurity diffusion under conditions of complete annihilation of native defects [3].

An analysis of angular dependences of cyclotron-resonance spectra for electrons and holes and also study of quantized electrical conductivity [3, 5] have shown that the ultrashallow boron-diffusion profiles (extending to a depth of 5–20 nm according to the data obtained by secondary-ion mass spectroscopy [4, 6]) obtained by the above method consist of two-dimensional heavily doped barriers, between which the self-ordered quantum wells (QWs) are formed. Depending on the conditions of nonequilibrium diffusion, the processes of self-ordering of dopants may stimulate the formation of both transverse and longitudinal impurity superlattices. A certain advantage of impurity-related QWs and superlattices consists in the fact that they can be formed even in elemental semiconductors, for example, in the course of formation of silicon *p–n* junctions and transistor structures, in which the effects of transport of individual electrons and holes are pronounced [7, 8].

However, technological implementation of more complex devices of silicon nanoelectronics (for example, various combinations of single-electron memory cells and transistor structures) requires that the controlled sequences of longitudinal and transverse QWs be reproducibly formed; in turn, these sequences are defined by the form of the surface deformation potential that arises in the course of nonequilibrium diffusion of impurities. The most pronounced fluctuations in the deformation potential are observed if the KO or substitutional mechanisms of impurity diffusion are dominant; this is due to spatial separation of counter fluxes of self-interstitials or vacancies [3]. In this case, it should be expected that native defects that are not involved in the nonequilibrium impurity diffusion can form microdefects, which thread through the entire

depth of the ultrashallow diffusion profiles. Thus, in addition to the ordered QWs, a self-organized system of microdefects (anti-dots) may emerge in the course of nonequilibrium impurity diffusion; this system can affect the dynamics of ballistic transport of nonequilibrium charge carriers within the ultrashallow diffusion profiles.

In this paper, we report the results of studies of the surface of Si(100) with diffusion profiles of boron; the data were obtained by scanning tunneling microscopy (STM). We first consider the effects of the impurity-diffusion temperature and the thickness of the preliminary deposited oxide layer, which defines the magnitude and form of the surface deformation potential, on the characteristics of microdefects formed within the ultrashallow diffusion profile. We then analyze the interrelation between the sizes of microdefects and their spatial distribution; this interrelation forms the basis of the fractal mechanism for self-organization of zero-dimensional systems in the course of nonequilibrium impurity diffusion. Since the self-ordered systems of microdefects (anti-dots) incorporated into the impurity superlattices can constitute the basis for the formation of microcavities, we study the spectral dependences of the reflection and transmission coefficients in the visible and infrared regions of the spectrum in order to determine the characteristics of the above systems. In conclusion, we demonstrate for the first time an enhancement of the QW luminescence and the intracenter luminescence of a point defect, with the QW and the defect residing within the above microcavity.

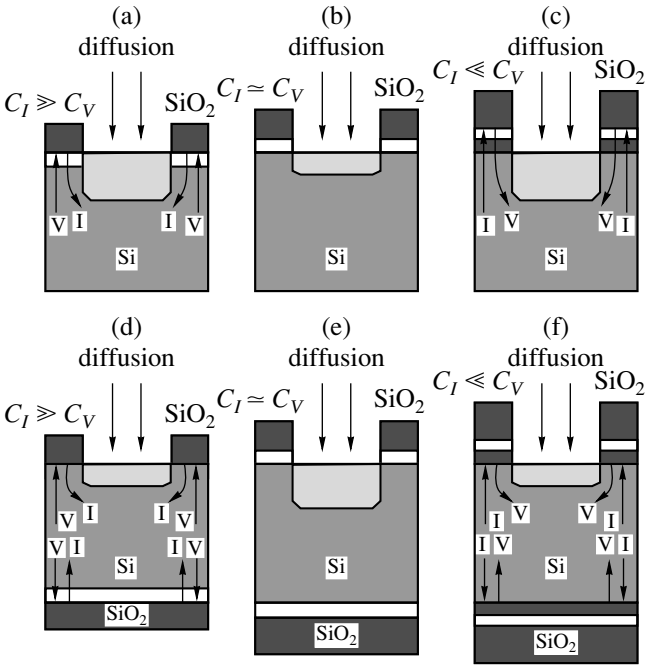

Fig. 1. Schematic representation of the procedure for obtaining the ultrashallow diffusion profiles of doping impurity under the conditions of injection of [(a) and (d)] self-interstitials I and [(c) and (f)] vacancies V in the presence of the oxide layer grown preliminarily [(a)–(c)] on only the operating surface and [(d)–(f)] on both surfaces of the substrate. C_I and C_V represent the nonequilibrium concentrations of self-interstitials and vacancies, respectively.

2. ULTRASHALLOW DIFFUSION PROFILES OF BORON IN SILICON

We used single-crystal *n*-Si(100) wafers with a thickness of 350 μm and a resistivity of 1.0 Ω cm as substrates in obtaining the ultrashallow diffusion profiles of boron. Preliminarily, both surfaces of the wafer were oxidized in an atmosphere of dry oxygen at a temperature of 1150°C. The oxide-layer thickness was governed by the oxidation time. It is noteworthy that the preliminary oxidation of both surfaces of the wafer was primarily used to accumulate both the self-interstitials (Fig. 1d) and the vacancies (Fig. 1f) in the substrate, which is attained if there is a thin and a thick surface oxide layer, respectively. Such an effect cannot be achieved if the operating surface alone is oxidized, which corresponds to the conditions of gettering the residual impurities; in this case, the self-interstitials and vacancies are involved in the formation of microdefects in the vicinity of the back surface of the substrates (Figs. 1a, 1c). After oxidation was over, we used photolithography to open the windows at the operating surface of the wafer in order to perform a short-term diffusion of boron from the gas phase.

By varying the diffusion temperature (T_d = 800, 900, and 1100°C) and the thickness of the preliminarily deposited oxide layer d_{SiO_2}, we managed to determine the optimal conditions for predominance of the KO and vacancy mechanisms for the boron diffusion and establish the criteria for their parity. A high level of generation of primary defects ensuring that the primary-defect diffusion is enhanced or retarded was attained not only by the preliminary accumulation of these defects in the substrate but also by the additional introduction of dry oxygen and chlorine compounds into the boron-containing gas phase.

An analysis of the obtained boron concentration profiles in Si(100) by the secondary-ion mass spectroscopy (Fig. 2) shows that the parity between the KO and vacancy diffusion mechanisms, which results in an abrupt retardation of impurity diffusion, is established at T_d = 900°C. In addition, we should expect that, due to intense annihilation of self-interstitials and vacancies, the fluctuations of the surface deformation potential can be minimized at a given temperature and under the existence of the oxide layer of a medium thickness. In the case of predominance of either the KO mechanism (T_d = 1100°C) or the vacancy mechanism (T_d = 800°C) of boron diffusion in silicon, the largest fluctuations in the surface deformation potential apparently arise in the presence of the thin and thick oxide layers, respectively.

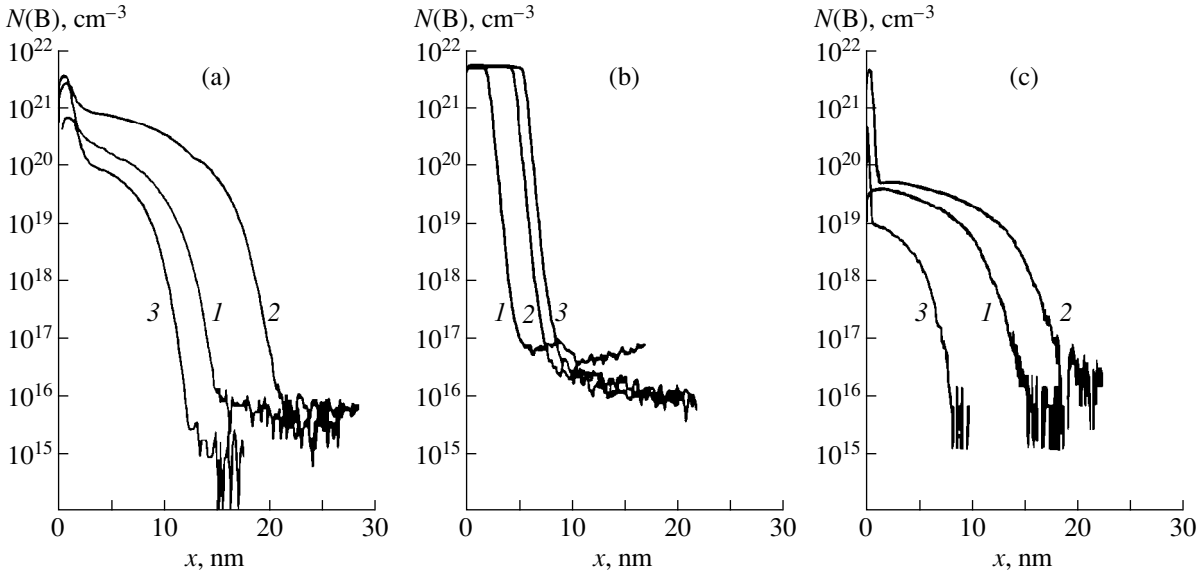

Fig. 2. The ultrashallow distributions of boron N(B) over the depth x in n-Si that were obtained at different diffusion temperatures T_d after the oxide layer with the thickness d_{SiO_2} was grown on both surfaces of the Si(100) wafer. Here, d_{SiO_2}/d_0 = (*1*) 0.17, (*2*) 1.0, and (*3*) 1.28; T_d = (a) 800, (b) 900, and (c) 1100°C. The oxide-layer thickness is defined by the duration of the silicon-wafer oxidation, and d_0 corresponds to the average oxide-layer thickness for which parity is attained between the KO and vacancy mechanisms of impurity diffusion.

The above assumption was verified by the analysis of angular dependences of the cyclotron resonance [3, 5], which made it possible to identify the longitudinal QWs within the ultrashallow boron-diffusion profile obtained under the conditions of parity between the KO and vacancy mechanisms of diffusion; conversely, the transverse QWs that are perpendicular to the ultrashallow-profile surface are dominant at T_d = 800 and 1100°C. In what follows, the influence of the surface deformation potential on the characteristics of ultrashallow boron profiles in Si(100) is analyzed on the basis of the data obtained by STM with an electromagnetic system of a coarse approach of the sample to the tip (Fig. 3a); this system operates both at room and liquid-helium temperatures. The study we report was performed at room temperature.

3. SCANNING TUNNELING MICROSCOPY OF SELF-ORDERED MICRODEFECTS AT THE SURFACE OF ULTRASHALLOW DIFFUSION PROFILES OF BORON IN SILICON (100)

Figures 4–6 show three-dimensional STM images of the surface-fragment topography for the boron diffusion profiles in silicon (100); the profiles were obtained for various diffusion temperatures (T_d) and oxide-layer thicknesses (d_{SiO_2}) and under different spatial resolutions.

As was mentioned above, the use of high diffusion temperatures (T_d = 1100°C) drastically enhances the diffusion of boron that penetrates into the silicon single crystal under the conditions of predominance of the KO mechanism. In turn, if the diffusion is carried out at relatively low temperatures (T_d = 800°C), the dominant role is played by the vacancy mechanism that implies the dragging of boron atoms by nonequilibrium vacancies. In addition, at moderate diffusion temperatures (T_d = 900°C), a parity between the two impurity-diffusion mechanisms can be attained, which causes a complete annihilation of self-interstitials and vacancies and ensures a drastic retardation of dopant diffusion. The diffusion rate also strongly depends on the oxide-layer thickness (d_{SiO_2}), because it defines the dominant type of excess defects. Vacancies stimulate the impurity diffusion predominantly for large values of d_{SiO_2}, whereas, for small thicknesses of the oxide, the impurities are largely dragged by self-interstitials.

Thus, if the diffusion temperature is T_d = 800°C and there is a thick layer of preliminarily deposited oxide, doping with boron was performed under the conditions of predominance of the vacancy mechanism of the impurity diffusion [4]. This means that there were a large number of vacancies at the initial stage of the diffusion. However, these vacancies were distributed nonuniformly throughout the crystal. It is evident that there were much fewer vacancies in the vicinity of bulging formations with a height of about 200 nm (Fig. 4a) than in the regions between these formations. These formations apparently constitute microdefects composed of interstitial atoms. Such a distribution of microdefects,

which arises due to fluctuations in the deformation potential, becomes evident as early as in the course of the window opening in the oxide layer in order to perform the impurity diffusion. In the course of photolithography, the etchant based on the hydrofluoric acid removes not only the oxide layer but also undercuts the silicon near-surface layer. The undercutting occurs in different ways: in the regions where there are less vacancies and the density is larger, it proceeds more slowly than in the regions where there are a large number of vacancies. As a result, there exists a relief of deformation potential (with a height, however, of much less than 200 nm) at the initially smooth surface of the window opened for the impurity diffusion. Boron was diffused from the gas phase at a temperature of 800°C through the surface, which was not quite smooth. At such a temperature, the diffusion proceeds only via vacancies and is dominant in the regions where there are many vacancies. In Fig. 4a, these regions are represented by dark areas. In the course of diffusion, the oxide layers outside the window opened by photolithography continue to supply the vacancies that predominantly move to the aforementioned regions with an initially high concentration of vacancies; thus, impurity diffusion is stimulated in these regions. As a result, the potential relief pattern in these regions is depressed with respect to the microdefects, into which the impurity atoms virtually do not penetrate. Thus, a selective etching of the surface occurs. For large accumulation of vacancies, the impurity diffusion along the crystallographic axis [100] occurs so rapidly that it is possible to identify the crystallographic directions [110] and [100] corresponding to the largest enhancement of impurity diffusion in the context of the vacancy mechanism (Fig. 6c). Different processes occur in the crystal regions where the impurity diffusion is retarded. In Fig. 4a, these regions constitute the microdefects. In the course of impurity diffusion, these microdefects represent the sinks for migrating silicon interstitials, which is reflected in an increase in the size of microdefects. A depression in the center of microdefects is related to the fact that the migration rate of silicon interstitials is highest along the crystallographic direction ⟨111⟩. As a result, the capture of silicon interstitials by microdefects occurs predominantly over the microdefect surface; i.e., the microdefects grow faster along their outer contour (along the equivalent crystallographic directions ⟨111⟩) than at their center. Thus, the sizes of microdefects that were first observed immediately after opening a window in the oxide increase in the course of the impurity diffusion. It is worth noting that the microdefects thread through not only the entirely of the diffusion profile but also through the remaining volume of the sample [9]; thus, self-ordered systems of large quantum anti-dots are formed (Fig. 3a).

When analyzing the results of studies of the boron diffusion profile obtained at $T_d = 800$°C and in the presence of the medium-thickness oxide layer (Fig. 4b), we should take into account that, in this case, the number

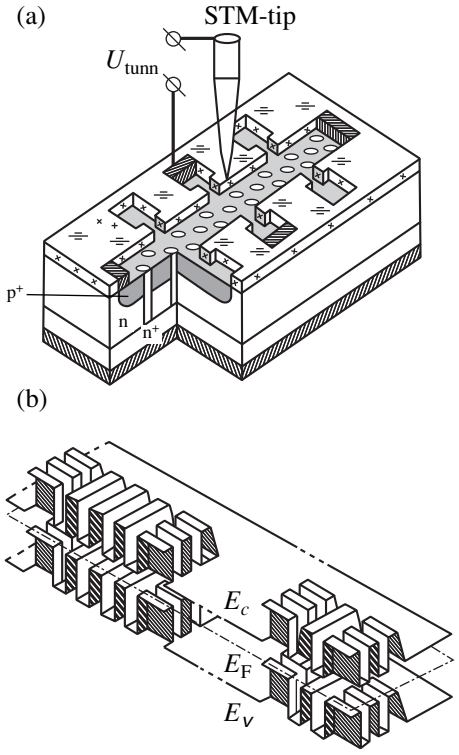

Fig. 3. (a) The planar structure used in STM studies of self-ordered systems of quantum anti-dots within the ultrashallow diffusion p^+-profile; U_{tunn} stands for the applied voltage. (b) Three-dimensional representation of the single-electron band structure of longitudinal and transverse QWs formed between the diffusion p^+-barriers of a self-ordered microcavity; the edges of the conduction band (E_c) and the valence band (E_v), as well as the Fermi level position (E_F), are shown.

of vacancies in the vicinity of the etched silicon surface (100) within the diffusion window is close to the number of interstitials. However, notwithstanding the fact that the vacancies and interstitials mostly annihilate each other, the boron atoms are dragged by vacancies as before due to the low temperature of the impurity diffusion. Nevertheless, the boron diffusion profiles forms relatively slowly due to the small number of vacancies accumulated in the volume in the stage of preliminary oxidation. In addition, the observed diffusion profile is more uniform due to a decrease in fluctuations of the surface deformation potential; this is reflected in the fact that the microdefects observed at the surface are much smaller in size (Fig. 4b) than in the case of the thick oxide layer (Fig. 4a).

Figure 4c shows an STM image of the surface of the diffusion profile obtained at the same diffusion temperature, but with a thin layer of preliminarily grown oxide. The presence of the thin oxide layer implies that there are comparatively few vacancies in the vicinity of the etched (100) surface within the diffusion window; in contrast, the clusters of silicon interstitials, which

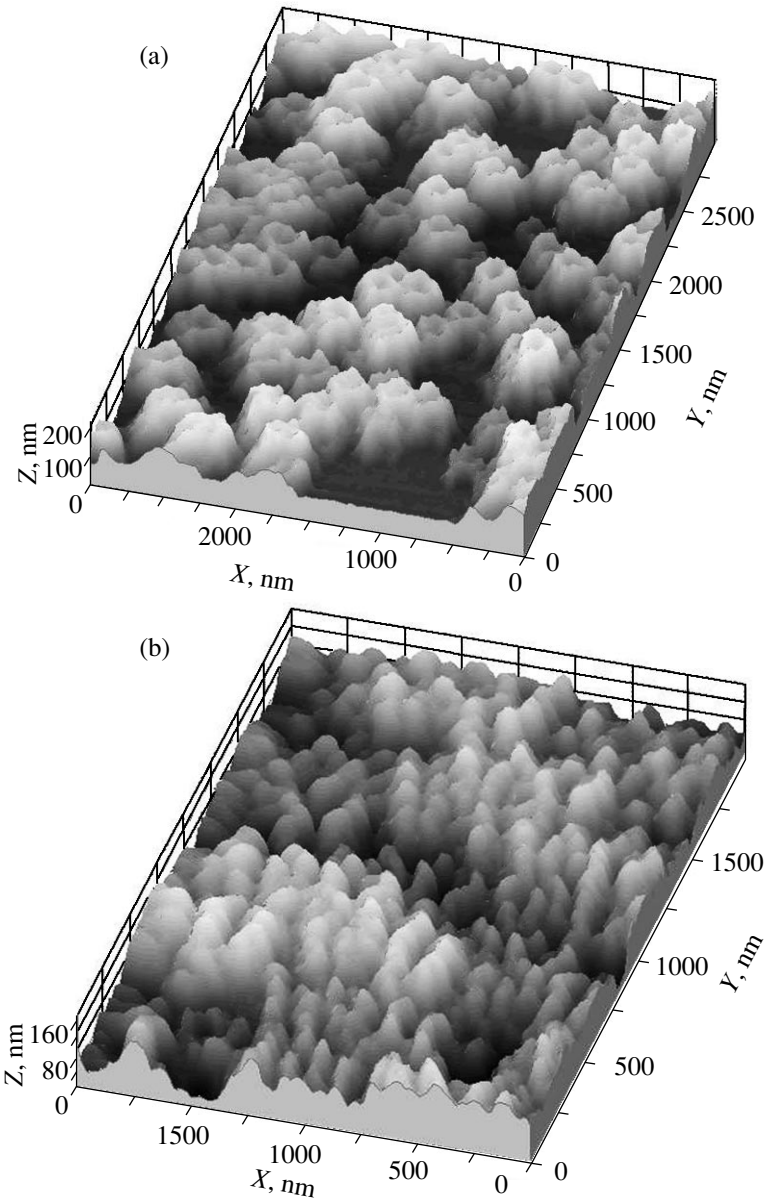

Fig. 4. Three-dimensional STM images of the surface region of ultrashallow boron-diffusion profiles in Si(100); the profiles were obtained at a diffusion temperature of T_d = 800°C in the presence of a preliminarily grown oxide layer: (a) with a thick layer (d_{SiO_2}/d_0 = 1.28); (b) with a layer of medium thickness (d_{SiO_2}/d_0 = 1.0); and (c) with a thin layer (d_{SiO_2}/d_0 = 0.17). Here, $X \parallel$ [001] and $Y \parallel$ [010].

serve as nuclei for formation of large and crystallographically oriented microdefects in the course of impurity diffusion, are dominant in this region. The above microdefects have a fine structure that is manifested even in the small surface fragments. As can be seen from Fig. 4c, there is a preferential direction at the (100) surface of silicon single crystal; this direction corresponds to the crystallographic axis [111], along which the microdefects are oriented. Such a crystallographic orientation of microdefects along either of two equivalent directions [111] lying in the (110) plane is caused by residual stresses, which frequently occur when a silicon ingot is cut into wafers. In this case, the diffusion of silicon self-interstitials can effectively decorate the direction of the largest (smallest) stress. It is noteworthy that the diffusion coefficient for silicon self-interstitials is largest along the crystallographic direction [111], whereas their diffusion along the direction [100] is suppressed to a large extent; conversely, the diffusion of vacancies is most rapid in the direction [100] and is retarded in the direction [111]. Such a dependence of diffusion rates of native defects in the crystallographic direction similarly affects the tensors of the nonequilibrium-diffusion coefficients for the

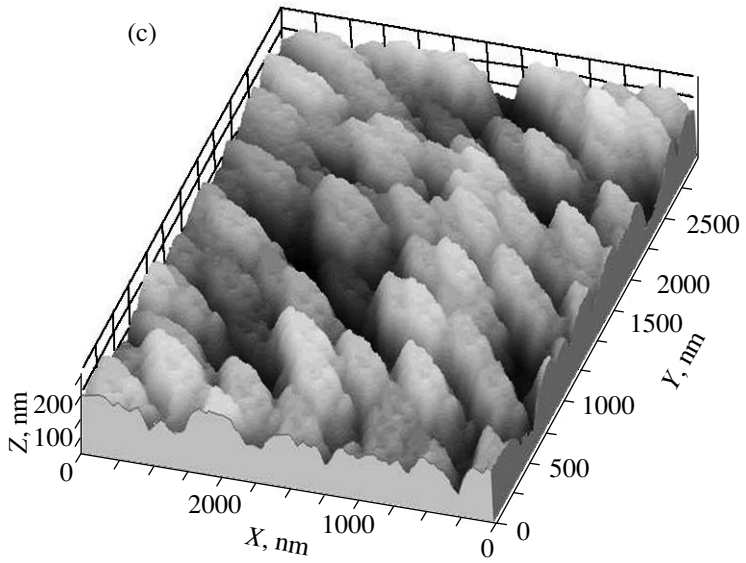

Fig. 4. (Contd.)

vacancy- and KO-controlled mechanisms [10, 11]. Because of this, the boron diffusion is retarded at T_d = 800°C under the conditions when there is a thin oxide layer at the surface; in this case, the microdefects oriented along the [111] axis that corresponds to the direction of the most rapid diffusion of silicon self-interstitials are dominant at the surface of the diffusion profile. In the case of a thick oxide layer, vacancies are dominant in the vicinity of the etched surface; thus, the residual silicon interstitials have to diffuse in the course of impurity diffusion along the [100] axis, which defines the direction of the microdefect growth under these conditions.

Thus, the initial deformation-potential distribution that depends on the thickness of the preliminarily grown oxide layer defines not only the crystallographic orientation of diffusion fluxes of impurity atoms but also the optimal growth direction for microdefects, which penetrate through the diffusion profile.

The STM images of the surface fragments of the boron diffusion profile obtained at the diffusion temperature of T_d = 900°C in the presence of the oxide layer of medium thickness are shown in Figs. 5a–5c. In this case, we have parity between the two mechanisms of diffusion, which makes it possible to obtain the most shallow diffusion profiles. The size of microdefects formed in the course of diffusion under the above technological conditions is appreciably smaller (Fig. 5) than that of microdefects formed at the surface at a diffusion temperature of 800°C. In addition, the roughness of the surface over the diffusion profiles is also moderate. Under these conditions, the ultrashallow diffusion profile forms appreciably more slowly than it does at T_d = 800°C due to intense annihilation of primary defects. Because of this, the excess fluxes of nonequilibrium interstitials and vacancies do not arise in the course of impurity diffusion; as a result, the magnitude of the deformation-potential fluctuations defined by the conditions of preliminary oxidation remains unchanged. Thus, the formation of the ultrashallow impurity profiles under conditions of parity between the diffusion mechanisms is accompanied by smoothing of the corresponding surface relief in the absence of appreciable fluctuations in the surface deformation potential.

It is worth noting that the shape of microdefects and, in particular, the special features of their spatial distribution at the surface of the diffusion profile, are well reproduced when the resolution of the recorded STM images is increased (Figs. 5a–5c, 4a, 6c). In other words, we observe complete interrelation between the sizes of microdefects and their spatial distribution irrespective of the magnitude of fluctuations in the surface deformation potential; this magnitude is larger in the diffusion profiles obtained at T_d = 800°C than in the case of parity between the diffusion mechanisms (T_d = 900°C). Such a hierarchy of microdefects, which is independent of the initial spread in their sizes, is indicative of a fractal mechanism of the microdefect formation in circumstances where the nonequilibrium fluxes of self-interstitials and vacancies are separated to a great extent owing to generation of fluctuations in the deformation potential at the silicon–oxide interface.

The suggested mechanism of forming the surface relief for ultrashallow diffusion profiles is substantiated by examination of an STM image of a surface fragment for the diffusion profile obtained at the diffusion temperature of 1100°C (Figs. 6a, 6b). At this temperature, the impurity diffusion is stimulated under the conditions when the KO mechanism is dominant; the role of this mechanism is enhanced owing to the presence of a thin layer of the preliminarily grown oxide at the surface. Because of this, the impurity diffusion and the

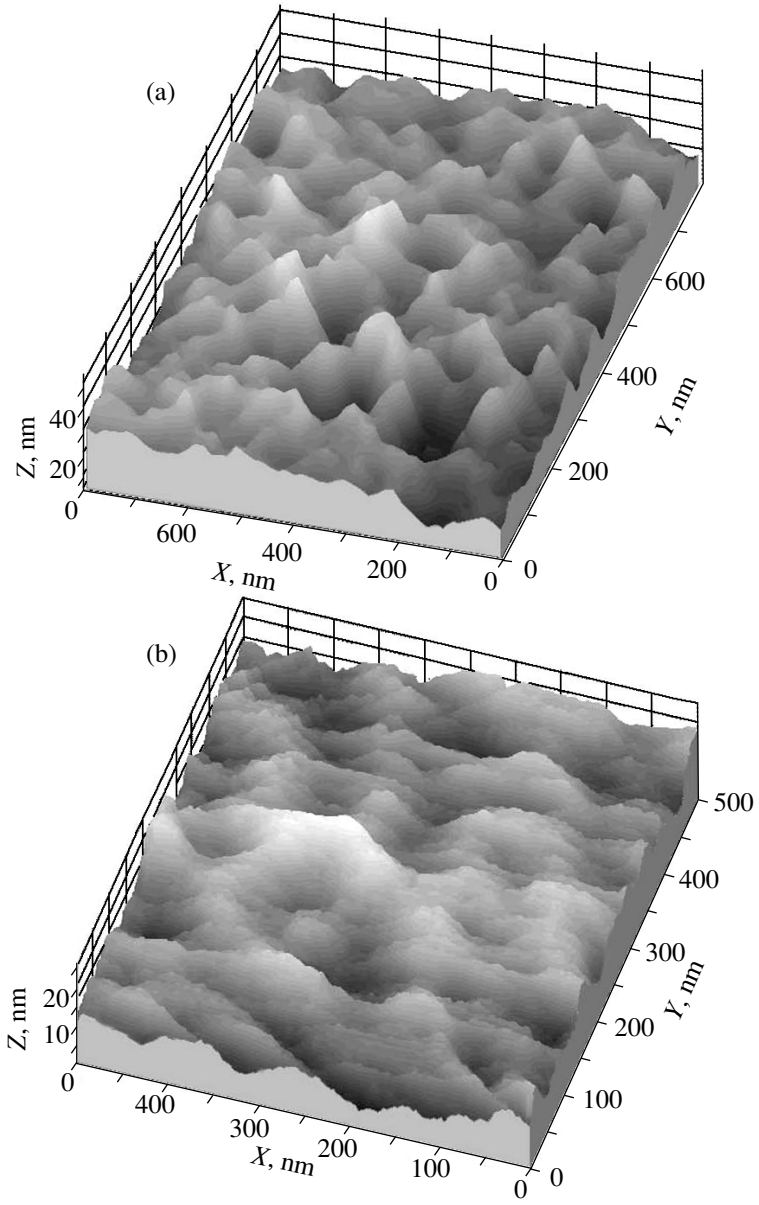

Fig. 5. Three-dimensional STM images of the surface region of ultrashallow boron-diffusion profiles in Si(100); the profiles were obtained at the diffusion temperature of T_d = 900°C in the presence of a preliminarily grown oxide layer with medium thickness (d_{SiO_2}/d_0 = 1.0). Here, $X \parallel [001]$ and $Y \parallel [010]$. The images (a), (b), and (c) correspond to different spatial resolutions.

microdefect formation are accelerated along either of two equivalent axes [111] lying in the (110) plane that is perpendicular to the operating (100) silicon surface (Fig. 6a); the above axes correspond to the highest migration rate of silicon interstitials. It is important that there are no large microdefects at the surface of the boron diffusion profile obtained at T_d = 1100°C; this is caused by intense interaction of self-interstitials with the dopant under the conditions where the KO diffusion mechanism is predominant. In this case, most silicon interstitials stimulate the impurity diffusion and are not involved in the formation of microdefects at the sites where there are fluctuations of the deformation potential.

Thus, a comparative analysis of STM images shown in Figs. 4a and 6a shows that the microdefects originating in the course of nonequilibrium impurity diffusion consist predominantly of silicon self-interstitials, whereas the migration of nonequilibrium vacancies does not give rise to similar defects. Apparently, this is due to a low mobility of vacancies compared to the mobility of self-interstitials.

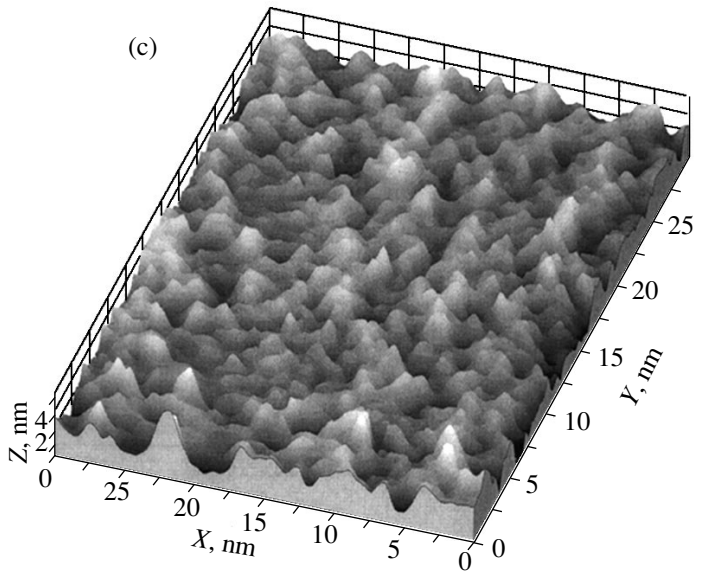

Fig. 5. (Contd.)

The observed microdefects constitute the systems of anti-dots incorporated into the impurity superlattices that comprise the ultrashallow diffusion profiles [3, 12], which makes it possible to recognize these microdefects as the basis for formation of self-ordered microcavities (Fig. 7). In order to identify these unconventional microcavities whose characteristics are defined by the sizes and distribution of microdefects, we studied the spectral dependences of the reflection and transmission coefficients in the visible and infrared regions of the spectrum.

4. OPTICAL PROPERTIES OF SELF-ORDERED ANTI-DOTS AT THE (100) SILICON SURFACE

Self-ordered microcavities incorporated into the impurity superlattices at the (100) silicon surface (Fig. 3b) reduce appreciably the reflection coefficient of light in the short-wavelength region of the spectrum; this reflection is due to direct band-to-band transitions in narrow QWs (with a width of $d \approx 2$ nm) formed in the plane of the ultrashallow diffusion p^+-profile [3, 6, 8]. In the foregoing, we referred to these QWs, which are

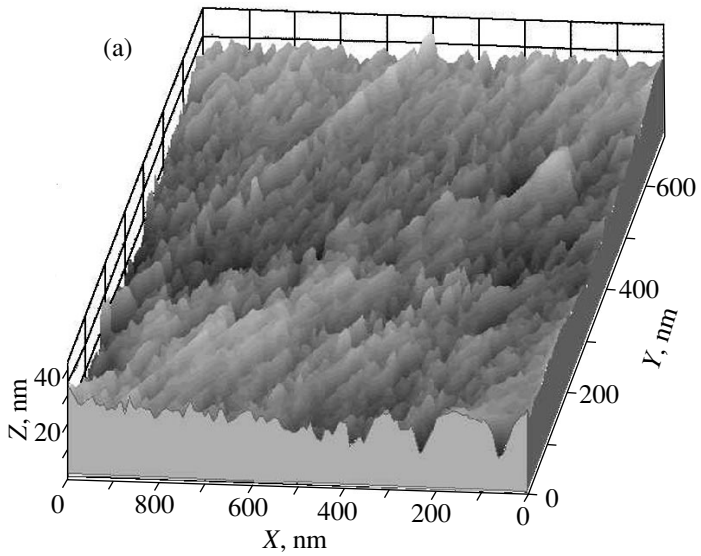

Fig. 6. Three-dimensional STM images of the surface region of ultrashallow boron-diffusion profiles in Si(100); the profiles were obtained at the diffusion temperature of T_d = [(a) and (b)] 1100 and (c) 800°C in the presence of a preliminarily grown oxide layer with the relative thickness d_{SiO_2}/d_0 = [(a) and (b)] 0.17 (a thin layer) and (c) 1.28 (a thick layer). Here, $X \parallel [001]$ and $Y \parallel [010]$.

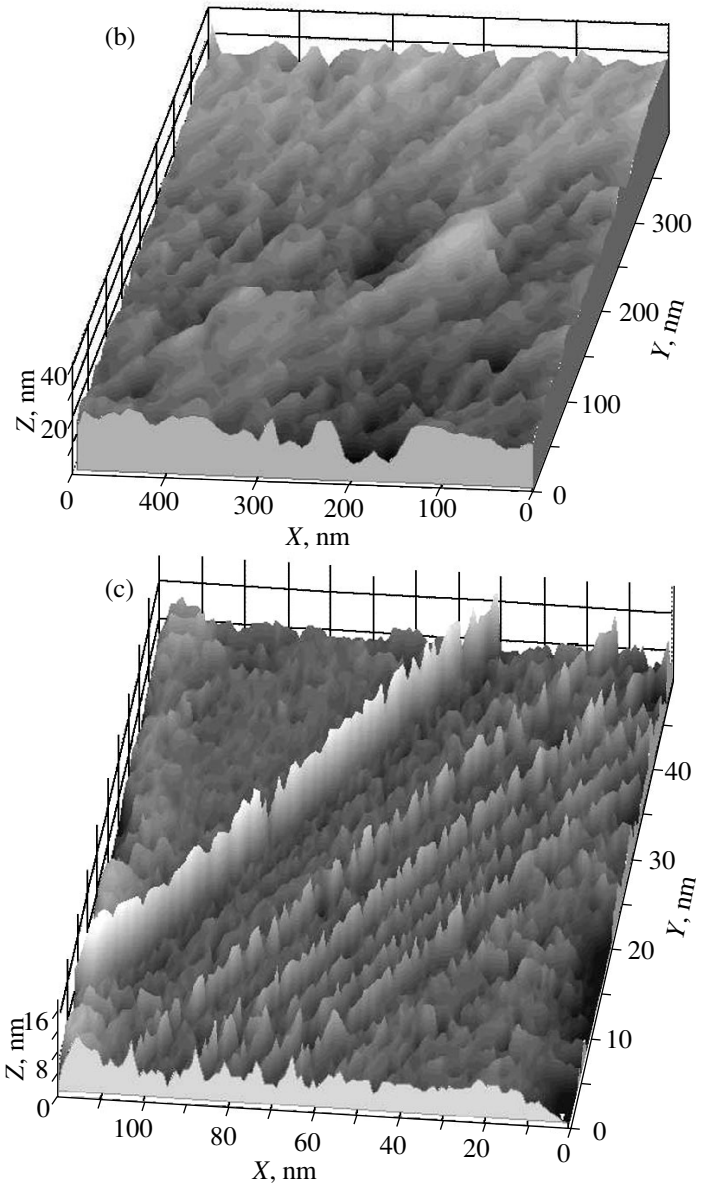

Fig. 6. (Contd.)

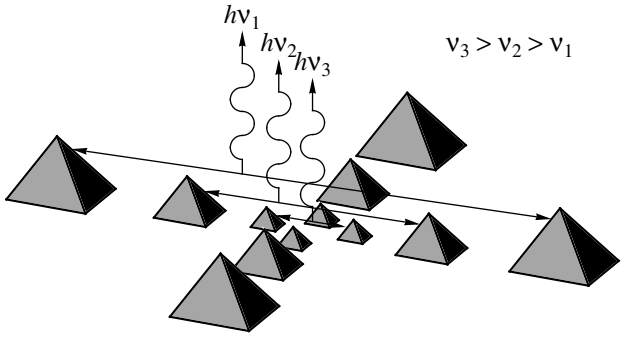

Fig. 7. A model of a system of microcavities based on quantum anti-dots obtained as a result of the fractal mechanism of diffusion doping under conditions of the primary-defect injection.

components of the impurity superlattice, as longitudinal QWs.

The reflection spectra $R(\lambda)$ were studied using a UV-VIS Specord M-40 spectrophotometer produced by Carl Zeiss Jena and equipped with an Ulbricht sphere for the reflectivity measurements. Figure 8 shows the spectra of reflection of light from ultrashallow diffusion p^+-profiles obtained at different boron-diffusion temperatures.

A decrease in $R(\lambda)$ compared with the case of moderately doped silicon single-crystal, as well as a broadening of the peaks at the wavelengths of $\lambda = 354$ and 275 nm, are characteristic of all the samples studied; the above peaks are related to transitions between the

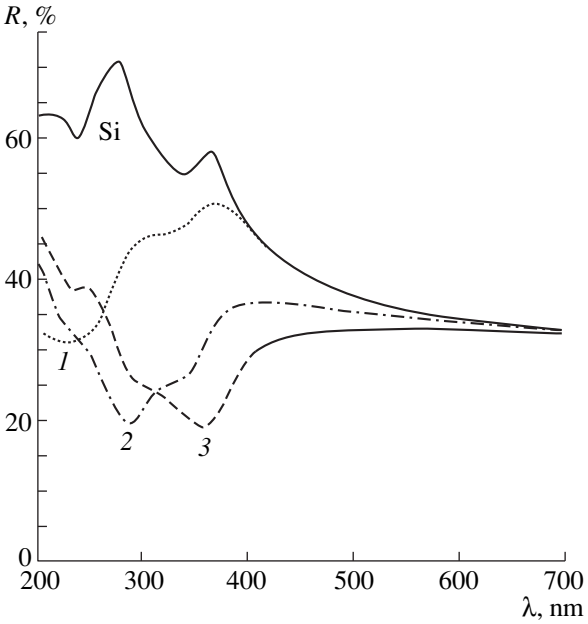

Fig. 8. Spectral dependence of the coefficient $R(\lambda)$ of the reflection of light from the surface of a Si(100) single crystal and from ultrashallow Si p^+–n junctions in the (100) plane; these junctions were obtained at different boron-diffusion temperatures and for differing thicknesses of the preliminarily grown oxide layer. Curve *1* corresponds to Fig. 6c; curve *2*, to Fig. 5b; and curve *3*, to Fig. 6b.

Γ–L valleys and in the vicinity of the point X in the Brillouin zone, with the former of the above peaks being assigned to the direct transitions Γ'_{25}–Γ_{15}, L'_3–L_1, and Γ'_{25}–Γ_2, whereas the latter peak is attributed to the transitions X_4–X_1 and Σ_4–Σ_1.

An analysis of the spectral dependence of the reflection coefficient shows that the presence of microcavities self-assembled between the self-ordered microdefects with medium sizes reduces $R(\lambda)$ most profoundly in the short-wavelength region of the spectrum (200–330 nm), whereas the presence of larger microdefects is conducive to effective reflection of light in the region of longer wavelengths ($\lambda > 330$ nm). It follows from the comparison of $R(\lambda)$ with the STM data that the position of a minimum in the reflection coefficient in the spectral dependence $R(\lambda)$ and the microcavity size are interrelated and satisfy the Bragg condition; i.e., we have $x = \lambda/2n$, where x is the cavity size, λ is the wavelength, and n is the refractive index of silicon (see Figs. 8, 6c, 5b, 6b).

The presence of large quantum anti-dots (see, e.g., Fig. 4a) incorporated into a system of narrow silicon QWs makes it possible to obtain microcavities having distributed feedback and corresponding to λ [μm] < $1.24/E_g$ [eV], where E_g is the band gap of silicon; the characteristics of these microcavities are determined from the spectral dependences of the transmission coefficient in the infrared region of the spectrum. Figure 9 shows the spectral dependences of the transmission coefficient measured at room temperature using an IFS-28 Bruker infrared Fourier spectrometer for the studied ultrashallow diffusion profiles.

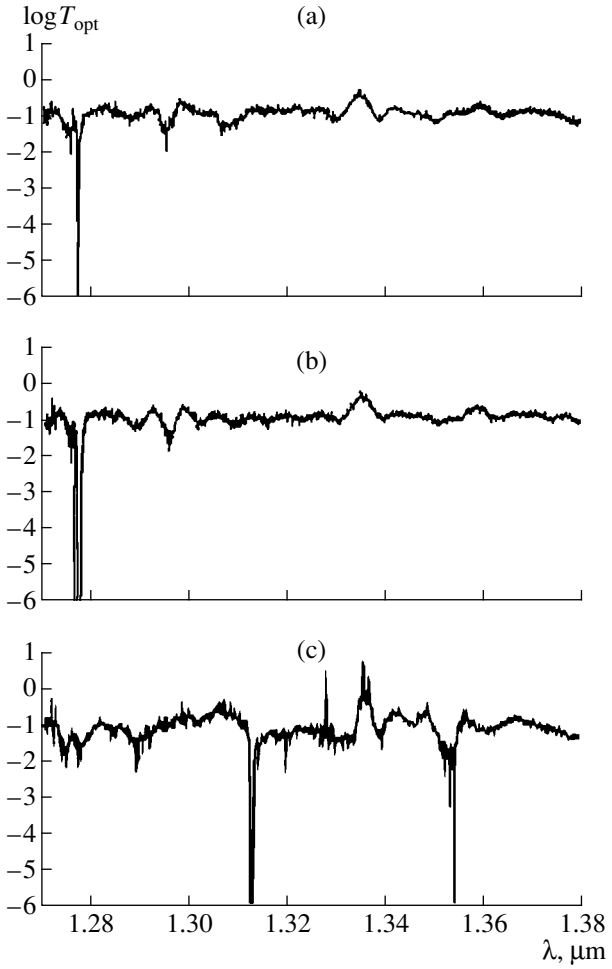

Fig. 9. Spectral dependence of the coefficient of transmission of light T_{opt} through a self-ordered system of quantum anti-dots within the ultrashallow diffusion p^+-profile; this dependence makes it possible to determine the characteristics of incorporated microcavities. (a) Corresponds to Fig. 4a; (b) corresponds to Fig. 5; and (c) corresponds to Figs. 6a and 6b. T = 300 K.

The spectral dependences we report are clearly indicative of the presence of self-ordered microcavities whose sizes determined from the STM images are consistent with the corresponding wavelengths in accordance with the Bragg condition. The presence of longitudinal narrow QWs ($d \approx 2$ nm) within the microcavities made it possible to detect the Rabi splitting (Fig. 9c); the latter is an important characteristic of microcavities incorporated into systems of semiconductor superlattices [13, 14]. An additional indication that the absorption lines defined by intraband transitions of holes in a p-type QW with $d \approx 2$ nm (see

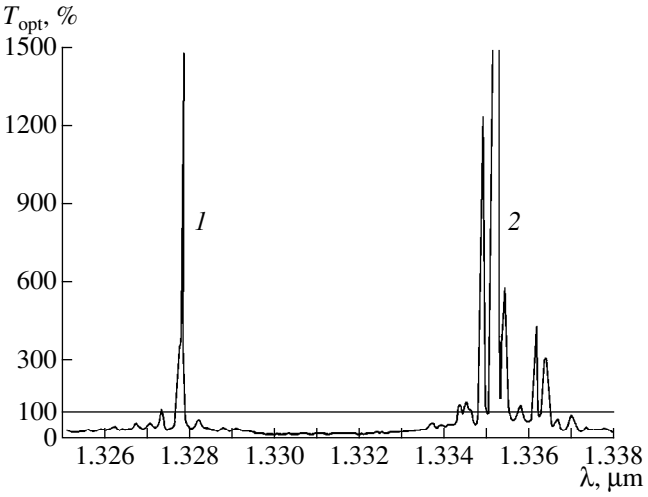

Fig. 10. Spectral dependence of the coefficient of transmission of light T_{opt} at 300 K through the ultrashallow diffusion p^+-profile in Si(100); the profile was obtained at T_d = 1100°C (Figs. 6a, 6b), and this dependence is indicative of enhancement of (*1*) luminescence from QW and (*2*) intracenter luminescence of the point defect residing within the microcavity in a system of self-ordered quantum anti-dots (see Fig. 9c).

Fig. 3b) are related to the Rabi splitting is the observed enhancement of luminescence in the corresponding range of wavelengths (Fig. 10).

The spectral line peaked at 1.3278 μm (see Fig. 10) is apparently related to the intraband luminescence of holes in the course of their tunneling between longitudinal QWs within the microcavity (Fig. 3b). The tunneling occurs due to the presence of the built-in electric field within an ultrashallow diffusion p^+-profile at the surface of *n*-Si(100); this electric field is simply the field of the p^+–*n* junction.

The allowed spectrum observed in the wavelength range of λ = 1.3335–1.3375 μm (Fig. 10) may be related to a point defect residing within the cavity. A tentative analysis of the energy spectrum indicates that residual copper-containing centers, which originate in the course of doping from the gas phase, are involved in the formation of this spectrum. The number of lines in the spectrum is indicative of the splitting of the center's ground state under the effect of the electric field of the p^+–*n* junction.

It is noteworthy that the enhancement of intracenter and interband luminescence induced by the point impurity centers residing in silicon microcavities is quite an important problem; the solution to this problem would make it possible to increase drastically the efficiency of intracenter luminescence of Er^{3+} ions in silicon light-emitting diodes designed for fiber-optical communication links [15].

CONCLUSION

The use of scanning tunneling microscopy made it possible to assess the influence of the impurity-diffusion temperature and the parameters of preliminary oxidation on the characteristics of the surface relief pattern in ultrashallow diffusion profiles of boron in Si(100).

It was found that the initial deformation-potential distribution governed by the thickness of the preliminarily grown oxide defined the crystallographic dependence of the impurity-diffusion coefficient under conditions of dragging both the vacancies and the interstitials by the excess fluxes; the above potential distribution also defines the spatial distribution and optimal growth direction of the self-ordered microdefects that are induced by these fluxes and thread the diffusion profiles of the doping impurity.

It is shown that the spread in the sizes of observed microdefects that constitute the self-assembled systems of quantum anti-dots reflects the magnitude of the deformation-potential fluctuations and decreases with decreasing temperature of impurity diffusion. In addition, we revealed the interrelation between the sizes of quantum anti-dots and their spatial distribution; this interrelation is indicative of a fractal mechanism of formation of self-ordered zero-dimensional systems under conditions of strong interaction between the nonequilibrium fluxes of impurity atoms and those of primary defects.

The production of self-assembled systems of quantum anti-dots incorporated into a system of silicon QWs made it possible to form microcavities with distributed feedback; the characteristics of these were determined using the spectral dependences of the reflection and transmission coefficients in the visible and infrared regions of the spectrum, respectively.

We demonstrated for the first time an enhancement in luminescence from a QW and in intracenter luminescence of a point defect, with both the QW and the defect residing within the aforementioned microcavity.

ACKNOWLEDGMENTS

This work was supported by the Federal Programs "The Physics of Solid-State Nanostructures" (project no. 97-1040), "Promising Technologies and Devices of Microelectronics and Nanoelectronics" (project no. 02.04.301.89.5.2), and "Integration" (project no. 75:2.1).

REFERENCES

1. R. Nötzel, Semicond. Sci. Technol. **11**, 1365 (1996).
2. H.-J. Gossman and J. M. Poate, in *Proceedings of the ICPS-23, Berlin, 1996*, Vol. 4, p. 2569.
3. N. T. Bagraev, E. I. Chaikina, L. E. Klyachkin, *et al.*, Superlattices Microstruct. **23** (2), 337 (1998).

4. N. T. Bagraev, W. Gehlhoff, L. E. Klyachkin, and A. Näser, Defect Diffus. Forum **143/147**, 1003 (1997).
5. W. Gehlhoff, N. T. Bagraev, and L. E. Klyachkin, Solid State Phenom. **47/48**, 589 (1995).
6. N. T. Bagraev, W. Gehlhoff, L. E. Klyachkin, *et al.*, Mater. Sci. Forum **258/263**, 1683 (1997).
7. N. T. Bagraev, L. E. Klyachkin, A. M. Malyarenko, and W. Gehlhoff, in *Proceedings of the ICPS-23, Berlin, 1996*, Vol. 2, p. 1241.
8. N. T. Bagraev, L. E. Klyachkin, A. M. Malyarenko, and W. Gehlhoff, Superlattices Microstruct. **23** (6), 1333 (1998).
9. N. T. Bagraev, L. E. Klyachkin, A. M. Malyarenko, *et al.*, Fiz. Tekh. Poluprovodn. (Leningrad) **24** (9), 1557 (1990) [Sov. Phys. Semicond. **24** (9), 973 (1990)].
10. A. N. Andronov, N. T. Bagraev, L. E. Klyachkin, and S. V. Robozerov, Fiz. Tekh. Poluprovodn. (St. Petersburg) **32**, 137 (1998) [Semiconductors **32**, 124 (1998)].
11. A. N. Andronov, N. T. Bagraev, L. E. Klyachkin, *et al.*, Fiz. Tekh. Poluprovodn. (St. Petersburg) **33** (1), 58 (1999) [Semiconductors **33**, 51 (1999)].
12. A. N. Andronov, N. T. Bagraev, L. E. Klyachkin, *et al.*, Fiz. Tverd. Tela (St. Petersburg) **41** (10), 1871 (1999) [Phys. Solid State **41** (10), 1719 (1999)].
13. R. Houdré, R. P. Stanley, and C. Weisbuch, *et al.*, in *Proceedings of the ICPS-23, Berlin, 1996*, Vol. 4, p. 3071.
14. R. Houdré *et al.*, Phys. Rev. B **49**, 16761 (1994).
15. N.T. Bagraev, A.D. Bouravleuv, W. Gehlhoff, *et al.*, Phys. B **273/274** (1/4), 967 (1999).

Translated by A. Spitsyn

Semiconductors, Vol. 34, No. 6, 2000, pp. 712–716. Translated from Fizika i Tekhnika Poluprovodnikov, Vol. 34, No. 6, 2000, pp. 737–741.

LOW-DIMENSIONAL SYSTEMS

Ballistic Conductance of a Quantum Wire at Finite Temperatures

N. T. Bagraev*, V. K. Ivanov, L. E. Klyachkin*, A. M. Malyarenko*, and I. A. Shelykh****

** Ioffe Physicotechnical Institute, Russian Academy of Sciences, Politekhnicheskaya ul. 26, St. Petersburg, 194021 Russia*

*** St. Petersburg State Technical University, Politekhnicheskaya ul. 29, St. Petersburg, 195251 Russia*

Submitted December 30, 1999; accepted for publication December 30, 1999

Abstract—The temperature-dependent ballistic conductance of a quantum wire is calculated without consideration of carrier scattering. The contribution to the conductance (G) from size–quantization subbands with $E_j - \mu \gg kT$ is described by the Landauer–Büttiker formula $G = 2e^2/h$, where e is the elementary charge, h is Planck's constant, $\mu(T)$ is the electrochemical potential, E_j is the j-th subband bottom, T is temperature, and k is the Boltzmann constant. The contribution from other subbands decreases as their number increases, being exponentially small for higher subbands. The quantum staircase disappears when kT approaches the energy spacing between the size–quantization levels. Such temperature quenching of the quantum staircase at gate potentials corresponding to a stepwise change in the ballistic conductance is observed in studies of the quantized conductance of a silicon quantum wire. © *2000 MAIK "Nauka/Interperiodica".*

The conductance of a single ballistic quantum wire at zero temperature can be described within the weak-pulling-voltage approximation by the Landauer–Buttiker formula [1, 2]:

$$G = 2\frac{e^2}{h}N(\mu_0), \tag{1}$$

where μ_0 is the electrochemical potential of carriers at zero temperature and is equal to the Fermi energy and where $N(\mu_0)$ is the number of occupied size–quantization (SQ) subbands, as determined by the Fermi level position relative to their bottom. N can be changed by applying a gate voltage V_g, which changes the carrier density in the wire and, therefore, the value of $\mu_0 \equiv E_F$.

As follows from (1), the conductance at $T = 0$ is independent of the pulling voltage V; i.e. the current–voltage (I–V) characteristic is linear. At the same time, the dependence of the conductance on the gate voltage V_g, is stepwise [3, 4]. Deviations from formula (1) may be observed because of carrier transitions between the SQ subbands under the action of the pulling voltage [5]. Such transitions are the most probable for values of V_g corresponding to conductance steps, which would cause the dependence $G(V_g)$ to be smooth and the I–V characteristics to be nonlinear.

Of interest is the problem of the ballistic conductance of a quantum wire at a finite temperature, when the number of occupied SQ subbands is, strictly speaking, indeterminate, since there exists a finite temperature-dependent probability of finding an electron in any of them. The subband occupancy is determined by the Fermi distribution

$$n(\varepsilon) = \frac{1}{e^{(\varepsilon-\mu)/kT}+1}, \tag{2}$$

where $\varepsilon = E_j + p^2/2m$ (E_j is the j-th SQ subband bottom), μ is the temperature-dependent electrochemical potential determined from the equation

$$n = \frac{2}{2\pi\hbar} \times \sum_{j=0}^{+\infty}\int_{-\infty}^{+\infty}\left[1+\exp\left(\frac{E_j + p^2/2m - \mu}{kT}\right)\right]^{-1} dp = \frac{1}{\pi\hbar}\sum_{j=0}^{\infty} I_j. \tag{3}$$

At an arbitrary temperature, the integrals appearing in (3) can be calculated only numerically. However, of interest is the limiting case of kT sufficiently small in comparison with $|E_j - \mu|$. In this case, the integrals in (3) can be classified into two types:

$$\begin{aligned} 1)\ &\frac{E_j-\mu}{kT} \gg 0, \\ 2)\ &\frac{E_j-\mu}{kT} < 0. \end{aligned} \tag{4}$$

In calculating integrals of the first type, the unity in (3) can be neglected. In this case, the Fermi distribution

reduces to the Boltzmann distribution; thus, we have

$$I_j^{(1)} = \exp\left(\frac{\mu - E_j}{kT}\right)\int_{-\infty}^{+\infty}\exp\left(-\frac{p^2}{2mkT}\right)dp = \sqrt{2\pi mkT}\exp\left(\frac{\mu - E_j}{kT}\right). \quad (5)$$

The integrals of the second type are calculated by the conventional procedure [6], which yields

$$I_j^{(2)} = \int_{-\infty}^{+\infty}\left[1 + \exp\left(\frac{E_j + p^2/2m - \mu}{kT}\right)\right]^{-1} dp = \sqrt{2m}\int_0^{+\infty}\left[1 + \exp\left(\frac{\varepsilon - \zeta_j}{kT}\right)\right]^{-1}\varepsilon^{-1/2}d\varepsilon. \quad (6)$$

Changing the variable $\eta = (\varepsilon - \zeta_j)/kT$ and expanding the function $(\zeta_j + \eta kT)^{1/2}$ in powers of η up to second-order terms, we obtain

$$I_j^{(2)} = \sqrt{8m}\int_{-\infty}^{+\infty}\left[\zeta_j^{1/2} + \frac{kT}{2\zeta_j^{1/2}}\eta - \frac{(kT)^2}{8\zeta_j^{3/2}}\eta^2\right]\frac{e^{-\eta}}{(1+e^{-\eta})^2}d\eta = \sqrt{8m}(\mu - E_j)^{1/2}\left[1 - \frac{\pi^2(kT)^2}{24(\mu - E_j)^2}\right]. \quad (7)$$

Thus,

$$n = \frac{\sqrt{8m}}{\pi\hbar}\sum_{E_j < E_F}(\mu - E_j)^{1/2}\left[1 - \frac{\pi^2(kT)^2}{24(\mu - E_j)^2}\right] + \frac{\sqrt{2\pi mkT}}{\pi\hbar}\sum_{E_j > E_F}\exp\left[\frac{\mu - E_j}{kT}\right]. \quad (8)$$

The dependence $\mu(n, T)$ is determined by solving this equation for μ, which is only possible when the SQ spectrum $\{E_j\}_{j=0}^{\infty}$ of the wire is known.

If we consider the case of a single SQ subband with bottom $E_0 = 0$, then, at a sufficiently low temperature and for high carrier density, we obtain the following approximate expression:

$$\mu(n, T) = \frac{(\pi\hbar n)^2}{8m}\left[1 - \frac{\pi^2(kT)^2}{24\mu_0^2}\right]^{-2}. \quad (9)$$

The exact form of the dependence $\mu(n)$ for this case is presented in Fig. 1.

Let us consider now the conductance of a ballistic quantum wire at a certain prescribed temperature and electrochemical potential (determined by the carrier density) for a given SQ spectrum $\{E_j\}_{j=0}^{\infty}$. We calculate the contribution to the conductance from an SQ subband with some number j, neglecting inter-subband

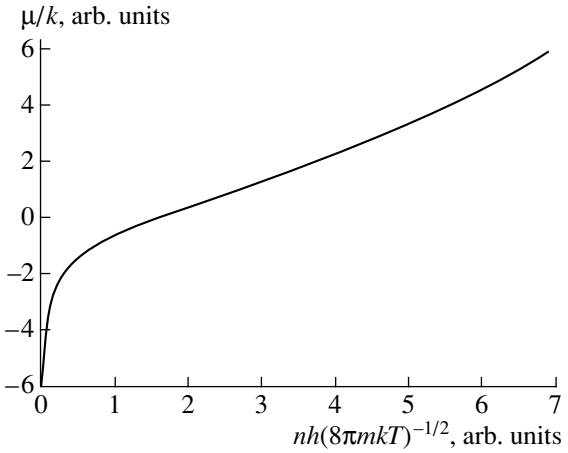

Fig. 1. Calculated dependence of the electrochemical potential μ on the carrier concentration in the quantum wire with a single size-quantization subband ($E_0 = 0$) at $T = 1$ K.

transitions of carriers. To start, let us consider a derivation of this kind for $T = 0$. In this case, empty subbands with $E_j < \mu_0$ make no contribution to the conductance at all. To calculate the conductance of an occupied subband, two infinitely large reservoirs of electrons are considered, separated by a point contact that replaces the quantum wire. The difference between the electrochemical potential to the left and to the right of the contact is equal to the product of the electron charge by the pulling voltage applied to the wire: $\mu_1 - \mu_2 = eV$. Only states with energy E in the range of $\mu_2 < E < \mu_1$ contribute to the conductance. Thus, the conductance is given by

$$G = I/V = \frac{2e}{V}\sum_{\mu_2 < E < \mu_1} v_x = 2\frac{e}{m}\sum_{\mu_2 < E < \mu_1} p_x = \frac{e}{\pi m\hbar}\int_{\sqrt{2m(\varepsilon - eV)}}^{\sqrt{2m\varepsilon}} pdp = 2\frac{e^2}{h}. \quad (10)$$

In the case of a finite temperature, we have to take into consideration that the energy distribution of electrons is broadened and electrons with any energy can contribute to the current with some probability. Calculating the current through the contact as a difference of the currents flowing from left to right and vice versa, we obtain

$$G_j = \frac{e}{\pi m\hbar V}\int_0^{\infty} p\{f(p, \mu_1, T)[1 - f(p, \mu_1, T)] - f(p, \mu_2, T)[1 - f(p, \mu_2, T)]\}dp = \frac{e}{\pi m\hbar V}\int_0^{\infty} p[f(p, \mu_1, T) - f(p, \mu_2, T)]dp \quad (11)$$

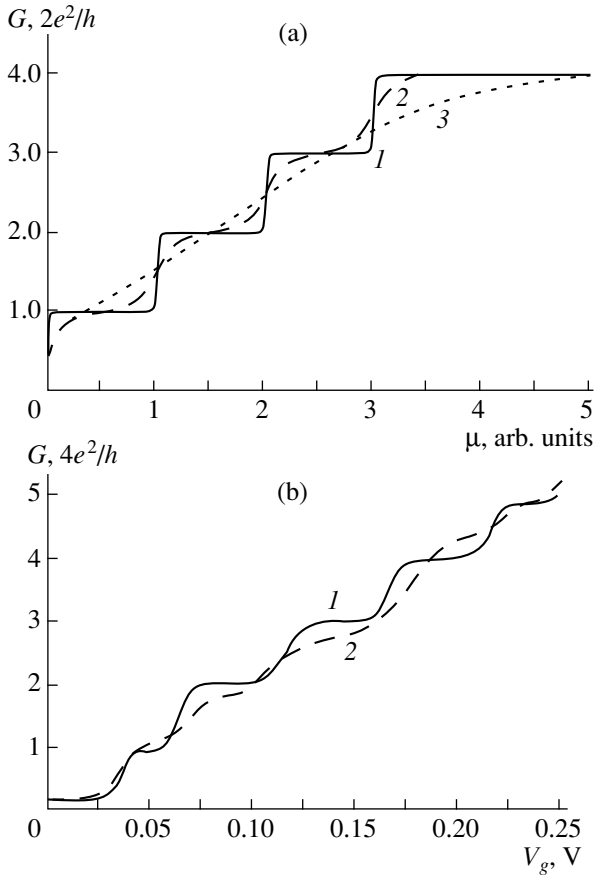

Fig. 2. Quantized conductance at different temperatures. (a) Calculated dependence of the conductance on the electrochemical potential μ at T = (*1*) 0, (*2*) $0.1\Delta E/k$, and (*3*) $0.6\Delta E/k$. (b) Experimental dependence of the conductance on the gate voltage V_g at T = (*1*) 77 and T = (*2*) 300 K.

$$= \frac{e}{\pi m\hbar V}\int_0^\infty p[\,f(p,\mu_1,T) - f(p,\mu_1 - eV,T)\,]dp,$$

where $f(p, \mu, T)$ stands for the Fermi distribution. Thus,

$$G_j = \frac{e}{\pi m\hbar V}\int_0^\infty p\left[\frac{1}{1+e^{(E_j-\mu_1)/kT}e^{p^2/2mkT}}\right.$$

$$\left. - \frac{1}{1+e^{(E_j-\mu_1+eV)/kT}e^{p^2/2mkT}}\right]dp \qquad (12)$$

$$= \frac{2ekT}{hV}\ln\left[\frac{1+e^{(\mu_1-E_j)/kT}e^{eV/kT}}{1+e^{(\mu_1-E_j)/kT}}\right].$$

It can be seen that the conductance at a finite temperature depends both on the carrier density and on the applied pulling voltage. In the limit of weak pulling voltages, we have

$$G_j = \frac{2e^2}{h}\frac{e^{(\mu_1-E_j)/kT}}{1+e^{(\mu_1-E_j)/kT}}. \qquad (13)$$

Let us consider several limiting cases.

(i) Occupied subbands with a low bottom $(\mu_1 - E_j)/kT \gg 1$. In this case, we can neglect unity in the denominator of (13). Therefore, the conductance does not differ from its value at zero temperature

$$G_j = \frac{2e^2}{h}. \qquad (14)$$

(ii) $(\mu_1 - E_j)/kT \sim 0$. This situation occurs near regions of stepwise conductance change. Expanding the exponents in a series, we obtain

$$G = \frac{e^2}{h}\left(1 + \frac{m_1 - E_j}{kT}\right). \qquad (15)$$

It can be seen that, if the chemical potential coincides with the bottom of a subband, its contribution to the conductance is half the contribution of an occupied subband at $T = 0$.

(iii) High-lying subbands that are empty at zero temperature. For these subbands $(\mu_1 - E_j)/kT \ll 0$, so that

$$G_j = \frac{2e^2}{h}e^{(\mu_1-E_j)/kT} \ll 1. \qquad (16)$$

Thus, the contribution from these subbands to the conductance is exponentially small. For a sufficiently low carrier density, the condition $(\mu_1 - E_j)/kT < 0$ is fulfilled for all subbands, including the lowest subband. The dependence of the carrier density on the electrochemical potential can be written as a series. Let us consider here only the lowest subband. We have

$$\pi\hbar n = \int_{-\infty}^{+\infty}\frac{dp}{1+e^{(\mu_1-E_0)/kT}e^{p^2/2mkT}}$$

$$= \int_{-\infty}^{\infty}\frac{e^{p^2/2mkT}dp}{e^{p^2/2mkT}+e^{(\mu_1-E_0)/kT}} \qquad (17)$$

$$= \sqrt{2\pi mkT}\sum_{j=1}^{\infty}\frac{(-1)^{j+1}}{\sqrt{j}}e^{(\mu_1-E_0)/kT}.$$

If the density is so low that $e^{(\mu_1-E_0)} \ll 1$, we can retain only the first term of the expansion; thus,

$$e^{(\mu_1-E_0)/kT} \approx \hbar\sqrt{\frac{\pi}{2mkT}}n = \beta n \ll 1,$$
$$\beta = \hbar\sqrt{\frac{\pi}{2mkT}}. \qquad (18)$$

This condition clarifies the meaning of the term "low density." Thus, the conductance is given by

$$G \approx \frac{e^2}{h}\beta n = e^2\pi\sqrt{\frac{2\pi}{mkT}}n. \quad (19)$$

It can be seen that, in contrast to the case of $T = 0$, the ballistic conductance apparently falls to zero when the carrier density within the quantum wire decreases. Taking into account the two leading terms of the expansion, we readily obtain a correction to the conductance that is quadratic in carrier density:

$$G \approx \frac{e^2}{h}(\beta n + \beta^2 n^2/2). \quad (20)$$

The above consideration of the conductance dependence on the electrochemical potential at different temperatures (see (13), Fig. 2a) shows the following. The quantum staircase observed at $T = 0$ is smoothed when the temperature is elevated and disappears when kT becomes of the same order of magnitude as the gap between SQ subbands ΔE.

Such temperature suppression of the ballistic conductance at partial SQ subband filling was first observed by measuring the quantized conductance as a function of voltage applied to a silicon quantum wire shorter than the mean free path. The carrier transport in such a quantum wire is not accompanied by Joule loss, since inelastic scattering is suppressed. Therefore, electrons and holes will demonstrate ballistic properties under one-dimensional (1D) transport conditions [1–4].

Fabrication of silicon quantum wires with ballistic properties became possible owing to the use of diffusion techniques of nanotechnology and formation of the self-organized impurity quantum wells (QWs). QWs of this kind are formed inside ultrashallow p^+ profiles during nonequilibrium boron diffusion on the (100) silicon surface [7–9].

The depth of an ultrasharp diffusion profile and the boron concentration in it, measured by secondary-ion mass spectrometry, are 10 nm and 10^{21} cm^{-3}, respectively. The presence of a single QW between heavily doped impurity barriers inside the p^+ diffusion profile was revealed while analyzing the angular dependences of the cyclotron resonance [7, 10]. Owing to the pyroelectric properties of the two-dimensional (2D) barriers, an electric field applied in the QW plane gives rise to transverse confinement of carriers on the one hand and effects their transport on the other [8, 9]. Depending on the uniformity of boron distribution within the pyroelectric barriers, the applied electric field can form both uniform and modulated quantum wires [8, 9].

One of the most important consequences of fabrication of quantum wires possessing ballistic properties is quantized conductance. This phenomenon is observed when varying the gate voltage, which controls the Fermi level position relative to the SQ subbands and thereby can change the number of carriers in the quantum wire [2, 3]. In this case, the dependence of G on the gate voltage V_g is stepwise, since the conductance of a quantum wire changes abruptly every time the Fermi level coincides with one of the SQ subbands (see Fig. 2a). Such a stepwise dependence of the conductance was observed while studying the above-mentioned smooth silicon quantum wire (2×2 nm^2), which was formed electrostatically in a p-type self-organized silicon QW (Fig. 2b). The Fermi level position is determined by the quantum wire cross section, the 2D hole density (~2.5×10^9 cm^{-2}), and the effective length of the 1D channel (~4 μm). It corresponds to the filling of 1D subbands of both heavy and light holes, which manifests itself in the quantum step height (Fig. 2b). It should be noted that the height of the quantum step corresponding to the filling of the first SQ subband (Fig. 2b) is somewhat smaller than the theoretically predicted value (~$4e^2/h$). This is presumably due to spin polarization of carriers in a zero magnetic field [11].

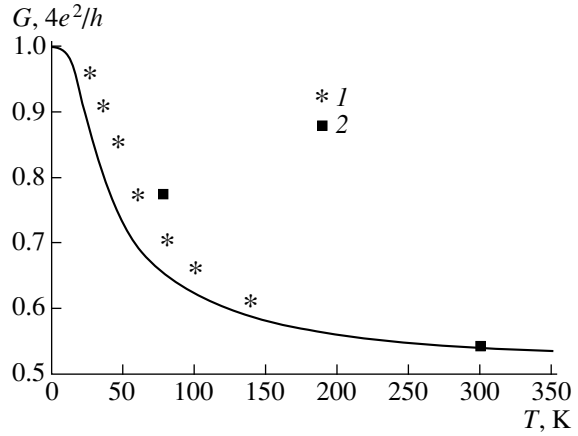

Fig. 3. Temperature dependence of quantized conductance: solid line corresponds to calculations by formula (13) and the points represent experimental data of (*1*) [12] and (*2*) those in Fig. 2b.

The observed temperature quenching of conductance near the quantum steps (Fig. 2b) agrees well with the calculated dependence (13) (Fig. 2a) if the energy gap (~96 meV, [9]) between the 1D subbands for the quantum wire under study is taken into account. The universality of (13) in describing the temperature dependence of conductance in a quantum wire is also confirmed by the similarity of the temperature quenching of quantum steps observed in studying two quantum wires with different parameters (Fig. 3).

Thus, the derived expression for the conductance of a ballistic quantum wire at finite temperature makes it possible to describe the temperature quenching of quantum steps exhibited by the conductance when the Fermi level passes through the SQ subbands. It is predicted that, in contrast to the case of $T = 0$, the ballistic conductance at a finite temperature tends to zero as the carrier concentration in the quantum wire decreases. A similar temperature quenching of quantum steps in

the dependence of the conductance on the gate voltage was observed while studying a silicon quantum wire. It is shown that the contribution of filled subbands to the ballistic conductance is well described by the Landauer–Büttiker formula in the limit of a weak pulling voltage. At the same time, in the case of partial occupancy, the conductance is half as large. This leads to temperature quenching of quantum steps in the dependence of the conductance on the Fermi level position, when kT approaches the energy gap between the SQ levels.

ACKNOWLEDGMENTS

This work was supported by the Russian Scientific Program "Physics of Solid Nanostructures" (project no. 97-1040), St. Petersburg Technical University (project no. 02.04.301.89.5.2), and the Russian Federal Program "Integration" (project no. 75:2.1).

REFERENCES

1. R. Landauer, J. Res. Dev. **1**, 233 (1957).
2. M. Büttiker, Phys. Rev. Lett. **57**, 1761 (1986).
3. D. A. Wharam, T. J. Thornton, R. Newbury, *et al.*, J. Phys. C **21**, L209 (1988).
4. B. J. van Wees, H. van Houten, C. W. J. Beenakker, *et al.*, Phys. Rev. Lett. **60**, 848 (1988).
5. L. P. Kouwenhoven, B. J. van Wees, C. J. P. M. Harmans, *et al.*, Phys. Rev. B **39**, 8040 (1989).
6. A. I. Ansel'm, *Introduction to the Theory of Semiconductors* (Nauka, Moscow, 1978).
7. N. T. Bagraev, E. I. Chaikina, L. E. Klyachkin, *et al.*, Superlattices Microstruct. **23**, 337 (1998).
8. N. T. Bagraev, L. E. Klyachkin, A. M. Malyarenko, and W. Gehlhoff, Superlattices Microstruct. **23**, 1333 (1998).
9. N. T. Bagraev, V. Gel'khoff, V. K. Ivanov, *et al.*, Fiz. Tekh. Poluprovodn. (St. Petersburg) **34**, 97 (2000) [Semiconductors **34** (2000) (in press)].
10. W. Gehlhoff, N. T. Bagraev, and L. E. Klyachkin, Solid State Phenom. **47/48**, 389 (1996).
11. C.-T. Liang, M. Y. Simmons, C. G. Smith, *et al.*, Phys. Rev. Lett. **81**, 3507 (1998).
12. Y. Nakajima, Y. Takahashi, S. Horiguchi, *et al.*, in *Extended Abstract of the International Conference SSDM, Yokohama, Japan, 1994*, p. 538.

Translated by S. Ktitorov

Semiconductors, Vol. 34, No. 6, 2000, pp. 717–722. From Fizika i Tekhnika Poluprovodnikov, Vol. 34, No. 6, 2000, pp. 742–747.

AMORPHOUS, VITREOUS, AND POROUS SEMICONDUCTORS

Kinetics of Light-Induced Degradation in *a*-Si:H Films Investigated by Computer Simulation [1]

M. N. Meytin*, M. Zeman, B. G. Budaguan*, and J. W. Metselaar****

** Moscow Institute of Electronic Engineering (Technological University), Moscow, 103498 Russia*

*** Delft University of Technology, DIMES-ECTM, P.O. Box 5053, 2600 GB Delft, The Netherlands*

e-mail: m.zeman@its.tudelft.nl

Submitted October 4, 1999; accepted for publication December 15, 1999

Abstract—In this work we investigated the stability of *a*-Si:H films under illumination and following recovery in darkness at different temperatures. The *a*-Si:H films were fabricated with 55 kHz PECVD and with conventional rf 13.56 MHz PECVD. We measured the steady-state photocurrent and the dark-current after switching off the light source as a function of time. We observed photocurrent degradation and the following recovery of the dark current. The kinetics of the photocurrent degradation as well as the dark-current recovery demonstrated stretched-exponential behavior. The results of these straightforward measurements in combination with computer simulation were used to determine the effect of light-induced degradation and thermal recovery on the density of states distribution in the band gap of *a*-Si:H. We have found that the photocurrent degradation and the corresponding increase in the total defect concentration have different kinetics. The different kinetics were also determined for the dark-current recovery and the corresponding decrease in the total defect concentration. The results point out that slow and fast types of defects in *a*-Si:H films control the kinetics of light-induced changes of the defect distribution in the band gap. A model is proposed that relates the origin of the fast and slow metastable defects with the distribution of Si–Si bond lengths. © *2000 MAIK "Nauka/Interperiodica"*.

INTRODUCTION

One of the important problems limiting the application of hydrogenated amorphous silicon (*a*-Si:H) material is the instability of its electronic properties and device performance under illumination. This phenomenon was observed by Staebler and Wronski [1] in 1977 and since then it has still not been fully explained. The most frequently used method for fabricating *a*-Si:H devices is 13.56 MHz plasma-enhanced chemical vapor deposition (PECVD). However, this method is characterized by a low growth rate (0.1–0.2 nm/s). For industrial applications, a higher growth rate of *a*-Si:H is desirable while maintaining the device quality properties of the material. The growth rate can be increased by applying a higher RF power or microwaves, but these layers show inferior electronic properties [2]. Recently, it was demonstrated [3] that *a*-Si:H films can be fabricated by 55 kHz PECVD with a high growth rate (higher than 1 nm/s) and device quality optoelectronic properties. Since these films exhibit microstructural inhomogeneities, we investigated their stability under illumination and following recovery in darkness at different temperatures and compared the results with the 13.56 MHz PECVD *a*-Si:H films.

We observed the photocurrent degradation and the following recovery of the dark current. The kinetics of the observed degradation and recovery are different for different temperatures. Existing models describe the photocurrent degradation as a process in which the defect concentration in the material increases. These additional defects introduce metastable states in the band gap of *a*-Si:H and cause a shift of the Fermi level towards the midgap [4]. The kinetics of the light-induced formation of defects in *a*-Si:H has been investigated by other teams by means of the analysis of the sub-band gap absorption spectra that change during light soaking [5].

In this work, we combined the measurements and computer simulation of photocurrent and dark current in order to investigate the metastable changes of the density of states (DOS) in the band gap of *a*-Si:H during the material degradation and recovery. We used the Amorphous Semiconductor Analysis computer program (ASA) developed at the Delft University of Technology [6].

EXPERIMENTAL

The *a*-Si:H films were fabricated from pure silane by conventional 13.56 MHz PECVD and 55 kHz PECVD [7] under the deposition conditions presented in Table 1. The films were deposited on a Corning 7059 glass substrate. The aluminum coplanar contacts were deposited for the conductivity measurements. The optical properties of the films were determined from the

[1] This article was submitted by the authors in English.

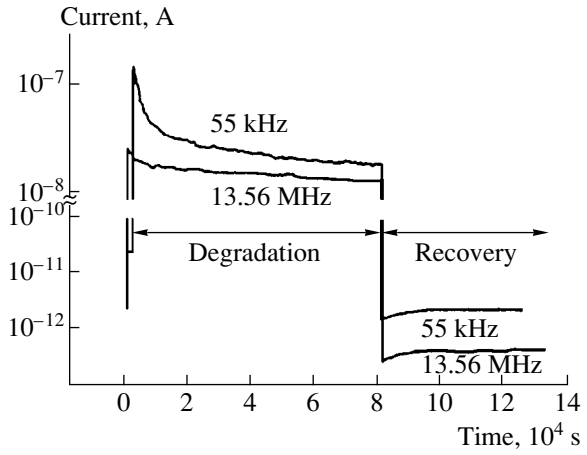

Fig. 1. The time change of the photocurrent during light-induced degradation and of the dark current recovery at 70°C in standard 13.56 MHz PECVD and 55 kHz PECVD *a*-Si:H layers.

reflection and transmission measurements and the double-beam photoconductivity measurement.

The measurements of current degradation under illumination were carried out at 50, 70, and 90°C. The samples were illuminated using metal halide lamps with a light intensity of 37.5 mW/cm^2. The steady-state photocurrent and the dark current after switching off the light source were measured as a function of time. Before each degradation-recovery cycle, the samples were annealed at 150°C for 30 min.

RESULTS

Figure 1 shows the time change of the photocurrent during degradation and of the dark-current recovery at 70°C for conventional 13.56 MHz and 55 kHz PECVD *a*-Si:H layers.

The behavior of degradation of the photocurrent and the recovery of the dark current is similar to the observed Staebler–Wronski effect (SWE) [8]. In order to deduce the parameters of kinetics of the light-induced degradation and recovery, the measured data of the photocurrent and dark current were normalized and fitted using the stretched-exponential dependence [4] expressed by (1):

$$\frac{\xi(t)-\xi(\infty)}{\xi(0)-\xi(\infty)} = \exp\left(-\left(\frac{t}{\tau}\right)^{\beta}\right), \qquad (1)$$

where $\xi(0)$ is the initial value of the fitted parameter, $\xi(\infty)$ is the saturated value of the fitted parameter, τ is characteristic time, β is the variance parameter, and t is time. Figure 2 shows the normalized photocurrent data (dots) for a 55 kHz PECVD sample measured at different temperatures and the corresponding fits (lines).

The parameters of the stretched-exponential function (τ, β) that were obtained from the fits to the normalized measured data are given in Table 2. Assuming that the characteristic time τ is thermally activated [9]

$$\tau = \tau_0 \exp(E_\tau/kT), \qquad (2)$$

where τ_0 is the preexponential factor and E_τ is the characteristic time activation energy, the values of E_τ were calculated for *a*-Si:H films.

SIMULATION

We applied the computer simulation of the photocurrent and dark current using the ASA program in order to investigate the effect of light-induced degradation and thermal recovery on the material properties. We based our approach on an assumption that the deg-

Table 1. The deposition conditions of *a*-Si:H films

Plasma frequency	Pressure, Pa	Power, mW/cm^2	T_s, °C	SiH_4 flow rate, sccm	Deposition rate, nm/s
13.56 MHz	70	15	194	40	0.2
55 kHz	70	50	225	200	0.8

Table 2. The parameters of the photocurrent degradation and the dark-current recovery kinetics of *a*-Si:H films measured at different temperatures. The parameters were obtained from the fits to the measured data using stretched-exponential function (1)

Samples	Temperature, °C	Degradation			Recovery		
		τ, s	β	E_τ, eV	τ, s	β	E_τ, eV
13.56 MHz PECVD	50	9020	0.61		–	–	
	70	3770	0.43	0.217	7533	0.6	0.38
	90	2550	0.92		3510	0.92	
55 kHz PECVD	70	1602	0.44	0.50	12300	0.94	
	90	362	0.95		5000	0.95	0.44

radation and recovery processes are mainly determined by metastable changes of the density of states distribution in the band gap of *a*-Si:H. Further, we assumed that

a) the time change of the photocurrent and dark current is related to the change in the total defect concentration (N_{db}) and the shift of the defect states distribution in the band gap. The band gap is represented by the mobility gap of *a*-Si:H;

b) the defect states are simulated by two equal Gaussian distributions, one representing donorlike defect states ($DB^{+/0}$) and the other acceptor-like defect states ($DB^{+/0}$), that are separated from each other by a correlation energy U (see Fig. 3);

c) band tails do not change during the degradation and recovery processes. The initial set of input parameters for simulations is given in Table 3.

The sensitivity study of the influence of the input parameters of the ASA model on the dark- and photocurrent showed that the dark current is strongly sensitive to the change of the peak position of the Gaussian distribution, while the photocurrent is controlled by the total defect concentration. Therefore, the data on the dark-current recovery were used to determine the kinetics of the shift of the peak of the Gaussian distribution. In this case, the energy level $E_{\mathrm{DB}}^{+/0}$, which is the peak of the Gaussian distribution of $DB^{+/0}$ states, was used as an adjustable parameter in simulations. The Fermi level position followed the changes of $E_{\mathrm{DB}}^{+/0}$ as $E_F = E_{\mathrm{DB}}^{+/0} + U/2$.

The time dependence of the peak position of Gaussian distribution $E_{\mathrm{DB}}^{+/0}$ for 13.56 MHz and 55 kHz PECVD samples at 70°C is presented in Fig. 4. The time dependence of the peak position was fitted using stretched-exponential function (1) and the kinetics parameter τ was determined. The characteristic time τ defining the time dependence of the shift of the peak position is in good agreement with the characteristic time τ of dark-current recovery. We conclude that the kinetics of dark-current recovery is controlled by the shift of the peak position of the Gaussian distribution of defect states.

We assume that the kinetics of photocurrent degradation is also controlled by a light-induced shift of the peak position of the Gaussian distribution of defect states and that the kinetics parameters τ and β are the same for both cases. Using this assumption for the peak position of the Gaussian distribution of the defect states, we simulated the photocurrent with the ASA program using the total defect concentration as an adjustable parameter in order to obtain good matching between the measured and simulated values. The time dependences of the measured and simulated photocurrents for *a*-Si:H samples at 70°C are shown in Fig. 5, and the corresponding time dependence of the total defect concentration, N_{db}, in Fig. 6. The calculated values of the defect concentration demonstrate the stretched-exponential behavior, saturating for long light-soaking times (Table 4).

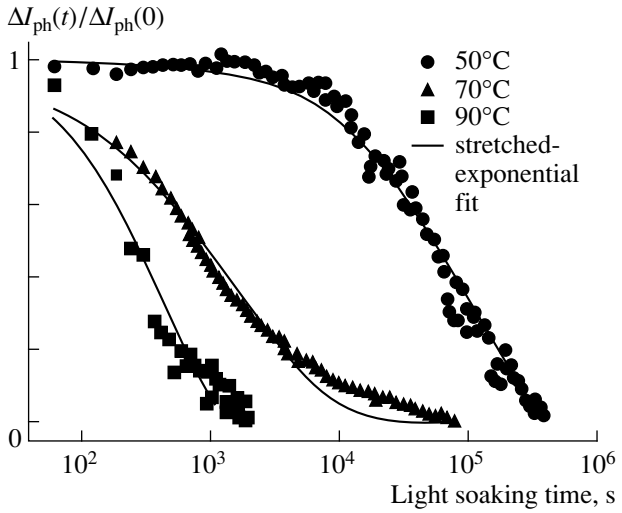

Fig. 2. Normalized plot of photocurrent degradation of a 55 kHz PECVD *a*-Si:H sample at different temperatures. The lines correspond to the stretched-exponential fit.

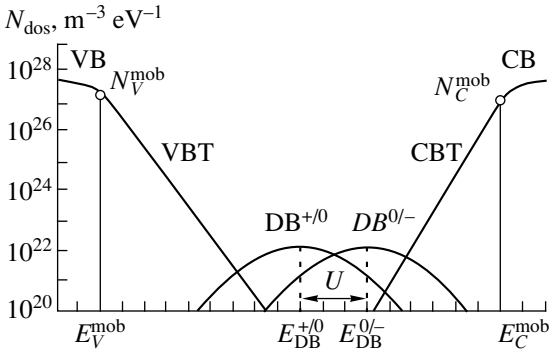

Fig. 3. The DOS distribution model used in simulations. VB (CB)—the parabolic distribution of valence (conduction) band, VBT (CBT)—the exponentially decaying valence (conduction) band tail, E_V^{mob} (E_C^{mob})—the energy level of VB (CB) mobility edge, and N_V^{mob} (N_C^{mob})—the density of states at the VB (CB) mobility edge. $E_{\mathrm{DB}}^{+/0}$ ($E_{\mathrm{DB}}^{0/-}$) is the energy level of the peak of the Gaussian distribution of $DB^{+/0}$ ($DB^{0/-}$) states and U is the correlation energy.

The correlation between the defect concentration N_{db} and the peak position of the Gaussian distribution of the defects during light-induced degradation is presented in Fig. 7. As one can see, the shift of the peak position of Gaussian distribution $E_{\mathrm{DB}}^{+/0}$ leads to an increase in the defects concentration N_{db}. The theoretical dependence of the defect density on the energy level of the defect in the band gap at equilibrium was calcu-

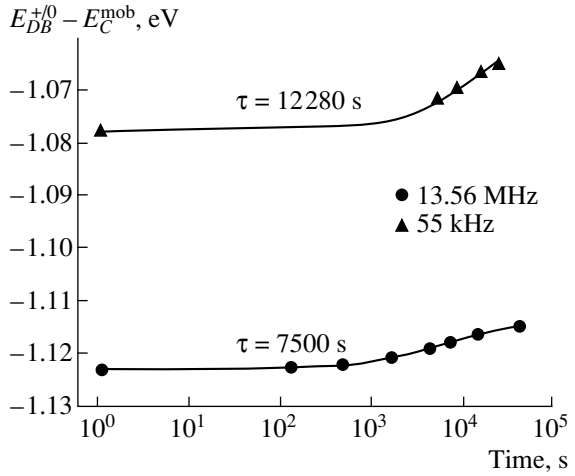

Fig. 4. The time dependence of the peak position of Gaussian distribution of defect states during recovery for different *a*-Si:H samples at 70°C. Solid lines correspond to the stretched-exponential fit.

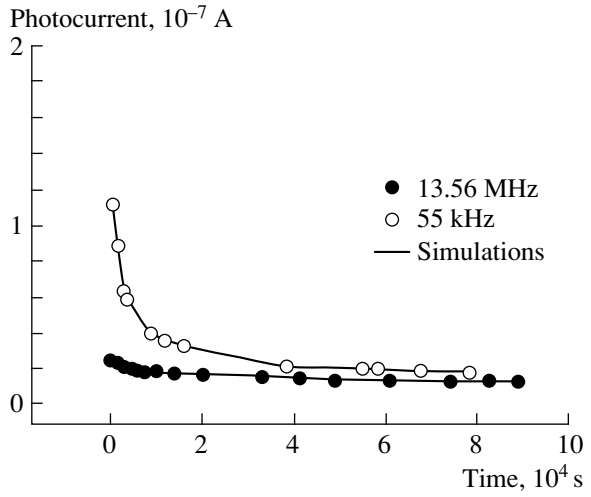

Fig. 5. The measured and simulated photocurrent for *a*-Si:H samples at 70°C.

lated according to the known model [4] by the following formula:

$$N_{db} = \left[\frac{N_{v0}E_0kT}{E_0 - kT}\right]\left[\frac{E_0}{kT}\exp\left(-\frac{E_d}{E_0}\right) - \exp\left(-\frac{E_d}{kT}\right)\right], \quad (3)$$

where N_{v0} is the density of states at the valence-band edge, E_0 is the Urbach energy, and E_d is the position of the defect state in the band gap. As one can see, the results of simulation are very close to the theoretical dependence at the equilibrium state. The discrepancy between the theoretical calculations using (3) and the results of simulation exists, because in (3) only a single defect level was assumed while in simulation the distribution of defects was used. The correlation between N_{db} and the peak position of Gaussian distribution is an intrinsic property of *a*-Si:H and is valid both for degradation and annealing processes taking place at the same temperature. This dependence was used to determine the time change in the defect density during annealing using the calculated data of the peak position during the dark-current recovery. The kinetics parameters determined from simulation with the ASA program both for the light-induced degradation and thermal recovery are summarized in Table 4.

Table 3. The set of initial input parameters for the simulations. CC—capture coefficient, CB (VB)—the mobility edge of the conduction (valence) band

General parameters	55 kHz	13.56 MHz
Tauc optical gap, eV	1.72	1.69
Mobility gap, eV	1.75	1.75
Urbach energy, eV	0.052	0.054
Dielectric constant	11.9	
Electron mobility, 10^{-4} m^2/(V s)	10.0	
Hole mobility, 10^{-4} m^2/(V s)	2.0	
Tail-state parameters:		
DOS at CB mob. edge, m^{-3} eV^{-1}	1×10^{27}	
DOS at VB mob. edge, m^{-3} eV^{-1}	1×10^{27}	
VB tail characteristic energy, eV	0.052	0.054
CB tail characteristic energy, eV	0.027	0.027
CC for neutral states, m^3/s	7×10^{-16}	
CC for charged states, m^3/s	7×10^{-16}	
Defect states parameters		
Standard deviation	0.144	
CC for neutral states, m^3/s	3×10^{-15}	
CC for charged states, m^3/s	3×10^{-14}	

DISCUSSION

As one can see from Table 2, the sample fabricated by 55 kHz PECVD is characterized by higher values of the potential barriers E_τ for the degradation and annealing process. Thus, the use of 55 kHz PECVD results in the slowing down of the process of photocurrent degradation and dark-current recovery, indicating the stability improvement of *a*-Si:H films. The analysis of the relationship between the stability and microstructure of 55 kHz *a*-Si:H is given elsewhere [7]. Here, we discuss the degradation and recovery kinetics of *a*-Si:H samples fabricated by different technologies.

A comparison of the measured kinetics parameters, which are listed in Table 2, and the kinetics parameters derived from simulations and presented in Table 4 shows that the photocurrent degradation and the defect creation processes are characterized by different kinet-

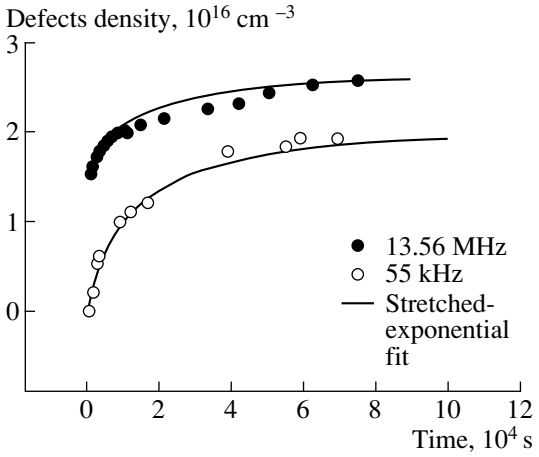

Fig. 6. The time dependence of the defect density as determined from the simulations of the photocurrent degradation for *a*-Si:H samples at 70°C. The lines are the fits using the stretched-exponential function.

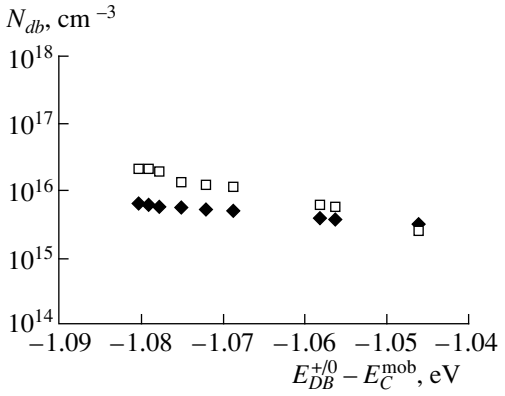

Fig. 7. The correlation between the defects density and the peak position of Gaussian distribution during light-induced degradation at 70°C for a 55 kHz PECVD *a*-Si:H sample. Diamonds correspond to the results of modeling, and squares correspond to the correlation between the peak position of Gaussian distribution at equilibrium.

ics. The same conclusion holds for the dark-current recovery kinetics and the defect annealing kinetics. These phenomena were also observed in SWE experiments, in which the change in defect density was monitored by CPM measurement [10]. Also, the activation energy E_τ of the characteristic time of the photocurrent degradation and dark-current recovery is not consistent with the corresponding E_τ values determined for the defect generation and annealing. This means that the Fermi level shift is controlled by a process characterized by an energy barrier differing from an energy barrier involved in a process that controls the formation of additional defects. Two different types of metastable states have been proposed [11, 12]: (i) the fast defect states, which are responsible for the shift in the Fermi level during degradation, and (ii) the slow states, which control the total concentration of the metastable defects. During the degradation, the slow defects are characterized by a higher activation energy E_τ of the characteristic time than the characteristic time activation energy corresponding to the fast states. According to the data presented in Table 4, the annealing activation energy E_τ of the characteristic time of the slow defects is less than E_τ of the fast states. Therefore, the slow states should be less stable than the fast ones. The configuration diagram presented in Fig. 8 illustrates the possible processes of creation and annealing of fast and slow defects.

According to known models [4], the creation and annealing of metastable dangling bonds that are associated with dispersive hydrogen diffusion can be presented as the following reaction:

$$\mathrm{Si{-}H + Si{-}Si} \rightleftharpoons \mathrm{DB + Si{-}H{-}Si}. \qquad (4)$$

The existence of the fast and slow-type defects suggests that there are either different quasi-chemical reactions for the defect equilibration process or there is a distribution of Si–Si bond lengths [13]. Assuming that the bond length disorder controls the metastable defect creation and annealing processes in *a*-Si:H, the higher values for slow defects formation energy can be explained. The difference between characteristic energy E_τ of the metastable dangling bond creation (Table 4) for a standard PECVD film and 55 kHz film suggests that these

Table 4. The kinetics parameters determined from simulation with the ASA program both for the light-induced degradation and thermal recovery

Samples	Defect generation					Defect annealing				
	τ, s	β	$N_{db}(0)$, cm^{-3}	$N_{db}(\infty)$, cm^{-3}	E_τ, eV	τ, s	β	$N_{db}(0)$, cm^{-3}	$N_{db}(\infty)$, cm^{-3}	E_τ, eV
55 kHz										
T = 70°C	16000	0.7	2.00×10^{14}	2.00×10^{16}	1.98	1670	0.42	2×10^{16}	8.10×10^{15}	0.10
T = 90°C	300	0.42	4.89×10^{16}	5.50×10^{16}		1380	0.71	5.56×10^{16}	5.39×10^{16}	
13.56 MHz										
T = 70°C	16730	0.643	1.55×10^{16}	2.69×10^{16}	0.26	1600	0.64	2.71×10^{16}	2.00×10^{16}	0.03
T = 90°C	9900	0.7	1.44×10^{16}	1.78×10^{16}		1500	0.7	1.81×10^{16}	1.56×10^{16}	

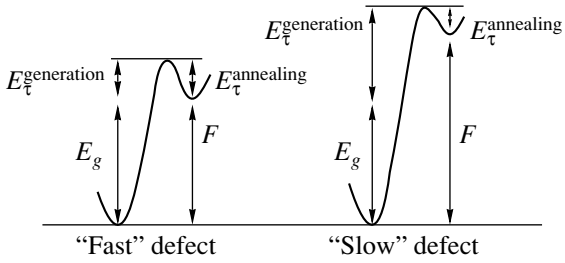

Fig. 8. The energy diagram of the fast- and slow-type defects. E_g is the mobility gap and F is the defect formation energy.

films can be characterized by different microstructures. A comprehensive study of the relation between light-induced metastability and the structural properties of amorphous silicon fabricated by the two techniques is required to fully justify this conclusion.

CONCLUSION

1. Computer simulation in combination with simple conductivity measurements is an effective tool for the analysis of degradation and annealing processes in amorphous silicon materials.

2. Kinetics of the dark conductivity recovery is controlled by the kinetics of the shift of the Fermi level rather than by the kinetics of the change of defect concentration.

3. Kinetics of the photoconductivity degradation is controlled by both the shift of the peak position of the Gaussian distribution of defect states and the change in the defect concentration.

4. It was found that the photoconductivity degradation and the increase in the total defect concentration have different kinetics. The same conclusion holds for the dark conductivity recovery and the decrease in the total defect concentration.

5. Slow and fast types of defects in *a*-Si:H bulk are introduced, which control the kinetics of light-induced changes of the defect distribution in the band gap.

6. It is proposed that the origin of fast and slow metastable defects is connected with microstructures of the films which influences the distribution of Si–Si bond lengths.

ACKNOWLEDGMENTS

This work was supported by the Netherlands Organization for Scientific Research (NWO), grant no. 047.005.09.96.

REFERENCES

1. D. L. Staebler and C. Wronski, Appl. Phys. Lett. **31**, 292 (1977).
2. P. Roca i Cabarrocas, J. Non-Cryst. Solids **164/166**, 37 (1993).
3. B. G. Budaguan, A. A. Sherchenkov, D. A. Stryahilev, *et al.*, in *Proceedings of the Electrochemical Society Symposium*, Paris, 1997.
4. R. Street and K. Winer, Phys. Rev. B **40**, 6236 (1989).
5. A. S. Abramov, A. I. Kosarev, P. Roca i Cabarrocas, and A. J. Vinogradov, Mater. Res. Soc. Symp. Proc. **420**, 659 (1996).
6. M. Zeman, J. A. Willimen, L. L. A. Vosteen, *et al.*, Sol. Energy Mater. Sol. Cells **46**, 81 (1997).
7. B. G. Budaguan and A. A. Aivazov, Mater. Res. Soc. Symp. Proc. (1998) (in press).
8. C. R. Wronski, in *Semiconductors and Semimetals*, Ed. by J.I. Pankove (Academic Press, New York, 1984), Vol. 21, Part C, p. 347.
9. J. Kakalios and W. B. Jackson, in *Amorphous Silicon and Related Materials*, Ed. by H. Fritzsche (World Scientific, Singapore, 1988).
10. R. Bube, L. E. Benatar, M. N. Grimbergen, and D. Redfield, J. Non-Cryst. Solids **169**, 47 (1994).
11. Liyou Yang and Liang-Fan Chen, Mater. Res. Soc. Symp. Proc. **297**, 619 (1993).
12. C. Godet and P. Roca i Cabarrocas, Mater. Res. Soc. Symp. Proc. **420**, 647 (1996).
13. Qiming Li and R. Biswas, Appl. Phys. Lett. **68**, 2261 (1996).

Semiconductors, Vol. 34, No. 6, 2000, pp. 723–727. Translated from Fizika i Tekhnika Poluprovodnikov, Vol. 34, No. 6, 2000, pp. 748–752.

AMORPHOUS, VITREOUS, AND POROUS SEMICONDUCTORS

The Staebler–Wronski Effect and Temperature Dependences of Photoconductivity in *p*-type *a*-Si:H

S. V. Kuznetsov

Moscow State University, Vorob'evy gory, Moscow, 119899 Russia

e-mail: sergkuz@mail.ru

Submitted November 24, 1999; accepted for publication December 15, 1999

Abstract—Temperature dependences of the photoconductivity of boron doped *a*-Si:H films both prior to and after prolonged illumination were studied. It was found that the photoconductivity of films under study in the temperature range 200–300 K (intermediate temperatures) is independent of the doping level and the concentration of deep recombination centers (dangling bonds). A model of recombination is used to explain the experimental results; according to this model, the occupancy function of neutral dangling bonds in *p*-type *a*-Si:H (and, consequently, also the photoconductivity) is determined by the parameters of the states of the valence band tail and is independent of the doping level and of the total concentration of dangling bonds. © *2000 MAIK "Nauka/Interperiodica".*

Since amorphous silicon with various levels of doping is widely used in the fabrication of optoelectronic devices, studies of *a*-Si:H photoconductivity dependence on such parameters as the doping level and concentration of defects are of interest. At present, the undoped *a*-Si:H and *a*-Si:H of *n*-type are the most extensively studied. In connection with this fact, *p*-type *a*-Si:H films with various doping levels were studied in this work. The films were prepared by decomposition of the gaseous mixture of monosilane (SiH_4) and diborane (B_2H_6) in the radio-frequency (RF) glow discharge [1]. The volumetric ratio of gases $k = [B_2H_6]/[SiH_4]$ in the reaction chamber varied from 3×10^{-7} up to 10^{-3}. This allowed us to obtain films with various doping levels. The remaining technological parameters of the sample preparation were identical.

The temperature dependences of photoconductivity in the films under study are shown in Fig. 1. As can be seen from Fig. 1, curves $\sigma_{ph}(10^3/T)$ have two characteristic regions for heavily doped *a*-Si:H films ($k = 3 \times 10^{-6}$, 10^{-3}): at high temperatures the photoconductivity decreases with heating; at low temperatures, the photoconductivity increases exponentially as the temperature increases. A third region (a more gradual decrease in photoconductivity with decreasing temperature) can be distinguished in the range of low temperatures on the temperature dependences of photoconductivity in lightly doped *a*-Si:H films ($k = 3 \times 10^{-7}$ and 10^{-6}), in addition to the above two characteristic regions of variations in σ_{ph}. As can be seen from Fig. 1, in the region of exponential photoconductivity increase with increasing temperature, the value of σ_{ph} depends weakly on the doping level of the films.

In order to explain special features of temperature dependences of photoconductivity in *p*-type *a*-Si:H, we consider a model of nonequilibrium carrier recombination developed by us in [1–3]. Instead of continuous distribution of the states of dangling-bond-type defects (*D*-centers) and the states in the band tails, we will consider discrete levels E_D, E_{D-U}, E_{tn}, and E_{tp} shown in Fig. 2. E_D and E_{D-U} are the energy levels of neutral (D^0) and negatively charged (D^-) states of *D* centers, respectively; E_{tn} and E_{tp} are the effective levels of traps for electrons and holes, respectively. The most important electronic transitions under the conditions of illumination are also shown in Fig. 2. It is known that the tail of the valence-band states is more extended as compared to the conduction-band tail. Therefore, the effective trapping levels for holes are located "deeper" than the electron trapping levels: $E_{tp} - E_v > E_c - E_{tn}$. According to [4, 5], $E_c - E_{tn} = 0.1$ eV, $E_{tp} - E_v = 0.3$ eV.

Since the concentration of D^- centers is negligibly small in *p*-type *a*-Si:H as compared to D^0 center concentrations, D^0 centers are the main recombination centers for nonequilibrium holes. In this case, the hole lifetime τ_p is determined by the D^0-center concentration N^0 [6]:

$$\tau_p = (c_p^0 N^0)^{-1}. \quad (1)$$

Here, c_p^0 is the coefficient of hole capture by the D^0 center.

The electroneutrality equation for *p*-type *a*-Si:H films in the dark and under illumination implies

$$p_t = p_{t0} = N_0^+ - N^+ = N^0 - N_0^0. \quad (2)$$

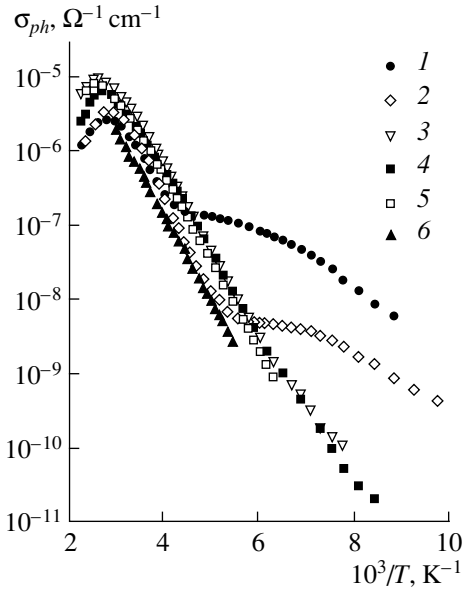

Fig. 1. Temperature dependences of photoconductivity in *a*-Si:H films with the doping level $k = 3 \times 10^{-7}$ (*1*), 10^{-6} (*2*), 3×10^{-6} (*3*), 10^{-5} (*4*), 10^{-4} (*5*), and 10^{-3} (*6*).

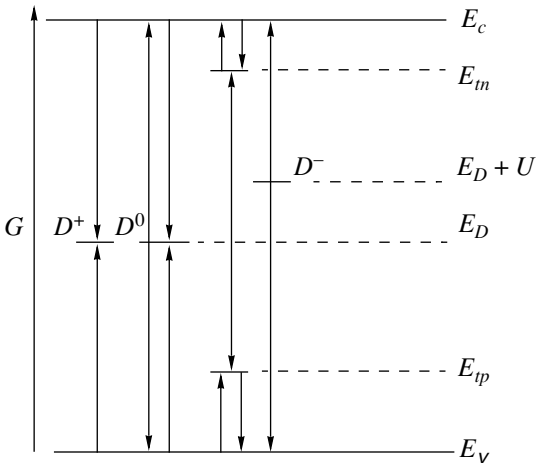

Fig. 2. Schematic representation of electron transitions for a simplified model of density of states in the mobility gap.

Here, p_{t0} and p_t are the equilibrium and nonequilibrium concentrations of holes in the valence-band tail (at the traps), respectively; N_0^0 and N^0 are the concentrations of D^0-centers in the dark and under illumination, respectively; and N_0^+ and N^+ are the concentrations of D^+ centers in the dark and under illumination, respectively. For a total concentration of D centers N_D, one can write:

$$N_D = N^- + N^0 + N^+ = N_0^- + N_0^0 + N_0^+. \quad (3)$$

Numerical solution of kinetic equations shows [2] that, for the case of *p*-type *a*-Si:H, the following relationships are valid:

$$p_t \gg p_{t0}, \quad N^0 \gg N_0^0. \quad (4)$$

Using (2) and (3), we obtain

$$p_t = N_0^+ - N^+, \quad (5.1)$$

$$p_t = N^0. \quad (5.2)$$

Relationship (5.1) signifies that the value of positive charge at the hole traps is equal to the change of the positive charge of D^+ centers.

In the steady-state case and at temperatures at which the main channel for hole recombination is the recombination via D^0 centers, we have

$$G = c_p^0 p N^0. \quad (6)$$

Here, p is the concentration of free holes under illumination and G is the optical generation rate of carriers.

Taking into account that the hole traps are in a thermodynamic equilibrium with the valence band, we derive the relationship between p and p_t:

$$p/p_t = (N_v/N_{pt})\exp[-(E_{tp} - E_v)/kT]. \quad (7)$$

Here, $(E_{tp} - E_v)$ is the energy position of the hole trapping level with respect to the top of the valence band, N_{tp} is the effective concentration of hole traps, and N_v is the effective density of states in the valence band.

It follows from (5.2)–(7) that

$$p = \{(GN_v)/(c_p^0 N_{tp})\}^{1/2}\exp[(E_v - E_{tp})/(2kT)]. \quad (8)$$

Thus, the photoconductivity is defined as

$$\sigma_{ph} = e\mu_p\{(GN_v)/(c_p^0 N_{tp})\}^{1/2} \times \exp[(E_v - E_{tp})/(2kT)]. \quad (9)$$

Let us analyze this expression for σ_{ph}. First of all, one should note that the relation $p_t = N^0$, employed when deriving expression (9), is a key relation for understanding the special features of recombination in *p*-type *a*-Si:H. This relation accounts for the fact that illumination results in the occupation of hole traps by holes and in the recharging of the D center: $D^+ + e \longrightarrow D^0$. In this case, the concentration of D^0 centers under illumination is equal to the concentration of holes p_t captured by the trapping states. Since the quantity p_t depends on the parameters of these states, relation (5.2), in view of (1), signifies that the hole lifetime is determined by the parameters of the states of the hole traps. This defines a special role of the valence-band tail in the recombination processes in *p*-type *a*-Si.

In addition, it follows from (4) that the concentration of D^0 centers under illumination significantly exceeds the equilibrium value of N_0^0 and is independent

of the total concentration of D centers N_D. This suggests that processes in p-type a-Si:H such as doping by acceptors and prolonged illumination followed by the enhancement of the total concentration of D centers would not affect the photoconductivity magnitude at intermediate temperatures.

It follows from (9) that the photoconductivity increases with increasing temperature according to the law $\sigma_{ph} \sim \exp[(E_v + E_{tp})/2kT]$. The photoconductivity enhancement under heating within the framework of our model has a simple physical meaning: the temperature increase enhances the probability of thermal emission of holes from the traps into the valence band, which, in turn, induces an increase in the flux of holes captured by D^0 centers. This results in the recharging of D centers $D^0 + h \longrightarrow D^+$, which causes the concentration of D^0 centers to diminish. Correspondingly, the hole lifetime increases, and, as a consequence, photoconductivity is enhanced. As follows from (9), the tangent of the slope of the curve $\ln\sigma_{ph}(1/kT)$ is equal to a half of the energy position of hole traps.

We now consider to what extent the recombination model suggested and, correspondingly, expression (9) agree with the experimental results. As was noted above, all the temperature dependences σ_{ph} have a portion of the exponential growth: $\sigma_{ph} \sim \exp(-E_A/kT)$, where, for the samples under study, $E_A = 0.22$–0.27 eV. Through a comparison with (9), we find that $E_A = (E_{tp} - E_v)/2$. Consequently, for all our a-Si:H samples, we have $E_{tp} - E_v = 0.44$–0.54 eV.

The photoconductivity increase with heating (see Fig. 1) changes for its decrease at $T > 360$ K. In our opinion, this is caused by the fact that, at high temperatures, the illumination influence upon the occupied states in the forbidden gap is insignificant and the concentration of D^0 centers is determined by the equilibrium statistics, i.e., $N_0 = N_0^0$. At the same time, it is known that N_0^0, in the case of $E_D - E_F > 0$, increases with temperature [7]. Therefore, in the range of high temperatures, the photoconductivity decreases with heating. Thus, the presence of the high-temperature maximum in temperature dependences is the result of transition from the nonequilibrium occupation of D^0 centers to their equilibrium occupation.

As can be seen from Fig. 1, for lightly doped films ($k = 3 \times 10^{-7}$ and 10^{-6}), formula (9) does not describe the experimental portion of temperature dependence of σ_{ph} in the region of low temperatures. In the previous publication [3], a weak temperature dependence of σ_{ph} at low temperatures for lightly doped p-type a-Si:H films is explained by the change of the photoconductivity type. Actually, D centers in lightly doped p-type a-Si:H in the dark are in the ground D^+ state. At low temperatures, the recharging of D-centers induced by the illumination can result in a significant enhancement

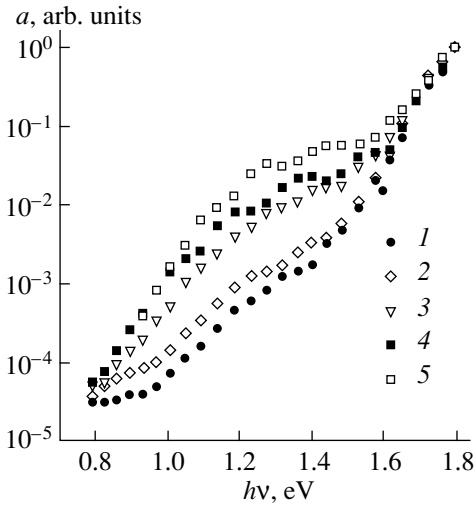

Fig. 3. Spectral dependence of the absorption coefficient of a-Si:H films studied with the doping level $k = 3 \times 10^{-7}$ (*1*), 10^{-6} (*2*), 3×10^{-6} (*3*), 10^{-5} (*4*), and 10^{-4} (*5*).

of D^0- and D^-- center concentrations, especially in the case where the total concentration of D centers is low. This causes an increase in the electron lifetime and a decrease in the hole lifetime. As a result, the photoconductivity is defined by the nonequilibrium electron transport.

As was noted above, the model suggested indicates that the photoconductivity is independent of the total concentration of D centers N_D in p-type a-Si:H. It is known that the data on N_D can be obtained from the absorption spectra $\alpha(h\nu)$ in a "defect region" (0.8–1.4 eV). The value of α in this absorption range (as a rule, for $h\nu = 1.2$ eV) is proportional to the value of N_D. The spectral dependences $\alpha(h\nu)$ obtained by the method of constant photocurrent are presented in Fig. 3 for the samples under study. As can be seen from Fig. 3, an increase in doping from $k = 3 \times 10^{-7}$ to $k = 10^{-4}$ results in the enhancement of defect concentration by almost 40 times. In this case, the photoconductivity actually does not change (Fig. 1). It is also known that the defect concentration in a-Si:H increases as a result of prolonged illumination [8]. Therefore, to check the independence of σ_{ph} of the total defect concentration in p-type a-Si:H films, the temperature dependences of photoconductivity were measured after the preliminary illumination of the films by light with the intensity of 100 mW/cm^2 at room temperature. The corresponding curves for films with doping level $k = 10^{-6}$ and 10^{-5}, respectively, are presented in Figs. 4 and 5. As can be seen from these figures, the prolonged illumination differently affects the dissimilar characteristic regions of $\log\sigma_{ph}(10^3/T)$ dependence. The region of exponential photoconductivity increase undergoes minor changes. At the same time, σ_{ph} at room temperature decreases significantly. For example, a preliminary illumination

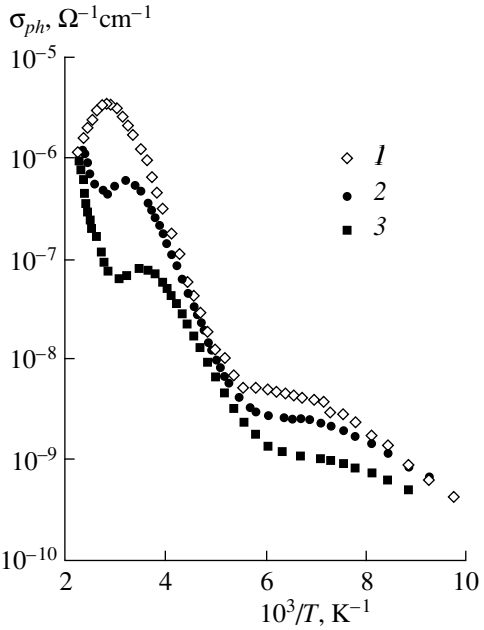

Fig. 4. Temperature dependence of photoconductivity in *p*-type *a*-Si:H films with the doping level $k = 10^{-6}$ prior to (*1*) and after preliminary illumination for 3 (*2*) and 15 (*3*) min.

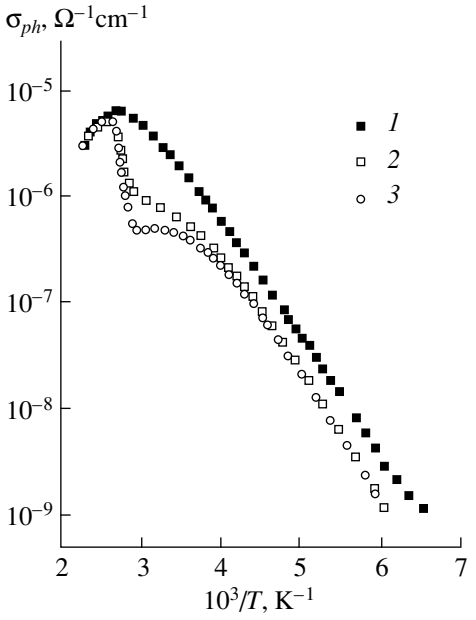

Fig. 5. Photoconductivity temperature dependence of *p*-type *a*-Si:H films with the doping level $k = 10^{-5}$ prior to (*1*) and after the preliminary illumination for 3 (*2*) and 15 (*3*) min.

for 15 min of the film with $k = 10^{-6}$ results in a more than 20-fold decrease in σ_{ph} at $T = 300$ K, and in a less than twofold decrease at $T = 200$ K. It can also be seen from Fig. 4 that prolonged illumination results in a shift of temperature boundaries of the region of exponential photoconductivity increase to lower temperatures. These results are completely consistent with our model. Actually, an increase in the total defect concentration (N_D) results in a decrease in the equilibrium concentrations of D^0 centers (N_0^0). Therefore, at high temperatures, when the concentration of D^0 centers is close to the equilibrium one, a decrease in photoconductivity is observed. In the low-temperature range where photoconductivity of the electron-type is assumed, a decrease in σ_{ph} as a result of preliminary illumination can be explained by the reduction of the efficiency of recharging of *D* centers due to an increase in their total concentration. This results in the fact that the change of photoconductivity type occurs at lower temperatures. For the sample with the doping level $k = 10^{-5}$, the same influence of preliminary illumination is qualitatively observed on the temperature dependence of photoconductivity. Thus, our experimental results confirm that, under intermediate temperatures, σ_{ph} is independent of the total concentration of *D* centers.

We note that the increase in photoconductivity with increasing temperature observed in Figs. 4 and 5 in the high temperature region $T > 330$ K for the samples exposed to the prolonged illumination is connected to the annealing of the defects induced by light.

The temperature dependences of the exponent in the power-low dependence of photoconductivity on the light intensity γ for the three samples under study is presented in Fig. 6. As can be seen from Fig. 6, at temperatures corresponding to the region of exponential photoconductivity increase, γ takes values close to 0.5, which agree with dependence $\sigma_{ph} \sim G^{1/2}$, as follows from the suggested model [see (9)]. Significant differences of experimental values of γ from 0.5 at other temperatures are related to the inapplicability of formula (9) at high temperatures (equilibrium occupation of *D*-centers) and at low temperatures, when one should take into account the tunneling recombination.

Thus, in this work, the temperature dependences of photoconductivity in *p*-type *a*-Si:H films with various boron doping levels were studied. It is established that a region of an exponential increase in σ_{ph} with increasing temperature is observed in the curves of the temperature dependence of photoconductivity. The value of σ_{ph} in this region is practically independent of the doping level, defect concentration, and preliminary illumination. In order to explain the results obtained, we suggested a recombination model, according to which the concentration of recombination centers for holes (D^0 centers) in *p*-type *a*-Si:H significantly differs from the equilibrium value under illumination and is determined by the parameters of valence-band-tail states. Therefore, according to the model suggested, the photoconductivity in *p*-type *a*-Si:H films with identical parameters of valence-band-tail states should not depend on the doping level or on the total defect con-

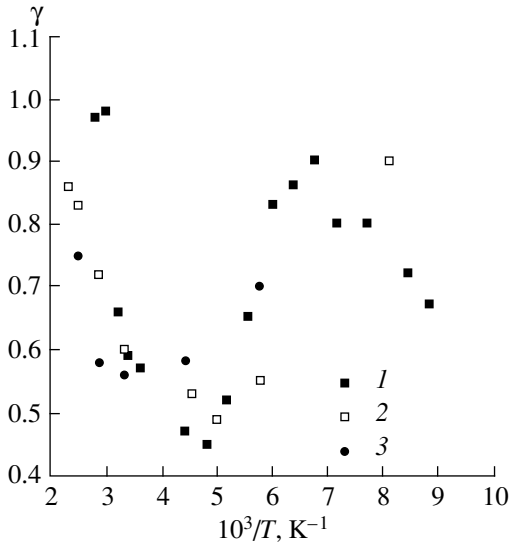

Fig. 6. Temperature dependences of the exponent in the photoconductivity dependence on the light intensity γ of *a*-Si:H with the boron doping level $k = 10^{-6}$ (*1*), 3×10^{-6} (*2*), and 10^{-4} (*3*).

centration of the dangling-bond-type. The recombination model suggested fully explains the influence of a prolonged illumination upon the temperature dependences of photoconductivity in *p*-type *a*-Si:H.

ACKNOWLEDGMENTS

I am grateful to A.G. Kazanskiĭ for his participation in the interpretation of the results and for fruitful discussions.

REFERENCES

1. A. G. Kazanskiĭ and S. V. Kuznetsov, Phys. Status Solidi B **168**, K19 (1991).
2. A. G. Kazanskiĭ and E. A. Shamonina, Fiz. Tekh. Poluprovodn. (St. Petersburg) **27**, 1688 (1993) [Semiconductors **27**, 932 (1993)].
3. A. G. Kazanskiĭ, I. V. Klimashin, and S. V. Kuznetsov, Fiz. Tekh. Poluprovodn. (Leningrad) **24**, 1628 (1990) [Sov. Phys. Semicond. **24**, 1016 (1990)].
4. F. Vaillant and D. Jousse, Phys. Rev. B **34**, 4088 (1986).
5. M. Hoheisel, R. Carius, and W. Fuhs, J. Non-Cryst. Solids **59/60**, 457 (1983).
6. R. H. Bube, *Photoconductivity of Solids* (New York, Wiley, 1960; Inostrannaya Literatura, Moscow, 1962).
7. M. Stutzmann and W. B. Jackson, Solid State Commun. **62** (3), 153 (1987).
8. M. Stutzmann, W. B. Jackson, and C. C. Tsai, Phys. Rev. B **32**, 23 (1985).

Translated by T. Galkina

Semiconductors, Vol. 34, No. 6, 2000, pp. 728–731. Translated from Fizika i Tekhnika Poluprovodnikov, Vol. 34, No. 6, 2000, pp. 753–756.

AMORPHOUS, VITREOUS, AND POROUS SEMICONDUCTORS

Modification of Optoelectronic Properties of Porous Silicon Produced in an Electrolyte Based on Heavy Water

B. V. Kamenev*, E. A. Konstantinova, P. K. Kashkarov, and V. Yu. Timoshenko

Moscow State University, Vorob'evy gory, Moscow, 119899 Russia

** e-mail: boris@ofme.phys.msu.su*

Submitted December 9, 1999; accepted for publication December 28, 1999

Abstract—The methods of infrared spectroscopy, electron spin resonance, and photoluminescence were used to study the porous-silicon layers formed by electrochemical treatment of Si in an HF : D_2O solution. In contrast with the samples prepared in a conventional electrolyte (HF : H_2O), a steady increase in the photoluminescence intensity in the course of routine oxidation of the sample was observed, with the hydrogen coverage of the silicon-skeleton surface retained. A mechanism for anomalous oxidation of the layers of porous silicon obtained in a mixture of HF and heavy water is suggested. © *2000 MAIK "Nauka/Interperiodica".*

1. INTRODUCTION

One of the important areas in the study of porous silicon (*por*-Si) is the analysis of the influence of the environment on the characteristics of the *por*-Si photoluminescence (PL). Of interest are both the theoretical aspect of this problem and its practical significance related primarily to the issues of stability of the *por*-Si surface and the possibility of using the *por*-Si samples as gas sensors.

It has been established that the *por*-Si is highly sensitive to various chemical treatments owing to the well-developed surface area of this material (up to 600 m^2/cm^3) [1]. Optical properties of *por*-Si are affected appreciably by these treatments [2]. It is noteworthy that the *por*-Si surface is coated predominantly with hydrogen atoms in the course of its preparation. However, this coating is not resistant to external effects. In particular, if the as-prepared *por*-Si is exposed to atmospheric air, a partial replacement of hydrogen atoms with oxygen atoms occurs; thus, an oxide coating is formed. Formation of such a coating is accompanied with an increase in the concentration of surface defects (the dangling bonds) that are effective centers of nonradiative recombination, as a result of which a degradation in the PL of *por*-Si is observed.

The authors of [3] attempted to replace the hydrogen coating with a deuterium coating. In doing so, it was found that the PL peak shifts to shorter wavelengths and the degradation of PL is significantly delayed. It was observed [4] that the rate of oxidation of *por*-Si in heavy water is much higher than this rate in ordinary water. The role of deuterium is still not quite clear. In connection with this, the objective of this work was to study optoelectronic properties of *por*-Si produced in an electrolyte containing heavy water.

2. EXPERIMENTAL

The *por*-Si samples to be studied were prepared by electrochemical etching of Si in an electrolyte containing heavy water, HF (48%) : D_2O = 1 : 1, with the current density equal to j = 50 mA/cm^2. The etching duration was 5 min. The thickness of the thus obtained layers of porous silicon (*por*-Si:D) was about 5 μm, with a porosity amounting to $p \sim 70$–75%.

The infrared (IR) transmission spectra of *por*-Si were measured using a Perkin-Elmer spectrometer in the range of 200–4000 cm^{-1}. In order to measure the PL, we used an automated system based on an MDR-23 monochromator and an FEU-136 photomultiplier. The PL was excited with nitrogen-laser radiation (with a wavelength of λ = 337 nm and a pulse duration of τ = 10 ns). The concentration of surface defects was measured by the electron-spin resonance (ESR) using a conventional SP-100Kh ESR spectrometer operating at 9.45 GHz and having a sensitivity of 5×10^{10} spin/G.

3. RESULTS AND DISCUSSION

The IR transmission spectra of as-prepared *por*-Si:D samples were indicative of the presence of Si–H_x bonds (~2100 cm^{-1}) and Si–D_x bonds (~1510–1530 cm^{-1}) and of an insignificant concentration of oxygen (~1000 cm^{-1}) (Fig. 1). The samples exhibited a PL band I_{PL} that was peaked at ~660 nm and had a relatively low intensity (Fig. 2). Exposure of the samples to atmospheric air for a month resulted in an increase in the magnitude of the oxygen-related absorption band, with the hydrogen concentration being apparently unchanged (Fig. 1). It is important that the PL intensity of *por*-Si:D remained virtually unchanged as a result of this treatment in contrast with the PL of porous Si prepared in conventional electrolytes (*por*-Si:H). In the case of the samples of

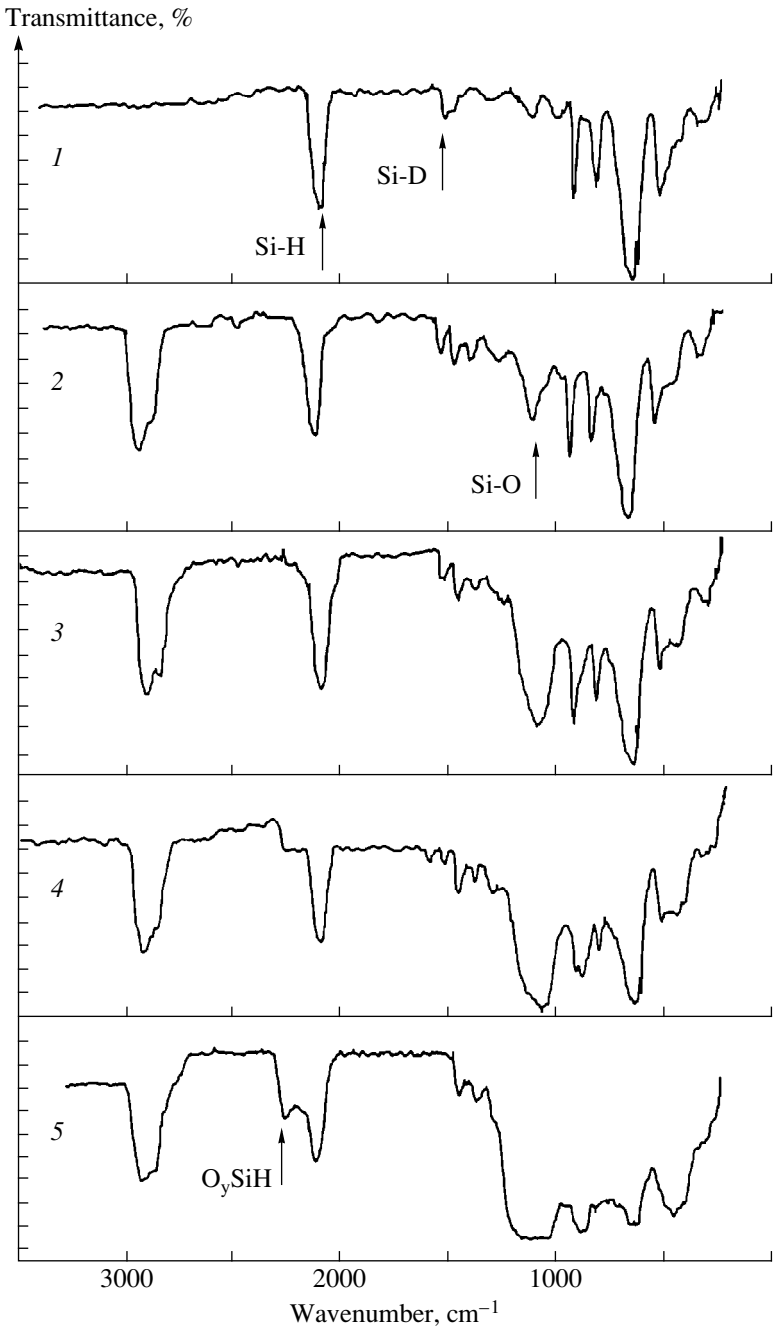

Fig. 1. The IR transmission spectra of (*1*) the as-prepared *por*-Si sample and of the *por*-Si samples exposed to atmospheric air for (*2*) 5, (*3*) 30, (*4*) 90, and (*5*) 450 days.

por-Si:H, a decrease in the concentration of Si–H bonds occurs as a result of exposure to atmospheric air; simultaneously, a decrease in PL intensity is observed, which is related to an increase in the concentration of surface defects [5]. Thus, the presence of deuterium at the surface of *por*-Si brings about a preservation of the hydrogen coating.

If the exposure to atmospheric air (natural oxidation) was prolonged, a significant increase in the PL intensity and the emergence of a band peaked at ~2250 cm^{-1} in the IR spectrum and related to the O_ySiH complexes were observed (Fig. 1). A simultaneous decrease in the intensity of ESR signal I_{ESR} was recorded, which indicated that the surface-defect concentration decreased. It is noteworthy that, in contrast to what was observed in *por*-Si:H, the concentration of defects in *por*-Si:D was found to be lower by almost an order of magnitude (Fig. 3). The above data are apparently indicative of a radically different mechanism of oxidation of *por*-Si:D. The oxidation process does not

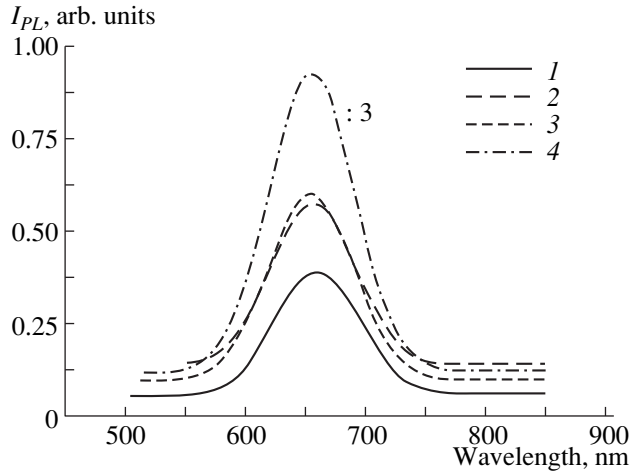

Fig. 2. PL spectra of (*1*) the as-prepared *por*-Si sample and samples exposed to atmospheric air for (*2*) 5, (*3*) 30, and (*4*) 90 days.

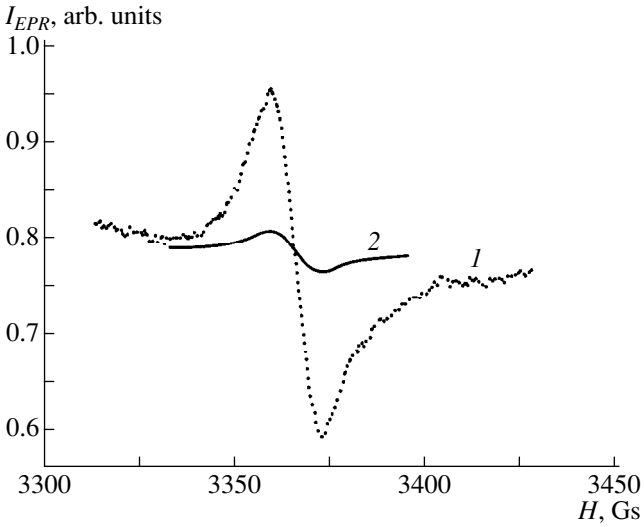

Fig. 3. The EPR signal from *por*-Si prepared (*1*) under conventional conditions and (*2*) in an electrolyte based on heavy water after exposure to atmospheric air for 450 days. *H* is the magnetic field.

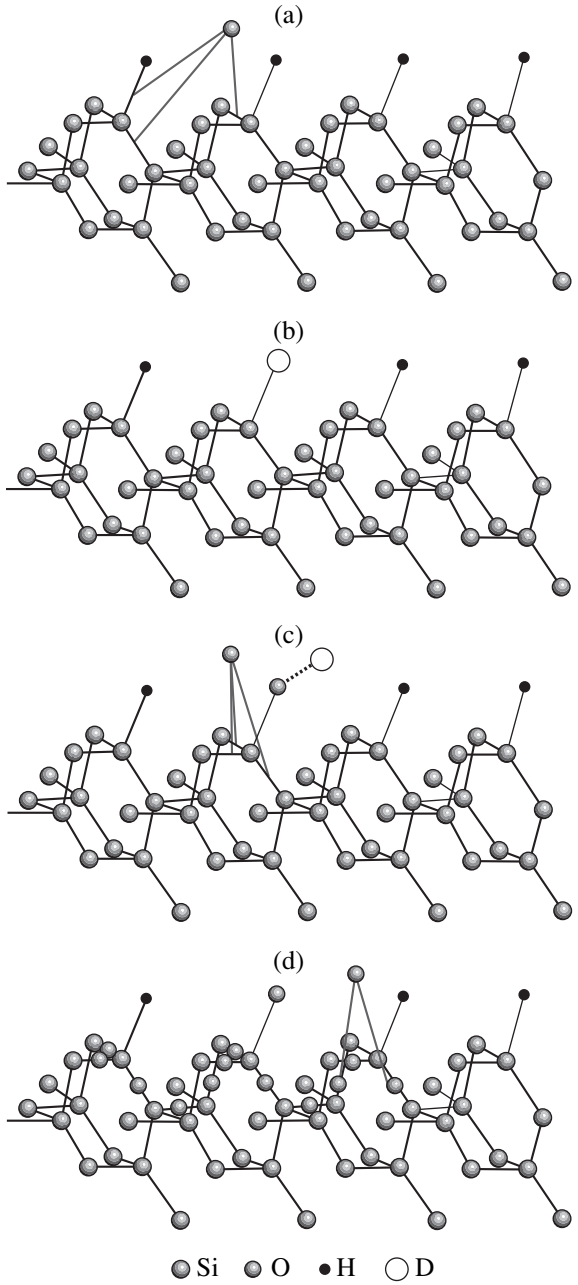

Fig. 4. A schematic representation of the *por*-Si oxidation.

affect the Si–H bonds. In this case, oxygen apparently breaks predominantly the "back" silicon bonds, which gives rise to O_ySiH complexes.

We now consider the possible causes of such an anomalous oxidation of *por*-Si:D. In the case of as-prepared porous silicon, two possible channels for oxidation can be distinguished [6, 7]. First, oxidation can occur at the Si–H bonds (the bond energy is ~72.1 kcal/mol [8]), and, as a result, the surface complexes Si–OH and SiO_x are formed. Second, oxygen can break the back Si–Si bonds (the bond energy is ~74.4 kcal/mol [8]) and initiate the formation of O_ySiH complexes (Fig. 4a). In the case of oxidation of *por*-Si:H exposed to atmospheric air, the first type of reaction is prevalent and is accompanied by an increase in the concentration of surface defects and, correspondingly, by a decrease in the PL intensity [5]. Taking into account the special features observed in the IR spectra that we measured (Fig. 1), we may assume that deuterium (along with hydrogen) in the form of individual localized Si–D complexes (Fig. 4b) is present at the surface of *por*-Si:D samples. As was mentioned above, the oxidation rate for *por*-Si in heavy water is much higher than that in light water [4]. Therefore, in the ini-

tial stage of oxidation, rapid formation of Si–OD complexes apparently occurs (Fig. 4c). However, the absence of the lines attributed to the Si–OD complexes (~1634 cm^{-1}) in the IR spectra (Fig. 1) suggests that such complexes are unstable and rapidly lose deuterium. As a result, a silicon atom bonded initially to deuterium is oxidized (Fig. 4c). The electron density is then shifted from the silicon atom to the oxygen atom, which has higher electronegativity. As a result, the energy of Si–Si bonds decreases. It is likely that this energy becomes lower than the energy of Si–H bonds. In this case, oxidation occurs predominantly with involvement of back Si–Si bonds (Fig. 4d). If the neighboring silicon atom is bonded to hydrogen (Si–H), the electron cloud is displaced closer to the oxygen atom [9], which results in an increase in the Si–H bond energy and in the formation of O_ySiH complexes at the *por*-Si:D surface (Fig. 4d). Consequently, the localized Si–D bonds serve as particular nucleation sites for oxidation of back Si–Si bonds. As a result, such a process becomes prevalent and the hydrogen coverage of *por*-Si is preserved.

4. CONCLUSION

We found that oxidation of *por*-Si:D in atmospheric air resulted in an increase in the PL intensity and in a decrease in the number of surface defects. The concentration of defects becomes lower by almost an order of magnitude than that for *por*-Si prepared under conventional conditions. We suggested that such an anomalous oxidation is based on the involvement of Si–D complexes localized at the surface of silicon nanostructures in the process of oxidation of back Si–Si bonds. For neighboring Si–H complexes, such a process brings about an increase in the Si–H bond energy and preserves the hydrogen coverage of the samples. Thus, the results obtained are indicative of modification of optoelectronic properties of porous silicon prepared in an electrolyte containing heavy water as compared to the corresponding properties of *por*-Si:H.

ACKNOWLEDGMENTS

This work was supported by the Russian Foundation for Basic Research (project no. 99-02-16664) and the Ministry of Science of Russian Federation under the Program “Surface Atomic Structures” (project no. 4.1.99).

REFERENCES

1. M. S. Bresler and I. N. Yassievich, Fiz. Tekh. Poluprovodn. (St. Petersburg) **27**, 873 (1993) [Semiconductors **27**, 475 (1993)].
2. B. V. Kamenev and V. Yu. Timoshenko, Poverkhnost, No. 11, 91 (1998).
3. T. Matsumoto, Y. Masumoto, S. Nakashima, and N. Koshida, Thin Solid Films **297**, 31 (1997).
4. D. N. Goryachev, G. Polisskiĭ, and O. M. Sreseli, Fiz. Tekh. Poluprovodn. (St. Petersburg) **32**, 1016 (1998) [Semiconductors **32**, 910 (1998)].
5. P. K. Kashkarov, E. A. Konstantinova, and V. Yu. Timoshenko, Fiz. Tekh. Poluprovodn. (St. Petersburg) **30**, 1479 (1996) [Semiconductors **30**, 778 (1996)].
6. D. Mawhinney, J. Glass, Jr., and T. Yates, J. Phys. Chem. B **101**, 1202 (1997).
7. W. Theiss, Surf. Sci. Rep. **29**, 91 (1997).
8. L. V. Gurvich, G. V. Karachevtsev, V. N. Kondrat’ev, *et al.*, in *Energies for Splitting the Chemical Bonds. Ionization Potentials and Electron Affinity* (Nauka, Moscow, 1977), p. 116.
9. A. Borghesi, G. Guizzetti, A. Sassela, *et al.*, Solid State Commun. **89**, 615 (1994).

Translated by A. Spitsyn

Semiconductors, Vol. 34, No. 6, 2000, pp. 732–736. Translated from Fizika i Tekhnika Poluprovodnikov, Vol. 34, No. 6, 2000, pp. 757–761.

AMORPHOUS, VITREOUS, AND POROUS SEMICONDUCTORS

Optical and Electrical Properties of Porous Gallium Arsenide

**N. S. Averkiev, L. P. Kazakova, É. A. Lebedev, Yu. V. Rud',
A. N. Smirnov, and N. N. Smirnova**

Ioffe Physicotechnical Institute, Russian Academy of Sciences, Politekhnicheskaya ul. 26, St. Petersburg, 194021 Russia

Submitted December 24, 1999; accepted for publication December 28, 1999

Abstract—Photoluminescence (PL), Raman scattering, and carrier transport have been studied for the first time in porous GaAs prepared on (111) oriented wafers of *n*-type crystalline GaAs (faces A and B). Peaks of the main PL band from faces A and B were observed at 1.82 and 1.88 eV, respectively. The electron drift mobility was found to be $\sim 4 \times 10^{-4}$ cm^2 V^{-1} s^{-1}. The nanocrystallite size in porous GaAs was determined both from PL spectra and from the Raman shift. The obtained values are close or equal to 6–8 nm. © *2000 MAIK "Nauka/Interperiodica".*

1. INTRODUCTION

A great number of studies concerned with preparation of porous silicon (*por*-Si) and investigations of its properties were initiated by the discovered possibility of modifying the physicochemical properties of the starting material (silicon) by a rather simple treatment, namely, by anodic etching. It seems rather promising to expand the application field of this technique to other semiconducting materials, in particular to gallium arsenide, which is one of the main materials of semiconductor electronics. In case of a positive result, this would extend the spectral range of luminescent electronics and allow the development of new types of light-emitting diodes and lasers. Moreover, new types of heterojunctions can be obtained using porous gallium arsenide (*por*-GaAs) as an intermediate layer. Efforts made in this direction have shown that this problem can be solved successfully [1]. Of particular interest is a comparison of properties of porous structures prepared from silicon and gallium arsenide, materials with very different physicochemical properties.

The problem of obtaining *por*-GaAs has been studied and its properties investigated in only a few works [2–5]. These were mainly concerned with the shift of the photoluminescence (PL) peak to shorter wavelengths upon subjecting the material to various treatments. The shift of the PL peak, observed in [2, 3], is presumably associated with the appearance of a surface layer of some other composition, and only the results obtained in [4, 5] suggest that this shift is due to quantum-confinement effects in GaAs nanocrystallites. There is no published data on the electrical properties of *por*-GaAs. In particular, carrier transport has not been studied at all.

Here, we report a technology for *por*-GaAs preparation. PL and Raman spectra were measured for the obtained samples and the carrier drift mobility was studied.

2. EXPERIMENTAL RESULTS AND DISCUSSION

2.1. Preparation of por-GaAs Samples

The *por*-GaAs samples were prepared by electrochemical etching of (111) oriented wafers of *n*-type GaAs with a carrier concentration of $\sim 7 \times 10^{15}$ cm^{-3}. At this orientation, etching channels were formed in a direction perpendicular to the sample surface. The etching was performed in an aqueous solution of hydrofluoric acid (8 : 1 by volume) with a sample illuminated with light from an incandescent lamp. The current density was 700–800 mA cm^{-2}. Etching channels were formed on both faces, A and B. With an electrolyte containing isopropyl alcohol, a film of some other color appeared on the sample surface and no etching channels were formed.

2.2. Photoluminescence

Spectra of steady-state PL $I_{PL}(\hbar\omega)$ were measured with excitation by an argon (photon energy $\hbar\omega \approx$ 2.4–2.7 eV and power of ~100 mW cm^{-2}) or a helium–cadmium lasers ($\hbar\omega \approx$ 2.82 eV and power of ~10 mW cm^{-2}). To eliminate possible unwanted radiation, a filter transmitting only the main laser radiation line was placed at the laser output and a filter completely absorbing the laser radiation was mounted at the monochromator entrance. The PL was analyzed using an MDR-3 monochromator with a 600-lines/mm grating and an FEU-62 photomultiplier. The PL spectra were normalized with regard to the spectral sensitivity of the photodetector and the optical transmission of the

measurement channel of the setup. The spectral resolution was no worse than 1 meV.

Figure 1 shows a spectral dependence of PL from faces A and B of a *por*-GaAs sample at two temperatures, $T = 300$ and 77 K. The PL spectra are characterized by the presence of a broad emission band lying in the region of fundamental absorption of GaAs. The full width at half-maximum of the band at 300 K is $\delta_{1/2} \approx 0.65$–$0.70$ eV. This value is smaller than that reported in [3] but larger than that in *por*-Si [5, 6].

At 300 K, the PL peak characteristic of face A typically lies at $E_A \approx 1.82$ eV, and that for face B, at $E_B \approx 1.88$ eV. The difference between these values, on the one hand, and the band gap of GaAs, on the other, is $\Delta E_A \approx 0.40$ eV and $\Delta E_B \approx 0.46$ eV, respectively. The difference between E_A and E_B may be due to specific physicochemical features of faces A and B and to the electric field distribution around a sample in the course of anodization.

Let us consider PL spectra from faces A and B typically observed at $T = 77$ K. The peak of PL from face A has practically the same energy position as the peak at 300 K. Different temperature dependences (positive, negative, or zero) of the PL peak energy have also been observed in *por*-Si. In particular, it was shown in [7] that whether the temperature dependence of the energy position of the PL peak is positive or negative is determined by the mechanism of light emission and, eventually, by the size of nano-objects constituting *por*-Si. Such temperature behavior of the PL peak may serve as evidence in favor of the existence of nanostructure in *por*-GaAs samples. On face B, the main band at $T = 77$ K vanishes. In their long-wavelength regions, spectra from faces B and A exhibit a narrow peak at 1.502 and 1.51 eV, respectively. This peak is apparently associated with quasi-interband transitions in the starting GaAs at 77 K.

The shift of the main PL band of *por*-GaAs samples obtained by anodic etching with respect to that of crystalline GaAs can be explained on assumption that size quantization of carrier energies occurs as a result of nano-object formation.

The change in the transition energy due to size quantization can be represented as [8]

$$\Delta E = \frac{\pi^2 \hbar^2}{2d^2}\left(\frac{1}{m_t^e} + \frac{1}{m_h^h}\right). \quad (1)$$

If we assume that the PL spectrum is formed by emission of a set of oscillators, the largest fraction of oscillators emit light with energy $E = E_{max}$, where E_{max} is the PL peak energy. The depth of a potential well for these nano-objects is given by

$$\Delta E = E_{max} - E_g, \quad (2)$$

where E_g is the band gap. Equating (1) and (2), we can estimate at ~6 nm the size of crystallites whose emission determines the PL peak energy for side B.

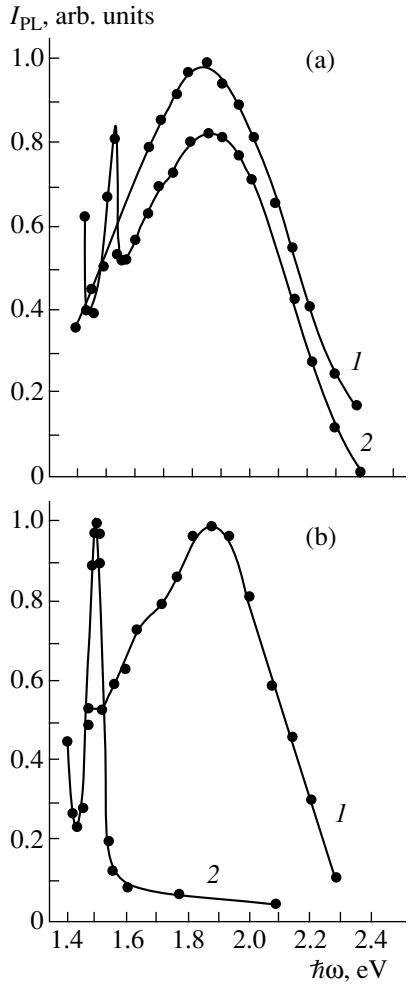

Fig. 1. PL spectra of *por*-GaAs from faces (a) A and (b) B at $T =$ (*1*) 300 and (*2*) 77 K.

2.3. Raman Scattering

Raman spectra were measured at room temperature in inverse configuration on an automated setup based on a DFS-24 double grating monochromator. An Ar^+ ion laser with a radiation wavelength of 488 nm was used as the excitation source. The spectral resolution was 1.5 cm^{-1}. The spectra were processed using special-purpose software.

Figure 2 shows the Raman spectra for crystalline GaAs and *por*-GaAs. The frequencies and linewidths of the optical modes of GaAs are, respectively, 292.3 and 4.1 cm^{-1} for the LO phonon and 269.0 and 4.5 cm^{-1} for the TO phonon. In passing from crystalline to porous GaAs, both phonon lines are shifted to lower frequencies and broadened. The most pronounced changes are observed for the spectrum taken from face B of sample no. 7 (curve *4*). The shift is 2 cm^{-1} at a linewidth of 5.1 cm^{-1} for the TO mode and 2.4 cm^{-1} at a linewidth of 7 cm^{-1} for the LO mode. Together with the changes

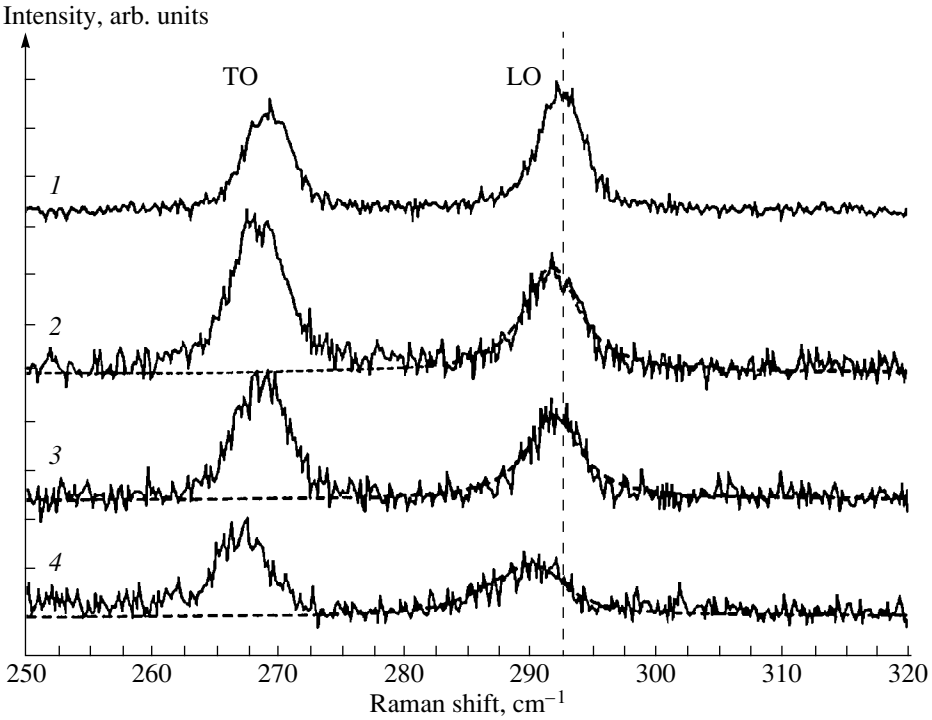

Fig. 2. Raman spectra $z(yy)\bar{z}$: of (*1*) crystalline GaAs; (*2* and *4*) *por*-GaAs, face B, etching time (*2*) 4 and (*4*) 6 min (sample no. 7); and (*3*) *por*-GaAs, face A, etching time 6 min. $L \approx$ (*2*) 15, (*3*) 17, and (*4*) 6–8 nm.

described above, intensity redistribution between the TO and LO modes occurs as well.

Comparison of our results with the data obtained in [9] suggests that the crystallite size in the samples under study ranges from 5 to 20 nm. This parameter was evaluated quantitatively using the phonon confinement model [10]. In terms of this model and under assumption of a spherical shape of GaAs nanocrystallites, the frequency dependence of the Raman intensity is described by

$$I_s(\omega) = \int_0^1 \frac{dq \exp(-q^2L^2/4)4\pi q^2}{[\omega - \omega(q)]^2 + (G_0/2)^2}, \qquad (3)$$

where q is expressed in units of $2\pi/a_0$, $a_0 = 5.65$ Å is the lattice constant of bulk GaAs, L is the crystallite diameter, and G_0 is the linewidth of the optical-phonon band in crystalline GaAs. As the dispersion relation for the longitudinal phonon, we used the expression $\omega(q) = 292.5 - 6.91q - 43q^2$. Dashed lines in Fig. 2 show the results of fitting for the LO mode. The crystallite size on face B of sample no. 7 was 6 nm. This value is close to $L = 8$ nm obtained in terms of the same model using a dispersion relation $\omega(q) = 269.5 + 22.5\cos(q\pi)$ from [11]. Thus, both estimates coincide with the value of L obtained for the same sample from PL data.

2.4. Charge-Carrier Transport

The drift mobility of carriers was studied in *por*-GaAs samples prepared by the technique described above. The samples had "sandwich" configuration. A crystalline GaAs wafer was used as the bottom electrode. A semitransparent aluminum top electrode was deposited by vacuum evaporation onto the porous GaAs layer. The resistance of the samples in an electric field of 10^3 V cm^{-1} was ~10^8 Ω for a top electrode area of $S \approx (1–2) \times 10^{-2}$ cm^2.

The drift mobility was studied by measuring the transit time of charge carriers [12]. The measurements were performed with high-level injection, with the transient photocurrent being space-charge limited (SCL) [13].

Nonequilibrium carriers were injected into the sample by means of a strongly absorbed radiation of an LGI-21 nitrogen laser (wavelength of 0.337 μm and pulse duration of ~8 ns). Photocurrent pulses associated with electron drift were analyzed. The small signal in the case of holes made observation of the drift of holes practically impossible.

Transient SCL currents were measured with ~1-ms-long pulses of voltage applied to the samples with a delay of ~300 μs between the instants of voltage turn-on and photoinjection.

Figure 3 shows oscillograms of photocurrent pulses observed in the case of electron drift. The shape of the obtained oscillograms of transient current $I(t)$ is typical of the SCL currents. The dependence $I(t)$ is character-

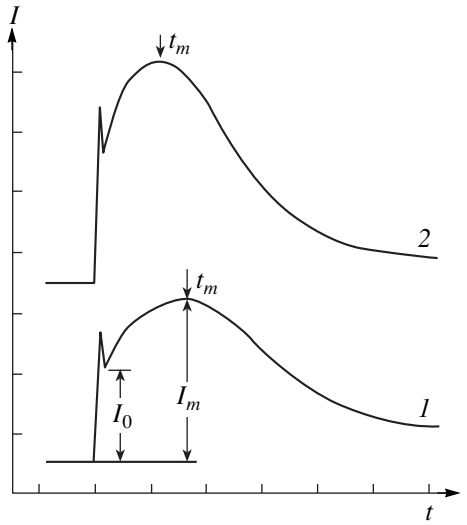

Fig. 3. Oscillograms of the transient photocurrent $I(t)$ associated with electron drift in *por*-GaAs. Voltage V = (*1*) 5 and (*2*) 6 V. The time scale is 10 μs per division, and the current scale is 2 μA per division.

ized by initial (I_0) and peak (I_m) currents. The current is practically independent of the intensity of the carrier-injecting radiation, with a quadratic dependence of the currents I_0 and I_m on voltage. However, the I_m/I_0 ratio is smaller than 2.7, the value characteristic of the ideal SCL current. This is apparently due to an insufficiently high injection level.

The time t_m corresponding to the peak current varies in inverse proportion to the voltage V applied to the sample.

Under SCL current conditions, the carrier drift mobility (μ) can be found both from the transit time

$$t_T = L_d^2/\mu V \quad (4)$$

related to t_m by $t_m = 0.8\ t_T$ and from the initial current density [13]

$$j_0 = I_0/S = \mu\varepsilon V^2/2.25\times 10^{13} L_d^3, \quad (5)$$

where L_d is the layer thickness and ε is the dielectric constant. Since the exact thickness of the layer in which carrier drift occurs was unknown, the system of equations (4) and (5) was used to find two quantities: L_d and μ. In doing so, it was assumed that, similarly to the case of *por*-Si [14], the dielectric constant of *por*-GaAs is approximately half as large as that in the crystalline material, i.e., $\varepsilon \approx 6$. The values of t_T and j_0 were determined from the t_m and I_0 values found from the experimental curves of transient SCL current. The system of equations (4) and (5) was solved to yield the electron drift mobility $\mu \approx 4.0\times 10^{-4}$ cm^2 V^{-1} s^{-1} and the thickness of the layer across which the carriers drift, $L_d \approx 2.1$ μm.

The relatively small value of L_d indicates that the deeper region of *por*-GaAs with coarser pores has low resistance. Consequently, the voltage applied to the sample drops across the near-surface layer with thickness on the order of 2.1 μm. It is in this high-resistance layer that nanocrystals are apparently located and where they manifest themselves in photoluminescence and Raman scattering.

Regarding the value of μ obtained for *por*-GaAs, it should be noted that it is close to the charge-carrier drift mobility in *por*-Si layers with structural units 3.5–5 nm in size [15]. This fact points to a certain similarity between *por*-GaAs and *por*-Si.

3. CONCLUSION

Thus, we developed a method for obtaining porous gallium arsenide layers on faces A and B of (111) oriented *n*-type GaAs wafers. The PL spectrum of *por*-GaAs is characterized by the main band peaked at E_A = 1.82 eV and E_B = 1.88 eV for faces A and B, respectively. The difference between these values and the band gap of the starting material is ΔE_A = 0.40 eV and ΔE_B = 0.46 eV. The shift of the PL peak for *por*-GaAs with respect to that for GaAs was used to estimate the nanocrystallite size in *por*-GaAs as ~6 nm. An estimate of the same parameter from the Raman spectra yielded 6–8 nm.

The electron drift mobility in *por*-GaAs layers is $\sim 4\times 10^{-4}$ cm^2 V^{-1} s^{-1}. The obtained value is close to the charge-carrier mobility in nanoporous silicon, which points to the similarity of the transport mechanisms in these materials.

4. ACKNOWLEDGMENTS

We are grateful to V.Yu. Davydov and N.I. Sablina for their assistance in conducting this study. This work was supported by the Program "Physics of Solid Nanostructures" (project nos. 97-1039 and 99-1107).

REFERENCES

1. V. V. Mamutin, V. P. Ulin, V. V. Tret'yakov, *et al.*, Pis'ma Zh. Tekh. Fiz. **25** (1), 3 (1999) [Tech. Phys. Lett. **25** (1), 1 (1999)].
2. A. A. Lebedev and Yu. V. Rud', Pis'ma Zh. Tekh. Fiz. **22** (6), 13 (1996) [Tech. Phys. Lett. **22**, 483 (1996)].
3. D. N. Goryachev and O. M. Sreseli, Fiz. Tekh. Poluprovodn. (St. Petersburg) **31**, 1383 (1997) [Semiconductors **31**, 1192 (1997)].
4. Yu. N. Buzynin, S. A. Gusev, M. N. Drozdov, *et al.*, in *Proceedings of the 2nd Russian Conference on the Physics of Semiconductors, Zelenogorsk, 1996,* Vol. 2, p. 123.
5. L. P. Sidorova, S. A. Gavrilov, and A. V. Emel'yanov, in *Proceedings of All-Russia Science and Technology Conference on Microelectronics and Nanoelectronics, Zvenigorod, 1998,* Vol. 2, PP3-33.

6. X. L. Zheng, W. Wang, and H. C. Chen, Appl. Phys. Lett. **60** (8), 986 (1992).
7. A. Shimizu, Y. Yamada, G. Isutsu, *et al.*, Jpn. J. Appl. Phys. **35**, L276 (1996).
8. V. M. Asnin, N. S. Averkiev, A. B. Churilov, *et al.*, Solid State Commun. **87**, 817 (1993).
9. X. S. Zhao, Y. R. Ge, J. Schroeder, and P. D. Persans, Appl. Phys. Lett. **65**, 2033 (1994).
10. R. Ashokan, K. P. Jain, H. S. Mavi, and M. Balkanski, J. Appl. Phys. **60**, 1985 (1986).
11. K. K. Tiong, P. M. Amirtharaj, F. H. Pollak, and D. E. Aspnes, Appl. Phys. Lett. **44**, 122 (1984).
12. W. E. Spear, J. Non-Cryst. Solids **1**, 197 (1969) .
13. M. A. Lampert and P. Mark, *Current Injection in Solids* (Academic, New York, 1970; Mir, Moscow, 1973).
14. L. P. Kazakova, A. A. Lebedev, and É. A. Lebedev, Fiz. Tekh. Poluprovodn. (St. Petersburg) **31**, 609 (1997) [Semiconductors **31**, 517 (1997)].
15. E. A. Lebedev, E. A. Smorgonskaya, and G. Polisski, Phys. Rev. B **57** (23), 14607 (1998).

Translated by M. Tagirdzhanov

Semiconductors, Vol. 34, No. 6, 2000, pp. 737–740. Translated from Fizika i Tekhnika Poluprovodnikov, Vol. 34, No. 6, 2000, pp. 762–765.

AMORPHOUS, VITREOUS, AND POROUS SEMICONDUCTORS

Effect of Nanocrystalline Inclusions on the Photosensitivity of Amorphous Hydrogenated Silicon Films

O. A. Golikova and M. M. Kazanin

Ioffe Physicotechnical Institute, Russian Academy of Sciences, Politekhnicheskaya ul. 26, St. Petersburg, 194021 Russia

Submitted December 28, 1999; accepted for publication December 28, 1999

Abstract—Photosensitivity of amorphous hydrogenated silicon films containing inclusions of Si nanocrystals, along with spectral characteristics of photoconductivity, were studied. A correlation between photosensitivity and features of the Raman spectra was established. The highest photosensitivity is observed in films with medium-range order formed to the maximum extent. © *2000 MAIK "Nauka/Interperiodica".*

1. INTRODUCTION

Films of amorphous hydrogenated silicon (*a*-Si:H) containing inclusions of a second phase with dimensions on the order of several nanometers, i.e., inhomogeneous nanostructured films, presently generate much interest, in both the scientific and applied fields. Indeed, it has been shown [1–5] that *a*-Si:H films of this kind show enhanced photosensitivity $K = \sigma_{ph}/\sigma_d$ (σ_d and σ_{ph} are the dark conductivity and photoconductivity). Their photosensitivity exceeds by orders of magnitude the values for the conventional *a*-Si:H of device quality, determined under identical conditions. This result was unexpected, since it was believed that the best photoelectric properties could be observed in the most homogeneous films.

The problems concerning the nature of the inclusions and the relation between the value of *K* and the presence of inclusions cannot be considered solved, even though it is quite necessary for further progress in the physics of nanostructured films. This study is, in our opinion, a step forward in solving these problems.

2. EXPERIMENTAL RESULTS AND DISCUSSION

a-Si:H films were prepared by the same method as those studied in [4–6].

Information on film structure was obtained using Raman spectroscopy. The spectra were measured using a U–1000 system (frequency range ω = 20–620 cm^{-1}, step 1 cm^{-1}, spectral width of the slit 5 cm^{-1}, measurement accuracy ±2.5 cm^{-1}). The wavelength of the exciting radiation was λ = 488 nm at a power of 100 mW [7]. Figure 1 shows typical spectra for some films: films of conventional *a*-Si:H (curve *1*) and nanostructured films (curves *2–4*). Bands at ω = 515–517 cm^{-1}, characteristic of Si(*nc*) nanocrystals, were observed near the TO-phonon band in some films (e.g., curve *2*). However, it was found experimentally that the distribution of nanocrystals in the films cannot be considered uniform. The nanocrystallite dimensions (d_R) and the contribution of the crystalline phase (X_c) were evaluated using conventional techniques to be d_R = 4–5 nm and X_c = 0.05–0.2. In addition, as is discussed below, the Raman spectra were also analyzed in the region of LA phonons, at around ω = 300 cm^{-1}.

The photosensitivity *K* was determined at room temperature; the σ_{ph} value was measured at incident photon energy $\hbar\omega$ = 2 eV and photocarrier generation rate $G = 10^{19}$ cm^{-3} s^{-1}.

With increasing X_c, the value of *K* decreased from 10^4 to 10^3. Nevertheless, if the dimensions of nanocrystalline Si inclusions are 4–5 nm and their contribution is about 5%, *a*-Si:H films still meet the requirements for conventional device-quality material as regards the value of *K*.

However, the Raman spectra of films with large values of *K* contain no bands characteristic of Si nanocrystals (Fig. 1, curves *3*, *4*). This, in all probability, is a consequence of the smaller dimensions of nanocrystals embedded in the amorphous matrix.

The data presented in Fig. 2 indicate that, judging from the value of *K*, formation of nanoinclusions is favored by higher deposition temperature T_s. It should be noted here that films with $K > 10^4$ are characterized by hydrogen content C_H increased approximately twofold as compared to conventional *a*-Si:H films deposited at the same temperatures [5].

Figure 3 presents *K* in relation to the activation energy of dark conductivity $\Delta E = (\varepsilon_c - \varepsilon_F)_{T=0}$, where *c* is the conduction-band bottom energy and *F* is the Fermi level. Points *1* refer to conventional *a*-Si:H. Although σ_{ph} falls for $\Delta E > 0.85$ eV, σ_d falls too [6], so that the value of *K* changes only slightly. Curve *2* refers to *a*-Si:H films containing Si nanocrystals as indicated by Raman spectroscopy; in this case, σ_{ph} falls more steeply than σ_d does, and, therefore, *K* decreases to

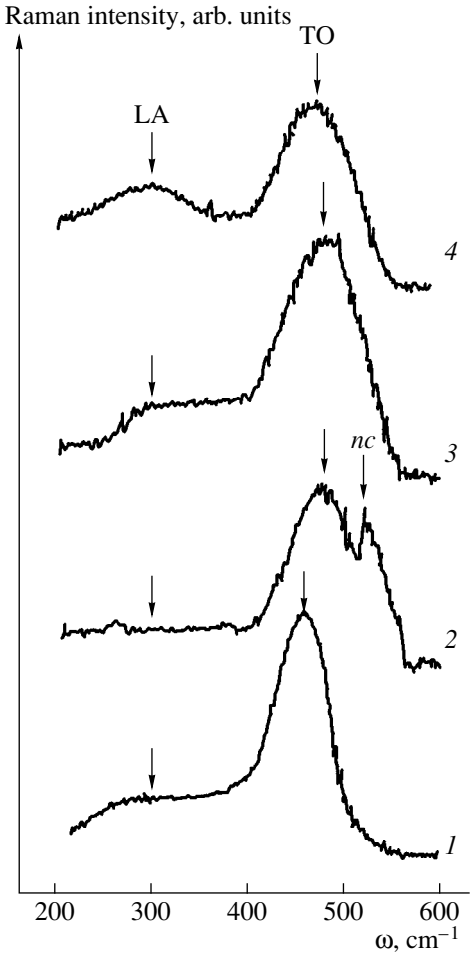

Fig. 1. Raman spectra for *a*-Si:H films: (*1*) for a conventional film; (*2*) for a film with $K = 10^4$ containing Si nanocrystalline inclusions ($d_R = 5$ nm and $X_c = 0.05$); (*3* and *4*) for films with $K =$ (*3*) 10^5 and (*4*) 10^6 containing smaller inclusions.

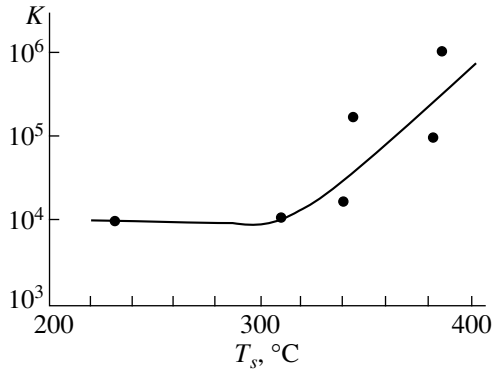

Fig. 2. Photosensitivity K as a function of film deposition temperature T_s. Silane pressure during deposition was 40–60 mTorr and RF discharge power density was 1.3–1.5 W cm^{-2}.

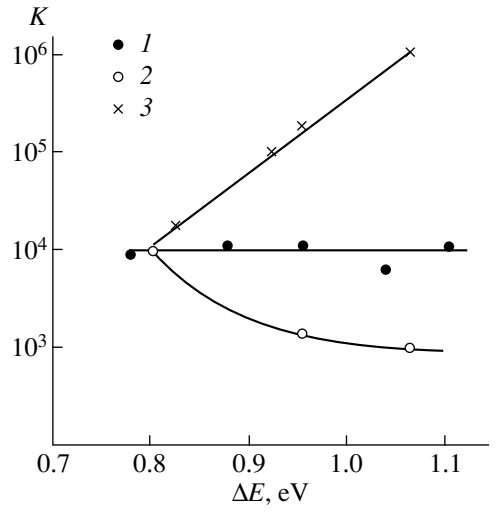

Fig. 3. Photosensitivity as a function of the dark conductivity activation energy: (*1*) for films of conventional *a*-Si:H; (*2*) for *a*-Si:H films with Si nanocrystalline inclusions revealed by Raman spectroscopy, and (*3*) for *a*-Si:H films in which Raman spectroscopy detects no Si nanocrystalline inclusions.

become as low as 10^3. Finally, points *3* refer to films in which no Si nanocrystals were revealed by Raman spectroscopy (see Fig. 1, curves *3*, *4*). As can be seen from Fig. 3, these films have the largest K, as high as 10^6, as a result of an increase in σ_{ph}. Thus, it follows from Fig. 3 that, for $\Delta E =$ const, the value of K is determined by the film structure.

In [4], we reported data on the spectral dependence of σ_{ph} for a film with enhanced photosensitivity. It was shown that an additional peak at $\lambda = 540$ nm is observed together with the main peak at $\lambda = 620$ nm. Since the corresponding energy ($\hbar\omega = 2.3$ eV) is close to the band gap E_g of nanocrystalline silicon, it was assumed that the spectral dependence of σ_{ph} can serve as a test for detecting Si nanocrystals in *a*-Si:H films in those cases when Raman spectroscopy fails to reveal them.

Here, we present spectral characteristics of photoconductivity for a number of *a*-Si:H films in relative units $\sigma_{ph}/\sigma_{ph(max)}$, where $\sigma_{ph(max)}$ is the peak value of the spectral dependence of photoconductivity (Fig. 4a).

Figure 4a presents data for a conventional *a*-Si:H film with $\Delta E = 0.92$ eV and $K = 10^4$ and also for three films with progressively increasing K. The curve for the conventional film is peaked at $\lambda = 640$ nm and shows no features; its asymmetry ratio is unity. The peaks for all other films are somewhat shifted to shorter wavelengths, and the curves themselves differ from one another and from the curve obtained for the conventional *a*-Si:H film. This refers to their spectral features for $\lambda = 540$ nm.

While the curve for a film with $K = 10^4$ shows a peak at $\lambda = 540$ nm, another film, with higher K, exhibits at

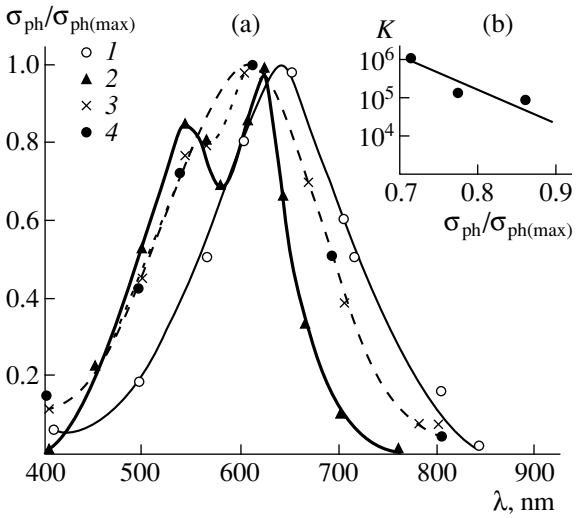

Fig. 4. (a) Spectral characteristics of photoconductivity for (*1*) films of conventional *a*-Si:H and (*2–4*) films with progressively increasing photosensitivity; and (b) correlation between photosensitivity and features of the spectral characteristics at $\lambda = 540$ nm.

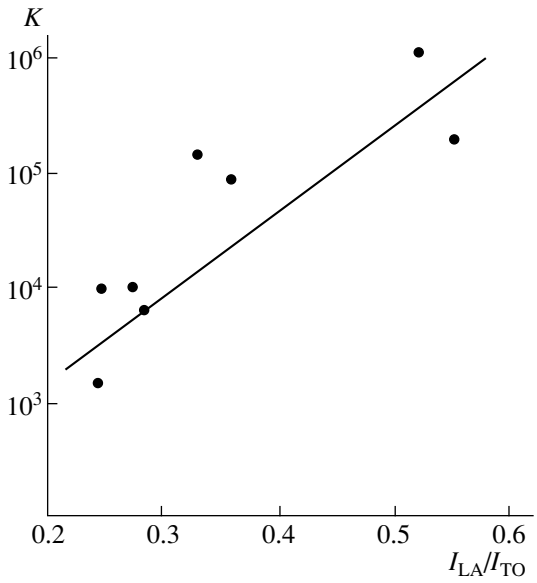

Fig. 5. Photosensitivity as a function of the I_{LA}/I_{TO} ratio.

this wavelength only a shoulder (Fig. 4a). Finally, the spectrum of the film with the highest K shows no features at $\lambda = 540$ nm. It should be emphasized, however, that, in contrast to conventional *a*-Si:H, the asymmetry ratio is 1.3 in this case.

The correlation between the values of K and the features of the spectral characteristics of σ_{ph} at $\lambda = 540$ nm is illustrated in Fig. 4b.

It follows from the data presented in Fig. 4 that, under certain critical conditions, the spectral characteristic of σ_{ph} is no more sensitive to the presence of Si nanocrystalline inclusions. These conditions apparently involve both decreasing dimensions of inclusions and their more uniform distribution throughout the films. In this case, the contribution from the crystalline phase apparently ceases to be significant.

We now return to the Raman spectra (Fig. 1). Let us consider the value of K in relation to the ratio I_{LA}/I_{TO}, where I_{LA} is the intensity of the LA band at $\omega = 300$ cm^{-1} and I_{TO} is the peak intensity of the TO band (Fig. 5). The ratio I_{LA}/I_{TO} is considered characteristic of the medium-range order in the film structure. Indeed, the LA band has been associated previously with the existence of inclusions in the form of clusters in *a*-Si:H films [8]. The same viewpoint is held now. In particular, the Raman spectra are calculated using models of *a*-Si:H with varied medium-range order (see, e.g., [9]).

The data presented in Fig. 5 indicate that an increase in K is directly related to the formation of a medium-range order in the film structure. A medium-range order formed to the maximum extent can be characterized as a uniform distribution of Si nanocrystalline inclusions, with defects at their boundaries completely passivated by hydrogen. The optimal dimensions of the inclusions remain unknown.

3. CONCLUSION

To summarize, we outline the principal results of this work and make conclusions on their basis.

(1) The photosensitivity K of *a*-Si:H films containing Si nanocrystalline inclusions with dimensions d_R = 4–5 nm falls from 10^4 to 10^3 with an increasing fraction of such inclusions (X_c = 0.05–0.2). In this case, no medium-range order is formed in the film structure. The inclusions are distributed in the amorphous matrix nonuniformly. Defects (Si–Si dangling bonds) at their boundaries, unpassivated by hydrogen, are additional centers of recombination for photocarriers.

(2) Spectral characteristics of σ_{ph} of films with $K \approx 10^5$ are sensitive to the presence of nanocrystalline Si inclusions. A medium-range order starts to form in the structure of such films.

(3) The highest value of K (up to 10^6) are observed in films with medium-range order formed to the maximum extent. As regards the structural ordering, these films occupy an intermediate position between the conventional *a*-Si:H and crystalline Si. As a result, the photoconductivity of such nanostructured films increases dramatically as compared to that of *a*-Si:H. At the same time, as demonstrated previously [1–3], their optical properties (E_g and a high absorption coefficient in the visible region of the spectrum) remain the same as in *a*-Si:H. It is this combination of properties that makes nanostructured films particularly promising for practical applications.

REFERENCES

1. P. Roca i Cabarrocas, S. Hamma, P. St'ahet, *et al.*, in *Proceedings of the 14th European Photovoltaic Energy Conference, Barcelona, 1997*, P5A.20.
2. P. St'ahel, S. Hamma, P. Sladek, and P. Roca i Cabarrocas, in *Abstracts of the ICAMS 17, Budapest, 1997*, Th-B214.
3. P. Roca i Cabarrocas, S. Hamma, S. N. Sharma, *et al.*, in *Abstracts of ICAMS 17, Budapest, 1997*, Th-B3/5.
4. O. A. Golikova and M. M. Kazanin, Fiz. Tekh. Poluprovodn. (St. Petersburg) **33**, 110 (1999) [Semiconductors **33**, 97 (1999)].
5. O. A. Golikova and M. M. Kazanin, Fiz. Tekh. Poluprovodn. (St. Petersburg) **33**, 336 (1999) [Semiconductors **33**, 335 (1999)].
6. O. A. Golikova and V. Kh. Kudoyarova, Fiz. Tekh. Poluprovodn. (St. Petersburg) **29**, 1128 (1995) [Semiconductors **29**, 584 (1995)].
7. O. A. Golikova and V. Kh. Kudoyarova, Fiz. Tekh. Poluprovodn. (St. Petersburg) **32**, 876 (1998) [Semiconductors **32**, 779 (1998)].
8. K. Maley and J. S. Lannin, Phys. Rev. B **36**, 1146 (1987).
9. Marinov, N. Zotov, N. Mousseau, and G. Barkema, in *Abstracts of ICAMS 17, Budapest, 1997*, Tu-P1/15.

Translated by M. Tagirdzhanov